Numerical Analysis of Cylindrical Cavities Used for Microwave Heating, Employing the Mode Matching Technique

A. P. Orfanidis[1], **G. A. Kyriacou**[1], **and J. N. Sahalos**[2]

[1]Democritus University of Thrace, Xanthi, Greece
[2]Aristotle University of Thessaloniki, Thessaloniki, Greece

Abstract— The analysis and design of a cylindrical cavity for microwave heating applications, including the feeding mechanism is proposed in this paper. The cylindrical cavity design aims at the production of a uniform field distribution, avoiding non-uniform heating and thermal runaway. The analysis of the device is based on the Mode Matching Technique. This has been proved to be an efficient and robust technique for the analysis of multiple discontinuities. The feeding structures maybe a circular, rectangular or coaxial waveguide. All quantities involved in the analysis are evaluated analytically achieving a fast and accurate method.

1. INTRODUCTION

The application of high power microwaves for thermal processing of dielectric materials, has received a great attention in the past. The benefits of using microwaves instead of conventional heating mechanisms are mainly due to the fact that microwave energy can penetrate the material achieving rapid internal heating. The main disadvantages are non-uniform heating and thermal runaway [1].

As rectangular cross-section cavities are mainly used, the amplitude field distribution depends on the cavity dimensions and the modes excited in the cavity. Even for a high order modes cavity there is a great fluctuation of the field distribution, resulting in non uniform heating of the material under process. Many techniques have been proposed to overcome this problem, such as the frequency variation and the field disturbance using a metallic blade. Frequency variation can be used only in relatively low power or small size devices, since high power microwave generators cannot alter their frequency. Moreover, the use of a metallic blade in a high power microwave cavity will produce high voltage arcs with unpredictable results.

The main strength of rectangular and in particular cubic cavities is the possibility of high order mode degeneration. Namely, up to 12 modes can be made to resonate at the frequency of operation. The always challenging question is, what is the appropriate excitation which optimally excites all modes, in order to achieve homogeneous heating energy deposition. Instead of working toward this direction, the present work tries to examine the possibility of producing uniform fields using cylindrical cavities either ordinary or with corrugated walls. The corrugations aim at the establishment of a hybrid HE_{11} mode which is expected to present a more homogeneous field distribution. The exact analysis of the cavity as well as the feeding mechanism will be performed using a closed-form mode matching technique. Since all the involved coupling integrals are evaluated analytically, this results in a very fast and compact technique without numerical instabilities. The dimensions of the cavity and the feeding source section will be designed aiming at the higher possible uniformity of the field amplitude. The feeding structure can be a circular, rectangular, coaxial waveguide or a combination of them. Its position will be optimized for the proper excitation of all necessary modes in the cavity. The material to be heated will be inserted to the cavity with the aid of a moving belt, since the device aims at industrial applications, as shown in Fig. 1. For this purpose, two openings will be included in the cavity, while $\lambda/4$ chokes will prevent microwave leakage [2].

2. GEOMETRY OF THE MICROWAVE HEATING STRUCTURE

A three dimensional view of the structure to be used for microwave heating is shown in Fig. 1(a). The structure is simplified for electromagnetic simulation convenience reasons. A vertical cross section of the simplified structure is shown in Fig. 1(b). In order to apply the Mode Matching technique the latter structure can be identified as comprised of waveguide sections as shown in Fig. 1(b). The purpose of the Mode Matching technique is to characterize each discontinuity between different waveguides through a generalized scattering matrix. In turn, all the discontinuity scattering matrices along with those of the waveguide section are combined together to yield a system matrix representing the whole structure.

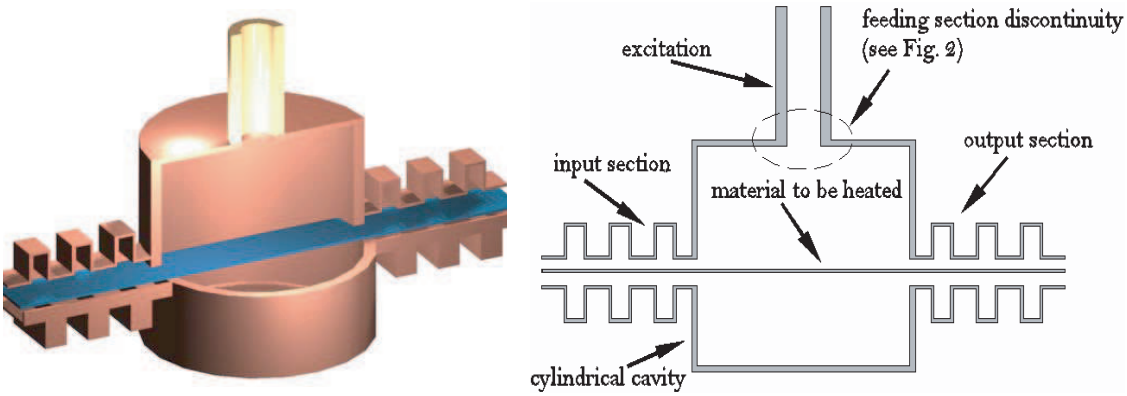

Figure 1: Microwave heating device, a) three dimensional view, b) vertical cross-section.

3. MODE MATCHING ANALYSIS OF A CYLINDRICAL CAVITY

The electromagnetic analysis of the device is based on a closed-form Mode Matching-Generalized Scattering Matrix method. The analysis of the feeding mechanism consists of a discontinuity between a circular waveguide and a smaller offset rectangular (Fig. 2(a)), circular or coaxial one (Fig. 2(b)). The best way to achieve this task is the analytical evaluation of the quantities involved in the analysis instead of any numerical integration. A mode matching technique handling offset circular and offset coaxial waveguides has been established in our previous work, [3]. Concerning, the offset rectangular-to-circular waveguide discontinuity, a similar mode matching is developed for the needs of the present work, as proposed in [4]. Let us briefly describe the basic ideas implemented in this technique.

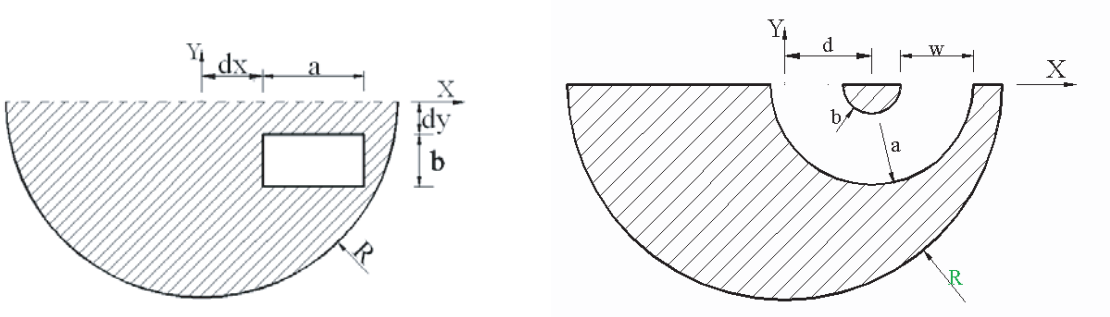

Figure 2: a) Discontinuity between a circular and an offset rectangular waveguide, b) Discontinuity between a circular and an offset coaxial waveguide.

Since the two waveguides of Fig. 2 are offset, their eigenfunctions are expressed with respect to a coordinate system having a z-axis coinciding with the waveguide axis of symmetry. These eigenfunctions must be expressed in a common coordinate system. Since the integration limits are described by the coaxial waveguide aperture, it was found more convenient to transform the eigenfunctions of the circular waveguide to the offset coordinate system of the coaxial one using the Graff's formula [5, p.363]. Then by properly transforming the eigenfunctions of the two waveguides from the cylindrical to rectangular coordinate system, the coupling integrals take the form of a product of Bessel functions with the same order. This expression is known as the Lommel integral and can be evaluated analytically, e.g., Abramowitz and Stegun [5, p.484]. In this way, the coupling integrals involved in the mode matching technique are evaluated analytically and finally the junction generalized scattering parameters are given in closed form.

Regarding the two apertures at the side walls of the cavity aiming at the introduction of the material to be heated in the cavity, these are also analyzed using the same method as proposed in [6]. It consists of a T-junction between a cylindrical and a rectangular waveguide, while the suppression of the energy leakage is made using $\lambda/4$ rectangular waveguide chokes.

4. NUMERICAL RESULTS

The first device analyzed was a circular cavity loaded with a dielectric disk at the middle of the cavity (see Fig. 1(b)). The excitation is made by a stepped concentric circular waveguide, while the two side wall openings were omitted for simplification reasons. The device consists of a cavity having $R = 268.7\,\text{mm}$, $l = 61.78\,\text{mm}$, a feeding waveguide with $R = 35\,\text{mm}$ and a circular dielectric disk with thickness $t = 10\,\text{mm}$, $\varepsilon_r = 4.0$ located at the center of the cavity. The analysis was made at $f_0 = 2.45\,\text{GHz}$, and the field distribution taking into account all the modes (propagating and evanescent) in the dielectric is shown in Fig. 3(a). It is obvious that the field distribution is far from being homogeneous. Next, in order to achieve a uniform transition between the feeding waveguide and the cavity, a taper section forming a conical section with taper angle $\alpha = 75^\circ$ was included. This is approximated by of a number of waveguides with stepped increasing radius. The resulting field distribution at the dielectric disk is shown in Fig. 3(b). Since higher order modes are excited in the cavity, the field maxima retains the form of concentric rings. This geometry can be used only in conjunction with a moving belt, in order to heat the material uniformly.

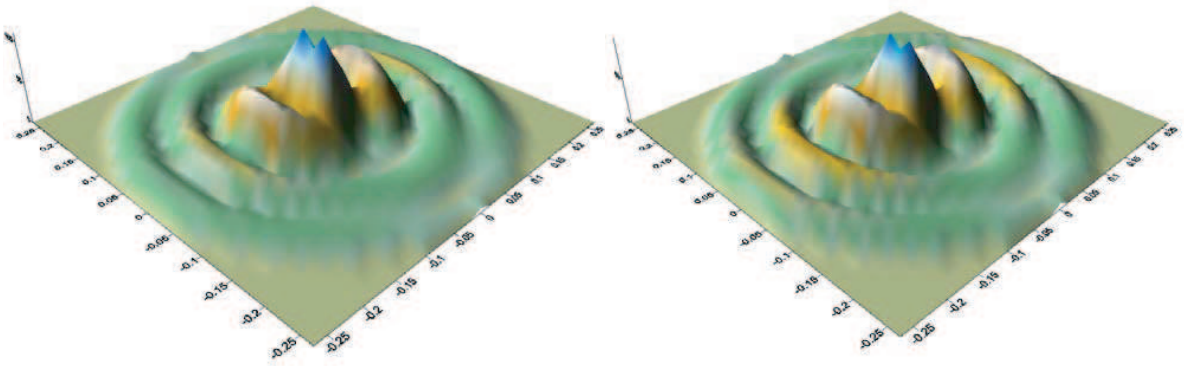

Figure 3: Field distribution for cylindrical cavity excited by a circular waveguide, a) Step excitation, b) Taper excitation.

Since the analysis involves offset waveguide discontinuities, multiple waveguides can be used in order to excite the cavity. Aiming at the generation of a more uniform field distribution at the material to be heated, the cavity was excited by two identical offset circular waveguides, located 240 mm apart, as shown in Fig. 4(a). The resulting field distribution at the dielectric disk is presented in Fig. 4(b). This geometry produces a uniform field distribution along the axis where the excitation is located. Hence, this is compatible with the moving belt structure of Fig. 1(a). Furthermore, a four waveguide excitation can produce a uniform distribution at two perpendicular axes.

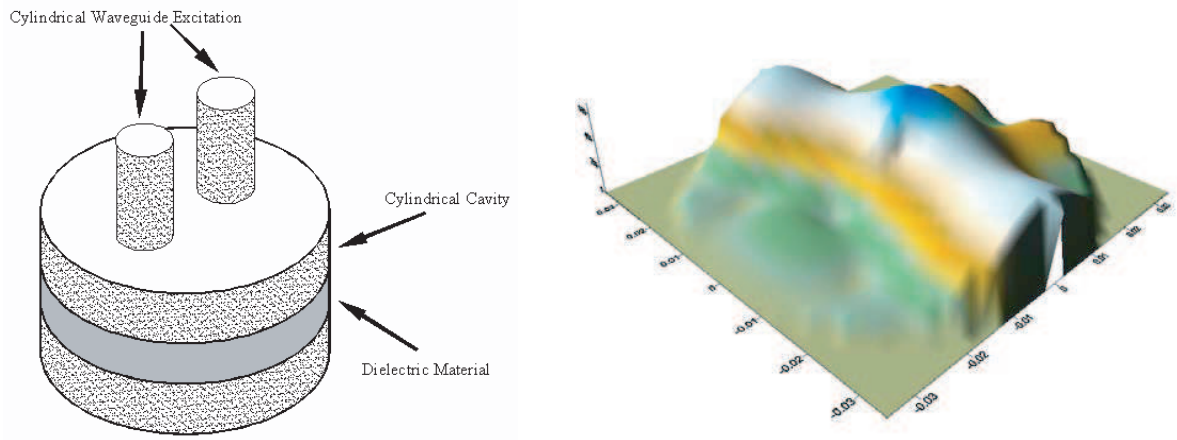

Figure 4: Cylindrical cavity excited by two circular waveguides, a) Geometry, b) Field distribution.

In the last geometry studied, the excitation of a HE_{11} hybrid mode is expected to yield a more uniform field distribution. For this purpose a TE_{11}-to-HE_{11} transformer was introduced, which consists of a corrugated circular waveguide section, as shown in Fig. 5(a). Ten corrugations were introduced, having a length of $\lambda/4$ at $f_0 = 915\,\text{MHz}$, width $w = 16.39\,\text{mm}$, spaced at $t = 32.78\,\text{mm}$, while the radius of the feeding waveguide and the cavity are 98 mm and 122 mm respectively. The length of the cavity is $l = 327.86\,\text{mm}$. The resulting field distribution is described in Fig. 5(b) and it presents relatively good homogeneity, except a small region at the center.

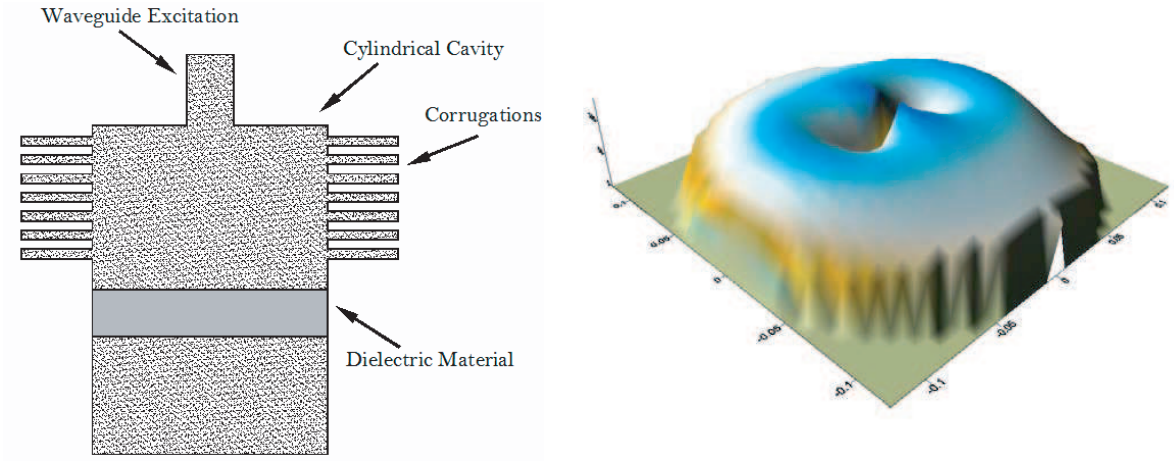

Figure 5: Cylindrical cavity excited by HE_{11} hybrid mode, a) Geometry, b) Field distribution.

5. CONCLUSIONS

The analysis of a cylindrical cavity structure used for heating purposes was presented in this paper. This is based on a closed form Mode Matching technique. The overmoded cylindrical cavity excited by a step or a tapered circular waveguide produces a non-uniform field distribution. To overcome this problem, multiple excitations must be used (multi-furcated circular waveguide) in order to achieve a uniform heating of the material. A single mode cylindrical cavity can produce a uniform field, if the HE_{11} mode is excited using a cylindrical corrugated section.

REFERENCES

1. Kriegsmann, G. A., "Cavity effects and hot spot formulation in microwave heated ceramic fibers," *Microwave Processing of Materials V, MRS*, Vol. 430, 181–186, 1996.
2. Robinson, M. P., J. D. Turner, D. W. P. Thomas, J. F. Dawson, M. D. Ganley, A. C. Marvin, S. J. Porter, T. M. Benson, and C. Christopoulos, "Shielding effectiveness of a rectangular enclosure with a rectangular aperture," *Electronics Letters*, Vol. 32, 1559–1560, 1996.
3. Orfanidis, A. P., G. A. Kyriacou, and J. N. Sahalos, "A mode matching technique for the study of cylindrical and coaxial waveguide discontinuities based on a closed form coupling integrals," *IEEE Trans. Microw. Theory Tech.*, No. 48, 880–883, 2000.
4. Wade, J. D. and R. H. MacPhie, "Scattering at circular to rectangular waveguide junction," *IEEE Trans. on Microwave Theory and Techniques*, Vol. MTT-34, 1085–1091, November 1986.
5. Abramowitz, M. and I. A. Stegun, "Handbook of mathematical functions," *Dover*, 1965.
6. Hwang, K. C. and H. J. Eom, "Scattering analysis for a circular to rectangular T-junction," *Microwave and Optical Technology Letters*, No. 3, Vol. 41, 231–234, 2004.

Driving Characteristics for Hybrid Electric Drive with Super-capacitor as Energy Storage Unit

D. Cundev and P. Mindl

Department of Electric Drives and Traction, Faculty of Electrical Engineering
Czech Technical University, Prague, Czech Republic

Abstract— This paper deals with calculation of the driving characteristics of the hybrid electric drive which uses super-capacitor as energy storage unit. Results has been obtained thought simulation of the driving regime of the experimental working stand for electric and hybrid car drive research, which was developed in the research Centre Josef Bozek at the Technical University in Prague. Computer program and algorithm for simulation of the drive regime is explained. Results of the simulation define the driving characteristics of the entire working stand.

1. INTRODUCTION

In the Research Center of Engine and Automotive Engineering Josef Božek at CTU in Prague has been realized project for development of hybrid electric drive. For that purpose, the experimental working stand has been created at the Department of Electric Drives and Traction at the Faculty of electrical engineering (FEE). Main characteristic of this hybrid drive is using of super-capacitor as accumulation unit instead of chemical battery. Also, the energy transformation is done by means of electrical power splitter (EPS).

As an instrument for further development of this type of hybrid drive with super-capacitor, simulation computer program has been made. Main purpose of this task is calculation of every essential value that characterizes the driving regimes of the hybrid drive. That represents complex working system with many functional units like internal combustion engine, super-capacitor, traction electrical motor, power converters, microcontrollers etc. In such case it is essential to know driving characteristics of this system for defined working regime.

2. LABORATORY MODEL OF THE HYBRID DRIVE

Model of the hybrid drive has been realized in laboratory at Department of electrical drives and traction on FEE, CTU in Prague. The scheme of the experimental working stand is shown on Fig. 1. Internal combustion engine (ICE) is simulated by a controlled electric AC induction motor. Produced power P_{ice} from ICE is divided to the mechanical power P_{mech} and electrical power P_{el1} by using electrical power splitter (EPS). EPS is special type of synchronous generator with permanent magnets on the rotor and stator capable for rotation. Rotor is firmly coupled with the shaft of ICE and stator of the EPS is firmly coupled with vehicle wheels and rotates with the speed proportional to the vehicle velocity V. That technical solution enables internal combustion engine to operate

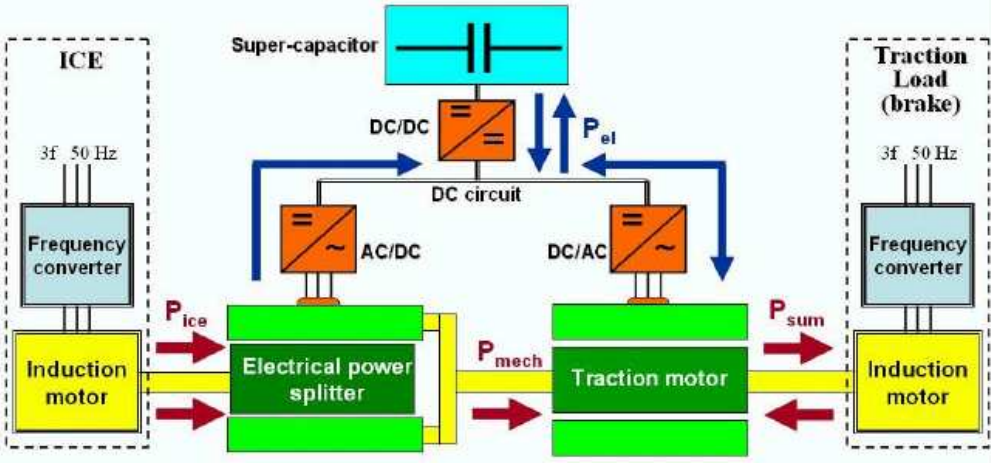

Figure 1: Experimental working stand of hybrid drive.

with constant revolutions (with high efficiency) during entire driving regime without dependence on actual vehicle speed. On the same shaft of the stator of EPS is inserted the induction traction motor (TM). EPS and TM are electrically connected through DC circuit and two traction AC/DC and DC/AC power converters. Traction load is simulated with another controlled AC induction motor.

A super-capacitor (SC) is connected to the DC circuit via DC-DC converter. Energy W_{sc} accumulated in SC is used to provide additional power P_{el} which is by means of TM transformed to the mechanical power P_{mech1}. After that P_{mech1} is added to P_{mech} and resulting sum of powers is directly transmitted to the vehicle wheels. Hybrid vehicle uses recuperative braking by changing of TM operational regime from motor to generator. During that period TM decelerates the vehicle and produced energy is accumulated in the super-capacitor SC.

3. CALCULATION OF THE DRIVING CHARACTERISTICS

Driving characteristics of the hybrid drive has been calculated by means of simulation program. Simulation has been made by means of MATLAB programming interface. In programming has been used the kinematical model described in publication [1]. Simulation starts with defining the driving characteristic of the vehicle speed V as a function of the time t (See Fig. 2):

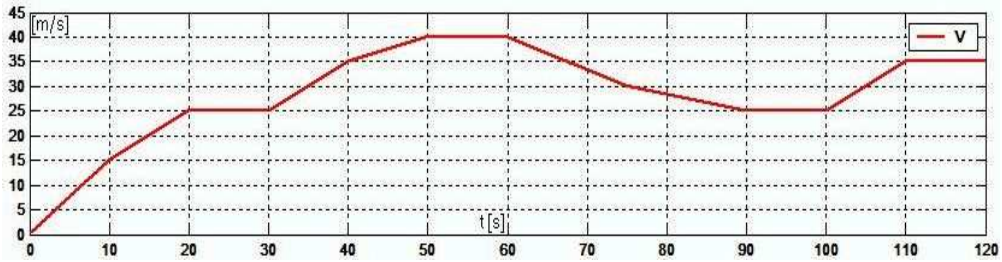

Figure 2: Driving characteristic of the vehicle speed V in function of time t.

By knowing the vehicle weight m and speed V, program calculates the car acceleration a_n, car trajectory distance S_n, needed acceleration force F_n, corresponding energy W_n. for each time sub-interval ($\Delta t_n = t_n - t_{n-1}$) of driving maneuver. By means of this calculated values, it can be calculated the characteristic of the average acceleration power P_a (see Fig. 3). Compensation of aerodynamics resistances has been performed by Equation (1) for additional power P_v:

$$P_v(t) = k_1 \cdot V^3(t) + k_2 V(t) \tag{1}$$

By that means is calculated the driving characteristic of the speed power P_v (Fig. 3):

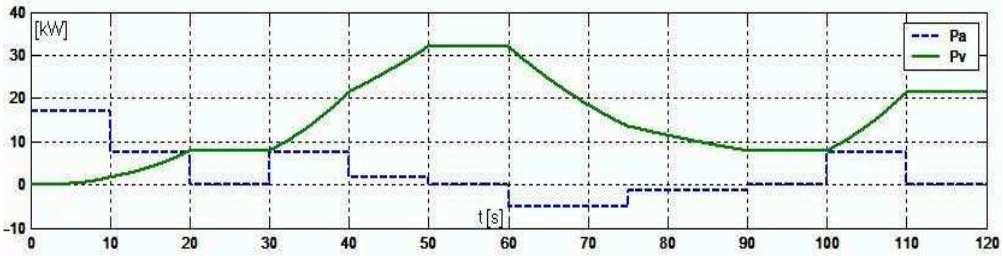

Figure 3: Characteristics of P_a and P_v in function of time t.

Power that is needed to be provided to the hybrid vehicle P_{sum} is sum (2) of acceleration power P_a and speed power P_v:

$$P_{sum}(t) = P_a(t) + P_v(t) \tag{2}$$

Driving characteristic of this value in time scale of the driving maneuver is presented in Fig. 4:

The power of the internal combustion engine P_{ice} follows the needed driving power P_{sum} for each time interval t_i (Fig. 4). Also P_{ice} depends on actual energy volume W_{sc} accumulated in the super-capacitor, which is determined from actual voltage U_{sc} of SC:

$$W_{sc} = \frac{C \cdot U_{sc}^2}{2} \tag{3}$$

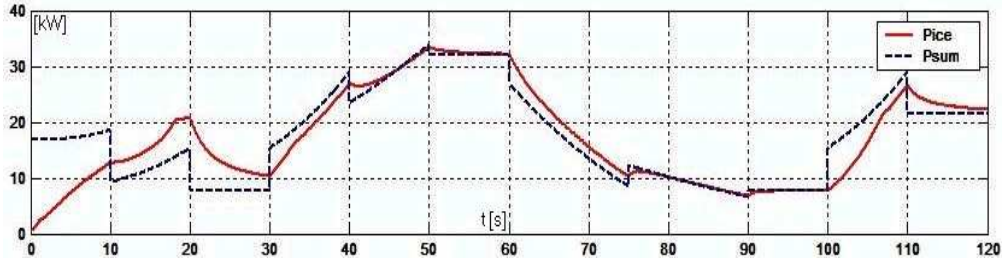

Figure 4: Characteristics of P_{ice} and P_{sum} in function of time t.

In order to perform the better efficiency of ICE changes of output power P_{ice} must be slow. Therefore P_{ice} follows the P_{sum} according to predefined algorithm. That's the main advantage of hybrid electric drive that can't be performed in classical cars in which the ICE must instantly and rapidly changed the working regime according to the actual power demands. That results with high fuel consumption and low efficiency.

Difference between the powers P_{ice} and P_{sum} defines the electrical power P_{el} which charges or discharges the super-capacitor. That is needed electrical power from DC circuit, calculated in accordance to relation (4) and in time scale is presented on Fig. 5.

$$P_{el}(t) = P_{sum}(t) - P_{ice}(t) \tag{4}$$

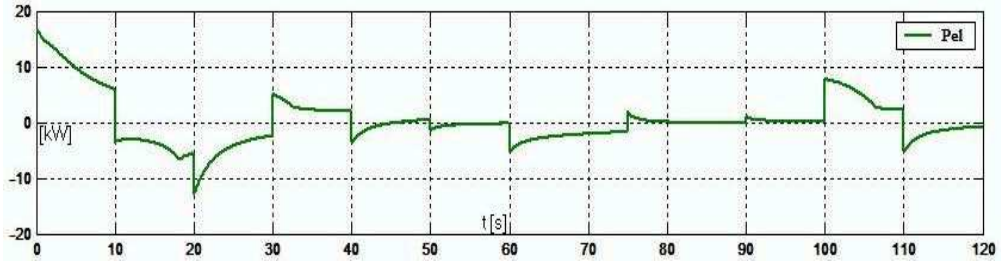

Figure 5: Characteristic of P_{el} in function of time t.

When P_{el} is positive ($P_{el} > 0$) SC is discharged, which means that driving regime demands higher power then is produced in ICE ($P_{sum} > P_{ice}$). In the case when $P_{el} < 0$ SC is charged, which means that produced power is higher then the demanded ($P_{ice} > P_{sum}$). That's in the time intervals when the voltage of SC is lower to the allowed minimal level and therefore ICE produces higher power.

Also, SC is quickly charged by recuperation. During braking, kinetic energy of the vehicle is transformed in to the electrical energy by TM which works in generator regime. It decelerates the vehicle and produced energy is used for super-capacitor charging.

P_{ice} provides power to drive the vehicle and also for charging the SC and keep the U_{sc} above the critical minimal level $U_{sc\,\min}$, which is half of the maximum SC voltage $U_{sc\,\max} = 56$ [V]. Driving characteristic of the voltage output of the SC is presented on Fig. 6.

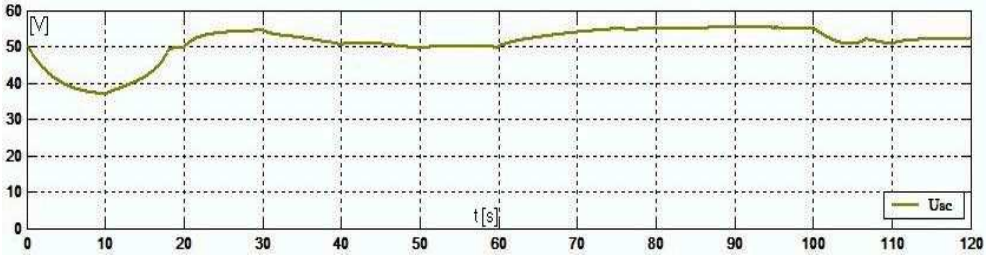

Figure 6: U_{sc} in function of time t.

According to the relation (3) output voltage of super-capacitor represents the accumulated energy W_{sc} in SC. Therefore characteristic on Fig. 6 also represents the indicator of the amount of accumulated energy in SC.

Knowing the actual voltage on SC (U_{sc}) and the needed electric power from SC (P_{el}), the charging or discharging current I_{sc} of the SC can be calculated (Fig. 7). I_{sc} must not exceed the maximum allowed current in SC which is $I_{sc\,\max} = 400$ [A].

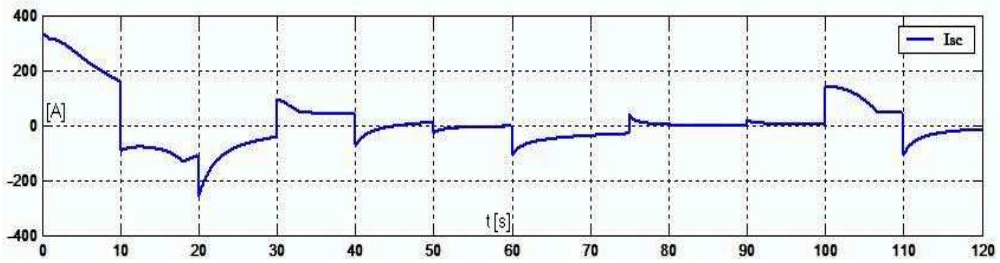

Figure 7: Characteristic of I_{sc} in function of time t.

4. CONCLUSION

In this paper are presented the driving characteristics of specific driving regime. The simulation program enables to perform calculation of characteristics of any kind of driving regime. For calculation is needed definition of vehicle speed. Program enable to taking into account other influences of the driving regime like the weight of the vehicle and the number accumulative units (super-capacitors).

The calculated driving characteristic represents capabilities of the hybrid system during different driving regimes. The work and the results presented in this paper gives contribution to the further development of the hybrid electric drive.

Future works will be oriented to the calculation of the driving characteristics under different conditions, like different weight of the vehicle, more accumulative units, different aerodynamic characteristics etc. Simulation program can be adapted for more complex algorithms to perform new calculated values in order to give more precise and realistic results. Modification of the program will be in correspondence with the laboratory results gained from the experimental working stand (Fig. 1).

ACKNOWLEDGMENT

Research described in the paper was supported by Josef Božek Research Center of Engine and Automotive Engineering at the Department of electrical drives and traction, Faculty of Electrical Engineering, CTU in Prague. Project is granted by the Czech Ministry of Education.

REFERENCES

1. Mindl, P., "Super-capacitor for car hybrid drive," *Proceeding of Conference EPO*, Plzen, June 2003.
2. Cerzovsky, Z. and P. Mindl, "Hybrid drive with super-capacitor energy storage," *FISITA Conference Barcelona*, F193m, 2004.
3. Cerzovsky, Z., P. Mindl, V. Fligl, Z. Halamka, P. Hanus, and V. Pavelka., "Power electronics in automotive hybrid drives," *EPE-PEMC2002*, Dubrovnik, Croatia, September 2002.
4. Cerzovsky, Z. and P. Mindl, "Double rotor synchronous generator used as power splitting device in hybrid vehicles," *31st FISITA World Automotive Congress*, Yokohama 2006.
5. Lettl, J. and S. Flígl, "Unconventional application of matrix converter system," *Proceedings of 11th Conference, Electronic Devices and Systems EDS 2004*, ISBN 80-214-2701-9, 488–492, Brno, September 9–10, 2004.
6. Zdenek, J., "System design and software architecture of traction vehicle control computer," *Proc. of 12th Int. Conf. EPE-PEMC2006*, ISBN: 1-4244-0121-6, 1205–1210, Portoroz, Aug. 2006.

Steady-state Analysis of Salient Poles Synchronous Motor with Damper Based on Determination of the Magnetic Field Distribution

D. Cundev and Z. Cerovsky
Department of Electric Drives and Traction, Faculty of Electrical Engineering
Czech Technical University, Prague, Czech Republic

Abstract— This paper deals with steady-state analysis of the magnetic field by using Finite Element Method (FEM) in salient poles synchronous motor with damper (SPSMD). The knowledge of electromechanical characteristics is very important in performance analysis of electrical machines, in general. In this paper it presents a methodology for numerical calculation of electromechanical quantities, starting with the determination of the magnetic field distribution and numerical computation of the electromechanical characteristics of SPSMD by using FEM.

1. INTRODUCTION

The Finite Element Method is very efficient tool for an electromagnetic field solution. The application of this method on the salient poles synchronous motor with damper (SPSMD) is described in this paper. This type of synchronous motor (SM) with damper ring (cage winding) on the rotor can be started by using asynchronous start without any additional technical starting equipment that is usually required for SM.

The FEM (Finite Element Method) in the recent years has been found as a very attractive method in the design and analysis of various types of electromechanical devices. By using this method almost all the necessary electric and magnetic quantities are determined for this type of electrical machine. In this paper it presents the methodology of using the FEM for computation of electromechanical characteristics.

For complex configurations as those in electrical machines, the FEM is powerful numerical method for solution of electromagnetic field problems. By the application of this method in the whole discredited domain of the machine under consideration, an important contribution to the magnetic field computation could be done. An optimal design of electrical machines requires the accurate calculation of the magnetic field distribution in the different cross-sections. This enables an accurate determination both the electromagnetic and electromechanical characteristics of the motor. The accuracy of the electromechanical characteristics depends on the precise calculations of electromagnetic field in the electrical machine.

2. MATHEMATICAL AND GEOMETRICAL MODEL OF THE MACHINE

CAD model of the machine is an essential basis for implementation of geometrical structure of the motor into the FEM calculation. For applied calculation of electrical machines, the appropriate geometrical CAD model of the machine and mathematical model are necessary. By precise determination of all coordinates of the structure, the 3D CAD model is created as is shown of Fig. 1.

The calculation of the magnetic field distribution in the SPSMD is started from the system of the Maxwell's Equations (1) and (2), which describes the magnetic field in closed and bounded systems. The main value that is calculated with FEM in entire structure of the machine is the magnetic vector potential A, expressed with the Maxwell equation:

$$B = rotA \tag{1}$$

as an auxiliary quantity. Knowing that

$$divB = 0 \tag{2}$$

the distribution of the magnetic field is expressed by the following non-linear differential equation known as Poisson's equation:

$$\frac{\partial^2 A}{\partial^2 x} + \frac{\partial^2 A}{\partial^2 y} + \frac{\partial^2 A}{\partial^2 z} = \mu J \tag{3}$$

where the μ is magnetic permeability as function of magnetic flux density $B(\mu = f(B))$.

In the special case, when there are no current sources in the domain under consideration ($J = 0$), the right side term of Equation (3) is zero, and the equation is recognized as Laplace's.

To perform magnetic field computation with FEM, entire structural entity of the machine must be defined as mathematical model consisted of Maxwell's, Laplace's and Poisson's equations.

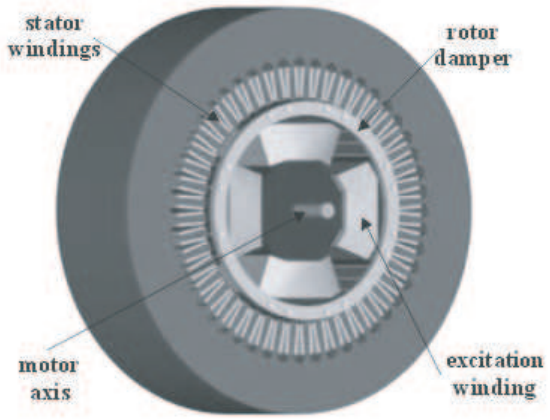

Figure 1: 3D CAD model of SPSMD.

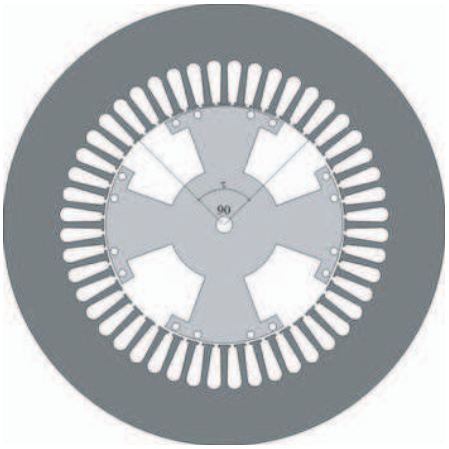

Figure 2: Cross-section of SPSMD.

3. FEM APPLICATION

As most suitable software for FEM calculation was ANSYS version 5.6 selected. Besides that this software has general application for FEM calculation like mechanical, structural integrity or thermal dissipation, it is quite convenient for computation of electrical and magnetic field dissipation in electrical machines.

In this software appropriate algorithm for calculation of all relevant characteristics of electrical machines is defined. The proposed algorithm is in this paper applied on the salient poles synchronous motor with damper (SPSMD), with rated data: 2.5 KW, 240 V, 1500 rpm, and delta stator winding connection. The SPSMD is heterogeneous, non-linear domain with particular B-H characteristics of magnetic core in stator and rotor, and with prescribed boundary conditions. Therefore, the Equation (3) in developed form, is the variable coefficient type, and can be solved by the numerical methods only. To realize this task, it is necessary that the proper geometrical CAD and mathematical modeling of the motor to be carried out. Therefore the geometrical cross-section of the motor is created from the CAD model which is presented in Fig. 2.

The beginning of the FEM calculations, it is requested to generate a correspondent mesh of finite elements. ANSYS is software that has option for generation of the most optimal finite element mesh

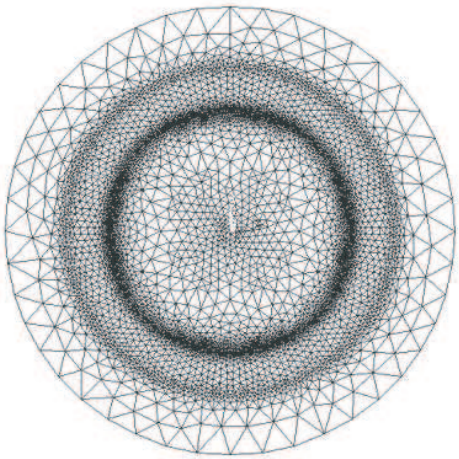

Figure 3: Finite elements mesh.

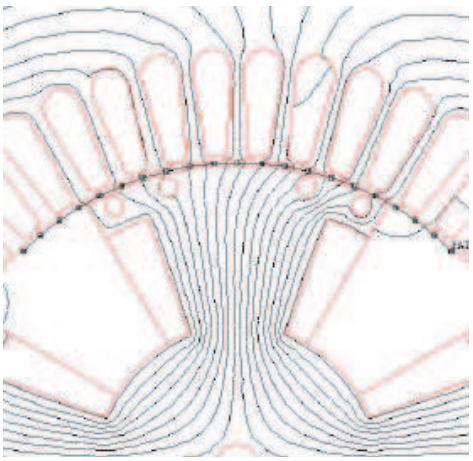

Figure 4: Middle line of the air-gap in SPSMD.

of the complex structures like SPSMD. The mesh must be dense enough for precise calculation and also optimal for not consuming a lot of the computational time.

After several attempts for optimal finite element mesh, the most appropriate mesh is generated. This mesh provides calculation with high precision and at reasonable computational time. In this case, the most convenient mesh type is chosen to be triangular, with 8195 nodes and 16344 finite elements, and is presented in Fig. 3:

The calculations are carried out as magneto-static case, at arbitrary rotor position. Computation has been performed for rated values of the currents in stator and rotor (excitation) windings in synchronous regime (damper winding is not active). Magnetic field distribution is shown (Fig. 5) for three characteristic cases:

a) When only the rotor winding is excited (the excitation winding) with nominal excitation current;

b) When only the stator winding is exited (armature winding) with nominal armature current;

c) And when the both stator and rotor winding are excited with nominal currents.

The rotor excitation winding is performed as concentrated over the pole body. The rated excitation current is $I_f = 5.5\,[\mathrm{A}]$ DC. The magnetic field distribution when only the rotor winding is energized at rated current is presented in Fig. 5(a).

In the stator slots, there are placed three phase distributed windings, in delta connection, and supplied by three-phase voltage source 240 [V] AC, with the rated current 4.63 [A]. The magnetic field distribution when only the stator windings are energized is presented in Fig. 5(b). (The current space vector lies in the quadrature axis).

The computations with FEM continue when both motor windings are energized at rated currents. The angle between the axes of the two previously excited fields is equal 90 degrees electrical (45 degrees mechanical in 4 pole machine). The Magnetic field distribution when both windings are energized is presented in Fig. 4(b).

4. MAGNETIC FLUX DENSITY

Besides the magnetic field distribution, the newest software calculation methods give opportunity for direct calculation of graphical presentation of all relevant electrical and magnetic quantities. Relation between the magnetic flux density B and the magnetic vector potential A is defined previously by the Equation (1). The values of the magnetic vector potential and its components in every node of the investigated domain of the salient pole synchronous motor with damper have been calculated as output results from the FEM. By using the procedure for numerical differentiation, over the Equation (1) in the developed form, the distribution of the magnetic flux density at the middle line of the air gap in the motor can be determinate (Fig. 6). The middle line of the air-gap in Salient Poles Synchronous Motor with Damper is shown on Fig. 4.

The curves of the magnetic flux density B, for the three different current flows, (previously defined with corresponding explanation concerning Fig. 5) are presented in the same manner in Fig. 6, respectively. For better understanding of the charts, the slotted segments of the stator magnetic core as well as the rotor, including damper winding slots, are presented along one pole pitch, i.e., for an angle α of 180 degrees electrical (90 degrees mechanical).

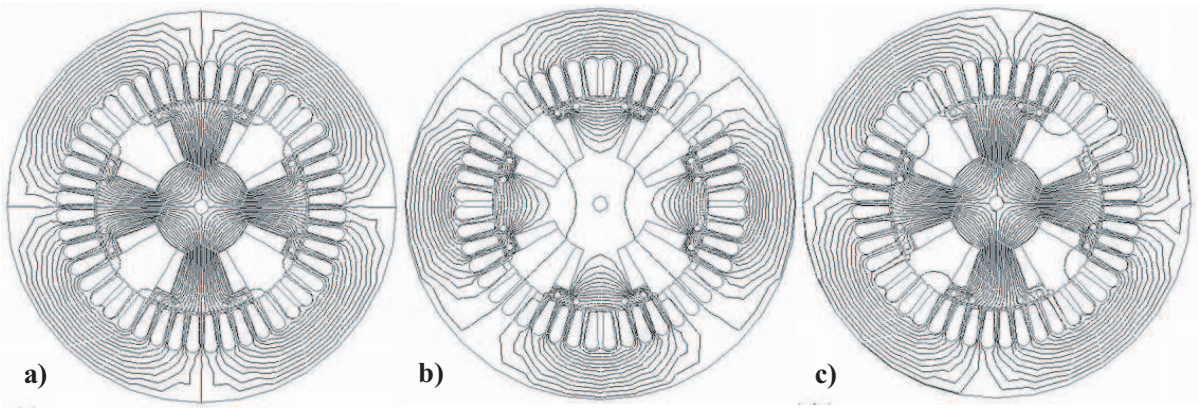

Figure 5: Magnetic field distribution for three cases of stator and rotor excitation.

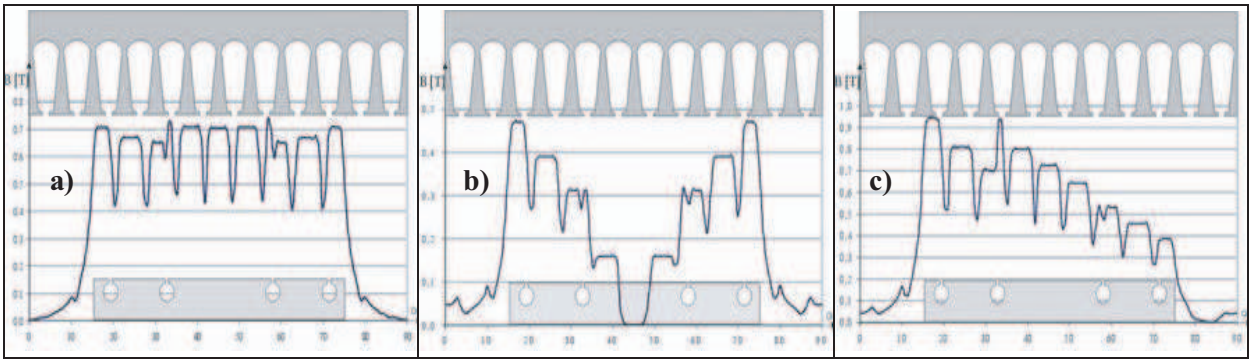

Figure 6: Distribution of the magnetic flux density B in the air gap along the one pole pitch.

Main flux Φ can be determined from the distribution of the magnetic vector potential A based on the field theory by using numerical integration of the magnetic vector potential

$$\Phi = \int_{\Sigma} B \cdot ds = \int_{\Sigma} rotA \cdot ds = \oint_{C} Adr \tag{4}$$

hence,

$$\Psi = w \cdot \Phi \cdot l \tag{5}$$

The FEM calculated characteristic of the air gap flux Ψ per pole in function of the rotor excitation current I_f at given rotor angular position is given on Fig. 7:

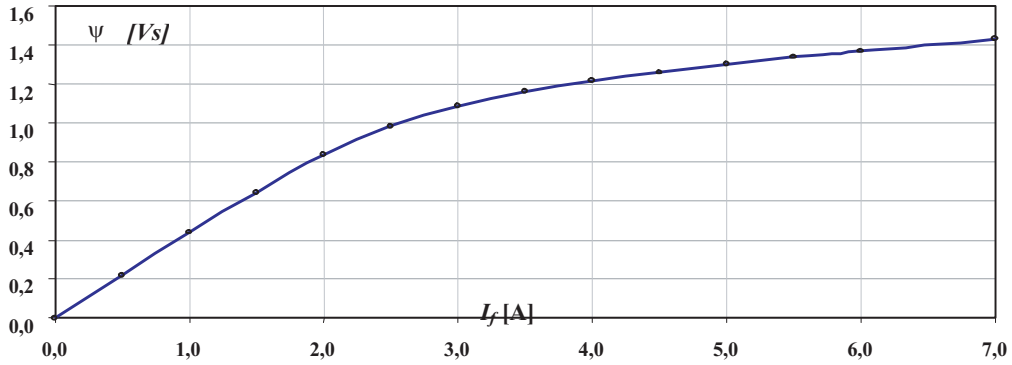

Figure 7: Air gap flux Ψ characteristic of the motor obtained by FEM.

5. CONCLUSIONS

In this paper, the methodology for the magnetic field calculation and analysis of electromagnetic characteristics of the salient poles synchronous motor with damper, by using the finite element method are presented. The calculations were carried out at given rotor position against the stator reference axis and for different excitation currents, i.e., the current in the stator windings only, in the excitation coil only and in both windings. The currents have the nominal value.

The results of the field computations are used for calculations of magnetic flux density B and air gap flux Ψ along the air gap. They are presented on the charts. All this characteristics can be used for a complex analysis of the motor behavior under different working conditions.

The extension of the work leads to the analysis of electromagnetic characteristics and determination of the parameters of the motor in different working conditions. Upon that, the main inductance in the air-gap of the salient poles synchronous motor with damper could be computed. The most interesting issue is analysis of the damper winding role during the starting performance of the synchronous motor.

REFERENCES

1. Cundev, D., L. Petkovska, and M. Cundev, "Non-linear analysis of a salient poles synchronous motor with damper," *ELMA 2002 Tenth International Conference on Electrical Machines, Drives and Power Systems, Proceedings*, 169–175, Sofia, Bulgaria, 13–14 September, 2002.
2. Cerovský, Z., "Käfigströme und Käfig verluste der Stromrichtermotoren," *Archiv für Elektrotechnik*, Vol. 64, 341–348, 1982.
3. Cundev, D. and L. Petkovska, "Computation of electromechanical characteristic of salient poles synchronous motor with damper based on FEM," *JAPMED03 Third Japanese-Mediterranean Workshop on Applied Electromagnetic Engineering*, 89–94, Athens, Greece, 19–21 May, 2003.
4. Cundev, D., "Determination of the magnetic field distribution of salient poles synchronous motor with damper using numerical calculations based on FEM," *International PhD-seminar Computation of Electromagnetic Fields, Proceedings*, 53–58, Budva, Serbia & Montenegro, 23–28 September, 2004.

On the Influence of Slot Width of Field Shapers in Electromagnetic Metal Forming of Aluminum Sheets

A. Farschtschi[1], **T. Richter**[1], **and H.-J. Roscher**[2]

[1]Chemnitz University of Technology, Germany
[2]Fraunhofer Institute IWU, Germany

Abstract— In industry there is currently a strong desire to use significantly more aluminum. Electromagnetic metal forming (EMF) is a suitable method to overcome the limitations of classical stamping when aluminum is used. One variation of forming is a hybrid method where the final forming after stamping is done by EMF using field shapers. A commercial Finite-Element-Analysis program, ANSYS, is used to simulate the transient electromagnetic field problem and to understand the work principle of the field shaper. Due to the complexity of the 3-dimensional simulation electromagnetic simulations are made neglecting structural dynamic effects. Hints on the implementation of such a complex model in ANSYS are given and the variation of the pressure distribution of the workpiece with the slot width of the shaper is examined. It is shown that the electromagnetic force on the workpiece has a linear dependency on the slot width of the shaper.

1. INTRODUCTION

In industry there is currently a strong desire to use significantly more aluminum. There are some obstacles in forming of aluminum by stamping methods, e.g., tearing and spring-back due to the elastic modulus of aluminum (compared to steel). Electromagnetic metal forming (EMF) works by the magnetic induction effect and causes much higher accelerations and velocities in sheet forming compared to stamping processes. That's why EMF as a method of high velocity forming can overcome these obstacles. One variation of forming is a hybrid method where the final forming after stamping is done by EMF. This method includes a field former device between the coil and workpiece (see Fig. 1).

The prediction of the deformation of the workpiece requires the solution of the magneto-structural differential equations including the couplings between the fast motion of the workpiece and the magnetic field. Computing the electromagnetic fields in moving conductors is a difficulty that most codes in literature cannot handle efficiently [8]. More simplified models, especially early models ([13, 9, 1, 5, 10]) base on the assumption that EM field transients are so fast that most deformation occur after the EM pulse and can be separated from the EM calculation. More recent models ([4, 6]) use the multiphysics formulation of ANSYS for the so-called soft coupling neglecting velocity effects. Basically, at each time step, the EM fields are computed in an updated geometry, which has been found from the deformation response of the previous time step. Codes with full coupling of electromagnetism and structural mechanics ([2, 12, 11]) are in progress but can handle no complex problems at time.

2. MODEL AND SOLUTION

2.1. Problem Description

Our aim is the examination of the the pressure distribution within the slot of the field shaper. Basing on our earlier experiences [3] the calculations were carried in ANSYS. Fig. 1 depicts the geometry of the simulated problem. A 7-winding flat spiral coil (inner radius 20 mm, height 4 mm, width 8 mm, distance between windings: 4 mm) is positioned 2 mm below the foot of the field shaper. The field shaper is made of copper (conductivity $5.8 \cdot 10^7\,\mathrm{Sm}^{-1}$), whereas the workpiece is an aluminum sheet (conductivity $3.8 \cdot 10^7\,\mathrm{Sm}^{-1}$, thickness 1.2 mm) is situated 2 mm above the head oft the field shaper. EMF with field shapers can result in a more sophisticated geometry. In literature ([7, 6]) most field shapers refer to electromagnetic metal forming of tubes. In contrast to these configurations our shaper is used in the EMF process after stamping of sheets and requires a more complex geometry of the the finite element model. The capacitor bank, the spiral coil and an external resistance and impedance provide the primary RLC circuit. The discharging of the capacitor bank creates the electromagnetic pulse resulting in large eddy currents in the field shaper and the workpiece. The model assumes the following:

1. Due to the complexity of our problem we concentrate on electromagnetism and neglect the deformation of the workpiece. Recent works ([2, 6]) suggest that most oft the deformation occurs after the EM pulse of the primary circuit. Hence we expect only little influence of the above approximation on the pressure distribution of the workpiece.

2. The eddy currents of the shaper and the workpiece create a magnetic field complementary to the primary field of the spiral coil. Since the thickness of the workpiece (1.2 mm) is greater than the skin depth (related to the frequency of the primary RLC circuit) the surrounding above the workpiece has a nearby vanishing magnetic field. The superposition of these two complementary fields results in a rapidly declining magnetic field outside the described apparatus. Therefore further metallic environment is neglected.

2.2. Geometry and Preprocessor

Every entity of the model is meshed with elements of appropriate degrees of freedom depending on the physical properties of the material (see Table 1)

Table 1: ANSYS elements.

Device	*Element type and meshing*	*Number*	*DOF*
Capacitor bank	**CIRCU124,2** Element represents the capacitance of the capacitor bank within the primary circuit (single-loop). The initial condition is VOLT $= U_0$ with the initial voltage U_0 of the capacitor bank.	1	VOLT
Impedance	**CIRCU124,1** Additional external impedance of the primary circuit	1	VOLT
Resistor	**CIRCU124,0** Ohmic resistance of the primary circuit	1	VOLT
Coil	**CIRCU124,7** This element represents the field-coupling of the primary circuit and is only reasonable usable in connection with the SOLID97,4 element.	1	VOLT, CURR
Coil	**SOLID97,4,0** Circuit-coupled 3-d conductor including eddy-current and proximity effects. Elements are 8-noded and were created by mapped meshing. The two faces of the spiral conductor are coupled in VOLT and CURR degree of freedom and connected to the single-loop external circuit using a CIRCU124 element.	2.400	A_x, A_y, A_z, VOLT, CURR
Field shaper	**SOLID97,1,0** The head is mapped meshed with 8-noded elements, whereas the foot is free meshed with 4-noded elements. The underneath of the foot and the boundary of the slot carry large eddy currents and are discretised within the skin depth (related to oscillation frequency of the primary circuit): The foot is extruded within the skin depth to obtain prism elements. The boundary of the slot is discretises with heaxahedral 8-noded elements with a width of the skin depth.	27.000	A_x, A_y, A_z, VOLT
Workpiece	**SOLID97,1,0** Mapped meshing with hexahedral 8-noded elements	12.000	A_x, A_y, A_z, VOLT
Air	**SOLID97,0,0** Free meshing with tetrahedral 4-noded elements. The volume of the surrounding air is a sphere to obtain infinity boundary elements with a single exterior surface.	130.000	A_x, A_y, A_z
Infinite boundary	**INFIN111,1** Prism elements are generated by extrusion of the surface of surrounding air. The boundary conditions are set to $A_x = A_y = A_z = 0$ at outer nodes. The discretisation along the extrusion direction has to be 1.	520	A_x, A_y, A_z

The border of the slot of the field shaper, its bottom and the height of the workpiece are meshed with elements owning a width comparable to the skin depth δ of the material:

$$\delta = \frac{1}{\sqrt{\pi \cdot f \cdot \mu_0 \cdot \sigma}} \tag{1}$$

The frequency f in (1) is taken from the em pulse of the primary circuit ($\approx 7\,\text{kHz}$, see Fig. 3). σ is the electric conductivity of the materials of the shaper (copper) and the workpiece (aluminum). A typical discretisation of the field shaper and the workpiece is shown in Fig. 2.

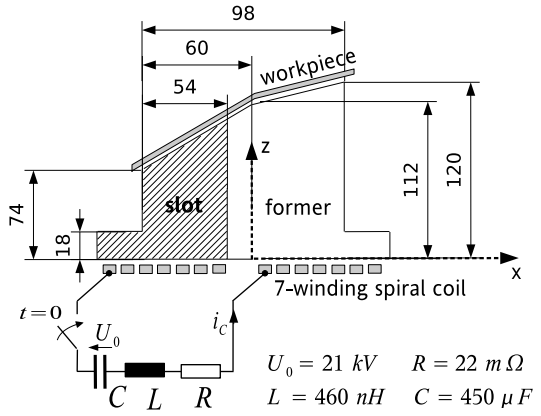

Figure 1: Sample geometry (lengths in mm).

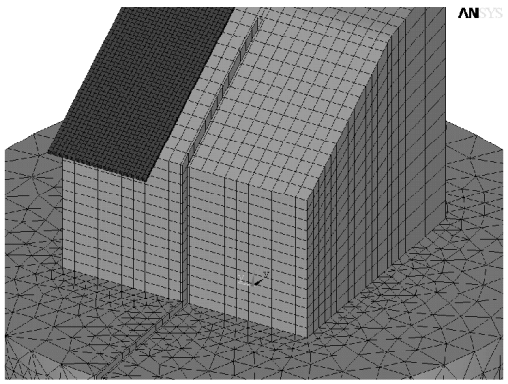

Figure 2: Typical discretisation of shaper and a part of the workpiece in ANSYS.

2.3. Solution

To ensure a stable calculation of the transient we choose following settings of the solution processor of ANSYS:

- All components of the vector potential at infinite boundaries were set to 0. The initial voltage of the capacitor bank was set to U_0.
- A time dependent analysis was requested with a fixed step size of $\Delta t = 4\,\mu\text{s}$ (step changed loads).
- The first time step was carried out with a time step $0.01 \cdot \Delta\, t$ to guarantee reasonable initial values of the transient.
- The transient integration parameter was set to 1 (referred as backward Euler method).

3. RESULTS

The time dependent analysis was requested with varying a slot width (2, 4, 6 and 8 mm). Fig. 3 shows the transient of the discharging current of the capacitor bank. The components of the total force can be separated into two parts:

- Since the workpiece overhangs the border of the head of the former stray fields induce eddy currents at the border of the workpiece. The force on these eddy currents will depend on the shape of the workpiece.
- The main aim of this work is the examination of forces generated by eddy currents around the slot. As Fig. 4 shows even the separation of these forces from the total force shows a strong linear dependency of these forces on the the slot width.

An increasing slot width results in a higher pressure on the aluminum sheet and a more non-uniform pressure distribution around the slot (see Fig. 5. Above facts imply that the design of the former will be a compromise between the uniformity of pressure distribution and a maximum amount of total force. A time–dependent analysis was requested with varying a slot width (2, 4, 6 and 8 mm).

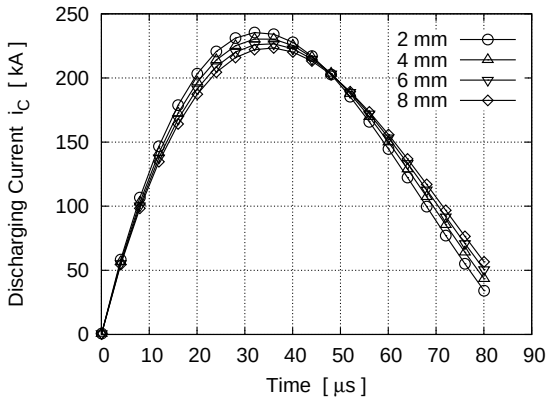

Figure 3: Current transients of the capacitor bank.

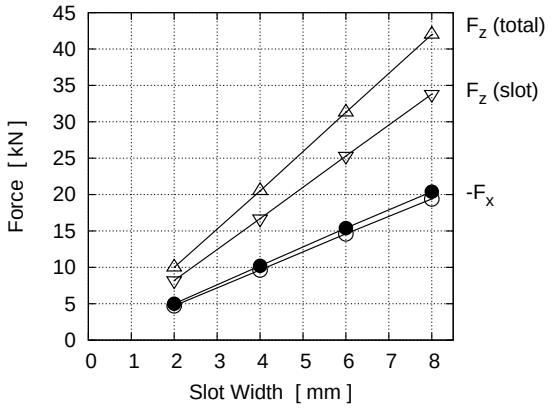

Figure 4: x and z components of forces on workpiece at 36 µs. The force components across the slot were separated from the total components and show a strong linear dependency on slot width.

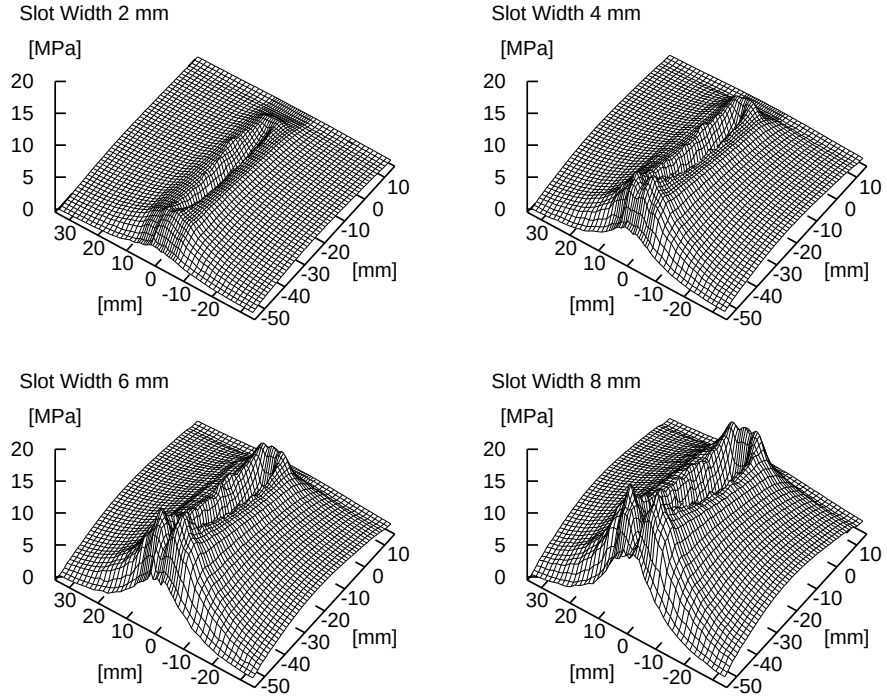

Figure 5: Distribution of z component of pressure across the slot at 36 µs.

4. CONCLUSION

We carried out an EM simulation of the field shaper shown in Figs. 1 and 2. Recent works ([2, 6]) suggest that an electromagnetic simulation neglecting the movement of the workpiece is still valid and can give an survey of the time-dependent pressure distribution of the workpiece during the first half-wave of the electromagnetic pulse. It was shown that the pressure on the workpiece around the slot of the shaper shows a clearly linear dependency on he width of the slot.

REFERENCES

1. Deng, J., C. Li, Z. Zhao, F. Tu, and H. Yu, "Numerical simulation of magnetic flux and force in electromagnetic forming with attractive force," *Journal of Materials Processing Technology*, Vol. 184, No. 2, 190–194, 2007.
2. Unger, A., M. Stiemer, B. Svendsen, and H. Blum, "Multifield modeling of electromagnetic metal forming process," *Journal of Materials Processing Technology — Proceedings of the 11th International Conference on Metal Forming 2006*, Vol. 177, No. 1–3, 270–273, 2006.

3. Farschtschi, A., T. Richter, and H.-J. Roscher, "Application of finite network theory to the transient process in electromagnetic forming," *Proceedings of PIERS2006 in Cambridge*, 465–469, 2006.
4. Oliveira, D. A., M. J. Worswick, M. Finn, and D. Newman, "Electromagnetic forming of aluminum alloy sheet: Free-form and cavity fill experiments and model," *Journal of Materials Processing Technology*, Vol. 170, No. 1–2, 350–362, 2005.
5. Yu, H., C. Li, Z. Zhao, and Z. Li, "Effect of field shaper on magnetic pressure in electromagnetic forming," *Journal of Materials Processing Technology*, Vol. 168, No. 2, 245–249, 2005.
6. Mamalis, A. G., D. E. Manolakos, A. G. Kladas, and A. K. Koumoutsos, "Physical principles of electromagnetic forming process: a constitutive finite element model," *Journal of Materials Processing Technology*, Vol. 161, No. 1–2, 294–299, 2005.
7. Schaetzing, W., C. Goernandt, H.-P. Scheibe, and G. Wollenberg, "Berechnung teilbarer werkzeuge zur elektromagnetischen umformung," *Kolloquium Elektromagnetische Umformung*, 71–74, ISBN 3-00-011376, 16 May, 2003.
8. El-Azab, A., M. Garnich, and A. Kapoor, "Modeling of the electromagnetic forming of sheet metals: state-of the art and future needs," *Journal of Materials Processing Technology*, Vol. 142, No. 3, 744–754, 2003.
9. Bednarczyk, J., "Distributions of forces in the inductors used in metal processing in the pulse magnetic field," *Journal of Materials Processing Technology*, Vol. 133, No. 3, 340–347, 2003.
10. Li, C., Z. Zhao, J. Li, Y. Wang, and Y. Yang, "Numerical simulation of the magnetic pressure in tube electromagnetic bulging," *Journal of Materials Processing Technology*, Vol. 123, No. 2, 225–228, 2002.
11. Meriched, A., M. Féliachi, and H. Mohellebi, "Electromagnetic forming of thin metal sheets," *IEEE Transactions on Magnetics*, Vol. 36, No. 4, 1808–1811, 2000.
12. Bendjima, B., K. Srairi, and M. Féliachi, "A coupling model for analysing dynamical behaviours of an electromagnetic forming system," *IEEE Transactions on Magnetics*, Vol. 33, No. 2, 1638–1641, 1997.
13. Sung, H. L. and D. N. Lee, "Estimation of the magnetic pressure in tube expansion by electromagnetic forming," *Journal of Materials Processing Technology*, Vol. 57, No. 3–4, 311–315, 1996.

Amplification of Acoustic-electromagnetic Waves in GaN Films

A. García-B.[1], **V. Grimalsky**[2], **A. Silva**[1], **P. Rivera**[1], **A. Morales**[3], **and F. Marroquín**[1]

[1]Department of Mecatronics, University Polytechnics of Pachuca (UPP)
Carretera Cd. Sahagun, Pachuca Km. 20, Z.P. 43830, Hidalgo, México
[2]Autonomous State University of Morelos, CIICAp
Av. Universidad No. 1001, Z.P. 62209, Cuernavaca Mor., México
[3]Centro Nacional de Microelectrónica (CNM), Campus UAB
Bellaterra 08193, Barcelona, Spain

Abstract— The amplification of acoustic-electromagnetic waves in GaN due to coupling with amplified space charge waves and hypersonic waves in GaN is investigated theoretically in this work. The amplification of space charge waves due to negative differential conductance in GaN is analyzed and possible increments are calculated by local and non local approximation. The effect of non-local dependence can lead to some quantitative corrections for the increment of the amplification of space charge waves of millimeter wave range in GaN film.

1. INTRODUCTION

GaN has become of increasing interest for use in many semiconductor device structures. GaN offers some important advantages in various applications; especially it is a potential candidate for high temperature electronics, ultraviolet detectors and emitters and because of the GaN's large peak electron velocity makes it an important candidate for high frequency applications electronics as well [1, 2]. Other important investigation in GaN is the acoustic wave amplification, however at microwave frequencies ($f > 10\,\mathrm{GHz}$) exists a problem of excitation of hypersound and the traditional methods, like using comb-like transducers are not effective. A possible solution of this problem is the resonant coupling of acoustic waves with the microwave or millimeter electric field of space charge waves in GaN thin films possessing negative differential conductance. That is, under propagation in the bias electric field higher than the critical than the critical value for observing negative differential conductivity, the space charge waves is subject to amplification and its microwave electric field can achieve high values. In turn, due to piezoeffect or deformation potential this microwave electric field excites hypersonic acoustic waves. In [3] it was demonstrated that excitation is of a resonant character with respect to the frequency and the thickness of the GaAs thin film. A problem in GaAs films is the frequency range of amplification of space charge waves is to $f < 50\,\mathrm{GHz}$, however to increase the frequency range of amplification in hypersonic acoustic waves, it is rather better to use new materials possessing negative differential conductance at high frequencies (100 to 300 GHz) like GaN film [4]. By the way, the usefulness of hypersound at microwave or millimeter frequencies is very important like in filters and delay lines for the communication and control systems.

In this article, we present theoretical investigations of amplification of acoustic-electromagnetic waves in a GaN film with a sub-micron thickness. The amplification of space charge waves due to negative differential conductance in GaN is analyzed and possible increments are calculated by local and non local approximation. The effect of non-local dependence can lead to some quantitative corrections for the increment of the amplification of space charge waves of millimeter wave range in GaAs film.

2. SPACE CHARGE WAVES IN A THIN GAN FILM

Thin film semiconductor structures with negative differential conductivity caused by interline electronic transitions in strong electric fields in semiconductors such as n-GaAs or GaN are of major practical interest because they form of basis of devices utilizing space charge waves in semiconductors. These devices have extensive functional capabilities, similar to those of acousticelectronic devices, but unlike the latter can operate effectively to millimeter wave range.

In our case we consider n-GaN film of a sub-micron thickness placed onto a semi-infinite dialectic substrate. The bias electric field is directed along Z, the space charge waves are excited by an input antenna 1 and the propagation is along Z-direction too.

In our simulations, an approximation of two dimensional electron gas is used. The set of balance equations for concentration, drift velocity and averaged energy to describe the dynamics of space

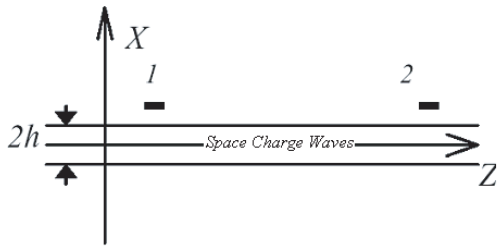

Figure 1: Geometry of the problem. The GaN film occupies the region $0 < x < 2h$. The input antenna is 1, the output one is 2.

charge waves within the thin n-GaN film, like in n-GaAs thin film [5], takes a form:

$$\begin{aligned}
&\frac{d\left(m\vec{v}_d\right)}{dt} = -e\left(\vec{E} - \frac{\vec{v}_d E_s}{v_s}\right); \quad \frac{dw}{dt} = -e\left(\vec{E}\vec{v} - E_s v_s\right); \\
&\frac{\partial n}{\partial t} + div\left(n\vec{v}_d - D\nabla n\right) = 0; \quad D = \frac{\tau_p}{m}T, \\
&T = \frac{2}{3}\left(w - \frac{1}{2}mv^2\right); \\
&\Delta\varphi = -\frac{e}{\varepsilon_0\varepsilon}(n - n_0)\cdot\delta(x); \quad \vec{E} = \vec{e}_z E_0 - \nabla\varphi + \vec{e}_z E_{ext}(z,t)\cdot\delta(x)
\end{aligned} \tag{1}$$

where v_d is drift velocity, w is the energy of electron, $m(w)$ is averaged effective mass $\tau_{p,w}(w)$ are relaxation times, T is electron temperature (energy units), n_0 is equilibrium value of two dimensional concentration of electron gas. E_0 is a bias drift field. It is assumed that a condition of occurring negative differential conductivity is realized. Because the signal frequencies are in millimeter wave range, it is possible to separate diffusion and drift motions. For a sake of simplicity, instead of relaxation times, the parameter E_s has been introduced like in GaAs.

$$\frac{m\left[w\right]}{\tau_p\left(w\right)} = \frac{E_s}{v_s\left(E_s\right)}; \quad \frac{w - w_0}{\tau_w\left(w\right)} = qE_s v_s\left(E_s\right) \tag{2}$$

In such a representation, a direct correspondence between local field dependence and non-local effects is well seen. Because a dependence $E_s = E_s(w)$ is unique, it is possible to express the parameters w and v_s through the value of E_s.

The drift velocity vs electric field dependencies are calculated along (100) direction and within the basal plane along the (1010) for both the zincblende and wurtzite phases, respectively, assuming free electron and ionized and impurity concentrations of $10^{17}\,\mathrm{cm}^{-3}$. The dependence of drift velocity and the average energy with electric field are presented in Figures 2(a) and (b) [6, 7], respectively. Average energy vs electric field dependencies show a behavior typical for compound semiconductor materials. Note that a local dependence between the drift velocity and the electric field is $v_d = v_s(E)$ (E/E).

A small millimeter electric signal $E_{ext} = E_m * \sin(\omega t) * \exp((-(z - z_1)/z_0)^2)$ is present in the input antenna. Here z_1 is a position of input antenna; z_0 is its half-width. When the small millimeter signal is applied to input antenna, the excitation of space charge waves in 2D electron gas takes place.

Amplification of space charge waves is investigated by dispersion equation, where the unperturbed (stationary) values of E_0, v_0 have been chosen in the regime of negative differential conductivity ($dV/dE < 0$). The results of direct simulations of k (ω) (angular frequency ω is real and $k = k' + ik''$ is complex) of set linearized Equations (1) is showed in Figure 3 with two approximations non-local (red points) and local (black points) approximation. We can see the imaginary part of the longitudinal wave number k'' of space charge waves for the case $dV/dE < 0$ as a function of frequency for two cases of approximations.

The amplification of space charge waves in GaN film occurs in a wide frequency range, and the maximal spatial increment for this case is $k'' = 2 \times 10^5\,\mathrm{m}^{-1}$ at the frequency $f = 160\,\mathrm{GHz}$. When compared with a case of the GaAs film, it is possible to observe an amplification of space charge waves in GaN films at essentially higher frequencies $f > 100\,\mathrm{GHz}$. To obtain an amplification of

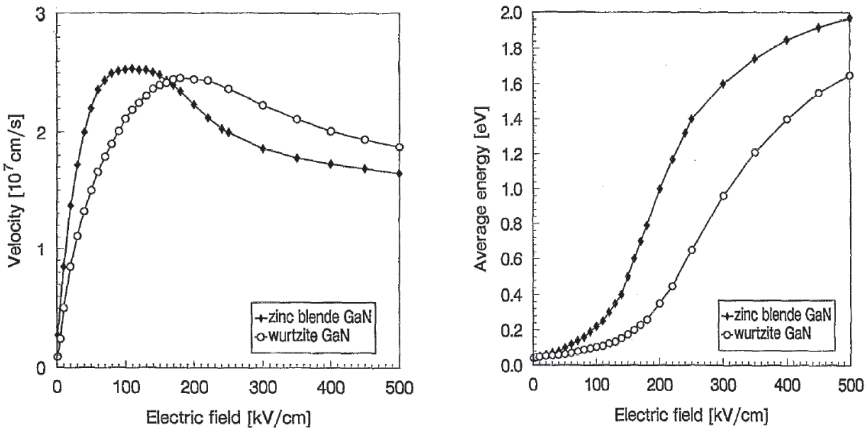

(a) (b)

Figure 2: Calculated steady state electron (a) drift velocity and (b) average energy in bulk GaN as a function of applied electric field along the (100) direction zincblende phase and within the basal plane along the (1010) direction in the wurtzite phase.

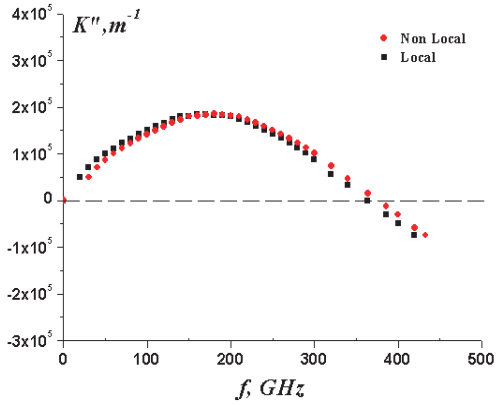

Figure 3: Spatial increment of instability k'' (ω) for local and non-local approximation. $E_0 = 150\,\mathrm{kV/cm}$, $n_0 = 0.8 \times 10^{17}\,\mathrm{cm}^{-3}$.

space charge waves of almost 20 dB, it is necessary to use the distance between input and output antennas of about 50 µm. Also, one can see that the effect of non-local dependence lead to some quantitative corrections about 6% for the increment of the amplification of space charge waves of millimeter wave range in GaN film.

The space charge waves are subject to amplification due to negative differential conductivity. But in GaN thin film, the space charge waves can be coupled with acoustic modes of the film, and the amplified space charge waves can excite effectively the hypersonic acoustic wave at the same frequency due to piezoeffect as was showed in [8], where the excitation of acoustic waves were considered for the GaN due to piezoeffect and deformation potential, the intervalley deformation potential assumed to be the same as GaAs, by means the equation of elasticity theory for mechanical displacement u takes place the form:

$$\rho \frac{\partial^2 u}{\partial t^2} = \frac{\partial}{\partial} \left(\rho s^2 \frac{\partial u}{\partial x} \right) + \frac{\partial}{\partial x} \left(\Gamma \frac{\partial^2 u}{\partial x \partial t} \right) \tag{3}$$

where ρ is the density elastic medium, s is the shear acoustic velocity, Γ is viscosity.

3. CONCLUSION

Theoretical results for the amplification of space charge waves with two approximations were reported in this paper. We found that the effect of non-local dependence lead to some quantitative corrections about 6% for the increment of the amplification of space charge waves of microwave or millimeter wave range in GaN film. We suggest using the non-local approximation to have a

good agreement with experiment results. Also, the amplification of acoustic-electromagnetic waves in GaN due to coupling with amplified space charge waves and hypersonic waves in GaN was investigated theoretically in this work.

ACKNOWLEDGMENT

This work was supported by project's UPP and by Dr. Lucinano Aguilera, director of post grade and research department of UPP.

REFERENCES

1. Internet site http://www.ioffe.ru/SVA/NSM/Semicond/GaN
2. Levinshtein, M. E., S. L. Rumyantsev, and M. S. Shur, *Properties of Advanced Semiconductor Materials: GaN, AlN, InN, BN, and SiGe*, Editors, John Wiley and Sons, 2001.
3. Grimalsky, V., E. Gutierrez-D., A. Garcia-B., and D. Koshevaya, "Resonant excitation of microwave acoustic modes in n-GaAs film," *Microelectronics Journal*, Vol. 37, No. 3, 395–403, 2006.
4. Pearton, S. J., J. C. Zolper, R.J. Shul, and F. Ren, "GaN: processing, defects, and devices," *Journal Appl. Phys.*, Vol. 86, No. 1, 1–79, 1999.
5. Carnez, B., A. Cappy, A Kaszinskii, E. Constant, G.Salmer, "Modeling of submicrometer gate field-effect transistor including effects of non-stationary dynamics," *J. Appl. Phys.*, Vol. 51, No. 1, 784–790, 1980.
6. Kolnik, J., I. Oguzman, and K. F. Brennan, "Electronic transport studies of bulk zincblende and wurtzite phases of GaN based on an ensemble Monte Carlo calculation including a full zone band structure," *J. Appl. Phys.*, Vol. 78, No. 2, 15 July, 1995.
7. Foutz, B. E. and L. F. Easten, "Comparison of high field electron transport in GaN and GaAs," *Appl. Phys. Lett.*, Vol. 70, No. 21, 2849–2851, 1997.
8. Grimalsky, V. V., S. Kosehevaya, L. M., Gaggero-S., and F. Diaz-A., "Excitation of hypersound due to coupling with space charge waves in GaN films," *Procc. in PIERS 2007*, 244–247, Beijin, China, March 2007.

Energy Emission from Evanescent Wave and Interference of Opposite Wave Streams: Near Field Coherent Scattering by Random Medium

Yu. N. Barabanenkov[1] and M. Yu. Barabanenkov[2]

[1]Institute of Radioengineering and Electronics, Russian Academy of Sciences
Mohovaya 11, 103907 Moscow, GSP–3, Russia
[2]Institute of Microelectronics Technology and High Purity Materials, Russian Academy of Sciences
142432 Chernogolovka, Moscow Region, Russia

Abstract— We present a basic formula for the coefficient of energy emission from an evanescent electromagnetic wave at scattering by a dielectric structure. The derived formula is interpreted in terms of interference of the evanescent wave incident onto dielectric medium with an evanescent component in its reflection from the medium. According to this formula the total amount of energy emission from evanescent wave at scattering by a 3D random medium is defined by the evanescent wave coherent reflection and can be evaluated with solution to a Dyson equation for the ensemble everaged angular spectrum amplitudes. The obtained formula enables one to estimate an upper limit of useful signal at information extraction from evanescent waves with the aid of a detection process where the evanescent waves have to couple on to propagating waves.

1. INTRODUCTION

Evanescent waves occur in different physical phenomena and suitable for several applications [1]. Recently an optical theorem for evanescent (near field) electromagnetic wave scattering by a dielectric structure was peseneted [2]. This optical theorem shows that an energy flux is emitted in the direction of the evanescent wave decay at mentioned scaattering. Note here the effect of energy emission from an evanescent wave is of basic importance for near field optics [3] bacause, in the detection process, evanescent waves have to couple on to propagating waves, even if the evanescent waves were enhanced previously, for example, by a negative refractive index material [4]. From the practice standpoint, it is worth finding a general and effective rule to estimate an upper limit of energy emission from an evanescent wave at scattering by a given material structure. The present report is devoted to resolving this problem for dielectric materials and, in particular, a 3D random medium. The last problem is especially intersting for devices used a waveguide propagation in the presence of turbulent medium around. Besides, the proposed analytical technique gives a better insight into the physical origin of evanescent waves couling to propagating waves.

The central point of the derivation is using a system of linear differential equations of the first order for angular spectrum amplitudes of local electromagnetic monochromatic waves going (propagating or decaying) forward and backward with respect to the embedding parameter into a 3D inhomogeneous dielectric medium. An original representation for the total energy flux along the embedding parameter is obtained as a pseudo-trace of the density matrix of angular spectrum amplitudes. The obtained representation reveals that energy emission from an evanescent wave explicitly relates with the interference between evanescent waves going (decaying) in opposite directions. This key result enables one to write the sought for energy emission coefficient in terms of the interference of an evanescent wave incident onto a dielectric medium with an evanescent component in its reflection from the medium. In particular, the evanescent wave coherent reflection by a 3D random medium slab is evaluated with a Dyson equation for the ensemble-averaged angular spectrum amplitudes. Some preliminary results of this work were presented earlier [5].

2. LINEAR SYSTEM FOR ANGULAR SPECTRUM AMPLITUDES

Following [2], we consider a dielectric medium with scalar dielectric permittivity $\epsilon(\vec{r})$ occupying a region between the planes $z = 0$ and $z = L$ of the Cartesian coordinate system x, y, z. The electric field $E^0_\alpha(\vec{r})$ of a monochromatic electromagnetic wave with frequency ω incident onto the left boundary plane $z = 0$ is written as $(2\pi)^{-2} \int d\vec{k}_\perp \exp(i\vec{k}_\perp\vec{r}_\perp)\ E^0_\alpha(\vec{k}_\perp)\exp(i\gamma_k z)$, where $\vec{k}_\perp$ is the transverse to the z axis component of a wave vector $\vec{k}$ and the Greek subscripts take the values x, y, z with agreement about the summation over repeated Greek subscripts in what follows. The

angular spectrum amplitude $E^0_\alpha(\vec{k}_\perp)$ of the incident electric field describes either a propagating or an evanescent wave, depending on whether $k_\perp < k_0$ and $\gamma_k = \sqrt{k_0^2 - k_\perp^2}$ is real or $k_\perp > k_0$ and $\gamma_k = i\sqrt{k_\perp^2 - k_0^2}$ is a purely imaginary quantities, respectively. The quantity k_0 is the wave number in the background with dielectric permittivity ϵ_0. An electromagnetic wave can be incident onto the right boundary plane $z = L$ with an angular spectrum amplitude $\tilde{E}^0_\alpha(\vec{k}_\perp)$ of the electric field.

Split virtually the dielectric medium under consideration into a stack of slices with splits between them, as in [5]. The local electric wave field $\hat{E}_\alpha(\vec{r})$ inside a split between slices is found to be

$$\hat{E}_\alpha(\vec{r}) = (2\pi)^{-2} \int d\vec{k}_\perp \exp(i\vec{k}_\perp \vec{r}_\perp) \gamma_k^{-1/2} \left[\exp(i\gamma_k z) F_{1\alpha}(\vec{k}_\perp, z) + \exp(-i\gamma_k z) F_{2\alpha}(\vec{k}_\perp, z)\right] \quad (1)$$

Here $F_{1\alpha}(\vec{k}_\perp, z)$ and $F_{2\alpha}(\vec{k}_\perp, z)$ are angular spectrum amplitudes of local waves inside splits, going forward and backward, respectively, and renormalized by multiplying on the factor $\gamma_k^{1/2}$. One should remember that quantities $\hat{E}_{x,y}(\vec{r})$ given by this equation are in fact the components of electric field inside the split but quantity $\hat{E}_z(\vec{r})$ is in fact $(1/\epsilon_0)\, D_z(\vec{r})$, with $\vec{D}(\vec{r}) = \epsilon(\vec{r})\vec{E}(\vec{r})$ being the displacement vector of the dielectric medium, according to the electromagnetic theory. As was shown in [5], a vector — column $F = (F_1, F_2)'$ with matrix elements F_1 and F_2 satisfies the following linear differential matrix equation of the first order

$$\frac{dF}{dz} = \Sigma_z \delta\mathbf{S} F \quad (2)$$

with radiative conditions on the slab boundaries

$$F_1(z = 0) = f; \quad F_2(z = L) = \tilde{f} \quad (3)$$

where $f_\alpha(\vec{k}_\perp) = \gamma_k^{1/2} E^0_\alpha(\vec{k}_\perp)$ and $\tilde{f}_\alpha(\vec{k}_\perp) = \gamma_k^{1/2} \tilde{E}^0_\alpha(\vec{k}_\perp)$ are renormalized angular spectrum amplitudes of incident waves going forward and backward, respectively. In Equation (2) $\Sigma_z = \begin{pmatrix} 1 & 0 \\ 0 & -1 \end{pmatrix}$ is the 2×2 block matrix generalization of the usual Pauli matrix σ_z. Symbol $\delta\mathbf{S}$ denotes a quantity in the equation $\mathbf{S} = \mathbf{I} + \delta\mathbf{S}\mathbf{\Delta z}$ for scattering matrix [2] of infinitesimaly thin slice of the medium, with slice thickness Δz tending to zero and $\mathbf{I}$ being the identity block matrix. Elements of an infinitesimal scattering matrix $\delta\mathbf{S}$ are given in [6] and written in terms of the spatial Fourier transforms $V(\overline{k}_\perp, z)$ and $v(\overline{k}_\perp, z)$ of the effective scattering potential $V(\vec{r}) = -k_0^2[\epsilon(\vec{r}) - \epsilon_0]/\epsilon_0$ and a function $v(\vec{r}) = -k_0^2[\epsilon(\vec{r}) - \epsilon_0]/\epsilon(\vec{r})$, respectively, with respect to the transverse to the z axis component of the position vector.

Note that a solution to the boundary problem (2) and (3) can give not only the angular spectrum amplitudes of local fields waves inside the medium but also the $\mathbf{S}$-matrix of the whole medium slab [2] as well, according to the limit relations

$$F_1(z = L) = \mathbf{A}\mathbf{f} + \tilde{\mathbf{B}}\tilde{\mathbf{f}}; \quad \mathbf{F_2}(\mathbf{z = 0}) = \mathbf{B}\mathbf{f} + \tilde{\mathbf{A}}\tilde{\mathbf{f}}, \quad (4)$$

which gives the renormalized tensor transmission $\mathbf{A}(\tilde{\mathbf{A}})$ and reflection $\mathbf{B}(\tilde{\mathbf{B}})$ coefficients of the whole medium slab in the case of wave incidence onto the left (right) slab boundary.

3. TOTAL ENERGY FLUX REPRESENTATION

Now let's seek for a representation for the total energy flux $\bar{P}_z(z)$ along the z axis inside a dielectric medium in terms of angular spectrum amplitudes of forward and backward going waves. To this end, substitute the local electric field (1) into a well known equality for the Poynting vector $\vec{P}(\vec{r})$ of a monochromatic electromagnetic field inside an inhomogeneous dielectric medium and integrate the z component of this vector over the (x, y)-plane. Some identical transformations lead to a desired result in the form of a pseudo-trace

$$\begin{aligned} \frac{8\pi\omega}{c^2} \bar{P}_z(z) \;=\; & (2\pi)^{-2} \int d\vec{k}_\perp H^{pr}(k_\perp) \left[\rho_{11\alpha\alpha}(\vec{k}_\perp, \vec{k}_\perp; z) - \rho_{22\alpha\alpha}(\vec{k}_\perp, \vec{k}_\perp; z)\right] \\ & + (2\pi)^{-2} \int d\vec{k}_\perp i H^{ev}(k_\perp) \left[\rho_{12\alpha\alpha}(\vec{k}_\perp, \vec{k}_\perp; z) - \rho_{21\alpha\alpha}(\vec{k}_\perp, \vec{k}_\perp; z)\right] \end{aligned} \quad (5)$$

Here the density matrix $\rho(z)$ of angular spectrum amplitudes is defined by $\rho_{ii'\alpha\alpha'}(\vec{k}_\perp, \vec{k}'_\perp) = F_{i\alpha}(\vec{k}_\perp, z)F^*_{i'\alpha'}(\vec{k}'_\perp, z)$, with the "star" superscript meaning a complex conjugate quantity. The symbols $H^{pr}(k_\perp)$ and $H^{ev}(k_\perp)$ denote projectors on a propagating $k_\perp < k_0$ and an evanescent $k_\perp > k_0$ waves, respectively. As can be seen, the contribution of propagating waves into the total energy flux along the z axis is related to angular spectrum intensities of forward and backward going waves, whereas the contribution from evanescent waves is explicitly related to a cross-product of angular spectrum amplitudes of opposite going (decaying) waves. Besides, the contribution from evanescent waves into this energy flux can also be related to the interference of opposite going (decaying) evanescent waves.

4. COEFFICIENT OF ENERGY EMISSION FROM EVANESCENT WAVE

Let an evanescent electromagnetic wave $H^{ev}\tilde{f} = \tilde{f}$ be incident onto the right boundary plane of a dielectric medium. The limit relations (4) give the following expressions for the energy fluxes (5) on the left $(8\pi\omega/c^2)\bar{P}_z(0) = -(\tilde{\mathbf{A}}^\dagger\mathbf{H^{pr}}\tilde{\mathbf{A}}\tilde{\mathbf{f}}, \tilde{\mathbf{f}})$ and the right $(8\pi\omega/c^2)\bar{P}_z(L) = -2\Im\left(H^{ev}\tilde{\mathbf{B}}\tilde{\mathbf{f}}, \tilde{\mathbf{f}}\right) + (\tilde{\mathbf{B}}^\dagger\mathbf{H^{pr}}\tilde{\mathbf{B}}\tilde{\mathbf{f}}, \tilde{\mathbf{f}})$ boundary planes. The first of these expressions actually represents the energy emission effect [2] from an evanescent wave. In a lossless dielectric medium, both expressions are equal to each other and so

$$2\Im\left(H^{ev}\tilde{\mathbf{B}}\tilde{\mathbf{f}}, \tilde{\mathbf{f}}\right) = \left(\tilde{\mathbf{A}}^\dagger\mathbf{H^{pr}}\tilde{\mathbf{A}}\tilde{\mathbf{f}}, \tilde{\mathbf{f}}\right) + \left(\tilde{\mathbf{B}}^\dagger\mathbf{H^{pr}}\tilde{\mathbf{B}}\tilde{\mathbf{f}}, \tilde{\mathbf{f}}\right) \tag{6}$$

This identity is written in terms of a scalar product for vector functions of $\vec{k}_\perp$ and coincides with the projection of extended optical theorem [2] onto evanescent waves. The "dagger" superscript in (6) denotes a complex conjugate transpose of a tensor operator and the symbol $\Im$ means an imaginary part of the quantity. On the left hand side of identity (6), the quantity $H^{ev}\tilde{\mathbf{B}}\tilde{\mathbf{f}}$ presents an evanescent component of the angular spectrum amplitude in reflection from a medium slab of an evanescent wave incident onto the slab, and the scalar product under the sign $\Im$ characterizes the interference of these two opposite going (decaying) evanescent waves.

An analogy can be derived between the identity (6) obtained for energy emission from an evanescent wave and the basic formula of wave extinction [7] as a result of interference of a propagating wave incident onto an object with a forward scattered propagating wave. To this end, let introduce, $C_{emiss} = 2\Im\left(H^{ev}\tilde{\mathbf{B}}\tilde{\mathbf{f}}, \tilde{\mathbf{f}}\right)$, a coefficient of energy emission from an evanescent wave. This emission coefficient describes the energy transform from an evanescent wave incident onto a dielectric slab boundary to waves propagating in both directions of transmission through and reflection from the slab. Defined by identity (6), the emission coefficient magnitude is large enough to make negative the energy flux (5) on the right boundary plane of a dielectric slab, similar to the energy flux on the left boundary plane. Following the analogy with [7], consider also the quantity $Q_{emiss} = (c^2/8\pi\omega)C_{emiss}/\bar{P}^0_\perp$ where $\bar{P}^0_\perp$ denotes a total energy flux in an evanescent wave incident onto the medium slab, evaluated along the direction perpendicular to that where this evanescent wave decays. The quantity Q_{emiss} is a dimensionless efficiency factor of energy emission from an evanescent wave. The total energy flux mentioned above in an evanescent wave needs some comments. In the special case where an incident evanescent wave is a s-polarized plane electromagnetic wave, with the electric field $\tilde{E}^0_\alpha$ and the transverse component $\vec{k}_\perp$ of the wave vector directed along the y- and x axes, respectively, the Poynting vector of an incident evanescent wave is directed along the x axis and given by $(8\pi\omega/c^2)P^0_x(z) = k_x \mid \tilde{E}^0_y \mid^2 \exp(2 \mid \gamma_k \mid z)$. Let the phase zero point of the incident evanescent wave be shifted to the boundary plane of incidence, $\tilde{E}^0_y \rightarrow \tilde{E}^0_y \exp(i\gamma_k L)$, and let's evaluate the energy flux in this wave across a (y, z)-plane area $\mid y \mid \leq \Delta L_y/2$ and $0 \leq z \leq L$ along the x axis. The total energy flux $\bar{P}^0_x$ in the incident evanescent wave is given now by $(8\pi\omega/c^2)\bar{P}^0_x = \Delta L_y(k_x/2 \mid \gamma_k \mid) \mid \tilde{E}^0_y \mid^2$. A similar result can be obtained for a more general case of an s-polarized incident evanescent quasi-plane wave beam if the above quantity $P^0_x(z)$ is considered to be the Poynting's vector x-component averaged over the (x, y)-section of the incident evanescent beam.

5. DYSON EQUATION FOR ENSEMBLE-AVERAGED ANGULAR SPECTRUM AMPLITUDES

Apply the above technique based on identity (6) to study the energy emission from an evanescent wave at scattering by a $3D$ random lossless dielectric medium slab. We start with a general

observation that the boundary problem (2) and (3) is equivalent to an integral matrix equation

$$F(z) = F^{(0)} + \int_0^L dz' h^{(0)}(z, z')\nu(z')F(z') \tag{7}$$

In the right hand side of this equation the first term is a vector — column $F^{(0)} = (f, \tilde{f})'$ with matrix elements taken from the boundary conditions (3). Integrand of the second term includes a diagonal matrix $h^{(0)}(z, z') = diag(H(z-z'), -H(z'-z))$, which is a special Green function of a homogeneous slab, with the Heaviside step function $H(x) = 1$ as $x \geq 0$ and $H(x) = 0$ as $x < 0$. The last but one factor of the integrand is a matrix $\nu(z) = \Sigma_z \delta\mathbf{S}$. Next we think $\nu(z)$ as random matrix process and make averaging the Equation (7) over the statistical ensamble of this matrix realizations. Using the Bourret approach [8] (see also [9]) leads to a Dyson equation for the ensemble-averaged $\langle F(z)\rangle$ angular spectrum amplitudes

$$\langle F(z)\rangle = F^{(0)} + \int_0^L dz' \int_0^L dz'' h^{(0)}(z, z')\mu(z', z'') \left\langle F(z'')\right\rangle \tag{8}$$

with a mass operator $\mu(z, z') = \left\langle \nu(z)h^{(0)}(z, z')\nu(z')\right\rangle$.

The Dyson Equation (8) is solved in approximation of scalar waves for an s-polarized incident evanescent quasi-plane wave beam. We suppose also that a seeking solution $\langle F(z)\rangle$ is small changed in scale of correlation radius r_0 of the scattering potential correlation function $\langle V(\vec{r})V(\vec{r}')\rangle$. Under adapted approximations a solution to Equation (8) is written in terms of effective complex dielectric permittivity $\epsilon_1(k_\perp)$ of a random medium slab and leads to the following physically transparent expression for the ensemble-averaged coefficient of the energy emission from an incident evanescent wave

$$\langle C_{emiss}\rangle = 2\,(2\pi)^{-2} \int d\vec{k}_\perp H^{ev}(k_\perp) \Im\, R(k_\perp) \mid \gamma_k \mid \mid \tilde{E}_y^0(k_\perp) \mid^2 \tag{9}$$

In the right hand side of this expression, the quantity $R(k_\perp) = R_\infty \left[1 - exp(2i\gamma_{1k}L)\right] \left[1 - R_\infty^2 exp\right.$ $\left.(2i\gamma_{1k}L)\right]^{-1}$ is a usual coherent reflection coefficient of an s-polarized wave from a homogeneous slab with the effective dielectric permittivity $\epsilon_1(k_\perp)$. Denote also $R_\infty = (\gamma_k - \gamma_{1k})/(\gamma_k + \gamma_{1k})$ the $L \to \infty$ limit of $R(k_\perp)$ in (9) and $\gamma_{1k} = \sqrt{k_1^2 - k_\perp^2}$ where k_1 is the wave number in a medium with dielectric permittivity $\epsilon_1(k_\perp)$.

For a random medium slab thick enough in the scale of an evanescent wave oscillation period in the transverse plane, $k_\perp L >> 1$, let replace the reflection coefficient in the integrand of (9) by its limit for a semi-infinite slab taking approximately $\Im\, R(k_\perp) \cong (\Im\, \epsilon_1(k_\perp)/\epsilon_0)\ (k_0^2/4 \mid \gamma_k \mid^2)$. Substitution of the integral (9) into the expression for the efficiency factor of energy emission from an evanescent quasi-plane beam at scattering by a random medium slab gives

$$\langle Q_{emiss}\rangle \approx \frac{\Im\, \epsilon_1(k_{0x})}{\epsilon_0}\ \frac{k_0^2}{k_{0x}}\ \Delta L_x \tag{10}$$

Here $k_{0x} > k_0$ and ΔL_x are the transverse component of an incident evanescent beam wave vector and an effective x-dimension of the (x, y)-section of the beam, respectively. The last step is to estimate the effective dielectric permittivity imaginary part, which is accomplished with a simple formula, $\Im\, \epsilon_1(k_{0x})/\epsilon_0 \approx 2/k_0\ell$, where $1/\ell = \langle V^2\rangle r_0^3$ is the extinction coefficient [9], with ℓ being the mean free path. This formula is derived in the limit of point effective inhomogeneities (scatterers) of the random medium, $k_{0x}r_0 << 1$.

The finally obtained expression $\langle Q_{emiss}\rangle \approx 2(k_0/k_{0x})(\Delta L_x/\ell)$ means that the energy emission factor from an evanescent beam at scattering by a random medium of point scatterers varies inversely with the evanescent wave parameter k_{0x}/k_0, which is large in the extreme near field limit, and directly with the beam linear dimension $\Delta L_x/\ell$ in the scale of the mean free path ℓ taken along the direction where an evanescent wave is oscillating.

6. CONCLUSION

Summarizing, an explicit relation between the effect of energy emission from an evanescent electromagnetic wave at scattering by a lossless dielectric structure and interference of an incident evanescent wave with an evanescent component in its reflection by the structure was established.

With this productive physical relation, the efficiency factor of energy emission from an evanescent quasi-plane beam at scattering by a 3D random medium slab in terms of imaginary part for effective complex dielectric permittivity was evaluated. It was found that the slab thickness can be of the order of an evanescent wave oscillation period along the slab boundary.

ACKNOWLEDGMENT

This work is supported by the grant from Russian Foundations for basic Research number 06-02-17451; by the Russian Academy of Sciences projects "Passive multichannel radio — and acousto — thermotomography of a human body in the near zone", "Creation and properties' investigation of new types of photonic crystals based on semiconductor and magnetic materials for the development of optoelectronic elements of infocommunication nets".

REFERENCES

1. De Fornel, F., *Evanescent Waves: from Newtonian Optics to Atomic Optics, Springer Series in Optical Science*, Springer, Berlin, 2001.
2. Gulyaev, Y. V., Y. N. Barabanenkov, M. Y. Barabanenkov, and S. A. Nikitov, "Optical theorem for electromagnetic field scattering by dielectric structures and energy emission from the evanescent wave," *Phys. Rev. E.*, Vol. 72, 026602, 2005.
3. Jutamulia, S. (Ed.), *Near-Field Optics*, MS172, SPIE, New York, 2002.
4. Pendry, J. B., "Negative refraction makes a perfect lens," Phys. Rev. Lett., Vol. 85, 3966, 2000.
5. Barabanenkov, M. Y., Y. N Barabanenkov, Y. V. Gulyaev, and S. A. Nikitov, "Energy emission from evanescent wave and interference of opposite wave streams," *Phys. Lett. A.*, Vol. 364, 421, 2007.
6. Barabanenkov, Y. N. and M. Y. Barabanenkov, "Energy invariants to composition rules for scattering and transfer matrices of propagating and evanescent waves in dielectric structures," 10, *PIERS Symposium, Proceedings*, Cambridge, USA, 26–29 March, 2006.
7. Born, M. and E. Wolf, *Principles of Optics*, Pergamon, New York, 1964.
8. Bourret, R. C., "Stochastically perturbed fields with applications to wave propagation in random media," *Nuovo Cimento*, Vol. 26, 1, 1962.
9. Barabanenkov, Y. N., "Transfer of trapped electromagnetic radiation in an ensemble of resonant mesoscopic scatterers," 415, *Wave Scattring in Complex Media: From Theory to Applications*, Van Tiggelen, B. A and S. E. Skipetrov (Eds.), Kluwer, Dordrecht, 2003.

Near Field Effect in Microwave Radiation of Periodically Heated Plane-like Thermal Source

Yu. N. Barabanenkov[1] and M. Yu. Barabanenkov[2]

[1]Institute of Radioengineering and Electronics, Russian Academy of Sciences
Mohovaya 11, 103907 Moscow, GSP-3, Russia
[2]Institute of Microelectronics Technology and High Purity Materials
Russian Academy of Sciences, 142432 Chernogolovka, Moscow Region, Russia

Abstract— We consider an evanescent wave created by a plane-like source of thermal microwave radiation in the form of thin slab with thickness tending to zero and condactivity tending to infinity, such that their product becomes constant. The slab temperature is supposed to be periodically varying along the x-axis on the slab and has the form of series in a $1D$ diffraction grating spectral orders. This diffraction grating is placed in the near field zone of the slab and consists of the cylindrical rulings which are parallel to the y-axis and placed periodically along the x-axis. The diffraction grating is used as a signal probe and the signal energy is evaluated according to recently elaborated general theory of energy emission from evanescent wave. It is shown analytically that the intensity of energy emission from evanescent waves of thermal radiation through the diffraction grating should have an interference pattern at diffraction grating moving parallel the heated slab. In this case the diffraction contrast of the pattern is defined by the temperature variation along the heated slab and the grating height above the slab.

1. INTRODUCTION

In 1953, Rytov [1] has predicted theoretically the near-field (quasistationary) component in thermal radiation of absorbing dielectric media. Carminati and Greffet [2] extended Rytov's analysis and showed that a long-range spatial coherence may exist in near-field of light thermally emitted into free space by an apaque materials supporting resonant surface waves, such as surface-plasmoms or surface phonon polaritons. Gaikovich et al. [3] discovered experimentally a near-field effect in thermal radio emission of an absorbing dielectric medium, having shown in fact that the effective depth of the receiver emission formation appears to be less than the skin-layer depth and depends on the size of the receiver antenna and its height above the the surface. Coello et al. [4] investigated experimantally a local control of evanescent microwaves using a scanning near-field microwave microscopy (SNMM). It is interesting to note that in the SNMM a signal probe-small matallic sphere is used that acts as a scatterer of the evanescent field, leading to creation of homogeneous (propagating) waves which can be easily detected and avalueted with the aid of the general treatment [5] of the energy emission effect from evanescent wave at scattering by dielectric structures.

In this report we would like to show that the SNMM mentioned can be used with some modification of signal-probe also for local control of evanescent microwaves in thermal radiation from periodically heated plane-like thermal source and consider a specific near field coherent effect related to spatial variation of source temperature.

Our analytical consideration is based on extended optical theorem [5] for energy flux created at evanescent wave scattering by a dielectric structure and on a model of $1D$ diffraction grating with line-like rulings studied in this reference.

2. EXTENDED OPTICAL THEOREM

Let a volume or surface dielectric structure with scalar dielectric permittivity $\epsilon(\vec{r})$ occupies a region between planes $z = 0$ and $z = L$ of Cartesian coordinate system x, y, z. The electric field of monochromatic electromagnetic wave with frequency ω to be incident onto the left boundary plane $z = 0$ is written as (see details in [5]) $(2\pi)^{-2} \int d\vec{k}_\perp \exp(i\vec{k}_\perp \vec{r}_\perp) E^\circ_\alpha(\vec{k}_\perp) \exp(i\gamma_k z)$. Here $\vec{k}_\perp$ is the transverse to the z axis component of a wave vector $\vec{k}$, and the angular spectrum amplitude $E^\circ_\alpha(\vec{k}_\perp)$ of the incident electric field describes either propagating or evanescent wave, depending on $k_\perp < k_\circ$ and $\gamma_k = \sqrt{k_\circ^2 - k_\perp^2}$ is real or $k_\perp > k_\circ$ and $\gamma_k = i\sqrt{k_\perp^2 - k_\circ^2}$ is purely imaginary quantity, respectively. The quantity $k_\circ$ is the wave number in a background with dielectric permittivity $\epsilon_\circ$. The angular spectrum amplitudes of electric field, transmitted through and reflected from the structure, are written in terms of the tensor operator transmission $A_{\alpha\beta}(\vec{k}_\perp, \vec{k}'_\perp)$ and reflection $B_{\alpha\beta}(\vec{k}_\perp, \vec{k}'_\perp)$

coefficients of plane wave, which may be evanescent, as $(2\pi)^{-2}\int d\vec{k}_\perp\, A_{\alpha\beta}(\vec{k}_\perp,\vec{k}'_\perp)E^\circ_\beta(\vec{k}'_\perp)$ and $(2\pi)^{-2}\int d\vec{k}_\perp\, B_{\alpha\beta}(\vec{k}_\perp,\vec{k}'_\perp)E^\circ_\beta(\vec{k}'_\perp)$, respectively. An electromagnetic wave may be incident upon the right boundary plane $z=L$ with angular spectrum amplitude $\tilde{E}^\circ_\alpha(\vec{k}_\perp)$. In this case the angular spectrum amplitudes of electric field, transmitted through and reflected from the structure, are written in terms of the tensor operator transmission $\tilde{A}_{\alpha\beta}(\vec{k}_\perp,\vec{k}'_\perp)$ and reflection $\tilde{B}_{\alpha\beta}(\vec{k}_\perp,\vec{k}'_\perp)$ coefficients of plane wave. The Greek subscripts take the values x,y,z with agreement about the summation over repeated Greek subscripts.

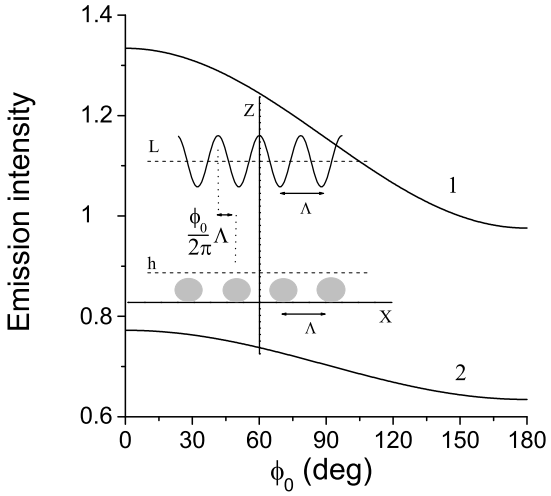

Figure 1: Solid curves are the results of numerical calculations of the dimensionless emission intensity $\langle I(L|ev)\rangle 2k_\circ^2/\langle|\xi|^2\rangle$ versus detuning $\varphi_\circ$ between position of the maximums of the first cosine harmonics of plane-like source of thermal radiation and line-like rulings of the $1D$ grating (see the inset). The values of the parameters are taken as: $\lambda_\circ = 10\,\mathrm{cm}$, $\Lambda = 8\,\mathrm{cm}$, $L-h = 0.5\,\mathrm{cm}$ (curve 1) and $1\,\mathrm{cm}$ (curve 2); $2|\hat{F}_1| = 0.8$. The inset schematically presents investigation of the energy emission effect from an evanescent wave generated by the plane–like source of electromagnetic thermal radiation (the solid line represents the first cosine harmonics) in the plane $z=L$. The position of the harmonics maximums and the line-like rulings of the 1D grating (gray filled circles) have a detuning $(\varphi_\circ/2\pi)\Lambda$.

We are interesting in a total energy flux $\bar{P}_z(z)$ along the z axis direction in the regions $z<0$ and $z>L$. This flux is given by integrating the z-component of the Pointing's vector for the total electromagnetic field over the x,y-plane. For a lossless dielectric structure the energy fluxes $\bar{P}_z(z)$ in the regions on the left and right from the boundary planes of the structure have the same value in accordance with the energy conservation law. Let an evanescent wave with the renormilized angular spectrum amplitude $\tilde{f}_\alpha(\vec{k}_\perp) = \gamma_k^{1/2}\tilde{E}^\circ_\alpha(\vec{k}_\perp)$ satisfied the condition $H^{ev}\tilde{f} = \tilde{f}$,where H^{ev} denotes a projector on evanescent waves, be incident on the right boundary of the structure. In this case the energy flux along the z axis is negative on both sides of the structure according to equations

$$\frac{8\pi\omega}{c^2}\bar{P}_z(z<0) = \frac{8\pi\omega}{c^2}\bar{P}_z(z>L) = -\left(H^{pr}\Delta\tilde{\mathbf{A}}H^{ev}\tilde{f}, H^{pr}\Delta\,\tilde{\mathbf{A}}H^{ev}\tilde{f}\right) \tag{1}$$

Here $\Delta\tilde{\mathbf{A}} = \tilde{\mathbf{A}} - \tilde{\mathbf{I}}$ is the deviation of a renormilized tensor operator transmission coeficient $\tilde{\mathbf{A}}$ from the identity tensor operator $\tilde{I}$(see [5]). This energy flux (energy emission) is created as an incident evanescent wave being scattered by a dielectric structure and propagates in direction of incident evanescent wave exponential decay. Note that the energy flux of the incident evanescent wave itself propagates across the direction of evanescent wave exponential decay.

Consider two applications of basic Equation (1) for the effect of energy emission from an evanescent wave upon its scattering by a dielectric structure.

3. ENERGY EMISSION FROM EVANESCENT WAVE UPON ITS SCATTERING BY ELECTRICAL DIPOLE

Let a dielectric structure in the form of an electrical dipole ($3D$ point-like scatterer) be placed in the point $\vec{r}_1$. In this simple case the basic Equation (1) takes a form

$$\frac{8\pi\omega}{c^2}\bar{P}_z(z<0)=\frac{8\pi\omega}{c^2}\bar{P}_z(z>L)=-\frac{1}{2}k_oQ_s\sum_\alpha|\tilde{E}^\circ_\alpha(\vec{r}_1|ev)|^2 \tag{2}$$

where Q_s denotes the scattering cross-section of the dipole and the incident electric field $\tilde{E}^\circ_\alpha(\vec{r}_1|ev)$ is of pure evanescent nature. The obtained result shows that the effect of energy emission from an evanescent wave upon its scattering by an electrical dipole enables one to obtain a direct information concerning the intensity distribution inside the evanescent wave, using the dipole as a scanning probe, as in [4]. From the practical point of view, it is more appropriate to use not one scanning dipole, but , for example, a system of dipoles. Therefore, the second application for the emission Equation (1) will be concerned with evanescent wave incidence upon $1D$ diffraction grating with line-like rulings ($2D$ point-like scatterers).

4. ENERGY EMISSION FROM EVANESCENT WAVE UPON ITS SCATTERING BY $1D$ DIFFRACTION GRATING WITH LINE-LIKE RULINGS

Let an evanescent electromagnetic wave be scattered by a $1D$ diffraction grating, whose rulings in the form of, e.g., cylinders with the radius R, are parallel to the y axis and placed periodically along the x axis with a period Λ. Suppose that the grating occupies a region $0<z<h<L$ denoting $h=2R$. The wave, with electric field being parallel to the rulings (TE-polarization), is incident upon a plane $z=L$ and has the form of series in the grating spectral orders

$$\tilde{E}^o_y(x,z)=\sum_\nu\exp\left[i\frac{2\pi\nu}{\Lambda}x-i\gamma(\nu)(z-L)\right]\tilde{E}^o_y(\nu) \tag{3}$$

Here $\gamma(\nu)=\sqrt{k_\circ^2-(2\pi\nu/\Lambda)^2}$, with spectral orders $\nu=0,\pm1,\pm2,\ldots$, and the phases of the spectral orders are evaluated from the reference plane $z=L$.

In the limit of grating with line-like ruling the basic Equation (1) gives according to [5] for the energy emission from evanescent wave a simple formula

$$\frac{8\pi\omega}{c^2}\bar{P}_z(z<0)=-\frac{1}{2}\Im\hat{b}|\tilde{E}^0_y(x=0,z=0|ev)|^2 \tag{4}$$

where a quantity $\hat{b}$ may be thought of as a cooperative scattering coefficient of a ruling of the grating and the incident electric field $E^0_y(x,z|ev)$ consists of evanescent spectral orders only.

To make the physical sense of expression (4) more clear, let denote the minimum (lower) evanescent wave spectral order ν, where $2\pi|\nu|/\Lambda>k_0$, by n_1, and $n_2=n_1+1, n_3=n_1+2,\ldots$, all other higher spectral orders of evanescent waves. Take further $E_k=\tilde{E}^0_y(n_k)+\tilde{E}^0_y(-n_k)$, where $k=1,2,3,\ldots$, to be an amplitude of a symmetrical function with respect to the variable x of an evanescent wave of the spectral order n_k and $\gamma_k=|\gamma(n_k)|$. Using these denotations we reduce the expression $I(L|ev)=|\tilde{E}^0_y(x=0,z=0|ev)|^2$ to the form

$$\begin{aligned}I(L|ev)&=\sum_k\exp(-2\gamma_kL)|E_k|^2+\sum_{k'>k}\exp\left[-(\gamma_{k'}+\gamma_k)L\right]\Gamma(k',k)\\&=\exp(-2\gamma_1L)|E_1|^2+\exp\left[-(\gamma_2+\gamma_1)L\right]\Gamma(2,1)+\exp(-2\gamma_2L)|E_2|^2+\ldots\end{aligned} \tag{5}$$

The coefficient of interference $\Gamma(k',k)$ between evanescent spectral orders $n_{k'}$ and n_k is defined by $\Gamma(k',k)=E_{k'}E^*_k+E^*_{k'}E_k=2|E_{k'}||E_k|\cos(\varphi_{k'}-\varphi_k)$, with $\varphi_{k'}$ and φ_k being phases of $E_{k'}$ and E_k, respectively. The second Equation (5) is written in approximation of two evanescent spectral orders n_1 and n_2 in the series (3).

Equation (5) can be a base for an interference — spatial spectroscopy of evanescent waves. Really the form of second Equation (5) is similar to the well known interference law of two monochromatic waves in optics. Such similarity means that the second Equation (5) describes implicitly an interference pattern in energy emission of evanescent spectral orders n_1 and n_2 through $1D$ grating with line-like rulings. To disclose the interference pattern hidden in the second Equation (5) we need considering in details a source construction of the incident evanescent wave.

5. PERIODICALLY MODULATED WHITE NOISE SOURCE

Returning to Equation (3) we will note that this type of incident electric wave field may be created, for example, by a plane–like source with an electric current density $\boldsymbol{j}(x,z)$ parallel to the y axis and confined inside a thin slab, $L-\Delta L/2<z<L+\Delta L/2$, with the ΔL thickness tending to zero and the current density tending to infinity, such that the product $j(x)=(4\pi\omega/ic^2)2\Delta L j_y(x,z)$ becomes constant. This kind of plane-like source may create a thermal radiation if the thin slab mentioned has conductivity σ tending to infinity, such that the product $\Delta L\sigma$ becomes constant. The plane-like source $j(x)$ may be chosen in this case to be periodically modulated along the x axis a spatial white noise $\xi(x)$, that is, $j(x)=F(x)\xi(x)$ where $F(x)$ is a periodic deterministic function. Following the fluctuation theory [6] of thermal electromagnetic radiation, the function $|F(x)|^2$ is supposed by [5] to be a specification of the radiating slab temperature $T(x)$ periodically varying along the x axis around the mean temperature $T_\circ$ as in the expansion

$$|F(x)|^2=\frac{T(x)}{T_\circ}=\sum_\nu \exp(i\frac{2\pi\nu}{\Lambda}x)\hat{F}_\nu \tag{6}$$

We put here next $\hat{F}_\nu=|\hat{F}_\nu|\exp(i\nu\varphi_\circ)$. In this case the radiating slab temperature is expanded in series along cosine harmonics, $2|\hat{F}_\nu|\cos[(2\pi\nu/\Lambda)(x+\varphi_\circ\Lambda/2\pi)]$, with amplitudes $2|\hat{F}_\nu|$ and detuning $\varphi_\circ$ between positions of the cosine maximums and the line-like ruling of the $1D$ grating (see the inset in Fig. 1). We specify further the two considered evanescent spectral orders in series (3) to be $n_1=1$ and $n_2=2$ and take into account only the first cosine harmonics of order $\nu=1$ with amplitude $2|\hat{F}_1|$ of the radiating slab temperature distribution. After these simplifications Equation (5)averaged over the ensemble of thermal fluctuation takes the form

$$\langle I(L|ev)\rangle=\frac{1}{2}\langle|\xi|^2\rangle\left(d_1^2+d_2^2+2d_1d_2|\hat{F}_1|\cos\varphi_\circ\right) \tag{7}$$

where an apparent condition $2|\hat{F}_1|<1$ should be held and $d_k=\exp(-\gamma_k L)/\gamma_k$; $k=1,2$.

This simplest interference pattern for averaged energy emission through the $1D$ grating with line-like rulings from evanescent waves created by the plane-like source of electromagnetic thermal radiation is depicted in Fig. 1. Equation (7) described this interference pattern is similar to known in optics as the interference law of two coherent in part light beams, with $|\hat{F}_1|$ being a degree of coherence of two evanescent spectral orders.

6. CONCLUSION

Summarizing, a specific near-field coherent effect in themal microwave radiation from periodically heated plane-like source has been considered analytically. The effect shows that temperature spatial variation can be cause for a spatial coherence of thermal radiation in near field zone of the termal source. This spatial coherence can be controled by moving of a diffraction grating along the plane source of thermal radiation in near field zone of the source.

ACKNOWLEDGMENT

This work is supported by the grant from Russian Foundation for Basic Research number 06-02-17451; the Russian Academy of Sciences projects "Passive multichannel radio — and acousto — thermotomography of a human body in the near zone", "Creation and properties' investigation of new types of photonic crystals based on semiconductor and magnetic materials for the development of optoelectronic elements of infocommunication nets".

REFERENCES

1. Rytov, S. M., *Theory of Electrical Fluctuations and Heat Emission*, Akedemii Nauk SSSR, Moscow,1953.
2. Carminati, R. and J. J. Greffet, " Near-field effects in spatial coherence of thermal sources," *Phys. Rev. Lett.*, Vol. 82, 1660, 1999.
3. Gaikovich, K. P., A. N. Reznik, V. L. Vaks, and N, V. Yurasova, " New effect in near-field thermal emission," *Phys. Rev. Lett.*, Vol. 88, 104302, 2002.
4. Coello, V., R. Villagomez, R. Cortes, and R. Lopez, "Near-field microscopy of evanescent microvawes," *Revista Mexicana de Fisica*, Vol. 51, 426, 2005.

5. Gulyaev, Y. V., Y. N. Barabanenkov, M. Y. Barabanenkov, and S. A. Nikitov, "Optical theorem for electromagnetic field scattering by dielectric structures and energy emission from the evanescent wave," *Phys. Rev. E.*, Vol. 72, 026602, 2005.
6. Rytov, S. M., Y. A. Kravtsov, and V. I. Tatarskii, *Principles of Statistical Radiophysics*, Springer, Berlin, 1988.

Operation of Evanescent Wave Intensity Using Metamaterials of Negative Permittivity and Permeability

Yu. N. Barabanenkov[1], **M. Yu. Barabanenkov**[2], **and S. A. Nikitov**[1]

[1]Institute of Radioengineering and Electronics, Russian Academy of Sciences
Mohovaya 11, 103907 Moscow, GSP-3, Russia
[2]Institute of Microelectronics Technology and High Purity Materials, Russian Academy of Sciences
142432 Chernogolovka, Moscow Region, Russia

Abstract— We present an independence phenomenon of electromagnetic evanescent wave enhancement and scattering inside a metamaterial with negative dielectric permittivity and magnetic permeability and with an inhomogeneity. The independence consists in that an evanescent wave scattering by local inhomogeneity does not bring influence on ability of the metamaterial rest part to enhance the evanescent wave at its transmission. This unique property of metamaterial is established analytically for the case of 2D inhomogeneity in dielectric permittivity and s-polarized electromagnetic wave. The extended boundary condition technique is used jointly with invariant embedding method and differential equation for the transfer matrix. The basic result is illustrated in two examples of inhomogeneities as linelike (2D pointlike) scatterer and a 1D diffraction grating with linelike rulings.

1. INTRODUCTION

As it was shown by Pendry [1] extending Veselago's [2] analysis, a planar left-handed material (LHM), for which both the dielectric permittivity ϵ and magnetic permeability μ are negative, having values of $\epsilon = -1$ and $\mu = -1$, can amplify (enhance) the electromagnetic evanescent waves at their transmission. Because the evanescent waves carry information on subwavelength details of an object, which is radiating or scattering these waves, the LHM slab can function as a superlens. One can see also the very interesting property of LHM to reconstruct the evanescent waves.

In this report we extend the Pendry's analysis on the case of LHM slab with a local inhomogeneity. Physically we consider an evanescent wave transmission through a LHM slab with the dielectric permittivity, $\epsilon(x, z) = -1 + \delta\epsilon(x, z)$, where $\delta\epsilon(x, z)$ is a 2D deviation (inhomogeneity), and a homogeneous magnetic permeability $\mu \to -1$. Our main result consists in that the scattering of evanescent wave by local inhomogeneity of dielectric permittivity does not bring influence on the LHM rest part ability to an evanescent wave enhancement at its transmission.

The central point of our derivation is using the extended boundary condition technique [3] that leads to a specific form of integral equation for the Green function, where the effects of evanescent wave enhancement by LHM and scattering by inhomogeneity are presented by singular surface and regular volume "potentials", respectively. We differentiate this integral equation with respect to the slab thickness and obtain following to Klytskin [4] the Riccati matrix differential equation for the slab reflection coefficient and the associated equation for the slab transmission coefficient. Applying some properties of this system of matrix equations studied by Reid [5] and Redheffer [6] we get a basic formula for the slab transmission coefficient. According to obtained formula a contribution of evanescent wave enhancement by LHM into the trasmission coefficient is described by two "inverse" exponential factors, similar to those in homogeneous slab, and contribution of scattering by inhomogeneity is written in terms of solution to differential equation [5, 7] for the transfer matrix. The basic formula is illustrated in two models of inhomogeneities as linelike (2D pointlike) scatterer and a 1D diffraction grating with linelike rulings similar to [8] but now in the LHM.

2. EXTENDED BOUNDARY CONDITION TECHNIQUE

Let the LHM slab under consideration occupies a region between the planes $z = 0$ and $z = L$ of the Cartesian coordinate system x, y, z. The surrounding background medium has the permittivity $\epsilon_0 = 1$ and permeability $\mu_0 = 1$. The electric field $\tilde{E}_y(x, z)$ of s-polarized monochromatic electromagnetic wave with frequency ω has the y-component only and can be expressed in terms of the Green function $G(x, z; x', z')$ and the current density $j_y^{src}(x, z)$ of electromagnetic field source as $\tilde{E} = (4\pi\omega\mu_0/ic^2)Gj_y^{src}$. Here one used an operator denotations and the Gaussian system of units. If the

source is placed in the right hand side (RHS) of the slab, $z > L$, it creates an electromagnetic wave with electric field $\tilde{E}_y^0(x,z)$ given by above equation in terms of the Green function $G_0(x-x', z-z')$ of background and to be incident onto the right boundary plane $z = L$ of the LHM slab.

We use next continuity of the electric field $\tilde{E}_y$ and the x-component of the magnetic field that is $(1/\mu)\partial\tilde{E}_y/\partial z$ on the slab boundaries and apply the extended boundary condition technique [3] deriving an integral equation for the Green function G. To make the derived equation more transparent physically let us introduce an effective volume scattering potential $V(x,z) = k_0^2 - k_1^2(x,z) = k_0^2\delta\epsilon(x,z)$, with $k_0 = \omega/c$ and $k_1 = k_0(\epsilon(x,z)\mu)^{1/2}$ being the wave number in the background and the LHM slab, respectively. It is useful also to employ the Fourier transform with respect to the x-component of the space position vector denoting the Fourier transforms of $G(x,z;\,x',z')$ and $V(x,z)$ by $G(q,q';\,z,z')$ and $V(q,z)$, respectively. After described preparations the integral equation for the Green function Fourier transform is written as

$$G(q,q';z,z') = \mu\frac{\exp[i\gamma_q(z'-z)]}{2i\gamma_q}\delta_{qq'} + \int_0^L dz'' \int_{q''} \frac{\exp(i\gamma_q\,|z-z''|)}{2i\gamma_q}\,\hat{V}(q,q'';z'')G(q'',q';z'',z') \quad (1)$$

as $0 < z < L$ and $z' > L$. Here $\gamma_q = \sqrt{k_0^2 - q^2}$, $\delta_{qq'} = 2\pi\delta(q-q')$, and $\int_q = (1/2\pi)\int dq$. A symbol $\hat{V}(q,q';z)$ means a singular potential defined by

$$\hat{V}(q,q';z) = V(q-q',z) + (1-\mu)i\gamma_q\,[\delta(z-\eta) + \delta(z-L+\eta)]\,\delta_{qq'} \quad (2)$$

with $\eta \to 0$ and $\eta > 0$. The regular volume part of this potential describes the wave scattering by inhomogeneity and the singular surface part describes the effect of evanescent wave enhancement by LHM.

Having resolved Equation (1), one can evaluate the defined in [8] operator coefficients of an inhomogeneous wave transmission through $\tilde{A}(q,q')$ and reflection from $\tilde{B}(q,q')$ the slab under consideration. Putting $\tilde{B}(q,q') = \exp[-i(\gamma_q + \gamma_{q'})L]R_L(q,q')$ and $\tilde{A}(q,q') = \exp(-i\gamma_{q'}L)T_L(q,q')$ we find relations, $R_L(q,q') = G(q,q';L,L)2i\gamma_{q'} - \delta_{qq'}$ and $T_L(q,q') = G(q,q';0,L)2i\gamma_{q'}$, which are used in the following sections.

3. RICCATY SYSTEM OF MATRIX EQUATIONS

Going to study the integral Equation (1) we first of all build a regularized version $v(q,q';z)$ of the potential (2), with replacing the delta-functions in the RHS of (2) to corresponding Heaviside step-functions defined on intervals $-\eta < z < 0$ and $L < z < L + \eta$, respectively, and having the hight equal to $1/\eta$. In solution to the integral Equation (1) one should make the limit transition $\eta \to 0$.

One can apply to Equation (1) with regularized potential the Klytskin technique [4] of differentiation with respect to the upper limit of integral. This technique leads to the Riccati matrix differential equation for the slab operator reflection coefficient and the associated matrix equation for the slab operator transmission coefficient. We introduce for convenience two auxiliary operators $\hat{R}_H$ and $\hat{T}_H$, with $H = L + \eta$, in terms of which the operator reflection and transmission coefficients of the slab are evaluated by the limit relations, $R_L(q,q') = \lim_{\eta\to 0}\mu[\delta_{qq'} + \hat{R}_H] - \delta_{qq'}$ and $T_L(q,q') = \lim_{\eta\to 0}\mu\hat{T}_H$. For the introduced auxiliary operators one can derive the Riccati matrix equation and the associated matrix equation, which are written in operator denotations as follows

$$\frac{d\hat{R}_H}{dH} = i(\gamma\hat{R}_H + \hat{R}_H\gamma) + (I + \hat{R}_H)\frac{1}{2i\gamma}v(I + \hat{R}_H) \quad (3)$$

with "initial" condition $\hat{R}_{H_0} = 0$ where $H_0 = -\eta$, and

$$\frac{d\hat{T}_H}{dH} = i\hat{T}_H\gamma + \hat{T}_H\frac{1}{2i\gamma}v(I + \hat{R}_H) \quad (4)$$

with "initial" condition $\hat{T}_{H_0} = I$ where I is identical operator $\delta_{qq'}$.

4. BASIC FORMULA FOR AN INHOMOGENEOUS LHM SLAB TRANSMISSION COEFFICIENT

We solve the matrix Equations (3) and (4) by three steps in intervals $(-\eta, 0)$, $(0, L)$, and $(L, L+\eta)$. Solutions in the first interval $(-\eta, 0)$ are diagonal and give by themselves the "initial" conditions for solution in the second interval written as

$$\hat{R}_0 = \frac{1-\mu}{1+\mu}\delta_{qq'}; \hat{T}_0 = \frac{2}{1+\mu}\delta_{qq'} \tag{5}$$

The "initial" conditions (5) are singular at $\mu \to -1$. To separate this singularity explicitly in solution to Equation (3) for the second interval $(0, L)$, we apply the Reid [5] and Redheffer [6] functional relations — semi-group property (RR-relations) proved by study a system of four matrix equations consisting the two Equations (3) and (4) and the two additional equations (RR-system). Actually the RR-system was considered under more general assumptions in [7] for blocks of the 2×2 block S-matrix of a dielectric structure and the RR-functional relations coincide with composition rules for the S-matrix. The RR-functional relations enable us to write out the solution to Riccati Equation (3) for the second interval in terms of solutions to the RR-system with standard zero-identical "initial" conditions and the first singular "initial" condition (5).

The RR-functional relations are used also by writing out the solutions to Equations (3) and (4) for the third interval $(L, L+\eta)$.

Formulating our main result, we apply another Reid's achievement as a theorem that solution to the RR-system of equations with standard zero-identical "initial" conditions is equivalent to corresponding solution to a linear differential equation for some 2×2 block matrix with the same "initial" conditions. This Reid theorem was proved also in [7] as some kind equivalence between solution to the Riccati system of equations for the 2×2 block S-matrix and solution to the linear differential equation for the 2×2 block transfer matrix M.

Let us suppose for physical transparency that inhomogeneity $\delta\epsilon(x, z)$ is restricted within a subslab, (z_1, z_2), where $0 < z_1 < z_2 < L$. Our main result consists in the basic formula for the operator transmission coefficient $T_L(q, q')$ of the LHM slab with local inhomogeneity evaluated in the limit $\mu \to -1$. This formula is written as

$$T_L(q, q')_{\mu\to -1} = \exp(-i\gamma_q z_1) \int_{q'} M_{11}^{-1}(q, q') \exp[-i\gamma_{q'}(L - z_2] \tag{6}$$

where $M_{11}^{-1}(q, q')$ denotes the inverse operator to operator $M_{11}(q, q')$, and the last quantity is $(1, 1)$ block of the transfer matrix M. The transfer matrix satisfies the differential equation

$$\frac{dM}{dz} = (Q_0 + Q_1)M \tag{7}$$

as $z_1 < z < z_2$ and "initial" condition in the form of diagonal block matrix $M = diag(I, I)$ as $z = z_1$. The block matrices Q_0 and Q_1 are given by

$$Q_0 = \begin{pmatrix} 1 & 0 \\ 0 & -1 \end{pmatrix} i\gamma_q \delta_{qq'} \quad \text{and} \quad Q_1 = \begin{pmatrix} 1 & 1 \\ -1 & -1 \end{pmatrix} (1/2i\gamma_q) V(q - q', z) \tag{8}$$

In the RHS of (6) the two inverse exponential factors $\exp(-i\gamma_q z_1)$ and $\exp[-i\gamma_{q'}(L - z_2]$ describe effect of evanescent wave enhancement after and before inhomogeneity, respectively, under condition that the both wave vectors q and q' are more then wave number k_0 in the background. The inverse block $M_{11}^{-1}(q, q')$ of the transfer matrix describes the evanescent wave scattering by inhomogeneity if the wave vector q' of incident wave is more k_0.

5. LINELIKE SCATTERER AND DIFFRACTION GRATING WITH LINELIKE RULINGS INSIDE LHM

Consider several illustrations to the basic formula (6).

In the case without inhomogeneity, $z_1 = z_2$, the inverse operator $M_{11}^{-1}(q, q') = \delta_{qq'}$ and the RHS of (6) becomes equal to $\exp(-i\gamma_q L)$, in accordance with the Pendry's result [1].

For approximative solution of Equation (7) one can use in a fruitful way a slow varying transfer matrix M_1 defined by $M = M_0 M_1$ where M_0 satisfies Equation (7) with the matrix Q_0 in the RHS only.

A linelike (2D pointlike) scatterer is defined as a thin dielectric rod infinitely extended along the y axis, intersecting the x, z plane near point (x_1, z_1) and having cross-section $\Delta x \Delta z$, with $\Delta x\,|q| << 1$ and $\Delta x\,|q'| << 1$ as well as $\Delta z\,|\gamma_q| << 1$ and $\Delta z\,|\gamma_{q'}| << 1$. In the case of linelike scatterer the equation for slow varying transfer matrix M_1 has in the RHS a block matrix as a product of matrix, $m = \begin{pmatrix} 1 & 1 \\ -1 & -1 \end{pmatrix}$ with property, $m^2 = 0$, and some degenerated scalar operator. Such kind of differential equation is resolved analytically that after substituting into the RHS of formula (6) gives

$$T_L(q,q')_{\mu\to -1} = \exp(-i\gamma_q L)\delta_{qq'} + \frac{i}{2}\hat{b}_1 \frac{1}{\gamma_q} \exp[-i(q-q')x_1] \exp(-i\gamma_q z_1) \exp[-i\gamma_{q'}(L-z_1] \qquad (9)$$

The scattering coefficient $\hat{b}_1$ of a linelike scatterer in the RHS of this equality is defined by

$$\frac{1}{\hat{b}_1} = \frac{1}{\delta\epsilon k_0^2 \Delta x \Delta z} - \frac{i}{2}\int_0^{q_{\max}} \frac{dq}{\pi}\frac{1}{\gamma_q} \qquad (10)$$

where the upper limit $q_{\max} \approx \min(1/\Delta x, 1/\Delta z)$ of integration with respect to the wave vector component q is defined by above conditions under which a thin dielectric rod may be thought as the linelike scatterer. The coefficient (10) is closely related to the monopole coefficient [9] of electromagnetic wave scattering by single cylinder in the Rayleigh limit and placed in the background, with having the dielectric deviation $\delta\epsilon = \epsilon - 1$. But we consider a single rod placed in the LHM slab an hence the rod dielectric deviation is $\delta\epsilon = \epsilon + 1$.

According to formula (9) the linelike scatterer can transform an incident enhanced evanescent wave with $|q'| > k_0$ into the scattered enhanced evanescent wave with $|q| > k_0$. Moreover the scattered wave may be more quasistatic and more enhanced than the incident evanescent wave, $|q| > |q'| > k_0$, depending on the change $q - q'$ of wave vector component at scattering. For instance, if position x_1 of the linelike scatterer has some dispersion of order Δx_1, the change of wave vector component at scattering will be order of $1/\Delta x_1$.

The diffraction grating with linelike rulings consists of a layer of linelike rods infinitely extended along the y axis and placed periodically along the x axis with a period Λ as in [8]. A solution to equation for slow varying transfer matrix M_1 for this case is similar with the case of linelike scatterer and results in the following pseudo- periodic form of the operator transmission coefficient

$$\begin{aligned} T_L(q,q')_{\mu\to -1} = \; & (1 + \frac{i}{2}\hat{b}\frac{1}{\gamma_q}) \exp(-i\gamma_q L)\delta_{qq'} \\ & + \frac{i}{2}\hat{b}\frac{1}{\gamma_q} \sum_{|\mu|\le\mu_{\max}} \exp(-i\gamma(\mu)z_1) \exp[-i\gamma_{q'}(L-z_1)]\delta_{q,q'+\frac{2\pi\mu}{\Lambda}} \end{aligned} \qquad (11)$$

Here $\gamma(\mu)$ denotes γ_q with $q = q' + 2\pi\mu/\Lambda$ and the sum is taking over diffraction grating spectral orders $\mu = \pm 1, \pm 2, \ldots$ The upper limit $\mu_{\max} \approx \min(\Lambda/\Delta x, \Lambda/\Delta z)$ of this sum is defined by conditions under which the rulings of the diffraction grating, having form of rods, may be thought as linelike scatterers.

The cooperative scattering coefficient $\hat{b}$ of a ruling inside grating is given in accordance with [8] by

$$\frac{2}{\hat{b}} = \frac{1}{\delta\epsilon k_0^2 \Delta x \Delta z/\Lambda} - i\sum_{|\mu|\le\mu_{\max}} \frac{1}{\gamma(\mu)} \qquad (12)$$

As one can see from formula (11) the diffraction grating with linelike rulings again can transform incident enhanced evanescent wave with $|q'| > k_0$ into the scattered enhanced evanescent wave. Besides the scattered wave with positive spectral order $\mu > 0$ is more quasistatic and more enhanced than the incident evanescent wave.

6. CONCLUSION

Summarizing, a basic formula was derived for transmission coefficient of a left handed material (LHM) slab, with simultaneously negative permittivity and permeability and with inhomogeneity. According to this formula, an enhanced by LHM evanescent wave can be transformed by inhomogeneity into a more quasistatic and hence more enhanced evanesced by LHM wave. The derived formula is demonstrating an independence phenomenon that effect of evanescent wave enhancement by LHM slab in area before and after inhomogeneity is not brought influence of inhomogeneity.

ACKNOWLEDGMENT

This work is supported by the grant from Russian Foundations for basic Research number 06-02-17451; by the Russian Academy of Sciences projects "Passive multichannel radio — and acousto — thermotomography of a human body in the near zone", "Creation and properties' investigation of new types of photonic crystals based on semiconductor and magnetic materials for the development of optoelectronic elements of infocommunication nets".

REFERENCES

1. Pendry, J. B., "Negative refraction makes a perfect lens," *Phys. Rev. Lett.*, Vol. 85, 3966, 2000.
2. Veselago, V. G., "Electrodynamics of materials with both negative ϵ and μ," *Sov. Phys. Usp.*, Vol. 10, 509, 1966.
3. Tsang, L., J. A. Kong, and R. Shin, *Theory of Microwave Remote Sensing*, Wilay, New York, 1985.
4. Klytskin, V. I., *The Imbedding Method in the Theory of Wave Propagation*, Nauka, Moscow, 1980 (in Russian).
5. Reid, W. T., "Solutions of a Riccati matrix differential equation as functions of initial values," *J. Math. and Mech.*, Vol. 8, 221, 1959.
6. Redheffer, R., "Inequalities for a matrix Riccati equation", *J. Math. and Mech.*, Vol. 8, 349, 1959.
7. Barabanenkov, Yu. N. and M. Yu. Barabanenkov, "Energy invariants to composition rules for scattering and transfer matrices of propagating and evanescent waves in dielectric structures," *PIERS Symposium*, *Proceedings*, 10, Cambridge, USA, 26–29 March, 2006.
8. Gulyaev, Yu. V., Yu. N. Barabanenkov, M. Yu. Barabanenkov,and S. A. Nikitov, "Optical theorem for electromagnetic field scattering by dielectric structures and energy emission from the evanescent wave," *Phys. Rev. E.*, Vol. 72, 026602, 2005.
9. Van de Hulst, H., *Light Scattering by Small Particles*, Wilay, New York, 1957.

Performance of a Folded Dipole with a Closed Loop for RFID Applications

Sung-Lin Chen and Ken-Huang Lin

Department of Electrical Engineering, National Sun Yat-Sen University, Taiwan

Abstract— Folded dipoles are commonly used in the RFID applications. In this paper, we propose an RFID tag design using a folded dipole with a closed loop structure. The closed loop makes impedance matching design more easily especially when the small resistance and large reactance of the antenna impedance are required. Design methodology, simulation and performance measurement results of an implementation are also presented in this paper.

1. INTRODUCTION

Radio Frequency Identification (RFID) is a technology used for object identification and has become very popular in retail, transportation, manufacturing and supply chin [1]. An RFID system is composed of tags, one or more readers and a data management system. A tag consists of an antenna and an Application Specific Integrated Circuit (ASIC) chip. The tag antenna acts as electromagnetic power receiver and transmitter for the chip. For the purpose of energy conversion, the tag chip includes a charge capacitor that causes the tag chip to have largely reactive characteristic impedance, making the antenna more difficult to match with the tag chip than with a general radio frequency system of 50-Ω characteristic impedance. The electromagnetic power from the antenna is maximally delivered to the tag chip when the antenna has a conjugate impedance of the chip [2]. Since the energy interaction between the chip and antenna is one of the most important issues, a successful antenna design is determined by conjugate impedance match between both components [3]. Several papers have been published on RFID tag antennas, including meander antenna [4], slot antenna [5], folded dipole antenna [6], inductively coupled spiral antenna [7], etc.. Some of them provide good concept for RFID tag antenna design aspects.

In this paper, we present a folded dipole antenna with a closed loop near the tag chip [8]. The required input resistance (R_i) and reactance (X_i) can be achieved separately by choosing appropriate geometry parameters. The proposed antenna can in particular find applications for the tag chips that require small resistance and large reactance. The design method, simulation results and read range performance measurement of this tag are included.

2. ANTENNA CONFIGURATION AND DESIGN METHOD

The configuration of the proposed folded dipole with a closed loop antenna is shown in Figure 1. The folded dipole part must be kept opening and it provides great freedom for impedance adjustment especially for the imaginary part, which is a very important feature for conjugate impedance matching design. This is achieved by tuning geometry parameters F_1, F_2 and F_3 [6]. After obtaining satisfactory imaginary part, the closed loop was added to the previous folded dipole antenna and the geometry parameters L_1 and L_2 for the requirement conjugate impedance were tuned. The closed loop can pull down the impedance of the antenna especially for the real part. This feature makes the design approach to the actual impedance of the tag chip in the real cases.

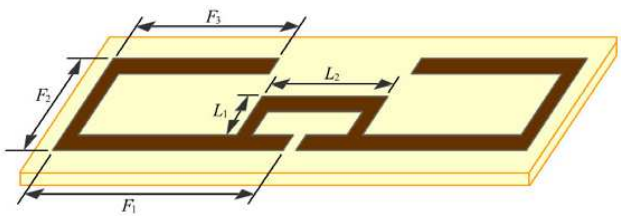

Figure 1: Structure of the proposed RFID tag antenna.

We examined the proposed antenna with a real case where the chip impedance is $22.0 - j130.0$. In our design, the operating frequency of the tag antenna was 925 MHz. The experimental model

was made of copper-clad substrate with $\varepsilon_r = 4.4$ and the thickness $h = 1.6\,\text{mm}$. The width of the copper line was $W = 1.44\,\text{mm}$. After imaginary part was matched properly, the parameters of the folded dipole F_1, F_2, and F_3 were adjusted. Then the closed loop structure was added into the folded dipole and the parameters of the closed loop L_1 and L_2 were tuned to achieve conjugate impedance of the tag chip. The design and simulation of the structure are performed using Ansoft HFSS 10.

3. RESULTS OF SIMULATION AND IMPLEMENTATION

The simulated input impedance of the folded dipole antenna without a closed loop is shown in Figure 2. The impedance response increases with F_3, but decrease with W. The variation R_i of is not significant, but X_i is sensitive to the total length of the folded dipole. According to this property, we tuned F_1, F_2 and F_3 to obtain the required X_i and disregard R_i at this step.

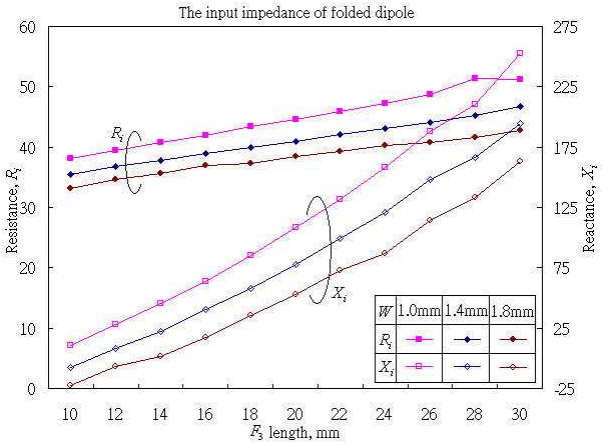

Figure 2: Input impedance of folded dipole with F_3 and W as the parameters ($F_1 = 40\,\text{mm}$, $F_2 = 20\,\text{mm}$).

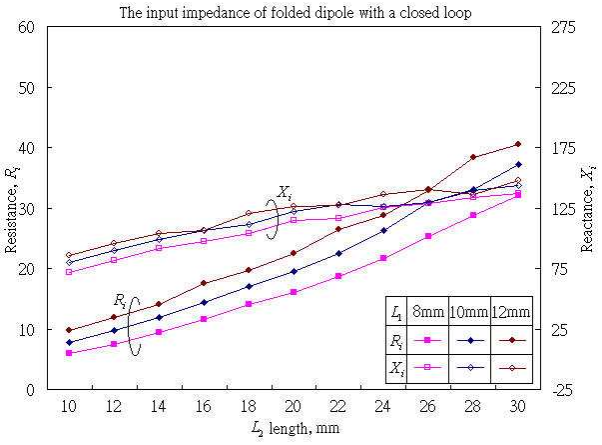

Figure 3: Input impedance of presented antenna structure with L_1 and L_2 as the parameters ($F_1 = 40\,\text{mm}$, $F_2 = 20\,\text{mm}$, $F_3 = 25\,\text{mm}$, $W = 1.4\,\text{mm}$).

The simulated input impedance of the fixed parameters folded dipole antenna with a closed loop is shown in Figure 3. With the closed loop, it clearly reduces the input impedance, particularly to the R_i. The imaginary part, X_i does not vary considerably with the parameters of the closed loop. The required impedance can be achieved easily by adjusting the parameters L_1 and L_2. Table 1 shows the parameters and simulated impedance for the target design.

Table 1: Parameters of the implementation tag.

Strap impedance	Folded dipole (mm)			Closed loop (mm)		Antenna impedance	Maximum read range
	F_1	F_2	F_3	L_1	L_2		
$22.0 - j130.0$	40	20	25	10	22	$22.5 + j127.8$	3.5 m

To verify the read range performance of the implementation using this antenna design, an RFID tag antenna with the parameters listed in Table 1 was made and tested. An RFID reader was set up to measure the read range performance of the RFID tag and the operation frequency band was 922–928 MHz. The radio power of the reader was approximately 750 mW and the gain of the linearly polarized reader antenna was 5.0 dBi, so the total transmit power is approximately 2.371 W EIRP (Effective Isotropic Radiated Power). The maximum read range of the RFID tag was approximately 3.5 m for the above specified test conditions. The result of the read range performance was also listed in Table 1.

According to the results of simulation and measurement, the input impedance R_i and X_i of the RFID tag antenna can achieve decoupled tuning with the proposed antenna configuration. In the other words, the parameters of folded dipole and closed loop can be tuned separately. Therefore,

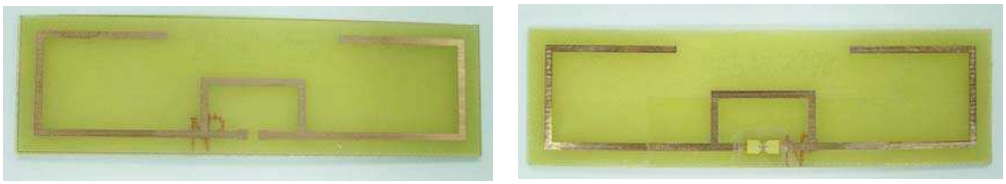

Figure 4: Photograph of RFID tag prototype: antenna and tag.

the proposed antenna configuration is very useful for the RFID tag antenna design, particularly suitable for impedance requirement of small real part and large imaginary part.

4. CONCLUSION

In this paper, we realized a folded dipole with a closed loop for RFID tag antennas design. The closed loop makes impedance matching more easily especially when small resistance and large reactance of the antenna impedance are required. In addition, the closed loop serves as short circuit to DC current, so it can eliminate electrostatic discharge (ESD) from damaging the tag chip. The design method presented here can also be applied to various impedances of the commercial tag chips which operate at other frequency bands.

REFERENCES

1. Finkenzeller, K., *RFID Handbook*, 2nd, John Wiley & Son, England, 2003.
2. Stutzman, W. L. and G. A. Thiele, *Antenna Theory and Design*, Wiley & Son, New York, 1998.
3. Foste, P. R. and R. A. Burberry, "Antenna problems in RFID systems," *IEE Colloquium on RFID Technology*, 3/1–3/5, London, UK, 1999.
4. Rao, K. V. S., P. V. Nikitin, and S. F. Lam, "Antenna design for UHF RFID tags: a review and a practical application," *IEEE Trans. Antennas Propagation*, Vol. 53, No. 12, 3870–3876, Dec. 2005.
5. Chen, S. Y. and P. Hsu, "CPW-fed folded-slot antenna for 5.8 GHz RFID tags," *Electronics Letters*, 25th, Nov. 2004.
6. Qing, X. and N. Yang, "A folded dipole antenna for RFID," *IEEE AP-S International Symposium*, Vol. 1, 97–100, 2004.
7. Cho, C., H. Choo, and I. Park, "Design of UHF small passive tag antennas," *IEEE AP-S International Symposium*, Vol. 2B, 349–352, 2005.
8. Chen, S. L. and K. H. Lin, "A folded dipole with a closed loop for RFID applications," *IEEE AP-S International Symposium*, 2007.

Radiation Characteristics of Optimized Ultra Wideband Printed Dipoles for Different Impulse Excitations

P. Cerny and M. Mazanek

Department of Electromagnetic Filed, Czech Technical University in Prague
Czech Republic

Abstract— In case of particular ultra wideband applications (i.e., radar, positioning, etc.), it is crucial to know the transient responses of antennas. This paper picks up the threads of the previous work [4], where the particle swarm optimization method searches for the dipole shape, which accomplishes two required parameters — good matching and minimal distortion. As a result, the optimized ultra wideband dipole is perfectly matched and minimally distorts the applied signal. The main part of the paper presents the transient radiation characteristics of optimized dipoles with common dipole element shape, such as the ideal dipole, dipole with balun transformer and monopole with planar ground plane. A particular attention is paid to the different impulse excitation. The spatial distributions of the fidelity and the spatially averaged fidelity is presented for three different excitation Gaussian signals.

1. INTRODUCTION

The ultra wideband (UWB) radio represents an emerging technology that attracts attention of both, industry and academia. An antenna represents the indispensable component of every radio system. Consequently, in this paper, the antenna is studied from the pulse radiation point of view. Firstly, the required ultra wideband antenna should be perfectly matched to the feeding line. Secondly, it could serve as a Gaussian impulse-shaping filter and, at the same time, radiate impulses similar to the higher orders of the Gaussian impulses.

Ultra Wideband Technology: The ultra wideband technology is defined as any radio technology using signals that have a spectrum occupying a bandwidth either greater than 20% of the centre frequency or a bandwidth greater than 500 MHz, see [1]. This represents the main difference from the narrow band technologies whose bandwidth typically does not exceed 10% of the centre frequency.

European Telecommunications Standards Institute (ETSI) and US Federal Communications Commission (FCC) defined the frequency mask, which determines the maximal radiated power of the ultra wideband signal. This mask indicates the frequency band ranging from 3.1 to 10.6 GHz within which the ultra wideband signal is transmitted with a maximum power. For the ultra wideband signals, the first derivative (or higher) of the Gaussian impulse is mostly used.

2. UWB ANTENNAS AND PARAMETERS

The key advantage of the planar dipoles is represented by the fact that they have omni-directional radiation patterns, substantially smaller dimensions and turn out to be more suitable for any communication devices, radars, positioning devices, etc. Moreover, the dipole antennas derivate the applied signal at the antenna port, [2, 3]. Basic shapes of wideband dipoles, such as elliptical, diamond and thick, are discussed in [2, 3, 5]. This paper presents the whole three dimensional spatial characteristics of the optimized antennas. The presentation of the radiated impulses to all directions would result in considerable amount of characteristics. In order to reduce the number of these characteristics, the spatial distribution of fidelity and spatially averaged fidelity are presented. The fidelity function is defined by Equation (1) and the spatially averaged fidelity is defined by Equation (2), [7]. These characteristics quantitatively describe the distortion of radiated impulses.

$$F(\theta,\phi) = \max_{\tau} \left| \frac{\int\limits_{-\infty}^{\infty} \left(\vec{E}(t,R,\theta,\phi) \cdot \vec{a}(\theta,\phi) T(t+\tau) \right) R dt}{\sqrt{\int\limits_{-\infty}^{\infty} \left| \vec{T}(t) \right|^2} \sqrt{\int\limits_{-\infty}^{\infty} \left| \vec{E}(t,R,\theta,\phi) \right|^2 R^2 dt}} \right| \tag{1}$$

$$SAF = \int\limits_0^{2\pi} \int\limits_0^{\pi} F(\theta,\phi) \sin\theta d\theta d\phi \tag{2}$$

3. DIPOLE SHAPE OPTIMIZATION PROCEDURE

The implementation of the optimization procedures contains optimization function, evaluating function, start conditions, object of optimization and its parameterization. The entire optimization process is implemented in MATLAB except for the part of evaluation function, which solves the simulated structure in the full-wave electromagnetic field simulator CST Microwave Studio. The discretization of the dipole structure is carried out by the following parameters: dipole element length by L, shape by $w_0 - w_{20}$ and dipole parts gap by s, see Fig. 1.

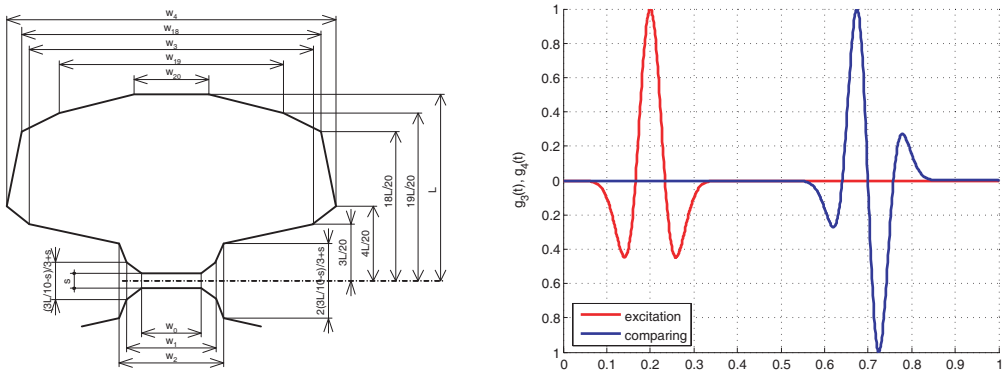

(a) (b)

Figure 1: (a) Optimized dipole dimensions, (b) Excitation impulse (left) and impulse used in computing of fidelity (right).

The particle swarm optimization (PSO) represents a robust stochastic evolutionary computation method benefiting from the movement and intelligence of swarms, [6]. The evaluating of the fitting function consists of the updating of dipole structure discretization parameters, solving the transient analysis of the dipole structure in CST and solving the fitting function (with the help of the results obtained by CST), [3]. The result shape of the optimization is shown in Fig. 2(a). This serrated shape was manually smoothed, see Fig. 2(b).

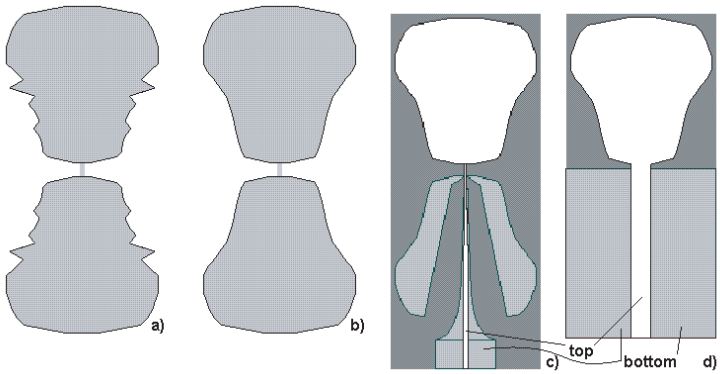

Figure 2: Optimized dipole shapes, (a) original shape using PSO, (b) smoothed shape, (c) dipole with balun transformer, (d) monopole with planar ground plane.

The radiated impulses are very similar to the third derivative of the Gaussian impulse. The obtained results are very similar and the difference between overall fitting functions equals approximately 0.13%. This very insignificant difference can be seen and the distortion of these impulses is exactly expressed in the Table 1. More details can be found in [4]. The presented spatial distribution of the fidelity and the spatially averaged fidelity are solved for three different excitation signals. The first signal is basic Gaussian impulse (G1), the second one is the first derivative of the Gaussian signal (G2) and the third excitation signal is the second derivative of the Gaussian impulse (G3). All these excitation signals have the parameter $\sigma = 48 \cdot 10^{-12}$.

Table 1: Summarization of results.

Fidelity fitting function	side radiation	front radiation
original shape	0.9457	0.9624
smoothed shape	0.9381	0.9666
dipole antenna	0.9435	0.9628
monopole antenna	0.9210	0.9680

3.1. Dipoles with Real Feeding Circuits

The feeding circuit represents an indispensable part of all antennas and determines significantly antenna parameters. The differential feeding port used for excitation of optimized dipoles in previous chapter is non-physical port and was used only for the simplification of the optimized structure and acceleration of the optimization process. On the other hand, it is necessary to feed the optimized structures by a circuit that would be more suitable and more satisfactory from the physical point of view. Two very different feeding circuits were used for dipoles feeding. These methods were designed to be used in printed structures.

The first obtained dipole structure involving the feeding balun transformer is depicted in Fig. 2(c). The second monopole structure including the planar ground plane is depicted in Fig. 2(d). The feeding parts of both dipole and monopole were tuned step-by-step in order to minimize the reflection coefficient in required frequency band. The values of fidelity fitting functions are compared for the dipole and monopole structures in Table 1. More details can be found in [4].

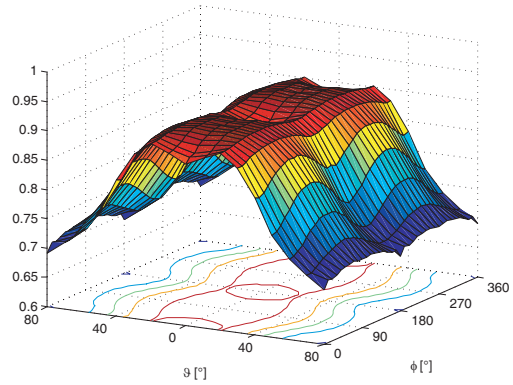

Figure 3: Spatial distribution of the fidelity function for smooth dipole — 1G exc.

4. TRANSIENT RADIATION CHARACTERISTICS OF DIPOLES

The spatial distribution of the fidelity function for the basic Gaussian impulse excitation is depicted in Fig. 3 for the smoothed ideal dipole. In case of the dipole antenna with the balun transformer or monopole antenna with the partial ground plane, the spatial distribution of the fidelity function is presented in Fig. 4(a) or in Fig. 4(b) respectively. Similarly, the spatial distributions of the fidelity function for the first and the second derivatives of the basic Gaussian signal are depicted in Figs. 5(a)–Fig. 5(f). The spatially averaged fidelity for all presented antennas and excitation signal are presented in Table 2.

Table 2: Summarization of results 2.

Spatially averaged fidelity	smoothed dipole	dipole antenna	monopole antenna
G1 excitation	0.8594	0.8278	0.8589
G2 excitation	0.8241	0.9098	0.9425
G3 excitation	0.9393	0.9058	0.9277

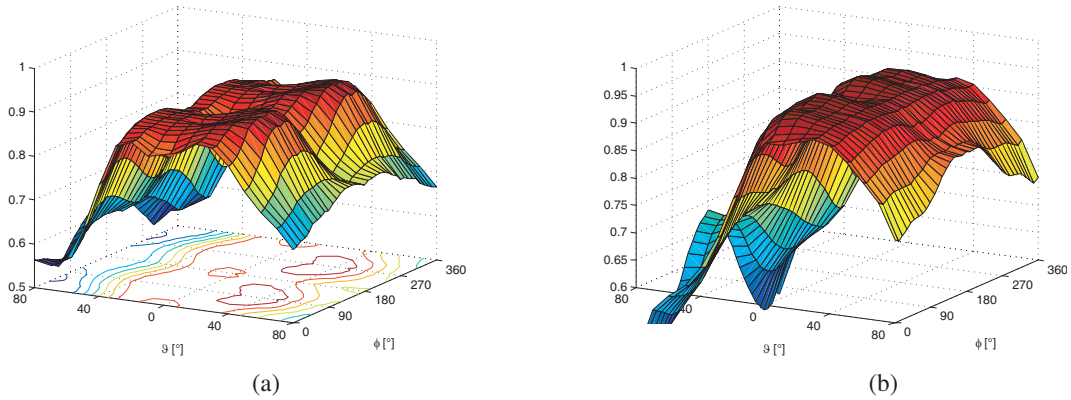

Figure 4: Spatial distribution of the fidelity function for (a) dipole antenna with balun transformer; (b) monopole antenna — 1G exc.

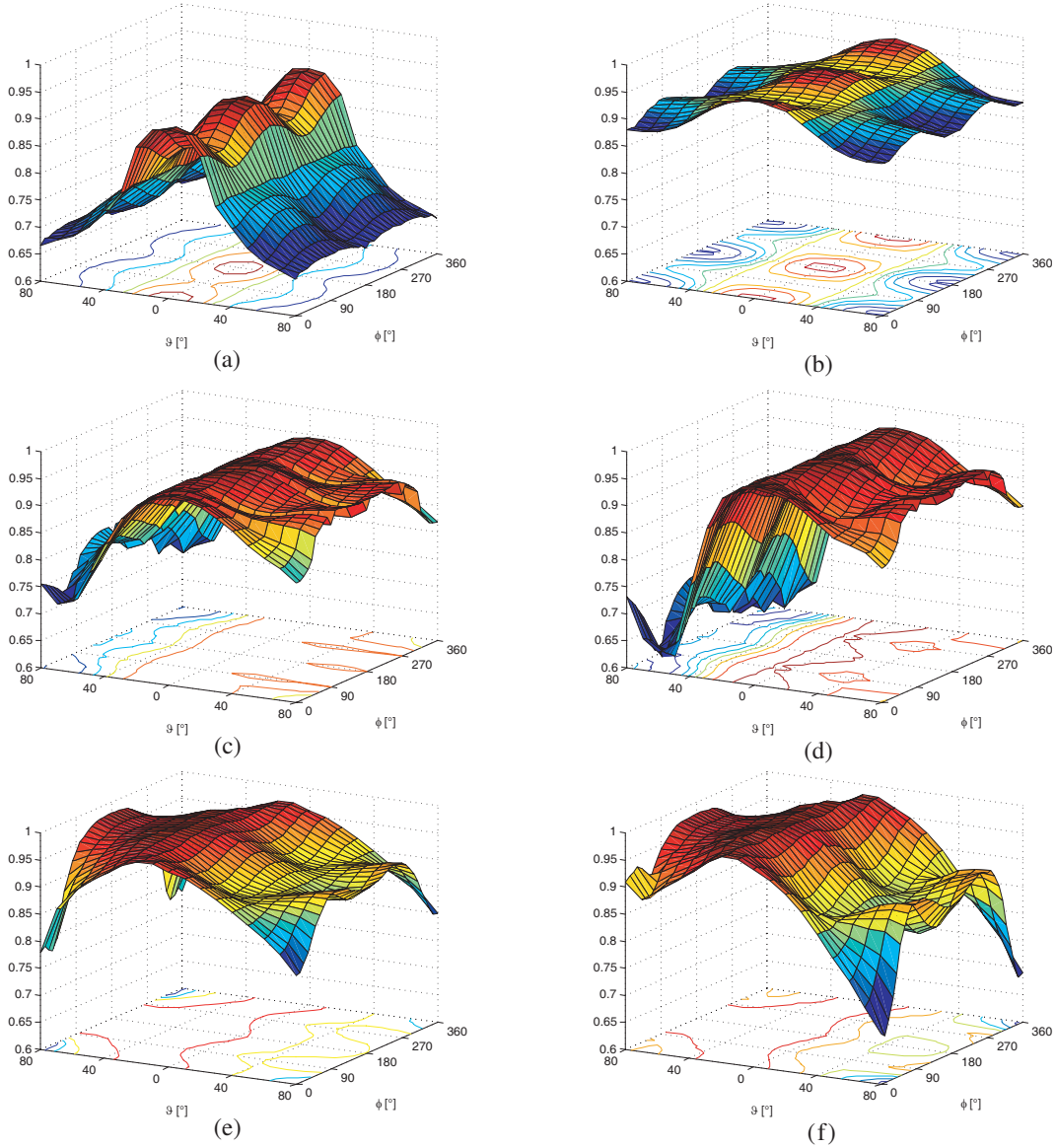

Figure 5: Spatial distribution of the fidelity function for: (a) smooth dipole — 2G exc., (b) smooth dipole — 3G exc.; (c) dipole antenna with balun transformer — 2G exc., (d) dipole antenna — 3G exc., (e) monopole antenna — 2G exc., (f) monopole antenna — 3G exc.

All presented characteristics are relatively similar. The dipole and monopole antennas are suitable for the impulse radiation in case of the first and the second derivative of the Gaussian impulse excitation (G2 and G3). The impulse radiation performance is worse for the basic Gaussian impulse excitation, see Table 2. In comparison to the front direction, the presented antennas radiate more distorted impulses to the side direction, see Table 1. The dipole antenna radiates bigger amount of energy to the bottom of the antenna and the monopole antenna radiates the bigger amount of radiated energy to the top of the antenna, see Fig. 5(c)–Fig. 5(f).

5. CONCLUSION

The optimization using PSO method of planar ultra wideband dipole shapes has been performed and its results have been presented and compared with results obtained by analysis of dipole and monopole antennas with feeding circuits in previous work, [4]. These dipoles and monopole offer very good performance.

The transient radiation characteristics of previously optimized antennas have been analyzed and presented in this paper. These antennas are optimized for the radiation of the third derivative of the Gaussian impulse with the second derivative excitation. In case of both the first and the second derivative of the Gaussian impulse excitation, the planar dipole antenna and the monopole antenna distort also minimally radiated impulses and are suitable for the radiating and receiving of ultra wideband implulses.

ACKNOWLEDGMENT

The research is a part of the activities of the Department of Electromagnetic Field of the Czech Technical University in Prague in the frame of the research project of the Ministry of Education, Youth and Sports of the Czech Republic No. LC06071 Centre of quasi-optical systems and terahertz spectroscopy. The measurement was supported by the project Research in the Area of the Prospective Information and Navigation Technologies MSM 6840770014.

REFERENCES

1. "Federal communications commission," *First Order and Report, Revision of Part 15 of the Commission's Rules Regarding UWB Transmission Systems, FCC 02-48*, April 22, 2002.
2. Cerny, P. and M. Mazanek, "Optimized ultra wideband dipole antenna," *Proceedings of the 18th International Conference of Applied Electromagnetics and Communications*, Dubrovnik, Croatia, 2005.
3. Cerny, P., M. Mazanek, P. Piksa, V. Sokol, and T. Korinek, "Transient response optimization of ultra wideband antennas (using particle swarm optimization)," *Proceedings of the European Conference on Antennas and Propagation*, 168, Nice, France, 2006.
4. Cerny, P. and M. Mazanek, "Optimization of Transient Response Radiation of Printed Ultra Wideband Dipole Antennas (Using Particle Swarm Optimization Method)," submitted to *RadioEngineering, Proceedings of Czech and Slovak Technical Universities and URSI Committees*, No. 2, 2007.
5. Schantz, H. G., "Bottom fed planar elliptical UWB antennas," *Proceedings of the Ultra Wideband Systems and Technologies*, 219–223, Reston, USA, 2003.
6. Robinson, J. and Y. Rahmat-Samii, "Particle swarm optimization in electromagnetics," *IEEE Transactions on Antennas and Propagation*, Vol. 52, No. 2, 397–407, 2004.
7. Miskovsky, P., J. M. Gonzalez-Arbesu, and J. Romeu, "Application of UWB antenna descriptors to lossy dipole performance assessment," *Antennas and Propagation Society International Symposium 2006, IEEE*, 175–178, Albuquerque, USA, 2006.

Collinear and Coparallel Principles in Antenna Design

M. Polivka and A. Holub
Department of Electromagnetic Field, Czech Technical University in Prague, Czech Republic

Abstract— The paper summarizes collinear principle (CollP) used for the design of enhanced directivity collinear arrays (CollAr) first. Various types of collinear arrays starting from historical wire design introduced by Franklin, going through coaxial collinear arrays as far as to the most recent CollAr implemented in microstrip line and patch technology are mentioned. Further supplementary principle of parallel line up arrangement of in-phase current sources to form coparallel array (CopAr) in presented. Two examples of CopAr based on planar extension of collinear microstrip patch antenna (PCoMPA) and branched F-type antenna are described in more details.

1. INTRODUCTION

Antenna arrays known as collinear arrays (CollAr) are based on in-phase feeding of radiating elements that are lined up serial and their radiation is typically omnidirectional perpendicular to the longitudinal axis of elements. The original idea has been introduces by Franklin [1]. He first designed CollAr from long wire that had $\lambda/4$ U-shaped sections to provide phase shift to maintain in-phase feeding of straight $\lambda/2$ parts of wire, see Fig. 1(a). Instead of U-shaped sections small inductors to ensure phase shift can also be used. The principle has been then applied by several researches in either coaxial [2], or microstrip line antenna technology [3, 4], see Figs. 1(b), (c), (d). These linear versions of collinear antenna arrays have nearly omnidirectional radiation pattern due to more or less longitudinal axis symmetry. However collinear microstrip patch antenna (CoMPA) first introduced in [5] has directive character as the ground plane is present as necessary part of patch type antennas.

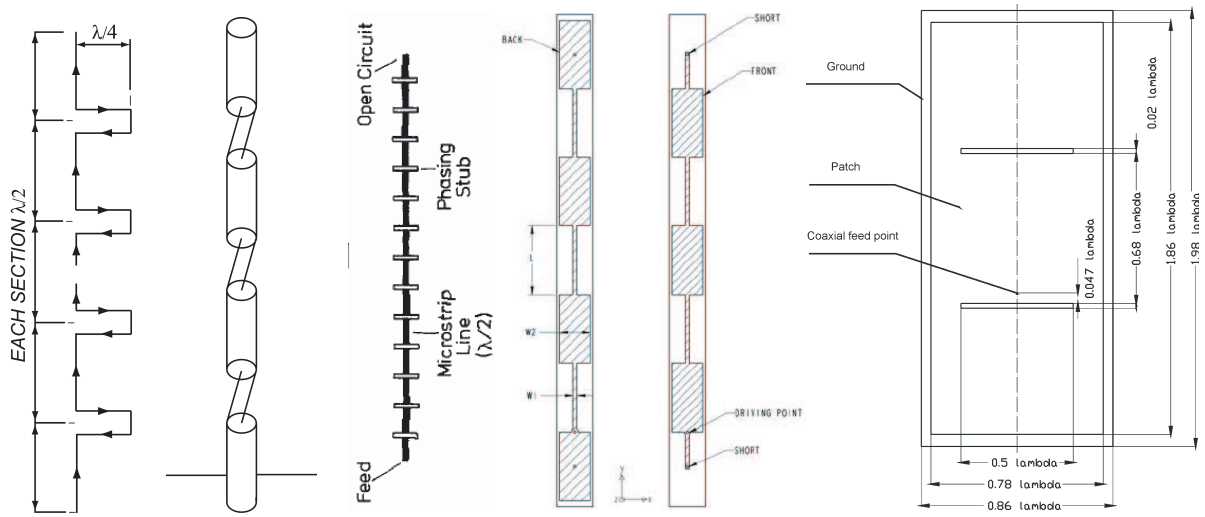

Figure 1: Geometry of several collinear arrays: (a) original Franklin dipole [1], (b) coaxial collinear [2], (c) microstrip line with a flat O shaped sections [3], (d) thin/thick section microstrip line [4], (e) collinear microstrip patch antenna [5].

If the line up of the radiating elements is parallel, the character of radiation is not omnidirectional but directional. The optimal distance between two elements to achieve highest directivity is approx. $\lambda_0/2$ supposing in-phase feeding. The directivity is again higher in dependence on the number of elements but in this case the radiation is provided through two beams backward and forward, perpendicular to the axis of the array, broadside with two beams. The antenna radiating in two opposite directions is not practical, hence the reflection plane is often used. This plate prevents

backward radiation and provides approx. 3 dBi directivity enhancement. This arrangement of in-phase radiating elements that are lined up parallel to the element axis is here called coparallel array (CopAr). The two designs of CopAr are presented here.

The first example of CopAr is a planar extension of collinear microstrip patch antenna (PCoMPA) that operate with TM_{03} and TM_{05} mode. Modular principle can be used to extent either longitudinal or lateral dimensions and consequently the directivity of an antenna. This antenna combine both collinear and coparallel principles. The second example of CopAr is a coparallel branched F-type antenna (CopFA) that use two and three parallel in-phase current source areas formed by monopole heel stubs perpendicular to the ground plane. It is an extension of classical wire F antenna realized in planar technology. Operational principle, and corresponding radiation properties of particular implementation of both CopArs for 2.4 GHz frequency band together with main advantages and drawbacks are described.

2. COLLINEAR/COPARALLEL PLANAR MICROSTRIP PATCH ANTENNA

As it is well-known that microstrip patch antenna (MPA) can be designed to operate with higher order modes. However radiation properties of higher order modes of simple rectangular or circular shaped MPA exhibit nulls in radiation pattern due to the presence of out-phase current density areas on patch surface. Using suitable patch shape modification that employs slots and notches to redistribute current density to form several in-phase source areas these nulls can be suppressed and enhanced gain can be achieved. Here TM_{0x} mode (where x determine the number of half current wavelengths in the resonant longitudinal dimension of the patch) of MPA is used. PE in the shape of inner slots and edge notches are then applied to the patch in such a way that they eliminate radiation from even out-phase half current wavelengths. Specific topology of the patch shape modified patch thus arise. The simplest example of the usage of described principle is MPA operating with TM_{03} mode with one central narrow slot placed in the middle of the patch. The slot of the length approx. $\lambda_g/2$ and width of a fragment of λ_g causes that second/even current wavelength flow around the slot, see Fig. 2(a). Currents in the vicinity of the slot circumference thus cancel their contributions to the radiated fields due to the out-phase orientation on opposite sides. Vector current distribution of longitudinally extended MPA operating with TM_{05} mode with two slots is illustrated in Fig. 2(b). The same effect of even half current wavelength flowing around both slots as in case of a patch operating with TM_{03} mode with one slot can be seen.

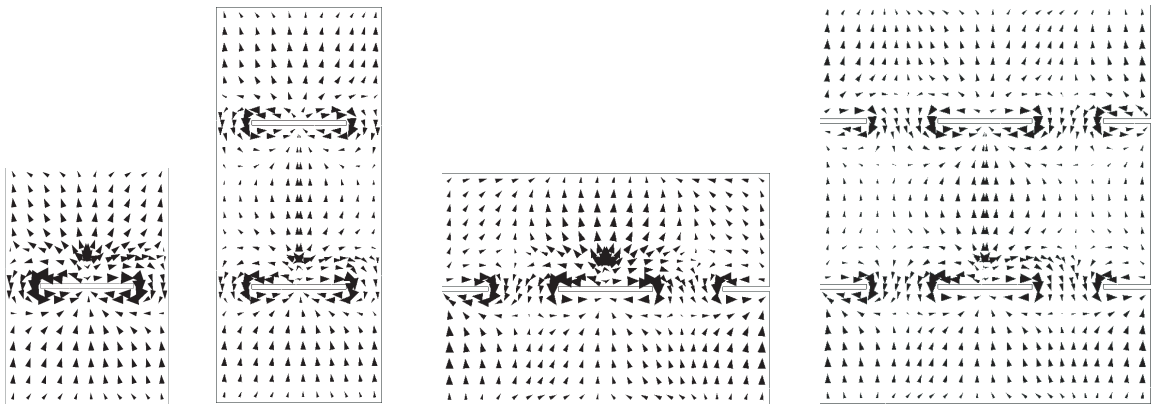

Figure 2: Vector surface current distribution on the CoMPA with (a) TM_{03} and (b) TM_{05} modes and PCoMPA with (c) TM_{03} and (d) TM_{05} modes (modeled in IE3D MoM simulator with infinite ground plane), (e) PCoMPA with TM_{05} mode separated into basic modules.

Further these radiators forming CollAr in microstrip patch technology can be laterally extended and complemented by a pair(-s) of approx. $\lambda_g/4$ edge notches perpendicular to the patch border to introduce coparallel principle, see Figs. 2(c), (d). The current distribution of TM_{03} and TM_{05} modes remains the similar and phenomenon of current flow around the slots and notches is maintained. As a result the $|J_y|$ current density component is dominant at the surface of the patch and the radiator exhibits broadside linearly polarized radiation with directivity enhancement. Domination of the $|J_y|$ component on the most of the patch surface is actually a necessary condition for reasonable low

cross-polar level. Advantage of a such arrangement compared to classical array is simple structure without separate feeding network. Disadvantage is of course unavailability to control amplitude distribution and phase of source currents on the structure and increased cross-polar ratio.

Figure 3 shows the CoMPA motif from Fig. 2(d) separated by dashed lines into basic building modules previously discussed arrangements. A hypothesis of further longitudinal and lateral extension based on these building blocks with appropriate number and position of inner slots and a pairs of lateral edge notches to further enhance directivity and gain can be stated.

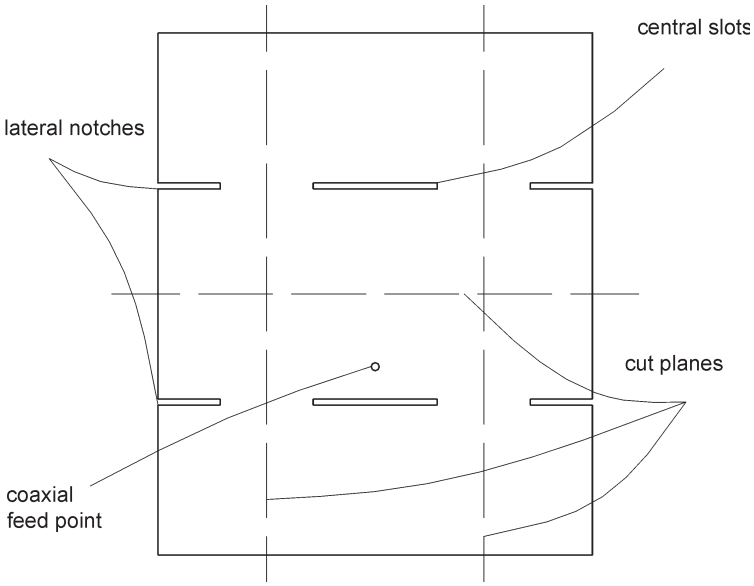

Figure 3: Schematic view of PCoMPA with TM05 mode separated into basic modules that can form independent CollAr and/or CopAr.

Radiation pattern of realized PCoMPA operating with TM_{05} [6] in 2.4 GHz frequency band with directivity 15.4 dBi and sidelobe level −10 dB can be seen in Fig. 4.

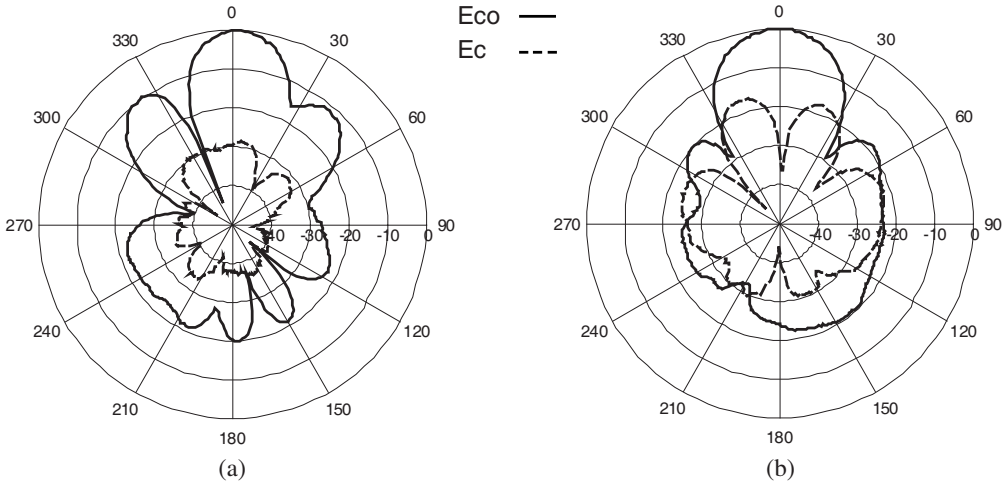

Figure 4: Measured co-polar (Eco) and cross-polar (Ex) components in dB of radiation pattern of PCoMPA operating with TM_{05} mode with two central slots and two pairs of lateral edge notches in (a) E-plane, (b) H-plane.

3. COPARALLEL BRANCHED F-TYPE F ANTENNA

Classical F antenna is a variant of monopole, where the top section has been folded down so as to be parallel with the ground plane. This is done to reduce the height of the antenna, while maintaining a resonant trace length. This parallel section introduces capacitance to the input impedance of

the antenna, which is compensated for by implementing a short circuit stub. The main radiating source area is the current density of the heel of monopole.

Directivity of such a structure is about 2.2 dBi and the radiation has an omnidirectional character, perpendicular to the vertical stub.

To implement coparallel principle to enhance directivity into the F antenna design two and three parallel stubs connecting with approx. $\lambda_g/2$ line conductors are introduced, see Fig. 5. As it can be seen by proper setting of connecting wire length in-phase parallel orientation of current density on stubs perpendicular to the ground plane can be excited. To further enhance directivity the reflection plane in the distance of $\lambda_g/4$ can be used [7]. The resulting measured radiation patterns can be seen in Figs. 6 and 7.

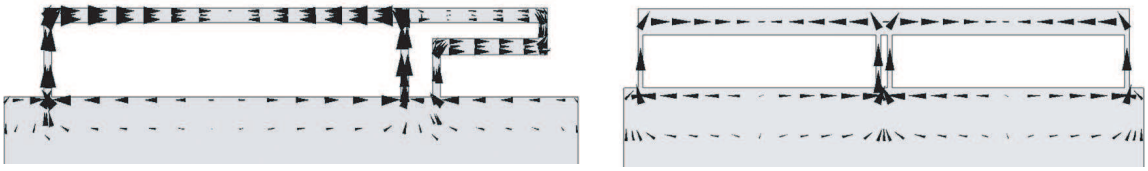

(a) (b)

Figure 5: Vector surface current distribution of (a) two element (b) three element branched F-type antenna.

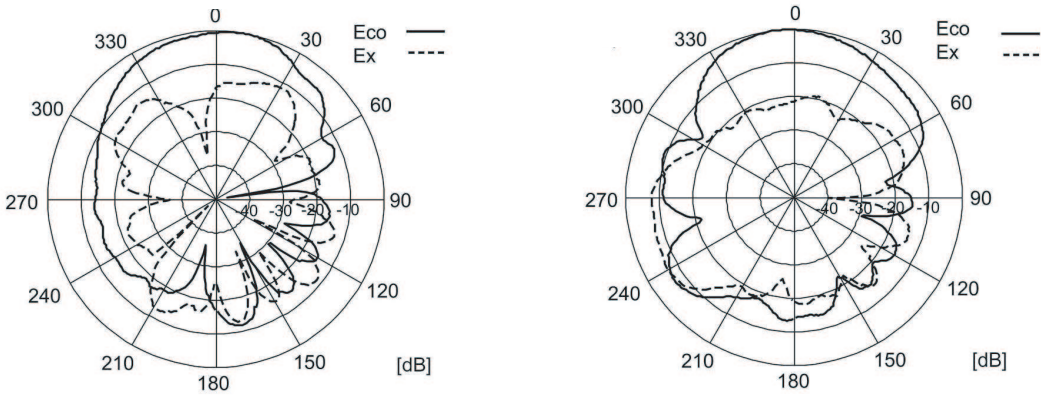

(a) (b)

Figure 6: Measured radiation pattern of two element branched F-type antenna, (a) H-plane, (b) E-plane.

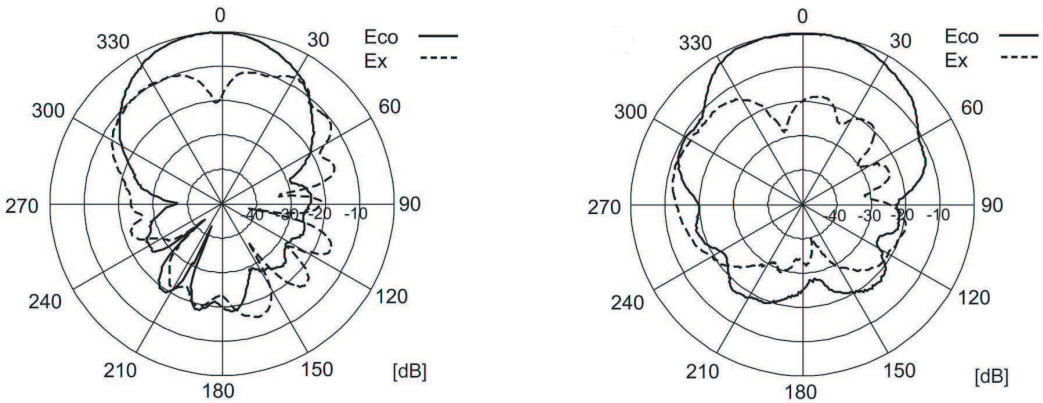

(a) (b)

Figure 7: Measured radiation pattern of three element branched F-type antenna, (a) H-plane, (b) E-plane.

Two and three element branched F-type antennas with reflecting plane has provided directivity

up to 10.7 dBi, see Table 1. The advantage of such an arrangement is a simple structure and relatively small dimensions. The drawback is a low front-back ratio which can be enhanced by larger dimensions of the reflection plane.

Table 1: Comparison of simulated directivities and impedance bandwidth for VSWR = 2 of classical single element F antenna, and two and three element branched F-type antennas with and without reflector plane.

Antenna	D [dBi]	B [MHz]	B [%]
F-antenna	2.2	240	9.8
2 elements F-antenna	4.75	245	10
3 elements F-antenna	6	100	4.1
2 elements + reflector	9.5	250	10.25
3 elements + reflector	10.7	97	3.7

4. CONCLUSIONS

Collinear principle in antenna design has been summarized based on historical development. Supplement principle denoted as coparallel principle has been presented on recent authors designs of collinear and coparallel arrays implemented in microstrip patch and F-type planar antenna technologies. Vector current distribution has been used to explain antenna operational principle. Main advantages and drawbacks of presented individual designs has been discussed.

ACKNOWLEDGMENT

This work has been conducted at the Department of Electromagnetic Field of the Czech Technical University in Prague and supported and by the grant of the Grant Agency of the Czech Republic No. 102/04/P131 "Multiband Planar Antennas with Compact-Shaped Radiators" and by the Czech Ministry of Education, Youth and Sports in the frame of the project Research in the Area of the Prospective Information and Navigation Technologies MSM 6840770014.

REFERENCES

1. Franklin, C. S., Brit. Patent No. 242342-1924, 1924.
2. Judazs, T. J. and B. B. Balsley, "Improved and theoretical and experimental models for the coaxial collinear antenna," *IEEE Tans. Antennas and Propagat.*, Vol. 37, 289–296, 1989.
3. Solbach, K., "Microstrip-Franklin antenna," *IEEE Tans. Antennas and Propagat.*, Vol. 30, No. 4, 773–775, 1982.
4. Bancroft, R. and B. Bateman, "An omnidirectional planar microstrip antenna," *IEEE Trans. Antennas and Propagat.*, Vol. 52, No. 11, 3151–3153, 2004.
5. Polivka, M., A. Holub, and M. Mazanek, "Collinear microstrip patch antenna," *Radioengineering*, Vol. 14, No. 4, 2–5, 2005.
6. Polivka, M. and A. Holub, "Planar version of collinear microstrip patch antenna," *Conference Proceedings MIKON 2006*, Vol. 2, 959–962, 2006.
7. Holub, A. and M. Polivka, "Branched F-type antenna," presented at *Radioelektronika 2007*, Prague, Czech Republic, 2007.

An Expression for the Intrinsic Coupling Unbalance of a Symmetrical 4 Port Directional Coupler in Terms of the Cross Ratio of Its 4 Eigenadmittances or 4 Eigenimpedances

G. P. Riblet
Microwave Development Laboratories, Inc.
Needham, MA 02494-14834, USA

Abstract— It is a well known theorem that if suitable matching networks are connected in each of the 4 ports of a lossless reciprocal 4 port device so that each of the ports of the overall device is matched ($S_{11} = S_{22} = S_{33} = S_{44} = 0$), then the overall 4 port is a directional coupler. That is in each case the coupling is zero to one of the three output ports. An important unknown quantity is the coupling unbalance between the remaining two output ports that results from this process. This quantity will be referred to here as the intrinsic coupling unbalance of the original unmatched 4 port. It is shown in this paper that for the most common case of a symmetrical lossless reciprocal 4 port, the intrinsic coupling unbalance (as a power ratio) is given by the cross-ratio of the unmatched circuit's 4 eigenadmittances or 4 eigenimpedances.

1. INTRODUCTION

In a recent article M. S. Gupta has called attention to the connection between the Smith Chart and Poincare's open disc model of hyperbolic geometry [1]. The Smith Chart is based on the fact that the complex output impedance Z_0 of a transmission line is related to the complex load impedance Z_L by a bilinear transformation. It is known that a bilinear transformation preserves angles. This is one of the requirements of the Poincare open disc model. Another requirement of this model is that there is an invariant distance metric. The invariance of the distance metric is based on the invariance of the cross-ratio. This is

$$\frac{(Y_1 - Y_3)(Y_2 - Y_4)}{(Y_1 - Y_4)(Y_2 - Y_3)} = \frac{(Z_1 - Z_3)(Z_2 - Z_4)}{(Z_1 - Z_4)(Z_2 - Z_3)}$$

where the four complex quantities $Y_1,\ Y_2,\ Y_3$, and Y_4 are related to the four complex quantities $Z_1,\ Z_2,\ Z_3$, and Z_4 by the same bilinear transformation. An excellent discussion of various simple physical models of hyperbolic geometry (including the Poincare model) has recently been given by the mathematician and science writer Roger Penrose [2]. In this contribution an additional application of the concept of the cross-ratio to microwave engineering will be given. One example of a bilinear transformation is an inversion. Now an admittance is related to an impedance by an inversion. Since the four eigenadmittances $Y_1,\ Y_2,\ Y_3$ and Y_4 of a symmetrical directional coupler are related to its four eigenimpedances $Z_1,\ Z_2,\ Z_3$, and Z_4 by an inversion, the above cross-ratio equation applies to them. In this paper it will be shown that the intrinsic coupling unbalance (as a power ratio) of a symmetrical lossless reciprocal 4 port network is given by the above expression for the cross-ratio of the eigenadmittances or eigenimpedances.

2. APPLICATION OF CROSS-RATIO INVARIANCE TO S-MATRIX EIGENVALUES

A one port reflection coefficient S is related to a terminating impedance Z or admittance Y by a bilinear transformation. Denoting the eigenreflection coefficients of the symmetrical coupler by $S_1,\ S_2,\ S_3$, and S_4, the invariance of the cross-ratio can be expanded to include them. Consequently,

$$\frac{(S_1 - S_3)(S_2 - S_4)}{(S_1 - S_4)(S_2 - S_3)} = \frac{(Y_1 - Y_3)(Y_2 - Y_4)}{(Y_1 - Y_4)(Y_2 - Y_3)}.$$

Now in the case of the symmetrical 4-port coupler, the S-matrix eigenvalues $S_1,\ S_2,\ S_3$, and S_4 are linearly related to the S-matrix entries $S_{11},\ S_{12},\ S_{13}$ and S_{14} [3]. Furthermore, two of these entries S_{11} and S_{13} will be zero for a matched coupler. In the case of a fully symmetrical reciprocal

4 port, we have that [3]

$$\begin{aligned} 4S_{11} &= S_1 + S_2 + S_3 + S_4 \\ 4S_{12} &= S_1 - S_2 + S_3 - S_4 \\ 4S_{13} &= S_1 + S_2 - S_3 - S_4 \\ 4S_{14} &= S_1 - S_2 - S_3 + S_4 \end{aligned}$$

It follows that the four eigenvalues or eigenreflection coefficients are given by

$$\begin{aligned} S_1 &= S_{11} + S_{12} + S_{13} + S_{14} \\ S_2 &= S_{11} - S_{12} + S_{13} - S_{14} \\ S_3 &= S_{11} + S_{12} - S_{13} - S_{14} \\ S_4 &= S_{11} - S_{12} - S_{13} + S_{14}. \end{aligned}$$

Upon substituting these expressions into the previous cross-ratio equation, one has that

$$\frac{(S_{13} + S_{14})(S_{13} - S_{14})}{(S_{13} + S_{12})(S_{13} - S_{12})} = \frac{(Y_1 - Y_3)(Y_2 - Y_4)}{(Y_1 - Y_4)(Y_2 - Y_3)}.$$

If port 3 is the isolated port of the directional coupler ($S_{13} = 0$), it follows that

$$\frac{{S_{14}}^2}{{S_{12}}^2} = \frac{(Y_1 - Y_3)(Y_2 - Y_4)}{(Y_1 - Y_4)(Y_2 - Y_3)}.$$

The coupling unbalance (as a power ratio) is given by the cross-ratio of the eigenadmittance (or eigenimpedances).

3. INVARIANCE OF EIGENADMITTANCE CROSS-RATIO UNDER EXTERNAL MATCHING

As it stands the previous equation for the coupling unbalance applies only if the symmetrical 4 port is functioning as an ideal directional coupler. In fact it will be shown in this section that it has a much more general interpretation whereby the cross ratio of the 4 eigenadmittances (or eigenimpedances) is considered to be the intrinsic coupling unbalance of a reciprocal symmetrical 4 port network. Suppose that identical 2 port matching networks are connected at each of the ports of the initially unmatched device. This will preserve symmetry. Let the eigenadmittances at the output ports of the overall device be ${Y_1}'$, ${Y_2}'$, ${Y_3}'$, and ${Y_4}'$.

These are related to Y_1, Y_2, Y_3, Y_4 by [4]

$$\begin{aligned} {Y_1}' &= \frac{C + DY_1}{A - BY_1} \\ {Y_2}' &= \frac{C + DY_2}{A - BY_2} \\ {Y_3}' &= \frac{C + DY_3}{A - BY_3} \\ {Y_4}' &= \frac{C + DY_4}{A - BY_4} \end{aligned}$$

where A, B, C, and D are the entries of the 2×2 voltage current transmission matrix of the matching networks. Clearly ${Y_1}'$, ${Y_2}'$, ${Y_3}'$, ${Y_4}'$ and Y_1, Y_2, Y_3, Y_4 are connected by a common bilinear transformation. Once again the cross-ratio must be preserved. It follows that

$$\frac{({Y_1}' - {Y_3}')({Y_2}' - {Y_4}')}{({Y_1}' - {Y_4}')({Y_2}' - {Y_3}')} = \frac{(Y_1 - Y_3)(Y_2 - Y_4)}{(Y_1 - Y_4)(Y_2 - Y_3)}$$

Now it is assumed that the new eigenadmittances ${Y_1}'$, ${Y_2}'$, ${Y_3}'$, ${Y_4}'$ correspond to those of a matched 4 port and hence a directional coupler. Consequently, the expression on the left yields the coupling unbalance from the result of the previous section. But the above equation tells us that we could just as well have obtained this result by using the eigenadmittances of the initial unmatched 4 port.

4. APPLICATION TO THE COMMON COUPLED-LINE DIRECTIONAL COUPLER

The most common directional coupler in general use is probably the single section backward-wave coupled-line coupler. The isolated port is the forward coupled port ($S_{13} = 0$). This coupler is usually analyzed by considering the response of the even and odd mode circuits. The even mode circuit is the 2 port circuit obtained with an open circuit at the symmetry plane separating the two transmission lines (characteristic admittance $= Y_{oe}$). The odd mode circuit is the 2 port obtained with a short circuit at this symmetry plane (characteristic admittance $= Y_{oo}$). However, this type of coupler can also be treated by considering the eigenadmittances Y_1, Y_2, Y_3 and Y_4 [4]. The even and odd mode 2 ports are themselves symmetrical circuits. Hence their eigenadmittances can be obtained by placing an open circuit and a short circuit at their common symmetry plane. An open circuited transmission line behaves like a capacitance and a short circuited transmission line behaves like an inductance. It has been shown that

$$\begin{aligned} Y_1 &= Y_{oe}t \\ Y_2 &= -\frac{Y_{oo}}{t} \\ Y_3 &= Y_{oo}t \\ Y_4 &= -\frac{Y_{oe}}{t} \end{aligned}$$

where t is the tangent of half of the electrical length of the coupled line section.

We can now determine the cross-ration of the eigenadmittances using the above expressions. This will give us the intrinsic coupling unbalance of the coupled line. The result is

$$\frac{{S_{14}}^2}{{S_{12}}^2} = -\frac{(Y_{oe} - Y_{oo})^2}{Y_{oe}Y_{oo}(t + 1/t)^2} = -\frac{(Y_{oe} - Y_{oo})^2 \sin^2}{4Y_{oe}Y_{oo}}$$

where sin is the sine of the electrical length of the coupled line section. Taking the square root we find that

$$S_{14}/S_{12} = j((\sqrt{Y_{oe}}/\sqrt{Y_{oo}}) - (\sqrt{Y_{oo}}/\sqrt{Y_{oe}}))(\sin/2).$$

The intrinsic coupling unbalance depends on the ratio of the even and odd mode coupled line characteristic admittances. Furthermore, the signals at the two output parts are out of phase by 90° as they should be. For arbitrary values of Y_{oe} and Y_{oo}, the symmetrical coupled-line 4 port will not be matched. However, at a given frequency it can be matched by connecting suitable quarter wave transformers at each of the 4 port [4]. If this is done, then the intrinsic coupling becomes the actual coupling at that frequency.

5. CONCLUSIONS

In this paper the notion of the intrinsic coupling unbalance of a symmetrical reciprocal lossless 4 port network has been introduced. This quantity was shown to be equal to the invariant cross-ratio of either the network's eigenadmittances or its eigenimpedances. The concept was illustrated using the case of the common coupled-line symmetrical 4 port. In this case simple expressions for the eigenadmittances are available.

REFERENCES

1. Gupta, M. S., "Escher's art, smith chart, and hyperbolic geometry," *IEEE Microwave Magazine*, Vol. 7, 66–76, Oct. 2006.
2. Penrose, R., *The Road to Reality*, Vintage Books, New York, 33–46, 2007.
3. Montgomery, C. G., R. H. Dicke, and E. M. Purcell, *Principles of Microwave Circuits*, McGraw-Hill, New York, 1948.
4. Riblet, G. P., "A directional coupler with very flat coupling," *IEEE Trans. Microwave Theory Tech.*, Vol. 26, 70–74, Feb. 1978.

Development of 60 GHz Band Fabry-Perot Resonator

K. Shibahara, **T. Suzuki**, **S. Theerawisitpong**, **Y. Takahashi**, **and Y. Watanabe**

Nippon Institute of Technology, Japan

Abstract— As the application of 60 GHz band has been expanding, the instrumentation of the complex dielectric constant of dielectric materials, ambient air and gases at this frequency band become important. This paper presents a design approach to a 60 GHz band specific Fabry-Perot resonator. The content includes (1) the evaluation of 100 GHz band Fabry-Perot resonator built by the current authors, (2) the determination of the coupling aperture size by using TML simulation, and (3) the design of a unified structure for the connection between the coupling aperture and the feeding waveguide.

1. INTRODUCTION

As the application of 60 GHz band has been expanding [1–6], the measurements of the complex dielectric constant of dielectric materials, ambient air and gases at this frequency band become important, so that the realization of high quality 60 GHz band specific Fabry-Perot resonator is required. In this research the resonator has the semi-conformal structure [7], which consists of a longitudinally movable curved mirror and a fixed plane mirror. On the latter surface two apertures are formed for input and output couplings with the cavity, and are mechanically connected to the corresponding feeding waveguides. After evaluating an in-house Fabry-Perot resonator, the design toward a high Q and suppressing leaks and mutual coupling except unavoidable coupling at apertures, is focused on determining the optimum aperture size and adopting a leak-free coupling structure between the aperture and the feeding waveguide. The aperture size is determined by using TML simulation, and for the aperture-to-waveguide coupling structure, a mechanical unified design is adopted.

In this paper, the evaluation of 100 GHz band resonator is at first presented. Then, the TML simulation to determine the aperture size is presented. Finally, the mechanism of a unified aperture-to-waveguide connection is discussed.

2. DESIGN AND MEASUREMENT

2.1. Design and Evaluation of 60–120 GHz Fabry-Perot Resonator (Phase 1 Model)

The constructed Phase 1 model is shown in Fig. 1, and its design parameters are listed in Table 1. The mirrors are made from Al-Cu alloy (Series 2000) and their surfaces are coated by silver. The diameter is 65 mm, and the distance of two mirrors can be varied 150 mm±5 mm. The diameter of coupling aperture is 1 mm.

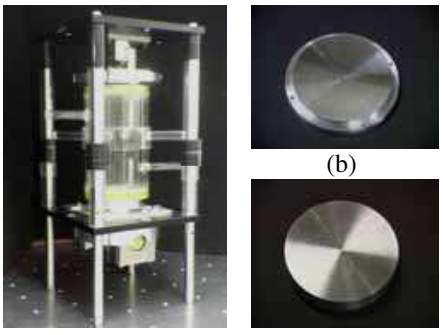

Figure 1: Phase 1 product, (a) Fabry-Perot resonator, (b) spherical, (c) plane mirror.

Mirror structure	Semi-confocal
Upper mirror	Spherical mirror (R305)
	ϕ 65 Al-Cu alloy (2000 series)
Downside mirror	Plane Mirror
	ϕ 65 Al-Cu alloy (2000 series)
Mirror distance	$L = 150 \pm 5$ (mm)
Wave guide	Band type WR-15 E-Bend
Coupling	2 Port(transmission type)
	Aperture size: $D = 1$ (mm)

Table 1: Resonator.

In the experimental evaluation, the quality factor with N_2 filled has been measured. As shown in Fig. 2, the quality factor increases as the frequency. But at 60 GHz, the quality factor is around 17500, which is too low due to small aperture size and possible leaks and coupling at the connection

between the aperture and the feeding waveguide. In Fig. 3, the O_2 absorption characteristic shows low variation at 50–55 GHz, the result to be most expected. From these two measurements, the improvement is focused on the determination of the aperture size and new design of leak-free aperture-to-waveguide connection.

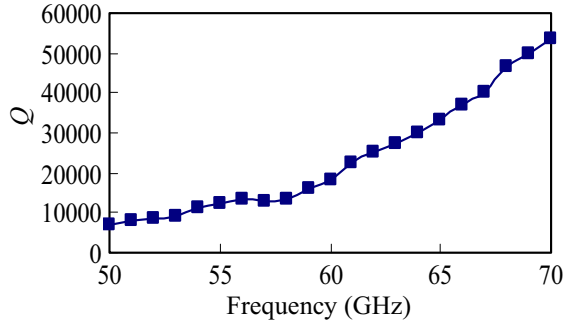

Figure 2: Resonator's Q filled with N_2.

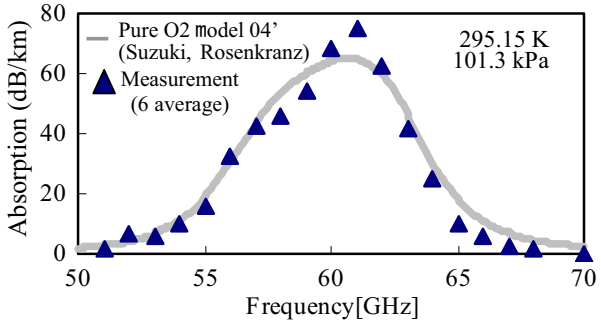

Figure 3: Pure O_2 absorption characteristics.

2.2. Determination of Aperture Size

The TML time-domain method by Micro-Stripes 7.0 [7] is used to determine the aperture size. The simulation model is depicted in Fig. 4. The mirror is inserted into the WR-15, and the transmission characteristic is evaluated by varying the aperture size from 0.1 mm to 1.67 mm. The results are shown in Fig. 5. The larger the aperture size, better the transmission, but the lower the Q. So, the aperture size is determined to be 1.67 mm.

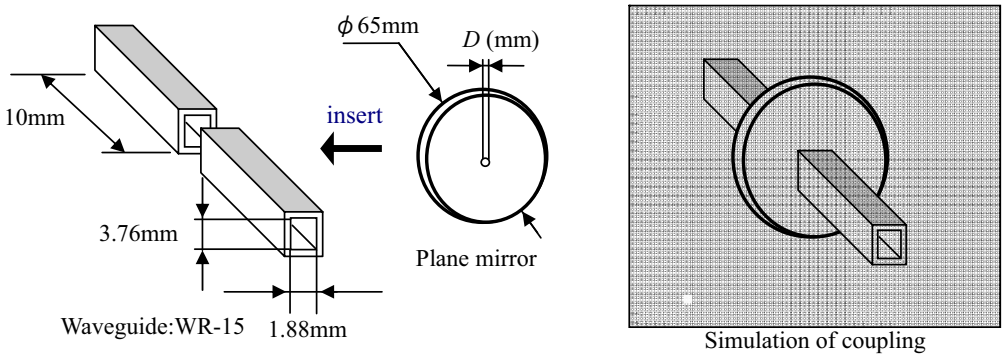

Figure 4: Transmission simulation model.

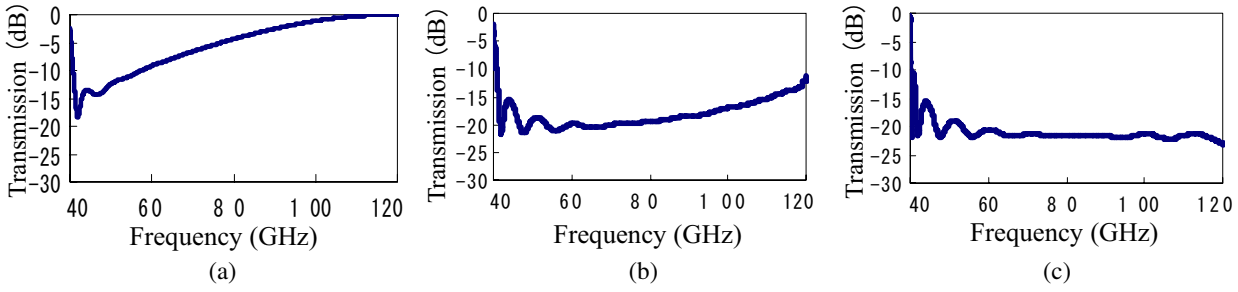

Figure 5: Transmission simulation characteristic, (a) $D = 1.67$ (mm), (b) $D = 1.0$ (mm), (c) $D = 0.1$ (mm).

2.3. New Design of Coupling Structure (Phase 2 Model)

In the Phase 1 model as shown in Fig. 6(a), two apertures for input and output coupling with the cavity are formed on the plane mirror, and they are mechanically connected to the corresponding feeding waveguides. The aperture thickness must be thin as much as possible to minimize the transmission loss. Desirably, the inevitable mutual coupling between input and output signals

takes only at the apertures. But in practice, in order to protect the thin apertures, some marginal gap is allowed between the apertures and the feeding waveguides. As a result, not only mutual coupling between two feeders but also leaks to outside the feeders are induced, so that the cavity Q as well as the accuracy of the resonant characteristics are degraded.

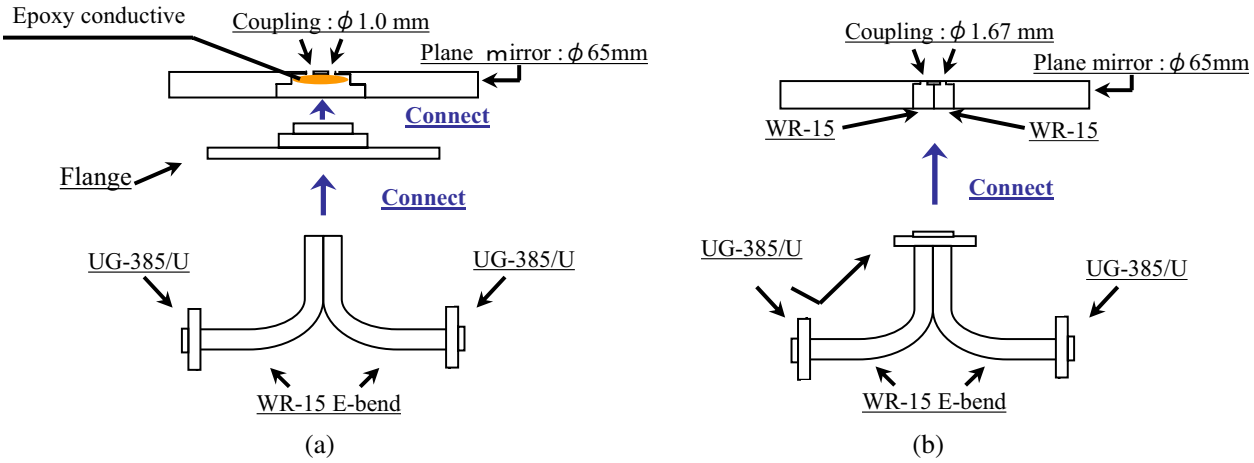

Figure 6: Comparison of coupling model, (a) coupling of phase 1 model, (b) coupling of phase 2 model.

The coupling structure of Phase 2 model is shown in Fig. 6(b). Below each aperture and through the mirror, the independent hole is formed, with the cross section being the same as the feeding waveguide. The tip of the feeder, protruding out of flange, is then mechanically connected in tight with the holes so that the feeder's mutual coupling as well as the leaks can be prevented. The measurement of Q characteristics has been undertaken.

3. CONCLUSION

The quality factor and the O_2 absorption characteristics of a Fabry-Perot resonator are analyzed by the measurement. The optimized diameter of the coupling ports is demonstrated and analyzed by simulation. The new model of Fabry-Perot with the optimized diameter of coupling ports has presented, and the result will be urge in the future.

REFERENCES

1. Sasanuma, H., T. Suzuki, Y. Yanagimoto, and Y. Watanabe, "Design and fabrication of 110 GHz band Fabry-Perot resonator for gas absorption measurement," *Proceedings of IEICE General Conference 2002*, B-2-48, 298, Tokyo, Japan, March 2002, (Japanese).
2. Suzuki, T., K. Sugimoto, Y. Yamagami, T. Negishi, and Y. Watanabe, "Local dielectric measurement by waveguide-type microscopic aperture probe," *Proceedings of PIERS 2006*, No. 0A4, 13–14, Cambridge, U.S.A., March 2006.
3. Nozokido, T., J. Bae, and K. Mizuno, "Scanning near-field millimeter-wave microscopy using a metal slit as a scanning probe," *IEEE Transactions on Microwave Theory and Techniques*, Vol. 49, No. 3, 491–499, 2001.
4. Negishi, T., T. Suzuki, K. Mitsugi, and Y. Watanabe, "Imaging by 60GHz band waveguide-type microscopic aperture probe," *Proceedings of ISAP 2006*, No. FC2, Singapore, November 2006.
5. Suzuki, T., T. Murakami, Y. Isaka, M. Ebara, Y. Watanabe, and P. W. Rosenkranz, "O_2 concentration characteristics at 60 GHz band diagnosis of temperature, pressure and concentration," *Proceedings of IRMMW 2004/THz 2004*, No. F6.3, 811–812, Karlsruhe, Germany, Sept. 2004.
6. Alder, J. F. and J. G. Baker, "Quantitative millimetre wavelength spectrometry," *Royal Society of Chemistry*, 23, 2002.
7. Christopoulos, C., *The Transmission-line Modeling Method: TLM*, IEEE Press, New York, 1995.

MUSIC-type Imaging of Dielectric Spheres from Single-Frequency, Asymptotic and Exact Array Data

S. Gdoura[1], **D. Lesselier**[1], **G. Perrusson**[1], **and P. C. Chaumet**[2]

[1]Département de Recherche en Électromagnétisme, Laboratoire des Signaux et Systèmes
CNRS-SUPÉLEC-UPS 11, 91192 Gif-sur-Yvette cedex, France
[2]Institut Fresnel, Université Aix-Marseille III, 13397 Marseille cedex 20, France

Abstract— Imaging of a dielectric sphere from its Multi-Static Response (MSR) matrix at a single frequency of operation is considered herein via a MUSIC-type, non-iterative method. Synthetic data are both asymptotic ones and data calculated by the Coupled Dipole Method (CDM) which, in contrast, models the wavefield in exact fashion. Comparisons of scattered fields, distributions of singular values, and MUSIC images are carried out. In particular, even far beyond the domain of application of the asymptotic modeling (on which the analysis of the MSR matrix is based), it is shown that fair localization of the sphere is achieved from CDM data.

1. INTRODUCTION

In recent works, an involved analysis of a 3-D MUSIC-type imaging of a small volumetric, dielectric and/or magnetic scatterer (or a set of such scatterers), based on an asymptotic formulation of the electromagnetic wavefield in a full Maxwell setting, has been proposed, refer to [1] in a free space configuration, to [2] with focus onto back-propagation, and to [3] for generalization to a half space. Yet, most of the numerical illustrations so far are from data calculated according to the asymptotic formulation itself (with addition of noise). Here the Coupled Dipole Method (CDM) [4], which involves no approximation, is used as the main calculation tool of the data to be inverted. The paper is organized as follows: The asymptotic method and the CDM are summarized first, before outlining the imaging procedure. Then, fields, distributions of singular values, and MUSIC images simulated according either method are proposed and discussed. A short conclusion follows. (Preliminary comparison results are in [5].)

2. MODELING OF THE SCATTERED FIELD

Let us consider in free space (permittivity ε_0, permeability μ_0) a planar (horizontal) array within the plane $z = h$, which is made of N ideal electric dipoles all orientated (for simplicity) in the vertical $\hat{z}$ direction. The array is operated at a single frequency ω (wavelength λ, wavenumber k) and it illuminates a collection of m non-magnetic spherical scatterers located in a prescribed search box somewhere below it (usually in the near-field of the array). The spheres are of radius $a_j = \alpha d_j$, where α is the order of magnitude of their size and d_j are multiplicative scale factors; their permittivities are ε_j, centers are at $\mathbf{x}_j$, and their volumes read as V_j, $j = 1, \ldots, m$. Let $\mathbf{E}_0^{(n)}(\mathbf{r})$ be the primary electric field at location $\mathbf{r}(\mathbf{r} \in \mathbb{R}^3)$ radiated from the nth dipole with amplitude I_n, and let $\mathbf{E}^{(n)}(\mathbf{r})$ be the total electric field in the presence of the scatterers. One has

$$\mathbf{E}_0^{(n)}(\mathbf{r}) = i\omega\mu_0 \underline{\mathbf{G}}(\mathbf{r}, \mathbf{r}_n) \cdot \hat{z} I_n \tag{1}$$

where $\underline{\mathbf{G}}(\mathbf{r}, \mathbf{r}_n)$ is the Green's dyad in free space (reciprocity $\underline{\mathbf{G}}(\mathbf{r}, \mathbf{r}_n) = \underline{\mathbf{G}}(\mathbf{r}_n, \mathbf{r})^t$ holds as usual). Then, the Lippman-Schwinger vector integral formulation of the field reads as

$$\mathbf{E}^n(\mathbf{r}) - \mathbf{E}_0^n(\mathbf{r}) = \sum_{j=1}^{m} \int_{V_j} d\mathbf{r}' \left[\omega^2 \mu_0 (\varepsilon_j - \varepsilon_0) \underline{\mathbf{G}}(\mathbf{r}, \mathbf{r}') \cdot \mathbf{E}^{(n)}(\mathbf{r}') \right]. \tag{2}$$

From that point,two solution methods can be employed to calculate the electric field at an arbitrary receiver location (e.g., at the nodes of an array, the same as the source one, or another one).

2.1. The Asymptotic Formulation of the Scattered Field

Assuming that $\alpha \ll \lambda$, a rigorous asymptotic field formulation (refer to aforementioned references) holds:

$$\mathbf{E}^{(n)}(\mathbf{r}) - \mathbf{E}_0^{(n)}(\mathbf{r}) = \sum_{j=1}^{m} \left[(i\omega\mu_0)^{-1} \underline{\mathbf{G}}(\mathbf{r},\, \mathbf{x}_j) \cdot \underline{\mathbf{M}}_j^{\varepsilon} \cdot \mathbf{E}_0^{(n)}(\mathbf{x}_j) \right] + \left[o\left((k\alpha)^3\right) \right]. \tag{3}$$

$\underline{\mathbf{M}}_j^{\varepsilon} = k^3\alpha^3 \frac{i\mu_0 c}{\varepsilon_0}(\varepsilon_j - \varepsilon_0)\underline{\mathbf{M}}(\varepsilon_j/\varepsilon_0;\, V_j)$ is the generalized polarization tensor, letting $\underline{\mathbf{M}}(\varepsilon_j/\varepsilon_0;\, V_j)$ be the polarization tensor associated to the scatterer of volume V_j and contrast $\varepsilon_j/\varepsilon_0$, and c is the speed of light. Let us notice that, since the scatterer is spherical, its polarization tensor $\underline{\mathbf{M}}(\varepsilon_j/\varepsilon_0;\, V_j)$ has explicit form $\frac{3\varepsilon_0}{\varepsilon_j + 2\varepsilon_0}|V_j| I_3$, where I_3 is the identity matrix in $\mathbb{R}^3$.

2.2. Calculation of the Scattered Field by CDM

The Coupled Dipole Method is based on the same integral formulation (2). But now, the scatterer under study is discretized into a set of L subunits arranged on a cubic lattice. If the size of the subunit is small enough vs. the wavelength of the illumination, the electromagnetic field is accurately assumed to be uniform over each subunit. Hence,the field at each subunit (here, V_j as the volume of subunit j), for $i = 1, \ldots, L$, reads as

$$\mathbf{E}(\mathbf{r}_i) = \mathbf{E}_0(\mathbf{r}_i) + \sum_{j=1}^{L} \omega^2\mu_0(\varepsilon_j - \varepsilon_0) \int\limits_{V_j} \left[\underline{\mathbf{G}}(\mathbf{r}_i,\, \mathbf{r}') \right] d\mathbf{r}' \cdot \mathbf{E}(\mathbf{r}'_j). \tag{4}$$

If $i \neq j$ one can approximate $\int\limits_{V_j} [\underline{\mathbf{G}}(\mathbf{r}_i,\, \mathbf{r}')]\, d\mathbf{r}' = V_j \underline{\mathbf{G}}(\mathbf{r}_i,\, \mathbf{r}'_j)$, which holds for the scatterers studied herein. The computation of the self term, i.e., $\int\limits_{V_j} [\underline{\mathbf{G}}(\mathbf{r}_i,\, \mathbf{r}')]\, d\mathbf{r}'$, is given in [4]. Then, the field at each subunit is obtained by solving the linear system (4). The scattered field at each position of observation follows as

$$\mathbf{E}(\mathbf{r}) = \sum_{j=1}^{L} \omega^2\mu_0(\varepsilon_j - \varepsilon_0) V_j \left[\underline{\mathbf{G}}(\mathbf{r},\, \mathbf{r}'_j) \right] \cdot \mathbf{E}(\mathbf{r}'_j). \tag{5}$$

3. MUSIC-TYPE IMAGING METHOD

Let us assume now that the receiver array is also made of ideal electric dipoles enabling us to collect the scattered electric field, and that it is coincident with the source array. Those N vertical electric dipoles are at $\{\mathbf{r}_1, \ldots, \mathbf{r}_N\}$. Transmitted amplitudes are I_n, $n = 1, \ldots, N$. For any $\mathbf{x}$ in $\mathbb{R}^3 \backslash \{\mathbf{r}_1, \ldots, \mathbf{r}_N\}$, matrices $G^e(\mathbf{x}) \in \mathbb{C}^{N\times 3}$ read as

$$G^e(\mathbf{x}) = \left[\underline{\mathbf{G}}(\mathbf{x},\, \mathbf{r}_1) \cdot \hat{z},\, \ldots,\, \underline{\mathbf{G}}(\mathbf{x},\, \mathbf{r}_N) \cdot \hat{z} \right]^t. \tag{6}$$

In the asymptotic framework, the Multi-Static Response (MSR) matrix $A \in \mathbb{C}^{N\times N}$, which is made of the scattered electric fields collected at each (vertical) receiver location in the array, each (vertical)dipole source of the said array radiating successively, can be decomposed as

$$A = \sum_{j=1}^{m} G^e(\mathbf{x}_j) M_j \left[G^e(\mathbf{x}_j) \right]^t. \tag{7}$$

It has been shown that the rank of $G^e(\mathbf{x})$ does not depend upon $\mathbf{x}$ in $\mathbb{R}^3 \backslash \{\mathbf{r}_1, \ldots, \mathbf{r}_N\}$, and is equal to 3 in the present configuration (refer also to [6]). Also, for m well-resolved scatterers, i.e., whenever the inner products (* as transpose conjugation) $G^{e*}G^e(\mathbf{x}_j)$ are close to 0 for $i,\, j = 1, \ldots, m$, each scatterer can be imaged independently, and rank is $3m$. Now, if the dimension s of the signal space is known or estimated in the absence of information on the number of scatterers, from the singular value decomposition $A = U\Sigma V^*$, the MUSIC algorithm applies: For any vector $e \in \mathbb{R}^3$, such as $||G(\mathbf{x}) \cdot e|| \neq 0$, and any $\mathbf{x}$ within the search domain, the estimator

$$W(\mathbf{x}) = 1/\sum_{i=s+1}^{N} |\langle U_i, G(\mathbf{x}) \cdot e \rangle|^2$$

peaks (to infinity, in theory) at the scatterers' centers. (This algorithm implies that $N > s$.)

4. NUMERICAL EXAMPLES

The frequency of operation is set to $f = 500\,\text{MHz}$, all lengths henceforth being given in meters. The planar transmitter/receiver array consists of 21×21 vertical electric dipoles distributed at the nodes of a regular mesh with a half-a-wavelength step size (here, $\lambda = 0.6$), and is placed at $h = 5\lambda$ symmetrically about the axis z. A single dielectric sphere with permittivity $\varepsilon_j = 5\varepsilon_0$ is centered at $\mathbf{x}_j = (-0.15, 0.15, 0.175)$. In each numerical example a different radius of the sphere is chosen.

4.1. Comparisons of the Scattered Field

In the first example the sphere is of radius 0.06 ($= \lambda/10$) at $\mathbf{x}_j$. It is illuminated by one vertical ($\hat{z}$-orientated) electric dipole at $(-3, -3, 3)$. One displays the normalized $\mathbf{E}_x$, $\mathbf{E}_y$ and $\mathbf{E}_z$ components of the scattered field at the position of the 21×21 dipoles. Figure 1 shows a comparison of the results provided by the asymptotic approach and by CDM. Both methods provide almost the same scattered field at the array location for this small $a = \lambda/10$ radius (its electric size, since its relative permittivity is 5, is however more than twice larger). Other simulations (not shown for lack of space) for other radii of the dielectric sphere have been carried out, and as expected, for larger and larger radii, the asymptotic formula (where the scatterer size only matters as a factor a^3) becomes more and more inaccurate.

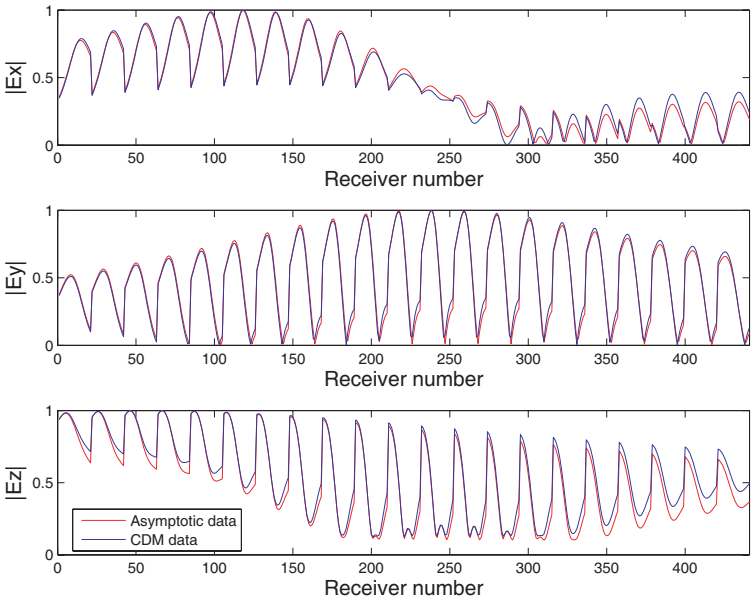

Figure 1: Comparison of asymptotic and CDM fields for a dielectric sphere of radius $\lambda/10$.

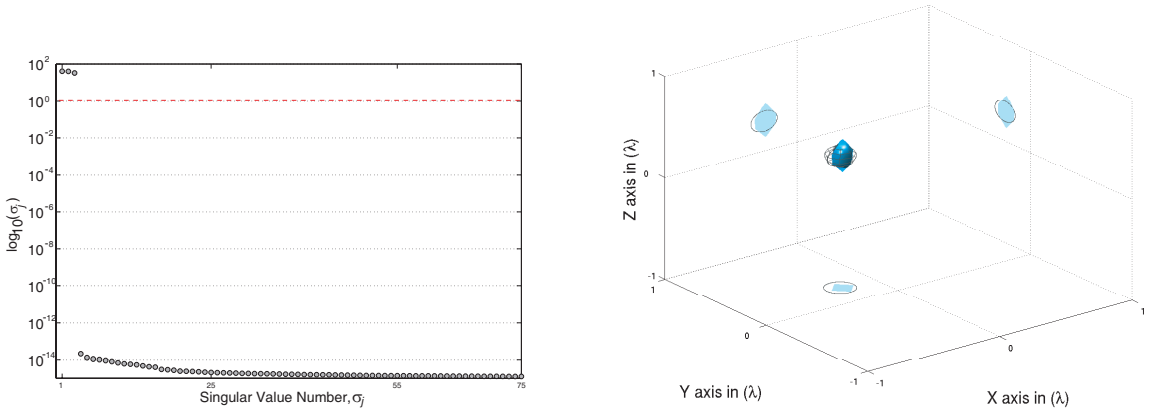

Figure 2: Distribution of the singular values (the first 75) of the MSR matrix calculated with the asymptotic method and 3-D representation of the MUSIC functional (isosurface 20% of the max value) calculated using the first three ones.

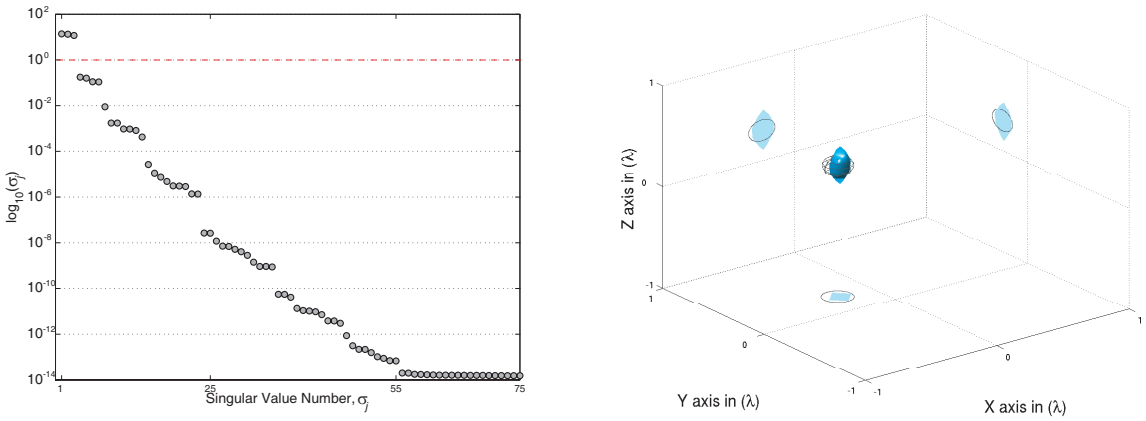

Figure 3: Same as in Figure 2 with CDM.

4.2. Distribution of Singular Values and Imaging by the MUSIC Procedure

4.2.1. Imaging a Sphere of Radius $a = \lambda/10$

In the second example one is considering the same dielectric sphere at $\mathbf{x}_j$ with radius $\lambda/10$. For each method (asymptotic one and CDM), the Multistatic Response matrix is constructed from the scattered field computed at the array. After singular value decomposition of this matrix via a standard code, the MUSIC algorithm as sketched before is applied within the search box (here a cube of side 2λ is chosen). In Figure 2 the results obtained in the asymptotic framework are

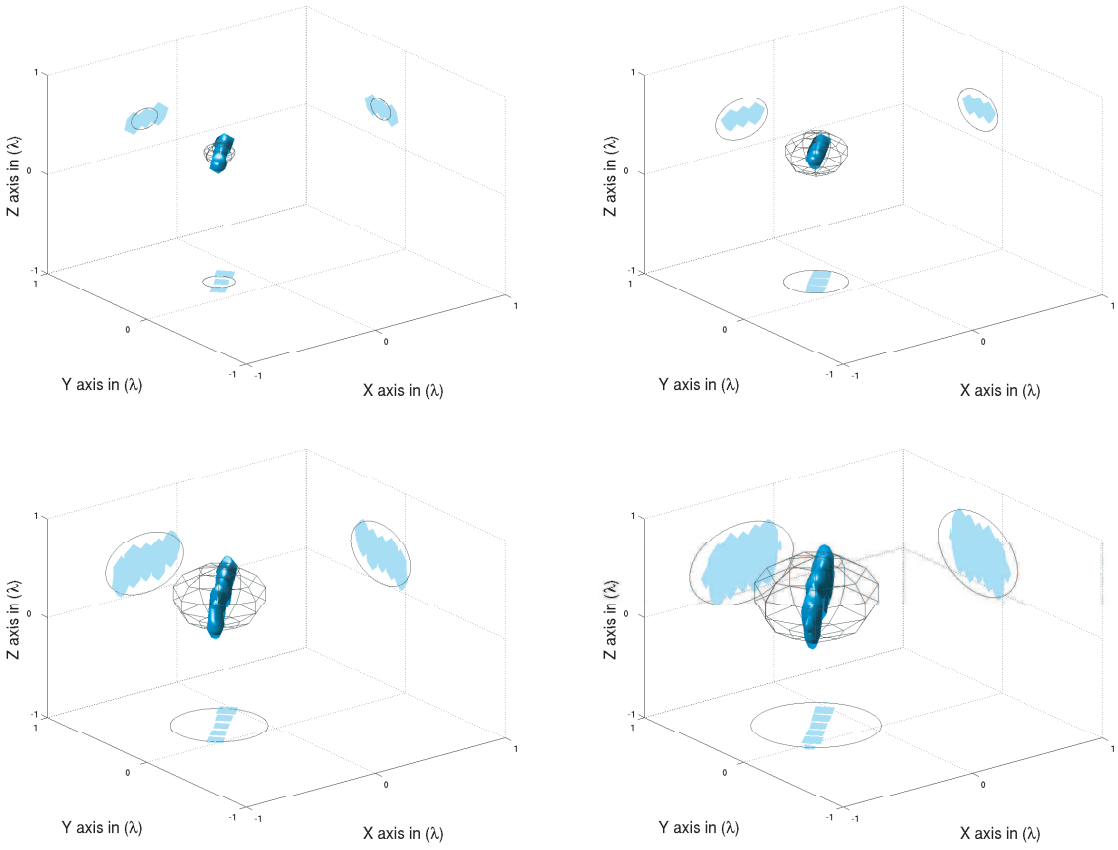

Figure 4: MUSIC images (isosurface 20% of the max value) calculated from CDM data with reference to the exact scatterer. Clockwise from top left, the sphere radius is $\lambda/10$, $2\lambda/10$, $3\lambda/10$, and $4\lambda/10$; 55, 75, 100, and 125 singular vectors are used in the procedure, respectively.

displayed, and in Figure 3 those resulting from the CDM. Let us observe that, as expected, only the three first singular values are significant in the asymptotic framework, all others being valued almost to zero. But with using CDM, even though the three first values are much larger than the others, and can safely be separated from them, a number of non-zero ones is appearing with slowly decreasing amplitudes. However, the two methods provide a similar, and excellent, image when using the corresponding 3 singular vectors only — using all vectors associated to most non-zero singular values from data provided by CDM, here the first 55 ones, one would still get a good estimate of the location of the sphere. Let us notice that the difference of behavior of the singular spectrum between asymptotic and exact approaches comes from the truncation at order $[o\left((k\alpha)^3\right)]$ inherent to the asymptotic modeling, which at first order does not involve any multipole contribution (modeled at the next order and further on).

4.2.2. Imaging of Spheres of Various Radii from CDM Data

Images obtained for larger radii than $\lambda/10$, i.e., $2\lambda/10$, $3\lambda/10$ and $4\lambda/10$, are shown in Figure 4. The singular spectrum of the multistatic response matrix computed from CDM data is obviously more complicated now, when $a > \lambda/10$, than in the case $a = \lambda/10$, and many more singular values of significant amplitude are observed and have to be accounted for in the imaging procedure, in tune with the higher complexity of the scattering phenomenon itself. That is, using the first three singular values does not yield the sphere location. But, by taking all (or at best most) non-zero ones, the location of the sphere is well retrieved, even for a large electrical size (about one-wavelength radius for the largest sphere) whilst it appears, further investigation pending, that one can get at least some estimate of the scatterer volume itself.

5. CONCLUSION

In this paper, one has investigated the robustness of the MUSIC-type imaging method against data acquired outside the asymptotic framework wherein the analysis of the Multi-Static Response matrix is carried out. In particular, one has exhibited that when the radius of the scattering sphere is of the order of $a \leq \lambda/10$, and twice more at least in terms of equivalent electrical size, the asymptotic data and the exact ones (those calculated by the Coupled Dipole Method) yield the same result. But, for larger and larger radii, the asymptotic formula becomes less and less valid, the imaging algorithm still working fairly well even though the scatterer is far from punctual.

ACKNOWLEDGMENT

The contribution of E. Iakovleva to the understanding and development of the MUSIC-type imaging method as applied herein is acknowledged.

REFERENCES

1. Ammari, H., E. Iakovleva, D. Lesselier, and G. Perrusson, "MUSIC-type electromagnetic imaging of a collection of small three-dimensional bounded inclusions," *SIAMJ. Scientific Computing*, Vol. 29, 674–709, 2007.
2. Iakovleva, E. and D. Lesselier, "Multi-static response matrix of spherical scatterers and the back-propagation of singular fields," Report L2S/2006/14, http://www.lss.supelec.fr.
3. Iakovleva, E., S. Gdoura, D. Lesselier, and G. Perrusson, "Multi-static response matrix of a 3-D inclusion in half space and MUSIC imaging," Report L2S/2006/05, http://www.lss.supelec.fr.
4. Chaumet, P. C., A. Sentenac, and A. Rahmani, "Coupled dipole method for scatterers with large permittivity," *Physical Rev. E*, Vol. 70, 03606, 2004.
5. Iakovleva, E. and D. Lesselier, "On the MUSIC-type electromagnetic imaging of a small collection of dielectric spheres from its multi-static response matrix using exact and asymptotic numerical data," *23rd Annual Review of Progress in Applied Computational Electromagnetics*, Proc. CD-ROM, Verona, March 2007.
6. Chambers, D. H. and J. G. Berryman, "Analysis of the time-reversal operator for a small spherical scatterer in an electromagnetic field," *IEEE Trans. Antennas Propagat.*, Vol. 52, 1729–1738, 2004.

Propagation Characteristics of a Nonlinear TM Surface Wave in a Parallel Plate Superconductor/Antiferromagnet Waveguide

Chien-Jang Wu
Department of Applied Physics, National University of Kaohsiung, Kaohsiung 811, Taiwan

Abstract— Nonlinear surface wave propagation properties for a symmetric planar antiferromagnet/superconductor/antiferromagnet waveguide are theoretically investigated. The attenuation constant and the phase constant, in the infrared frequency region, are numerically analyzed as a function of the thickness of superconductor. It is seen that both the attenuation constant and the phase constant decrease with increasing the thickness of superconducting film. In addition, numerical result in the total power flow reveals the existence of a threshold value in the propagation constant. Electromagnetic wave can propagate in the waveguide when propagation constant is greater than this threshold value.

1. INTRODUCTION

With the advantages of low loss, low dispersion, and wide bandwidth, planar superconducting transmission line or waveguide are widely applied in the signal processing in microwave superconductivity. Planar superconducting waveguide is a layered structure consisting of superconducting films and some relevant dielectric materials. Many reports on the microwave propagation characteristics for the planar superconducting transmission lines and waveguides for both the conventional and high-temperature superconductors are now available [1–5].

Propagation characteristics of the magnetostatic surface wave in the $YBa_2Cu_3O_{7-x}$ (YBCO)-yttrium iron garnet (YIG) layered structure was investigated by Tsutsumi et al. [6]. Magnetically tunable superconducting resonators and filters made by YBCO and ferrites have been fabricated and reported by the Lincoln Laboratory [7–8]. Hamada et al., studied the TM surface wave in a nonlinear antiferromagnet-semiconductor-superconductor layered waveguide structure [9]. Using ferromagnet-superconductor superlattice, the novel negative index of refraction was recently realized and reported by Pimenov et al. [10]. And more recently, a ferromagnet-superconductor-ferromagnet hybrid structure is used to theoretically investigate the inherent spin-valve effect [11].

In this work, we shall study the propagation characteristics for a symmetric planar waveguide, where a superconducting film is sandwiched by two semi-infinite antiferromagnets. Two-fluid model will be utilized to describe the complex permittivity of the superconductor. The antiferromagnet is characterized by the nonlinear permeability. A field solution of the TM wave for this structure is first derived. With this solution, we numerically investigate the associated phase constant and attenuation constant. Expression of its total power flow is also given. It is seen that there is a threshold value in the propagation constant, that is, the wave is allowed to propagate as the propagation constant is greater than this threshold one.

2. BASIC EQUATIONS

Planar symmetric waveguide in this study is depicted in Fig. 1, where a superconductor of thickness d is sandwiched by two semi-infinite antiferromagnets. We assume, as usual, that the thickness, d, and the penetration depth λ_L, of the superconductor are both very small to the width in y-direction. This assumption enables us to ignore the edge effects and thus there is no y dependence for any field. We now consider that a transverse magnetic (TM) wave with nonzero field components, H_y, E_x and E_z, propagates in the z direction. All fields are denoted by $F(x)\, e^{ik_0\beta z} e^{-i\omega t}$, where $k_0 = \omega/c$ is the free-space wave number, $\beta = \mathrm{Re}(\beta) + i\mathrm{Im}(\beta)$ is the reduced complex propagation constant, where the real part is the reduced phase constant whereas the imaginary part is the attenuation constant. We are going to derive an analytic dispersion equation that can be solved for β.

In the superconductor layer, the electromagnetic properties are described by the complex permittivity which can be obtained by using the two-fluid model together with Ampere's law, namely

$$\varepsilon_{sc}(\omega) = \left(1 - \frac{1}{\omega^2 \mu_0 \varepsilon_0 \lambda_L^2}\right) + j\frac{\sigma}{\omega\varepsilon_0}, \tag{1}$$

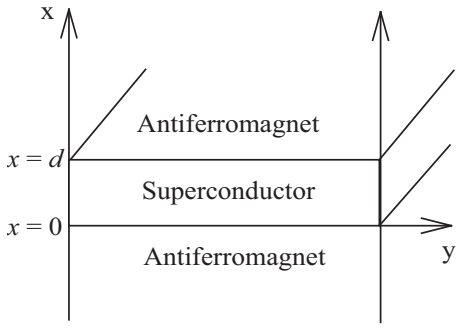

Figure 1: Configuration of a planar superconducting waveguide. The superconducting film with thickness, d, is sandwiched by two semi-infinite antiferromagnets. A TM wave isassumed to propagate along the z direction.

where the temperature-dependent London penetration length is

$$\lambda_L = \lambda_0 \Big/ \sqrt{1-(T/T_c)^4}, \tag{2}$$

with λ_0 the penetration depth at $T = 0\,\mathrm{K}$, and the normal-fluid conductivity is given by $\sigma = \sigma_0(T/T_c)^4$. As for the antiferromagnet considered here is a uniaxial one with a nonlinear permeability denoted by μ^{NL}. In the absence of an applied Zeeman field, the permeability tensor in response to the rf magnetic field is nonlinear and is diagonal given by [12]

$$\mu_{yy} = \mu^{NL}(\omega) = \mu^L(\omega) + \chi_{NL}(\omega)\left|h_y\right|^2, \tag{3}$$

where the linear permeability is given by

$$\mu^L(\omega) = 1 + \frac{2\omega_M\omega_A}{\omega_c^2-\omega^2}, \tag{4}$$

where $\omega_M = \mu_0\gamma M_s$, $\omega_A = \mu_0\gamma H_A$, $\omega_E = \mu_0\gamma H_E$, and $\omega_c = \sqrt{\omega_A^2 + 2\omega_A\omega_E}$ is the resonant frequency of the system. Here M_s is the saturation magnetization field, H_A is the anisotropy field, H_E is the exchange field of the crystal and γ is the gyromagnetic ratio. The nonlinear part $\chi_{NL}(\omega)\left|h_y\right|^2$ is always positive for a linearly polarized electromagnetic wave, indicating a self-focus antiferromagnetic crystal. In addition, we can treat $\chi_{NL}(\omega)$ as a constant since the condition, $|\partial\chi_{NL}/\partial\omega| << \partial\chi^L/\partial\omega$, is satisfied.

With the tangential magnetic field having the form of $H_y = h_y(x)e^{ik_0\beta z}e^{-i\omega t}$, the governing differential equations for each layer can be obtained by two Maxwell's curl equations, with the results

$$\frac{\partial^2 h_y}{\partial x^2} - k_0^2\left[\beta^2 - \varepsilon_{AF}\mu^L(\omega) - \varepsilon_{AF}\chi_{NL}(\omega)\left|h_y\right|^2\right]h_y = 0, \quad \text{for } x > d;\ x < 0. \tag{5}$$

$$\frac{\partial^2 h_y}{\partial x^2} - k_0^2\left(\beta^2 - \varepsilon_{sc}\right)h_y = 0, \quad \text{for } 0 < x < d \tag{6}$$

The corresponding tangential electric field in the superconductor layer can be determined via the following relations,

$$e_z = \frac{i}{\omega\varepsilon_{sc}\varepsilon_0}\frac{\partial h_y}{\partial x}, \tag{7}$$

which also holds for antiferromagnetic layers with a simple replacement, $\varepsilon_{sc} \to \varepsilon_{AF}$. Equation (5) is a nonlinear one that has a solution called the spatial soliton solution given by [13]

$$h_y = \frac{k_{AF}}{k_0}\sqrt{\frac{2}{\chi_{NL}\varepsilon_{AF}}}\operatorname{sech}\left[k_{AF}\left(x - x_0\right)\right], \quad x > d \tag{8}$$

where x_0 is the peak position of the field in the upper antiferromagnet, and

$$h_y = \frac{k_{AF}}{k_0}\sqrt{\frac{2}{\chi_{NL}\varepsilon_{AF}}}\text{sech}\left[k_{AF}\left(x - x_0'\right)\right], \quad x < 0 \tag{9}$$

where $x_0' = -(x_0 - d)$ is the peak position of the field in the lower antiferromagnet, and $k_{AF}^2 \equiv k_0^2\beta^2 - k_0^2\varepsilon_{AF}\mu^L(\omega)$. The solution for Eq. (6) is

$$h_y = A\sinh\left(k_{sc}x\right) + B\cosh\left(k_{sc}x\right), \quad 0 < x < d \tag{10}$$

where $k_{sc}^2 \equiv k_0^2\beta^2 - k_0^2\varepsilon_{sc}$. Using the continuous boundary conditions of tangential electric and magnetic fields at $x = 0$ and $x = d$, and after the elimination of A and B an exact transcendental equation determining the reduced propagation constant β can be obtained, that is

$$\tanh\left(k_{sc}d\right) = \frac{2\varepsilon_{AF}\varepsilon_{sc}k_{AF}k_{sc}\nu}{\varepsilon_{AF}^2k_{sc}^2 + \varepsilon_{sc}^2k_{AF}^2\nu^2}, \tag{11}$$

where

$$\nu = \tanh\left[k_{AF}\left(x_0 - d\right)\right]. \tag{12}$$

Equation (11) can be numerically solved if all the material parameters are available.

We next calculate the total power flow P of the wave propagation in the z-direction. The time-averaged total power flow down the z axis is the real part of the integration of Poynting vector. The power flow in the superconductor layer can be calculated as

$$P_{\text{sup}} = \frac{2\beta q_1^2P_0}{\varepsilon_{sc}\varepsilon_{AF}}\sqrt{1-\nu^2} \left\{\frac{1}{2}\left[1-\left(\frac{q_1\varepsilon_{sc}}{q_2\varepsilon_{AF}}\nu\right)^2\right]k_0d + \frac{1}{2}\left[1+\left(\frac{q_1\varepsilon_2}{q_2\varepsilon_{AF}}\nu\right)^2\right]\frac{\sinh(2k_{sc}d)}{2q_2} + \frac{q_1\varepsilon_{sc}\nu}{q_2^2\varepsilon_{AF}}\sinh^2(k_{sc}d)\right\}, \tag{13}$$

where $P_0 = 1/(2\omega\varepsilon_0\chi_{NL})$ and $q_1 = k_{AF}/k_0$, $q_2 = k_{sc}/k_0$. Calculation reveals that the power flow in the upper antiferromagnet is equal to that of the lower antiferromagnet, i.e.,

$$P_{nl,l} = P_{nl,u} = P_0\frac{2\beta q_1}{\varepsilon_3^2}(1+\nu). \tag{14}$$

The summation of Eqs. (13) and (14) is the total power flow and its the real part gives the total power flow down the z direction.

3. NUMERICAL RESULTS AND DISCUSSION

The material parameters used in the calculation are described as follows: The antiferromagnet is chosen as Ferrous Florid (FeF_2) with anisotropy field $H_A = 1.59 \times 10^4$ A/m, exchange field $H_E = 4.3 \times 10^4$ A/m, saturation magnetization $M_s = 4.46 \times 10^4$ A/m, and the relative permittivity $\varepsilon_{AF} = 4$ [9]. A typical high-temperature superconductor, YBCO is taken for the central layer. The parameters of this system are $T_c = 86$ K, $\lambda_0 = 0.22$ nm, and $\sigma_0 = 6.56 \times 10^6$ S/m [6]. In addition, the parameter in Eq. (12) is assumed to be constant, say $\nu = -0.16$ [14].

In Fig. 2, we demonstrate the calculated phase constant (a) and attenuation constant (b) as a function the thickness of superconductor at a frequency of 9×10^{12} rad/s and for three distinct temperatures, $t = 0.4$, 0.6 and 0.8. It can be seen that both decrease as the film thickness is increased, except the phase constant at $t = 0.8$ where there is a broad dip at $d \approx 17$ nm. The thinner in the superconductor layer, the larger the propagation constant is, indicating a preferable situation for the existence of this TM surface wave.

Figure 3 plots the calculated total power flow as a function of the propagation constant at a fixed frequency of 9×10^{12} rad/s and at a reduced temperature of $t = 0.6$. It is found to have a threshold propagation constant, $\beta_{th} \cong 2$ For a surface wave to propagate in such a structure the propagation constant should be greater than β_{th}. If β is smaller than β_{th}, then the propagation mode will not be expected since the power flow has turned out to be negligibly small. In addition, in the propagation mode the total power flow is not a sensitive function of the thickness of superconductor. This is due to the fact that the total power flow is mostly stored in the antiferromagnet compared to the superconductor.

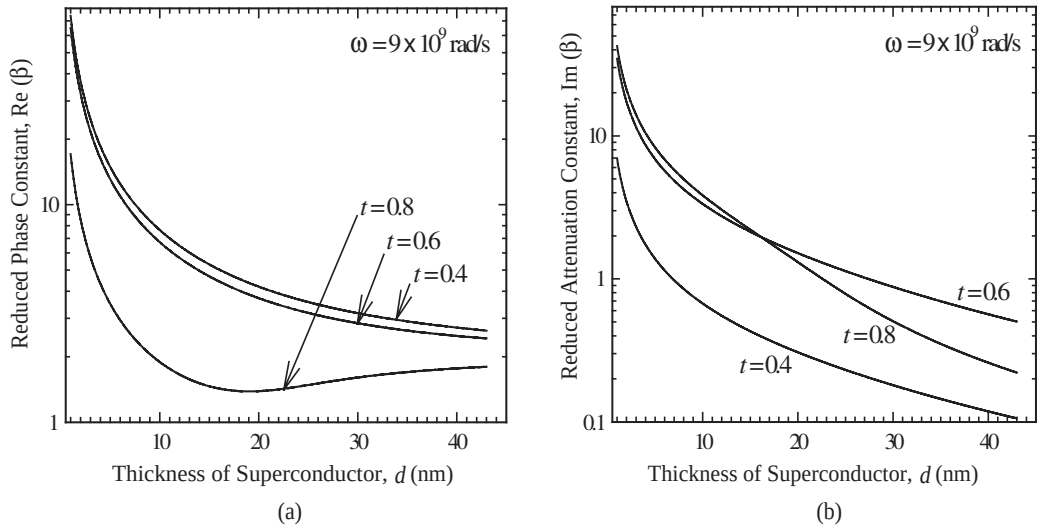

Figure 2: The thickness-dependent reduced phase constant (a) and attenuation constant (b) at $\omega = 9 \times 10^{12}$ rad/s and $v = -0.16$ for different reduced temperatures $t = 0.4$, 0.6, and 0.8.

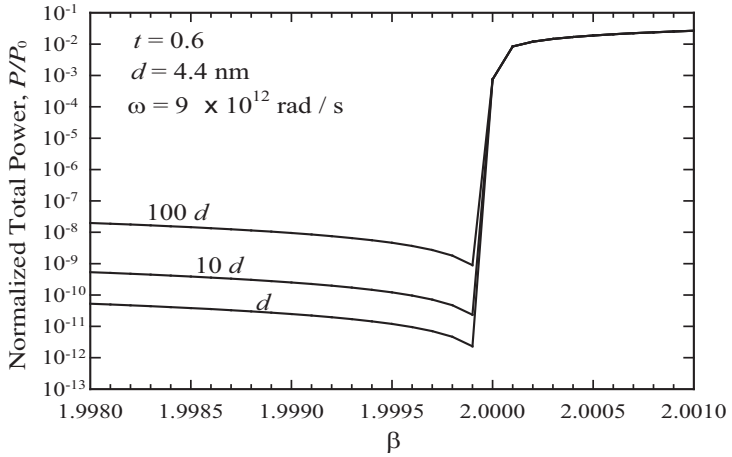

Figure 3: The calculated total power flow as a function of the propagation constant at the conditions of $\omega = 9 \times 10^{12}$ rad/s and $t = T/T_c = 0.6$.

ACKNOWLEDGMENT

The author is indebted to the financial support from the National Science Council of the Republic of China under grant No. NSC-95-2112-M-390-003-MY2.

REFERENCES

1. Swihart, J. C., *J. Appl. Phys.*, Vol. 32, No. 3, 461, 1961.
2. Abbas, F., L. E. Davis, and J. C. Gallop, *Physica C*, Vol. 215, 132, 1993.
3. Wu, C.-J., *IEEE Trans. Appl. Supercond.*, Vol. 9, No. 3, 4633, 1999.
4. Wu, C.-J., *J. Appl. Phys.*, Vol. 89, No. 7, 3986, 2001.
5. Wu, C.-J., *J. Appl. Phys.*, Vol. 96, No. 6, 3348, 2004.
6. Tsutsumi, M., et al., *IEEE Trans. Microwave Theory Technol.*, Vol. 44, No. 8, 1911, 1996.
7. Oates, D. E. and G. F. Dionne, *IEEE Trans. Appl. Supercond.*, Vol. 9, No. 2, 4170, 1999.
8. Adam, J. D., et al., *IEEE Trans. Microwave Theory Technol.*, Vol. 50, No. 3, 721, 2002.
9. Hamada, M. S., et al., *J. Supercond.*, Vol. 16, No. 2, 443, 2003.
10. Pimenov, A., et al., *Phys. Rev. Lett.*, Vol. 95, 247009, 2005.
11. Faure, M., A. I. Buzdin, and D. Gusakova, *Physica C*, doi: 10.1016/j.physc.2007.01.013.
12. Almeida, N. S. and D. L. Mills, *Phys. Rev. B*, Vol. 36, No. 4, 2015–2023, 1987.
13. Boardman, A. D. and T. Twardowski, *Phys. Rev. A*, Vol. 39, No. 5, 2481–2492, 1989.
14. Hamada, M. S., et al., *The Islamic Univ. J.*, Vol. 14, No. 2, 51–63, 2006.

A New GL Method for Solving Differential Equation in Electromagnetic and Phys-Chemical and Financial Mathematics

Jianhua Li, **Ganquan Xie**, **and Lee Xie**
GL Geophysical Laboratory, USA

Abstract— In this paper, we propose a new GL method for solving the ordinary and the partial differential equation. These equations govern the electromagnetic field etc. macro and micro physical, chemical, financial sciences and engineering. The differential equation is held on an infinite domain which includes a finite inhomogeneous domain. The inhomogeneous domain is divided into finite sub domains. We present the solution of the differential equation as an explicit recursive sum of the integrals in the inhomogeneous sub domains. The analytical solution of the equation in the infinite homogeneous domain is called as an initial global field. The global field is updated by local scattering field successively subdomain by subdomain. Once all subdomains are scattered and the updating process is finished in all the sub domains, the solution of the equation is obtained. We call our method as Global and Local field method, in short GL method. It is different from FEM method, the GL method directly assemble inverse matrix and solution. There is no big matrix equation needs to solve in the GL method. There is no needed artificial boundary and no absorption boundary condition for infinite domain in the GL method. We proved several theorems and proposed a triangle formula of the Greens functions that is the theoretical base of our GL method. The numerical discretization of the GL method is presented. We proved that the numerical solution of the 1-D GL method convergence to the exact solution when the size of the sub domain is going to zero. The error estimation of the GL method for solving 1-D wave equation is presented. The simulations show that the GL method is accurate, fast, and stable for solving elliptic, parabolic, and hyperbolic equations. The GL method has advantages and wide applications in the 3D electromagnetic (EM) field, 3D elastic and plastic etc seismic field, acoustic field, flow field, and quantum field. The GL method software for the above 3D EM etc field are developed.

1. INTRODUCTION

The analytical and numerical methods are two types of methods to solve differential equations. They are developed separately. The analytical method is available only for homogeneous infinite whole space or layered media domain or regular geometry domain. The numerical method is useful to solve differential equations in the irregular geometry and inhomogeneous domain. However, there are several difficulties and limitations in exist numerical approaches such as the finite element method (FEM) and finite difference method (FD) and the Born approximation. (1) The large matrix in FD and FEM is needed to solve. (2) In infinite domain, the artificial boundary and absorption conditions are necessary in FD and FEM method. (3) In the cylindrical and spherical coordinate, the original point and northern and southern pole points are singularities in FD and FEM 2 scheme. (4) The FEM and FD methods are hard to parallel. (5) The Born approximation can only be used for low frequency and low contrast materials. (6) The FD and FEM schemes of the high order differential equations are complicated. The new GL method proposed in this paper can resolve these difficulties.

Combining the advantages of the analytical and numerical approaches, and overcoming their difficulties and limitations, we develop the GL method which has the following merits: (1) There is no large matrix is needed to solve. In spite the domain how large is, only 3 by 3 or 6 by 6 matrices are needed to solve. For the some scale equations, there is no any matrix is needed to solve. (2) It is no longer needed to impose any artificial boundary and absorption boundary condition for the infinite domain. (3) The coordinate singularity in the cylindrical or spherical coordinate is resolved. (4) The GL method is a self parallel algorithm while the FEM and FD methods are hard to parallel. (5) Our GL method is available for high frequency and high contrast materials while the Born approximation can only be used for low frequency and low contrast materials. (6) The GL scheme of the high order differential equations is not complicated.

Our GL method can solve the elliptic, parabolic, and hyperbolic partial differential equations in the finite inhomogeneous domain which is included in the infinite homogeneous whole space or infinite layered domain. These equations govern the electromagnetic field etc. macro and micro physical, chemical, financial sciences and engineering. The inhomogeneous domain is divided into

several sub domains. We present the solution of the differential equation as a recursive sum of the integrals in the inhomogeneous sub domains. The analytical solution of the equation in the infinite homogeneous domain is called as an initial global field. The global field is updated by local scattering field successively subdomain by subdomain. Once the updating process is finished in all the sub domains, the solution of the equation is obtained. We call our method as Global and Local field method, in short GL method. We proved several theorems and a triangle formula of the Green's function that is the theoretical base of our GL method.

The numerical discretization of the GL method is presented. We proved that the numerical solution of the GL method is convergent to the exact solution when the mesh size of the sub domain is going to zero. The $O(h^2)$ convergent rate is obtained if the middle point and trapezoid integral is used, moreover, we obtain $O(h^4)$ super convergent rate when Gaussian integral is used. Many tests show that the GL method solution for wave equation is fast convergent to exact solution, but FEM solution is not. It has very widely applications in the mechanical problem, the heat diffusion, the electromagnetic, seismic wave propagation, antenna, radar, and nanometer materials. The 2D and 3D acoustic wave, electromagnetic field, elastic wave, and flow GL algorithms and software for many applications are developing.

The plan in this paper is as follows. The introduction is provided all in the Section 1. In the Section 2, we propose an integral equation of the wave field and Green's function. In the Section 3, we proposed our Global and Local field method. The fundamental theory of the GL method is proved in the Section 4. In the Section 5, we describe our GL method for the parabolic partial differential equation. In the Section 6, we use the GL method to solve the one dimensional wave equation. Simulations of the GL method for solving the 1-D wave equation are presented in the Section 7. In the Section 8, we describe the applications and conclusions.

2. INTEGRAL EQUATIONS

2.1. Wave Equation

We consider the following 3D wave equation in the frequency domain

$$\Delta u(r) + \frac{\omega^2}{c^2(r)} u(r) = s(r), \quad r \in R^3, \tag{1}$$

where r is space variable $r = (x, y, z)$, $r \in R^3$, $c(r)$ is the coefficient, so called wave velocity, which is inhomogeneous function in a finite bounded domain $\Omega \subset R^3$, $c(r) = c_b$ in $r \in R^3 \setminus \Omega$, c_b is a constant, ω is frequency, $u(r) = u(r, \omega)$ is the unknown wave field function $\Delta = \Delta_r$ is the Laplace operator, the $s(r)$ on the right hand of the Equation (1) is known source term in the finite domain, for example, we consider delta function source term, $s(r) = \delta(r - r_s)$, r_s is finite source point. If the $c(r) = c_b$ in whole space R^3, the solution $u_b(r)$ of the Equation (1) is called incident wave in the background media, $u_b(r) = \dfrac{e^{-ik_b|r-r_s|}}{4\pi|r-r_s|}$, $k_b = \dfrac{\omega}{c_b}$, and $k(r) = \dfrac{\omega}{c(r)}$. The solution of the Equation (1) satisfies the following radiation condition,

$$\lim_{r\to\infty} r\left(\frac{\partial u}{\partial n} - iku\right) = 0, \tag{2}$$

and $ru(r)$ is bounded in infinite.

2.2. Green's Function

The Green's function $G(r, r')$ of the Equation (1) satisfies

$$\Delta G(r, r') + \frac{\omega^2}{c^2(r)} G(r, r') = \delta(r - r'), \quad r \in R^3,\ r' \in R^3, \tag{3}$$

and the following radiation condition

$$\lim_{r'\to\infty} r'\left(\frac{\partial G(r', r)}{\partial n_{r'}} - ikG(r', r)\right) = 0, \tag{4}$$

and $r'G(r', r)$ is bounded in infinite, where r' is the virtual source point, $\delta(r-r')$ is the delta function. If $c(r) = c_b$ in whole space R^3, the Green's function is called background Green's function $G_b(r, r')$.

2.3. Integral Equation

Theorem 1. Suppose that the inhomogeneous domain is finite bounded and the source point r_s is also finite, then the wave Equation (1) is equivalent to the integral equation

$$u(r) = u_b(r) - \omega^2 \int\limits_{\Omega} \left(\frac{1}{c^2(r')} - \frac{1}{c_b^2} \right) G(r', r) u_b(r') dr', \tag{5}$$

where $u_b(r)$ is the incident wave on the background velocity media, $G(r', r)$ is the Green's function of the Equation (1).

Proof: To rewrite the equation (1) on the background velocity media as

$$\Delta u_b(r') + \frac{\omega^2}{c_b^2} u_b(r') = \delta(r' - r_s), \tag{6}$$

Using the Green's function $G(r', r)$ to time the Equation (6), we have

$$G(r', r)\Delta u_b(r') + \frac{\omega^2}{c_b^2} G(r', r) u_b(r') = G(r', r)\delta(r' - r_s), \tag{7}$$

Exchange r and r' in the Equation (3), and using $u_b(r')$ to time the Equation (3), we have

$$\Delta G(r', r) u_b(r') + \frac{\omega^2}{c^2(r')} G(r', r) u_b(r') = \delta(r' - r) u_b(r'), \tag{8}$$

Subtract (8) from (7), we have

$$\begin{aligned} G(r', r)\delta(r' - r_s) - \delta(r' - r) u_b(r') \;=\; & \frac{\omega^2}{c_b^2} G(r', r) u_b(r') - \frac{\omega^2}{c^2} G(r', r) u_b(r') \\ & + G(r', r)\Delta u_b(r') - \Delta G(r', r) u_b(r') \end{aligned} \tag{9}$$

To integrate (9) in r' in whole space and using the integral by parts, we have

$$\begin{aligned} u(r) \;=\; & u_b(r) - \omega^2 \int\limits_{S_R} \left(\frac{1}{c^2(r')} - \frac{1}{c_b^2} \right) G(r', r) u_b(r') dr' \\ & + \oint\limits_{\partial S_R} \left[G(r', r) \frac{\partial u_b}{\partial n}(r') - \frac{\partial G(r', r)}{\partial n} u_b(r') \right] ds(r'), \end{aligned} \tag{10}$$

where S_R is a sphere with radius R, S_R includes Ω, ∂S_R is the spherical surface and r, r_s is finite point. According to the radiation condition (2) and (4), we have

$$\lim_{|r'| \to \infty} \oint\limits_{\partial S_R} \left[G(r', r) \frac{\partial u_b}{\partial n}(r') - \frac{\partial G(r', r)}{\partial n} u_b(r') \right] ds(r') = 0 \tag{11}$$

because

$$\begin{aligned} & \lim_{|r'| \to \infty} \oint\limits_{\partial S_R} \left[G(r', r) \frac{\partial u_b}{\partial n}(r') - \frac{\partial G(r', r)}{\partial n} u_b(r') \right] ds(r') \\ = \; & \lim_{|r'| \to \infty} \oint\limits_{\partial S_R} \left[G(r', r) \frac{\partial u_b}{\partial n}(r') - ikG(r', r) u_b(r) + ikG(r', r) u_b(r) - \frac{\partial G(r', r)}{\partial n} u_b(r') \right] ds(r') \\ = \; & \lim_{|r'| \to \infty} \oint\limits_{\partial S_R} \left[G(r', r) \left(\frac{\partial u_b}{\partial n}(r') - iku_b(r) \right) + \left(ikG(r', r) - \frac{\partial G(r', r)}{\partial n} \right) u_b(r') \right] ds(r') \\ \leq \; & \lim_{|r'| \to \infty} 4\pi r'^2 \left| G(r', r) \right| \left| \left(\frac{\partial u_b}{\partial n}(r') - iku_b(r) \right) \right| + \left| \left(ikG(r', r) - \frac{\partial G(r', r)}{\partial n} \right) \right| \left| u_b(r') \right| \\ = \; & \lim_{|r'| \to \infty} 4\pi \left| r' G(r', r) \right| \left| r' \left(\frac{\partial u_b}{\partial n}(r') - iku_b(r) \right) \right| + \lim_{|r'| \to \infty} 4\pi \left| r' u_b(r') \right| \left| r' \left(ikG(r', r) - \frac{\partial G(r', r)}{\partial n} \right) \right| \\ = \; & 0. \end{aligned}$$

Also because the $c(r) - c_b \neq 0$ only in Ω, we have

$$u(r) = u_b(r) - \omega^2 \int\limits_{\Omega} \left(\frac{1}{c^2(r')} - \frac{1}{c_b^2} \right) G(r', r) u_b(r') dr',$$

this is the integral Equation (5). The sufficiency of the Theorem 1 is proved. Inversely, if the function $u(r)$ satisfies the integral Equation (5), taking operator $\Delta + \dfrac{\omega^2}{c^2(r)}$ on both sides of the Equation (5), we have

$$\begin{aligned} \Delta u(r) + \frac{\omega^2}{c(r)} u(r) &= \Delta u_b(r) + \frac{\omega^2}{c(r)} u_b(r) \\ &\quad -\omega^2 \int\limits_{\Omega} \left(\frac{1}{c^2(r')} - \frac{1}{c_b^2} \right) \left(\Delta G(r', r) + \frac{\omega^2}{c(r)} G(r', r) \right) u_b(r') dr', \\ \Delta u(r) + \frac{\omega^2}{c(r)} u(r) &= \Delta u_b(r) + \frac{\omega^2}{c(r)} u_b(r) \\ &\quad -\omega^2 \left(\frac{1}{c^2(r)} - \frac{1}{c_b^2} \right) u_b(r) = \delta(r - r_s). \end{aligned}$$

Because $u_b(r)$ and $G(r', r)$ satisfy the radiation conditions (2) and (4), from the integral Equation (5), $u(r)$ satisfies the radiation condition (2). The Theorem 1 is proved.

3. NEW GLOBAL AND LOCAL FIELD METHOD — GL METHOD

In this section, we proposed our Global and Local field Method — GL Method as follows:

(1) The domain Ω is divided into n sub domains Ω_k, $\Omega = \bigcup\limits_{k=1}^{n} \Omega_k$.

(2) Let $u_0(r) = u_b(r)$, $G_0(r'', r) = G_b(r'', r)$, $u_b(r)$ is the analytical incident wave on the homogeneous background media, $G_b(r'', r)$ is the analytical Green's function on the homogeneous background media. By induction, suppose that u_{k-1} and $G_{k-1}(r'', r')$ are calculated in the $(k-1)$th step, we solve the Green's function integral Equation (5) in the sub domain Ω_k to obtain $G_k(r'', r)$.

(3) Using the following integral formula in the sub domain Ω_k,

$$u_k(r) = u_{k-1}(r) - \omega^2 \int\limits_{\Omega_k} \left(\frac{1}{c^2(r')} - \frac{1}{c_b^2} \right) G_k(r', r) u_{k-1}(r') dr', \tag{12}$$

we calculate $u_k(r)$.

(4) The steps (2) and (3) form a finite iterations, $k = 1, 2, \ldots, n$. The $u_n(r)$ is the solution of our GL method.

4. THE FUNDAMENTAL THEORY OF THE GL METHOD

Theorem 2. If the Green's function $G_n(r', r)$ is calculated by GL method process (1)–(4) in the Section 3, then function $G_n(r', r)$ satisfies

$$\Delta_{r'} G_n(r', r) + \frac{\omega^2}{c^2(r')} G_n(r', r) = \delta(r' - r), \tag{13}$$

and the radiation condition (4), $G_n(r', r)$ is the Green's function of the Equation (1).

Proof: The proof of this theorem is longer and is omitted see [3].

Theorem 3. If the solution $u_n(r)$ and Green's function $G_n(r'', r)$ are calculated by GL method process (1)–(4) in the Section 3, then $u_n(r)$ satisfies the following integral equation,

$$u_n(r) = u_b(r) - \omega^2 \int\limits_{\Omega} \left(\frac{1}{c^2(r')} - \frac{1}{c_b^2} \right) G_n(r', r) u_b(r') dr', \tag{14}$$

and the far field radiation condition (2), $u_n(r)$ is the exact solution of the wave Equation (1).

Proof: We use induction processes to prove this theorem. The theorem is held when $n = 0$.

Suppose that the integral Equation (14) is held for any $m-1$, $\tilde{\Omega}_{m-1} = \bigcup\limits_{k=1}^{m-1} \Omega_k$, we have

$$u_{m-1}(r) = u_b(r) - \omega^2 \int\limits_{\tilde{\Omega}_{m-1}} \left(\frac{1}{c^2(r')} - \frac{1}{c_b^2} \right) G_{m-1}(r', r) u_b(r') dr'. \tag{15}$$

The mth step of the GL iteration gives

$$u_m(r) = u_{m-1}(r) - \omega^2 \int\limits_{\Omega_m} \left(\frac{1}{c^2(r')} - \frac{1}{c_b^2} \right) G_m(r', r) u_{m-1}(r') dr'. \tag{16}$$

Upon substituting the Equation (15) to (16) for $u_{m-1}(r)$, we obtain

$$\begin{aligned} u_n(r) &= u_b(r) - \omega^2 \int\limits_{\Omega_n} \left(\frac{1}{c^2(r')} - \frac{1}{c_b^2} \right) G_n(r', r) u_b(r') dr' \\ &\quad -\omega^2 \int\limits_{\bigcup\limits_{k=1}^{n-1} \Omega_k} \left(\frac{1}{c^2(r'')} - \frac{1}{c_b^2} \right) G_n(r'', r) u_b(r'') dr'' \\ &= u_b(r) - \omega^2 \int\limits_{\bigcup\limits_{k=1}^{n} \Omega_k} \left(\frac{1}{c^2(r'')} - \frac{1}{c_b^2} \right) G_n(r'', r) u_b(r'') dr'' \\ &= u_b(r) - \omega^2 \int\limits_{\Omega} \left(\frac{1}{c^2(r')} - \frac{1}{c_b^2} \right) G_n(r', r) u_b(r') dr'. \end{aligned} \tag{17}$$

The Equation (17) is the Equation (14). We have proved $u_n(r)$ satisfies the integral Equation (14). From Theorem 2, the function $G_n(r'', r)$, satisfies (13) and the radiation condition (4), $G_n(r'', r)$ is the Green's function of the Equation (1). From the Theorem 1, $u_n(r)$ satisfies the radiation condition (2) and is the exact solution of the wave Equation (1). The Theorem 3 is proved.

From the fundamental Theorem 2 and 3, our GL finite iteration is independent on the order of the sub domains. The solution $u_n(r)$ of the GL method is exact solution of the wave Equation (1).

5. GL METHOD FOR THE PARABOLIC PARTIAL DIFFERENTIAL EQUATION

Our GL method is useful for solving the wave equation, it is also useful for solving the elliptic equation and parabolic equation.

Theorem 4. Suppose that the inhomogeneous domain is finite bounded and the source point r_s is also finite, then the parabolic equation,

$$\Delta u(r) - \frac{i\omega}{c^2(r)} u(r) = \delta(r - r_s), \qquad r \in R^3, \tag{18}$$

is equivalent to the integral equation

$$u(r) = u_b(r) + i\omega \int\limits_{\Omega} \left(\frac{1}{c^2(r)} - \frac{1}{c_b^2} \right) G_n(r', r) u_b(r') dr', \tag{19}$$

where $u_b(r)$ is the incident field on the background media, $G(r', r)$ is the Green's function of the Equation (17) which satisfies the following radiation condition

$$\lim_{|r|\to\infty}\left|G(r,r') - B\frac{e^{-ik_b|r|}}{|r|}\right| = 0 \quad \text{and} \quad \lim_{|r|\to\infty}|r|^{\alpha}e^{-ik_b|r|} = 0, \quad \alpha \geq 1, \tag{20}$$

the solution $u(r)$ satisfies the radiation condition

$$\lim_{|r|\to\infty}\left|u(r) - A\frac{e^{-ik_b|r|}}{|r|}\right| = 0 \quad \text{and} \quad \lim_{|r|\to\infty}|r|^{\alpha}e^{-ik_b|r|} = 0, \quad \alpha \geq 1, \tag{21}$$

here $k_b = \frac{\sqrt{-i\omega}}{c_b}$, the A and B are constants independent on the space variable r.

Proof: The proof is similar to the proof of Theorem 1. Because the radiation condition (20) and (21), the surface integral (11) going to zero. The theorem is proved.

The Theorem 2 $\sim$ 3 are held for the parabolic equation. The radiation conditions (20) and (21) are stronger than (4) and (2), respectively. The detailed description of the GL method for solving the parabolic equation and elliptic equation will be presented in our other papers.

In the proofs of the Theorem 1 $\sim$ 3, we used the radiation conditions to vanish the surface integral. For clearly, we can add a small parameter diffusion term $-i\varepsilon\omega u(r)$ to the Equation (1) that guarantees the surface integrals going to zero as $|r| \to \infty$. Then we can rigorously prove the surface integral in Equation (11) is vanished as $\varepsilon \to 0$.

6. GL METHOD FOR SOLVING ONE DIMENSIONAL WAVE EQUATION

In the previous sections, we presented our GL method for solving 3D wave Equation (1). For examining the method, we use it to solve one dimension wave equation.

$$\frac{\partial^2 u}{\partial x^2} + \frac{\omega^2}{c^2(x)}u = \delta(x - x_s), \qquad x \in R. \tag{22}$$

The Green's function of the Equation (22) satisfies

$$\frac{\partial^2 G(x', x)}{\partial x'^2} + \frac{\omega^2}{c^2(x')}G(x', x) = \delta(x' - x). \tag{23}$$

when $c = c_b$ the Equations (22) and (23) become their corresponding background equations.

Theorem 5. The Theorem 1 and 2 are available for the one dimension wave Equation (22) and its Green's function Equation (23).

Proof: The proof is similar to the proof processes of the Theorem 1 and 2. Note that for the one dimensional case, when $x \to |\infty|$, the wave field and the Green's function are not decay to zero, fortunately, the boundary terms are still vanished. The Theorem 5 is proved.

7. SIMULATION OF THE GL METHOD FOR SOLVING 1-D WAVE EQUATION

7.1. Discretization of the GL Method

The discretization of the GL method for solving 1-D wave equation is as follows,

(7.1) The interval $[a, b]$ is divided to n sub intervals which is shown in (24),

$$a = x_1 < x_2 < \cdots < x_{k-1} < x_k < x_{k+1} < \cdots < x_n < x_{n+1} = b \tag{24}$$

(7.2) Let $u_0(x) = u_b(x)$, and $G_0(x', x) = G_b(x', x)$ are shown in the (25) and (26),

$$u_0(x) = u_b(x) = -\frac{e^{-ik_b|x-x_s|}}{2ik_b}, \qquad \omega > 0, \tag{25}$$

$$G_0(x', x) = G_b(x', x) = -\frac{e^{-ik_b|x'-x|}}{2ik_b}, \quad \omega > 0, \tag{26}$$

By induction, suppose that u_{k-1} and $G_{k-1}(x', x)$ are calculated in the $(k-1)$th step, we solve the Green's function integral Equation (27) in the sub domain Ω_k to obtain $G_k(r'', r)$. We use our GL method to solve 1-D wave equation and obtain an excellent accurate solution. We prove that the GL solution converges to the exact solution.

(7.3) The updating formula of the GL iteration is as follows

$$u_k(x) = u_{k-1}(x) - \omega^2 \int_{x_k}^{x_{k+1}} \left(\left(\frac{1}{c^2(x)} - \frac{1}{c_b^2} \right) G_k(x', x) u_{k-1}(x') \right) dx'. \quad k = 1, 2, \ldots, n. \tag{27}$$

(7.4) The $u_n(x)$ is GL solution of the 1-D wave Equation (22).

7.2. The Convergence

Theorem 6. Suppose that the trapezoid integral for $G_{k-1}(x'', x)$ and $u_{k-1}(x')$ in (27), the GL numerical solution $u_n^h(x)$ converges to the exact solution when $\max |x_{k+1} - x_k| = l \to 0$. Moreover, we have $\left| u_n^h(x) - u(x) \right| \leq ch^2$, where c is independent constant on the h.

Proof: The proof of Theorem 6 is ommited.

Theorem 7. Under the conditions of Theorem 6, if the numerical Gaussian integral in the (27) is used, then we have super convergent estimation $\left| u_n^h(x) - u(x) \right| \leq ch^4$.

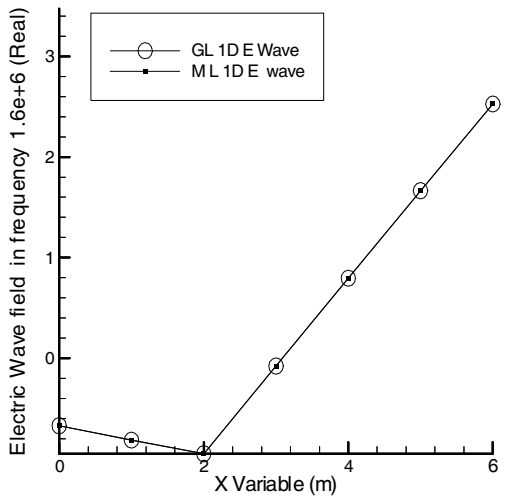

Figure 1: GL and exact electric wave with freq. $1.6e^6$ Hz.

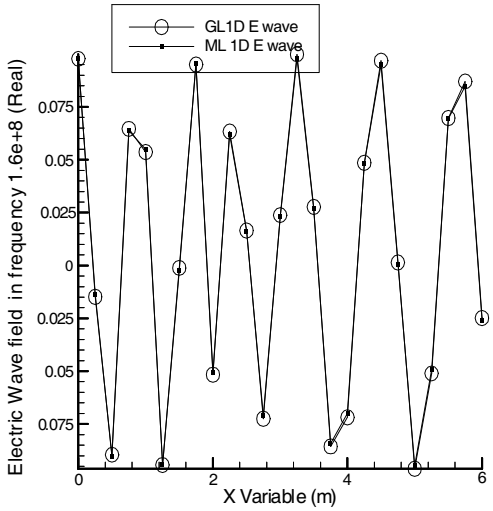

Figure 2: GL and exact electric wave with freq. $1.6e^8$ Hz.

7.3. Simulation

We use the GL method discretization (7.1)–(7.4) to solve the 1-D wave Equation (22) in the finite inhomogeneous interval $[0, 6]$. The interval $[0, 6] = [0, 2] \cup [2, 4] \cup [4, 6]$, $c_b = 3 \times 10^7$ m/s, $c_1 = 3 \times 10^7$ m/s on $[0, 2]$, $c_2 = 21,276,593$ m/s in $[2, 4]$, $c_3 = 17,336,030$ m/s in $[4, 6]$, a dipole source is located in the $x_s = 2,128$ frequencies are used, the minimum frequency is 1 Hz, the maximum frequency is 3.14×108 Hz. We obtained excellent wave field results by our GL method. The GL wave and exact wave field are displayed in the Figure 1–Figure 6. The 33 nodes are used and CPU time is 11 seconds in PC. For the high frequency wave, the GL solution are very match to the 1-D exact wave field, but the FEM solution fails to approximate the 1-D wave field.

8. APPLICATION AND CONCLUSION

Our GL method can be used to solve ordinary differential equation and the elliptic, parabolic, and hyperbolic partial differential equations. The 3D and 2D electromagnetic field GL modeling, 3D and 2D seismic field GL modeling, 3D and 2D acoustic field GL modeling, 2D QEM field GL modeling and 3D flow GL modeling are developing. Our GL method is useful for EM stirring

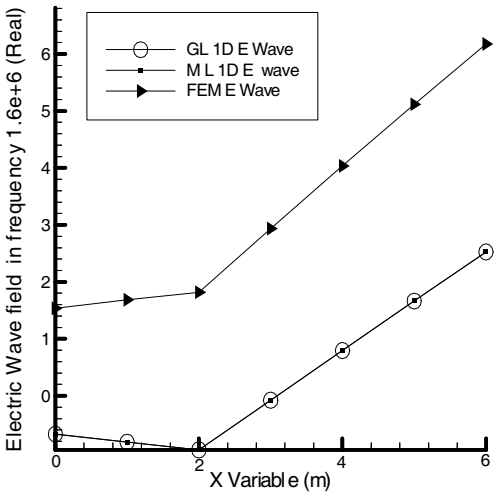

Figure 3: GL, exact and FEM electric wave with freq. $1.6e^6$ Hz.

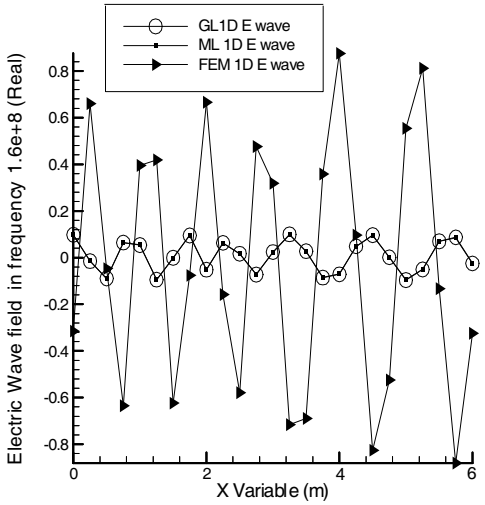

Figure 4: GL, exact and FEM electric wave with freq. $1.6e^8$ Hz.

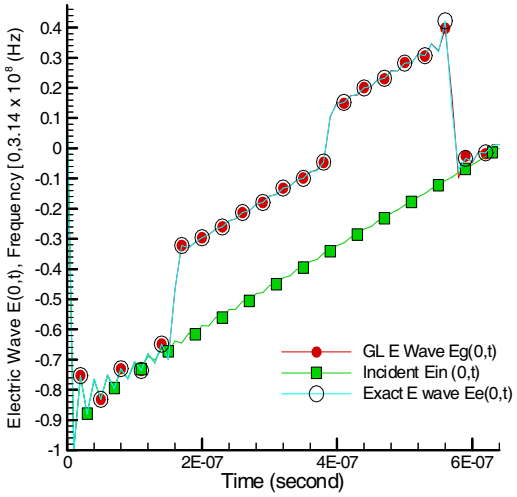

Figure 5: GL and Exact Electric wave E(0,t) in time domain.

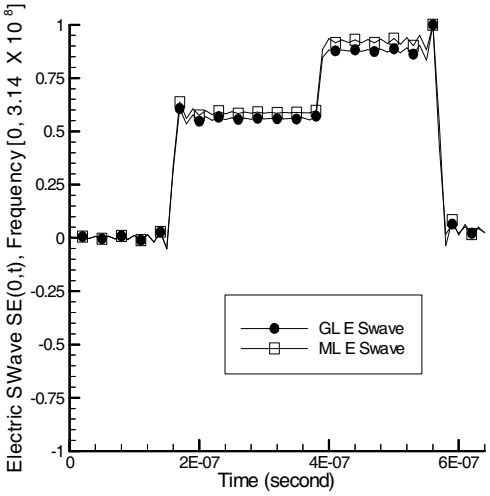

Figure 6: GL and Exact Scat. Electric Swave SE(0,t) on time.

caster, geophysics, antenna, radar, weather, seismic wave in Earthquake, nanometer material and materials. Biophysics, and underground flow in multiple pore media [3–10]. Our GL method is very accurate and it is much faster than FEM and FD method, usually, it is $10 \sim 20$ times faster than FEM method. The GL method is a self parallel algorithm and has high effective for GL hardware configuration. Our GL method is very useful for inversion. We have been working for the GL algorithms, software, and applications since 2002. Some recent publications of the works are listed as the references [1–10]. Because our GL method is a primary original research work, the following references are authors' papers. All GL Method discover and software patent rights are reserved by authors in GLGEO.

ACKNOWLEDGMENT

The authors are grateful to Professor P. D. Lax and Professor Lin Qun for his permanent attention and encouragement to our research works. Authors are grateful to Professor Xiao Xi Ding and Professor Lin Qun for their encouragements.

REFERENCES

1. Xie, G., F. Xie, L. Xie, and J. Li, "New GL method and its advantages for resolving historical difficulties," *Progress In Electromagnetics Research*, Vol. PIER 63, 141–152, 2006.

2. Xie, G., J. Li, L. Xie, and F. Xie, "A GL metro carlo EM inversion," *Journal of Electromagnetic Waves and Applications*, Vol. 20, No. 14, 1991–2000, 2006.
3. Xie, G., J. Li, L. Xie, and F. Xie, "GL EM modeling and inversion based on the new EM integral equation," Report of GLGEO, GLP05001, GLGEO has copyright and patent for the GL method, 2005.
4. Li, J., G. Xie, L. Xie, and F. Xie, "New stochastic AGLID EM modeling and inversion," *PIERS Online*, Vol. 2, No. 5, 490–494, 2006.
5. Li, J., G. Xie, L. Xie, and F. Xie, "A 3D GL EM modeling and inversion for forest exploration and felling," *PIERS Online*, Vol. 3, No. 4, 402–410, 2007.
6. Li, J., G. Xie, M. Oristaglio, L. Xie, and F. Xie, "A 3D-2D AGILD EM modeling and inversion imaging," *PIERS Online*, Vol. 3, No. 4, 423–429, 2007.
7. Li, J., G. Xie, and F. Xie, "New stochastic AGLID EM modeling and inversion," *PIERS Online*, Vol. 2, No. 5, 490–494, 2006.
8. Li, J., G. Xie, and J. Li, "3D and 2.5D AGLID EMS stirring modeling in the cylindrical coordinate system," *PIERS Online*, Vol. 2, No. 5, 505–509, 2006.
9. Xie, G., J. Li, F. Xie, and L. Xie, "3D GL EM and quantum mechanical coupled modeling for the nanometer materials," *PIERS Online*, Vol. 3, No. 4, 418–422, 2007.
10. Xie, G., J. Li, L. Xie, F. Xie, and J. Li, "The 3D GL EM-flow-heat-stress coupled modeling," *PIERS Online*, Vol. 3, No. 4, 411–417, 2007.

Interference Calculation for ATSC System against Interference from ISDB-T System Using Computational Simulation

Sung Woong Choi[1], **Tae Jin Jung**[2], **Wang Rok Oh**[3], **and Heon Jin Hong**[1]

[1]Radio & Broadcasting Technology Lab., ETRI, Korea
[2]Department of Electronic & Computer Engineering, Chonnam National University, Korea
[3]Division of Electrical & Computer Engineering, Chungnam National University, Korea

Abstract— In this paper, we proposed the method for calculating the interference protection ratio (PR) of the Advanced Television Systems Committee (ATSC) broadcasting system from the Integrated Services Digital Broadcasting-Terrestrial (ISDB-T) broadcasting system through the computational experiment. For this, the transmitter/receiver of the ATSC system and transmitter of the ISDB-T system were modeled. By integrating those, the computational simulator for setting up the PR of the ATSC system from the ISDB-T system was implemented. The ATSC TV signal was regarded as the desired one and the ISDB-T TV signal was regarded as the interfering one. In order to simplify the simulation complexity, it modeled sending/receiving signals of the IF band instead of those of the RF band. It was assumed that one received signal was considered in the channel modeling and there's no Additive White Gaussian Noise (AWGN) noise.

1. INTRODUCTION

According to the rapid development of the digital technology, the broadcasting environments are changing into the digital television transmission including the ATSC, ISDB-T, DVB-T, etc of the high quality and high-efficiency from the existing analog television transmission. In the transition to digital broadcasting, the methods that can efficiently use the limited broadcasting frequency resources are studied in many countries. Particularly, in the digital television broadcasting environment, since the countries using the different digital television broadcasting system (for example ATSC in Korea, ISDB-T in Japan) is positioned nearby, the interference is generated each other and the frequencies are unable to be efficiently used. Therefore, the mutual interference effect must be analyzed through setting up the PR which is interference allowed value between the different broadcasting systems and the digital broadcasting channel must be arranged to minimize the interference, then the broadcasting frequencies can be efficiently shared and used.

Until now, it is general that the field test data are used for setting up the PR between the broadcasting systems [1, 2]. But it needs much time and cost in order to collect and analyze the field test data. Therefore, by drawing method for setting up the PR based on the computational simulation, it is easy to calculate the PR about the corresponding system. In this paper, we proposed the method for calculating the PR of the ATSC broadcasting system from the ISDB-T broadcasting system through the computational experiment. For this, the transmitter/receiver of the ATSC system and transmitter of the ISDB-T system were modeled. By integrating those, the computational simulator for setting up the PR of the ATSC system from the ISDB-T system was implemented. The ATSC TV signal was regarded as the desired one and the ISDB-T TV signal was regarded as the interfering one. In order to simplify the simulation complexity, it modeled sending/receiving signals of the IF band instead of those of the RF band. It was assumed that one received signal was considered in the channel modeling and there's no AWGN. In ATSC receiver, the symbol error rate (SER) 0.2 of the trellis decoder input signal was used as the Threshold of Visibility (TOV) performance [3].

2. ATSC AND ISDB-T SYSTEM MODELING

2.1. ATSC 8VSB System Modeling

The ATSC system was specifically designed to permit an additional digital transmitter to be added to each existing NTSC transmitter. The ATSC Digital Television Standard was developed by the Advanced Television Systems Committee in the Unite States [4, 5]. The ATSC system was designed to transmit high-quality video and audio (HDTV) and ancillary data over a single 6 MHz channel. The ATSC Vestigial Sideband modulation with 8 discrete amplitude levels (8-VSB) system transmits data in a method that uses trellis-coding with 8 discrete levels of signal amplitude. A pilot

tone provided to facilitate rapid acquisition of the signal by receivers. Complex coding techniques and adaptive equalization are used to make reception more robust to propagation impairments such as multipath, noise and interference. It can reliably deliver about 19.39 Mbps of data throughput in a 6 MHz bandwidth.

Figure 2 presents a functional block diagram of 8 VSB transmitter and receiver. The 8-VSB transmitter can represent to three parts, the Forward Error Correction (FEC), the Insertion of the sync signals, and 8-VSB modulation.

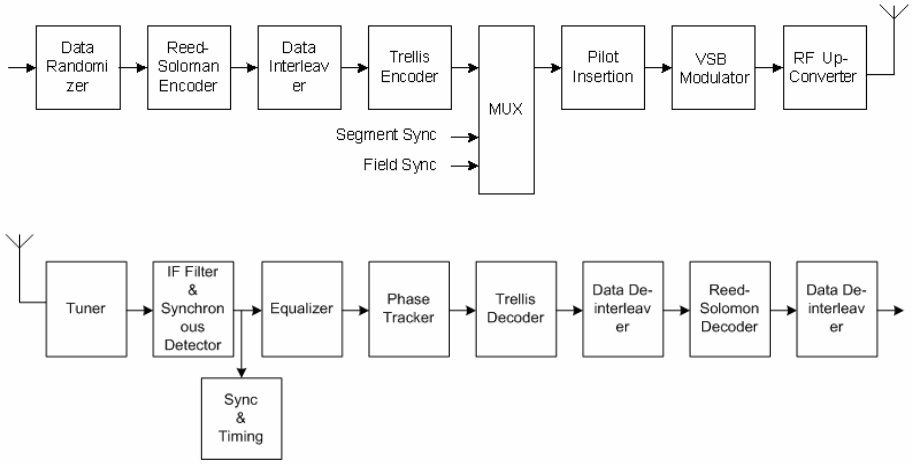

Figure 1: Functional block diagram ATSC transmitter/receiver.

Table 1: Parameters for ATSC 8VSB transmission modes.

Parameter	**ATSC 8VSB**
Bandwidth	6 MHz
Excess bandwidth	11.5%
Symbol rate	10.76 MSPS
Bits/Symbol	3
Trellis FEC	2/3 rate
Payload data rate	19.39 Mb/s
C/N threshold	14.9 dB

2.2. ISDB-T System Modeling

In this chapter, we review the ISDB-T system adopted as the standard of the digital broadcasting in the Japanese is reviewed [6]. The ISDB-T modulation scheme, also called BST COFDM (Band Segmented Transmission Coded-OFDM), was developed to broadcasting digital terrestrial TV with the use of flexible modulation. The 6-MHz channel band is divided into 13 segments of width 429 kHz each. In the same channel, it is possible to transmit one HDTV signal with 64QAM modulation and one signal of "one-segment TV for reception by a narrowband portable receiver. ISDB-T system uses frequency band of 188 MHz∼192 MHz and 2535 MHz∼2655 MHz, and applies to the frequency and time interleaving. The ISDB-T system uses RS (Reed-Solomon) code (204, 188, 8) as the outer code and the convolutional code as the inner code. The ISDB-T system uses 4 types of modulation of DQPSK, QPSK, 16QAM and 64QAM. It is classified as the various transmission modes according to 3 FFT modes of 2K, 4K, 8K and the combination of 4 guard intervals of 1/4, 1/8, 1/16, 1/32. It uses the MPEG-2 Layer II, AC-3, and the MPEG-2 AAC as the audio coding, the multiplex of the MPEG-2 mode.

Figure 2 presents a functional block diagram of ISDB-T transmitter. As shown in the figure, a transmitter is comprised of the RS encoder, the Hierarchical Processing, the Rate Conversion,

the Time and Frequency Interleaving, the OFDM Framing, the IFFT block and Guard Interval Insertion, etc. In the hierarchical processing, each hierarchical layer performs the Energy Dispersal, the Delay Compensation, the Bute Interleaving, the Convolutional encoding, and Modulation.

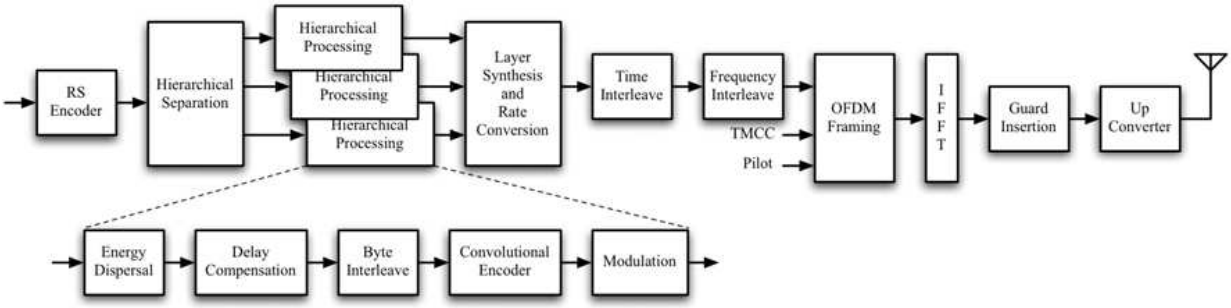

Figure 2: Functional block diagram of ISDB-T transmitter.

Table 2: Parameters for ISDB-T transmission modes.

Parameter	**ISDB-T**
Bandwidth	5.575 MHz
Symbol rate	8.127 MSPS
Modulation	64QAM
FEC	3/4
Guard Interval	1/16
Time Interleaver	200 ms
Data rate	19.3 Mbps
C/N threshold	18.9 dB

3. SIMULATION FOR PROTECTION RATIO

3.1. Simulation Method

Here, we describe the method for calculating the PR of the ATSC system from the ISDB-T system through the computational experiment. For this, the transmitter/receiver of the ATSC system and transmitter of the ISDB-T system were modeled. The wanted transmitter and receiver use the ATSC 8-VSB system and the interfering transmitter uses the ISDB-T system. In order to simplify the simulation complexity, it modeled sending/receiving signals in the IF band instead of those in the RF band. It was assumed that channel modeling considered one received signal and there's no AWGN. In ATSC receiver, the SER 0.2 of the trellis decoder input signal was used as the TOV performance.

Figure 3 shows the simulation block diagram for the protection ratio calculation for ATSC from ISDB-T. The implemented simulation system comprises 8-VSB transmitter/receiver and ISDB-T interfering signal transmitter. The transmitting signal moves to 5.38 MHz of the IF band after the Random Data Generator and Up-sampling, Pulse Shaping, and the Modulation of the ATSC 8-VSB system. Next, 8-VSB wanted signal in IF band is added with the ISDB-T interfering signal, and arrives the receiver end. Figure 4 shows the wanted/interfering signal modelling. The Δf is the difference between the center frequencies of interfering and desired signal and α is the relative power between the desired and interfering signal. The PR for the ATSC system from the ISDB-T system is measured by calculating the SER value. Figure 5 shows the flowchart for calculating the PR.

1) Set up the $\Delta f = 0$ and $\alpha = 1$.
2) By controlling the α, find the α when the SER value becomes 0.2, that is the protection ratio in co-channel.

3) Change the Δf.

4) By controlling the α, find the α when the SER value becomes 0.2.

5) Repeat 3), 4) until the Δf is final value.

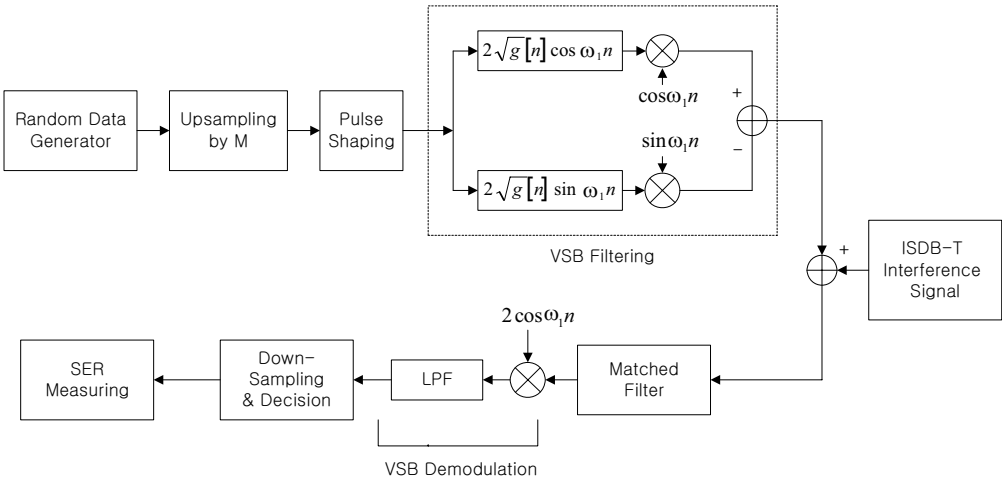

Figure 3: Simulation block diagram.

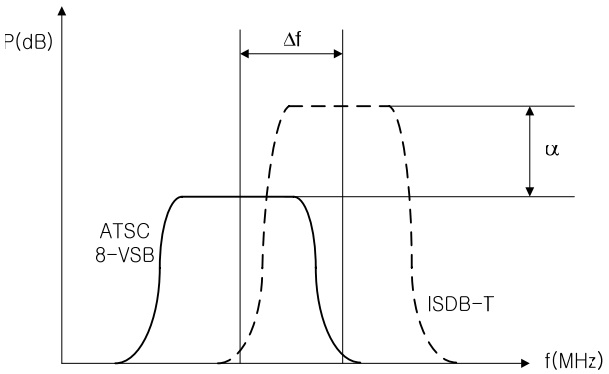

Figure 4: Wanted/interfering signal modeling.

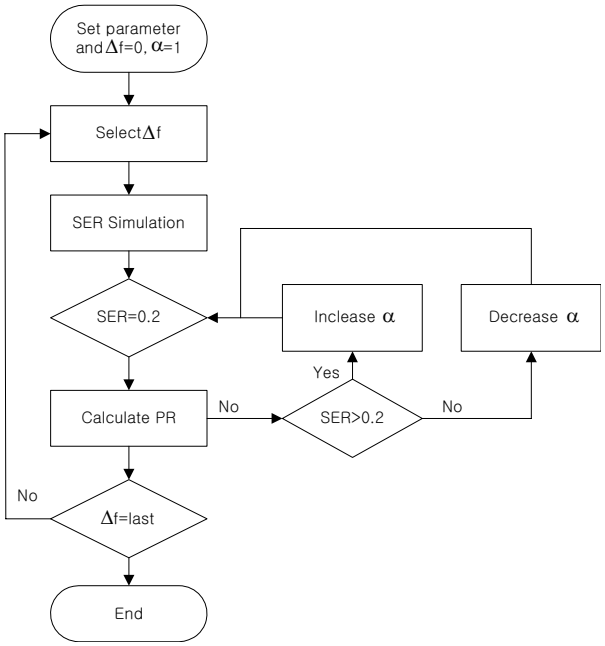

Figure 5: Flowchart for calculating protection ratio.

3.2. Simulation Result

Figure 6(a) shows the SER values in case of $\Delta f = 0$ (co-channel) and the $\Delta f = 2.5$ MHz. In Figure 6(b), when the SER = 0.2 the interference protection ratio, α value became about 5.65 (15 dB). This is similar to the co-channel PR for ATSC system from ATSC system.

Figure 7 shows PR values according to Δf. The maximum bandwidth of ISDB-T, 5.575 MHz is smaller than 6 MHz of ATSC, and PR value does not change in -1 to $+1$ of Δf. Except for such case, we can confirm that the PR value decreases as the Δf increases. Because the affect of the interference signal is decreased as the Δf increases, although it transmits relatively low power of the signal, SER = 0.2 can be obtained.

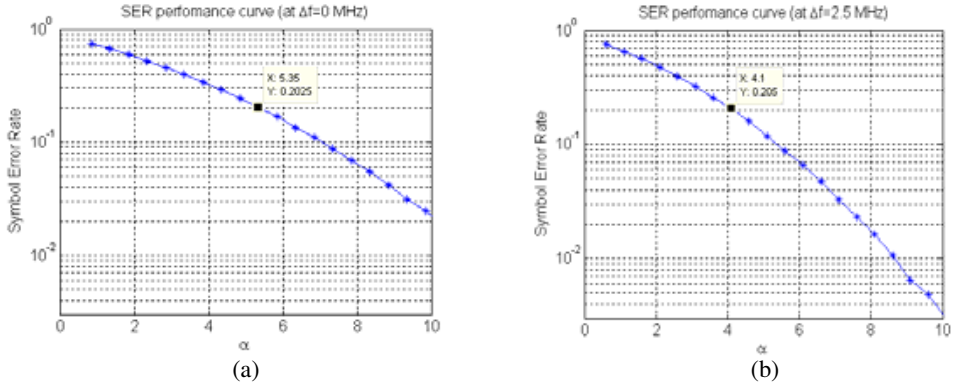

(a) (b)

Figure 6: SER according to Δf, (a) $\Delta f = 0$ (co-channel), (b) $\Delta f = 2.5\,\mathrm{MHz}$.

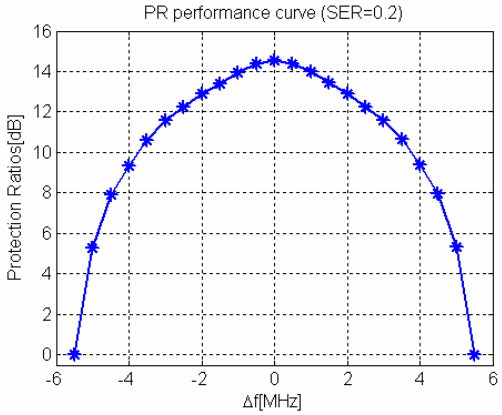

Figure 7: Protection ratios according to Δf [dB].

4. CONCLUSIONS

In this paper, we proposed the method for calculating the PR among broadcasting systems through the computational experiment, and calculate the PR value of the ATSC broadcasting system from the ISDB-T broadcasting system. As the technology develops, the new broadcasting system shows up. But whenever the new broadcasting system shows up, it is hard to find the PR through a measurement. Therefore, by using this kind of method, it will be able to easily calculate the PR between the new digital broadcasting systems.

REFERENCES

1. Doc, 11A/6, Digital Terrestrial Television Transmission — User's Needs and System Selection, Feb. 1998.
2. Protection Ratio Experiments and Results for ISDB-T.
3. Ghosh, M., "Blind decision feedback equalization for terrestrial television receivers," *Proceedings of the IEEE*, Vol. 86, No. 10, 2070–2081, Oct. 1998.
4. Doc. A/53, ATSC Digital Television Standard, Sept. 1995.
5. Mathematical Modeling of VSB-Based Digital Television Systems.
6. ITU-R Document 11A, Channel Coding, Frame Structure and Modulation Scheme for Terrestrial Integrated Services Digital Broadcasting (ISDB-T), Mar. 1999.
7. Bedicks, G., "Results of the ISDB-T system tests, as part of digital TV study carried out in Brazil," *IEEE Transactions on Broadcasting*, Vol. 52, No. 1, 38–44, Mar. 2006
8. Wu, Y., "Comparison of terrestrial DTV transmission systems: The ATSC 8-VSB, the DVB-T COFDM, and the ISDB-T BST-OFDM," *IEEE Transactions on Broadcasting*, Vol. 46, No. 2, Jun. 2000

Feasibility of Defect Detection in Concrete Structures via Ultrasonic Investigation

A. Musolino, **M. Raugi**, **M. Tucci**, **and F. Turcu**
Dipartimento di Sistemi Elettrici e Automazione, Via Diotisalvi, Pisa 2 56126, Italy

Abstract— In this paper we investigate the feasibility of a diagnostic method for the Non Destructive Testing (NDT) for concrete structure based on the ultrasonic wave propagation. The propagation of ultrasonic waves in solids is governed by the linear elasticity equation. The determination of the types of waves that can propagate on a given structure is a complex matter as they depend on the geometry, the frequency and the physical properties of the materials. The transverse waves propagation on plane structures has been considered with the aim of locate defects on the structure. The presence of a defect, usually a void, produces a reflected wave as ultrasounds do not propagate in air. The analysis of the characteristics of the reflected wave is used to localize the defect.

1. INTRODUCTION

Concrete is a composite material consisting of a binding of medium with particles like gravel, sand etc. embedded in the construction medium. Critical concrete structures need to be evaluated during their service to ensure that they have not deteriorated and are free from defects. Sonic, ultrasonic and impact echo test methods are three important methods that are widely used for non-destructive examination of concrete structures [1].

Usually these methods are used to inspect a portion of concrete structure (typically a wall or a column) located in correspondence of the equipment. The commercial devices commonly used are of difficult tuning with the specific structure that is under inspection; their user interfaces are not flexible and do not allow the interpretation of the measured data. Furthermore the conventional non destructive ultrasonic based techniques are able to inspect only a narrow zone (though deep) near the point where the excitation is applied and as a consequence a great number of tests have to be performed to inspect the whole structure.

By using the sonic tests it is possible to measure the transmission velocity of the elastic waves inside the wall from a generator of impulses (usually a servo hammer) to a receiver. Such transmission velocity increases with the medium density, adjusting correspondingly magnitude and frequency.

Impact-echo is based on the use of impact-generated stress (sound) waves that propagate through concrete and masonry and are reflected by internal flaws and external surfaces.

According to the relative positions between the point of the impulse and receipt, tests can be performed for:

- direct transmission: probe and transducer are positioned in symmetrical way on the opposite faces of the wall;
- semi-direct transmission: as above but in non-symmetrical way;
- indirect transmission: the transducer is on the same part as the sensor.

Other techniques based on ultrasounds have been introduced for destructive analysis in different engineering fields. In particular, in the case of plants with systems of pipes, ultrasonic waves, guided by the walls of the pipes themselves, have been used. The presence of a defect in the structure produces a reflected wave that can be detected by properly positioned sensors. The analysis of the waveforms of the sensors allows the localization of the defect.

The aim of this paper is to investigate the feasibility of a long distance inspection technique for concrete structure based on the propagation of the elastic ultrasonic waves on the structure itself. Such a technique would allow the inspection of large portions of the structure at distance from the application of the exciting pulse thus reducing the time needed to complete the investigation. Moreover this technique could allow the inspection of regions non directly accessible, as the elastic ultrasonic waves propagate for long distance and deep inside the structure and can be generated and detected by transducers and sensors that can be positioned at distance one from the other.

The paper is organized as follows: Section 2 will discuss the theoretical feasibility of the method by considering a number of numerical simulations of the propagation of the elastic waves on a concrete wall with defects variously positioned. Finally an algorithm for the localization of the defects is discussed in Section 3.

2. THEORETICAL ANALYSIS

In order to asses the validity of the method we performed a number of numerical analysis on a sample structure shown in Fig. 1. The figure shows the upper half of a concrete wall. The reported dimensions are in centimeters. The thickness is 15 cm. Table 1 shows the physical constant of the concrete that we have assumed throughout the paper. The transducer is able to impose an assigned displacement along the x-direction to a rectangular portion of the surface of the concrete wall. The waveform of this imposed displacement is shown in Fig. 2.

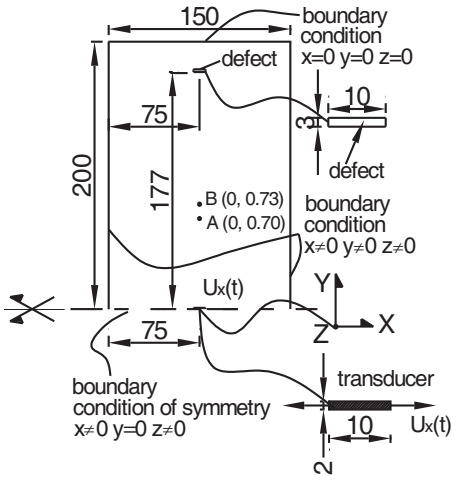

Figure 1: The analyzed concrete structure.

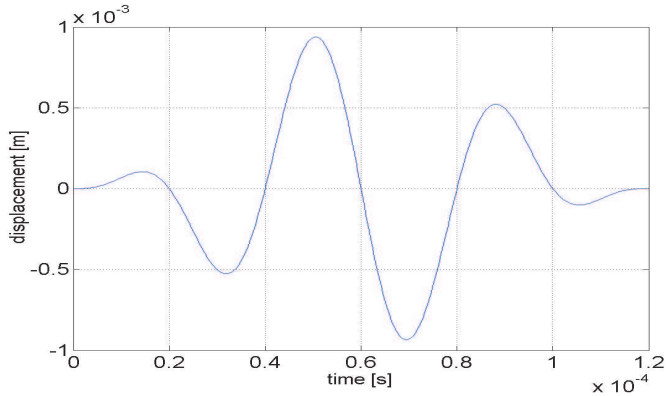

Figure 2: Displacement imposed by the transducer.

Table 1: Concrete data.

Elasticity modulus	$E = 2.2E + 10$	N/m^2
Poisson ratio	$v = 0.15$	
Mass density	$\rho = 2.4E + 3$	kg/m^3
Damping parameters	$\alpha_M = 5.0E - 04$	s^{-1}
	$\alpha_K = 1.0E - 08$	s
Lamè parameters	$\mu_L = 9.56E + 09$	N/m^2
	$\lambda_L = 4.099E + 09$	

We started performing the simulation of the propagation of an elastic wave on the wall without defects [2, 3]. Successively we examined three configurations characterized by the presence of defects of different shapes and in different positions. Firstly we considered a defect consisting of a crack long 10 cm and high 3 cm that passes through the wall on its entire thickness. Three positions have been chosen; the first one at the coordinates $x = 0$, $y = 1$ (the middle of the shown portion of the geometry), the second at $x = 0$, $y = 1.8$ (20 cm below the upper edge of the wall) and the third at $x = -0.4$ and $y = 1.0$.

Figures 3–5 show color maps of the computed x-displacement at properly selected instants. The effects of the presence of the defects are evident. In particular it is possible to recognize the presence of waves that travel from the defect backward to the transducer. This effect is particularly evident in the first two cases. All these figures provide important information on the propagation of the elastic waves in the structure under test. In particular it is possible to locate the regions that are "lighted" by the transducer and help in the choice of the positioning of the sensors. Obviously the Figs. 3–5 are not available when performing a realistic measurement as they would require a huge number of sensors for their construction while the number of sensors is used in practice seldom exceeds ten.

Figure 6 shows the x-displacements at the points A and B as in Fig. 1 with the defect positioned 20 cm below the upper edge of the wall. These are typical waveforms of the displacements. The

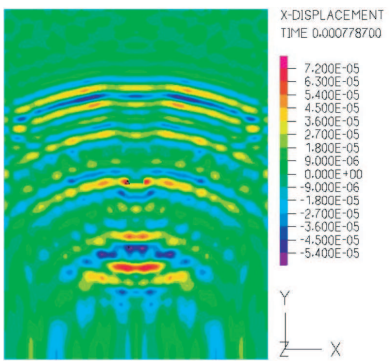

Figure 3: X-displacements at 0.78 ms.

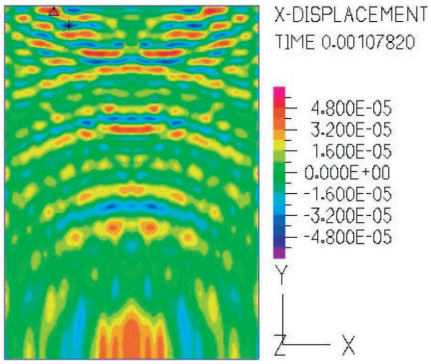

Figure 4: X-displacements at 1.08 ms.

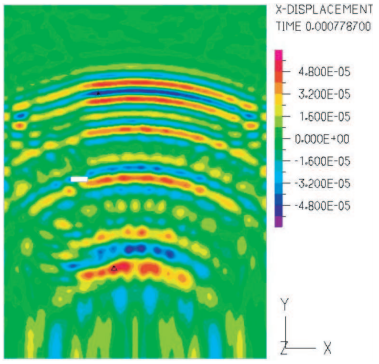

Figure 5: X-displacements at 0.78 ms.

recognition of patterns similar to that shown in Fig. 2 is not possible because of the presence of higher order modes in the propagation of the elastic waves as the thickness of the wall is comparable with the wavelength of the excitation. However, if two points are close one to the other it is possible to recognize the presence of a backward traveling wave.

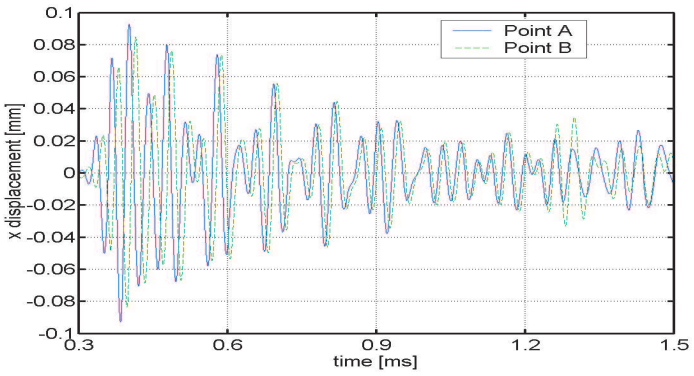

Figure 6: X-displacements at points A and B.

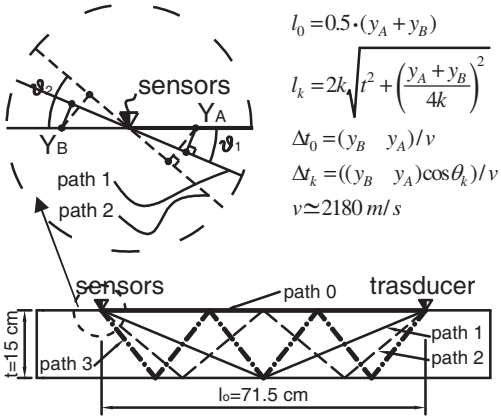

$$l_0 = 0.5 \cdot (y_A + y_B)$$

$$l_k = 2k\sqrt{t^2 + \left(\frac{y_A + y_B}{4k}\right)^2}$$

$$\Delta t_0 = (y_B \quad y_A)/v$$

$$\Delta t_k = ((y_B \quad y_A)\cos\theta_k)/v$$

$$v \simeq 2180\, m/s$$

Figure 7: Multipath model of wave propagation.

In the case of the presence of a forward traveling wave only it is possible to relate the two waveforms by properly delaying the curve at point A and making it "almost" equal to that at point B. The delay times may be evaluated by using a simple model based on the different lengths of the multiple paths that exist between the transducer and the sensors. Fig. 7 shows the direct path and a few other paths between the transducer and the mid point of A and B. The delay of the direct path is $\Delta t_0 = (y_B - y_A)/v$, ($v$ is the transversal velocity), that of the path ♯1 is $\Delta t_1 = ((y_B - y_A)\cos\theta_1)/v$ and so on. These different (decreasing) delays are assigned to different portions of the waveform by the following rule. Δt_0 is assigned to the portion of curve that starts at time $t_0 = l_0/v$ where l_0 is the length of the direct path (see Fig. 7) and lasts $\Delta T = 0.12$ ms sec (the time interval where the excitation is not zero, as reported in Fig. 2). Δt_1 is assigned to the portion of curve that starts at time $t_1 = l + 1/v$ (l_1 is the length of the path ♯1) and lasts $\Delta T = 0.12$ ms.

The correspondence built by this rule is a piecewise constant function. Once a proper smoothing is performed and the curve of the displacements at point A is accordingly shifted we obtain the result shown in Figs. 8 and 9. As can be inferred by the two figures the x-displacement at point B is a delayed replica of the displacement at point A until a time instant $\tilde{t}$ that is located somewhere in the interval $[t_1, t_2]$ ($t_1 = 1.26$ ms, $t_2 = 1.30$ ms). At this instant a backward traveling wave is added to the forward one. The total distance covered by the elastic wave in the time interval from 0 to $0.5 \cdot (t_1 + t_2)$ is about $d \simeq v \cdot \tilde{t} \simeq 2180 \cdot 1.28 \cdot 10^{-3} = 2.79 \cong 1.77 + 1.04$ that equals with a good approximation the sum of the distance of the defect from the transducer (1.77 m) and the distance of the defect to the position of point B (1.04 m).

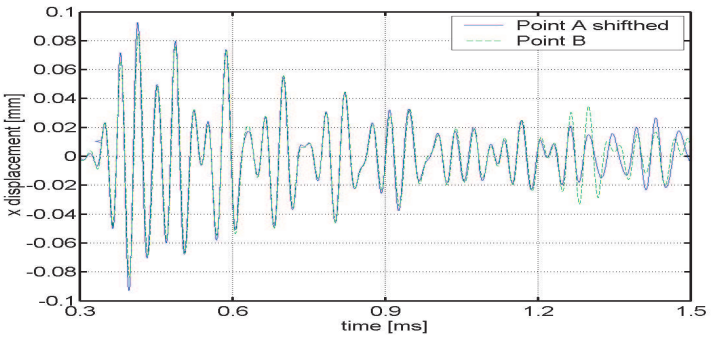

Figure 8: Comparison of x-displacements at points B and at point A shifted.

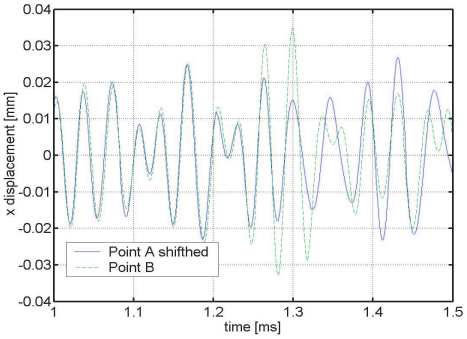

Figure 9: Enlarged portion of Fig. 8.

3. DEFECT LOCALIZATION

In a more general contest the transducer, the sensors and the defect are not aligned. Let us consider the arrangement of Fig. 10 where $N_S = 7$ couples of sensors similar to the couple above introduced are shown. The relationships for the evaluation of the lengths of the multiple paths and of the time delays can be readily derived by the ones previously used. The comparative analysis of the waveforms at each sensors couple provides a measure of the total length of the distance from the transducer to the defect and from the defect to the sensors couple. Let D_k be such a distance for the kth sensors couple. In an error free contest the data related to two sensors couples are sufficient to locate the defect by performing a triangulation. In this contest where errors may affect the knowledge of the D_k's a different approach is used. Let $(x_d,\, y_d)$ be the (unknown) coordinates of the defect; $(x_t,\, y_t)$ those of the transducer and $(x_k,\, y_k)$ those of the kth sensors couple.

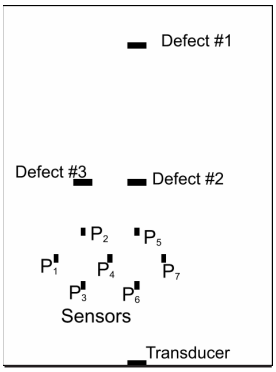

Figure 10: Arrangement of sensors.

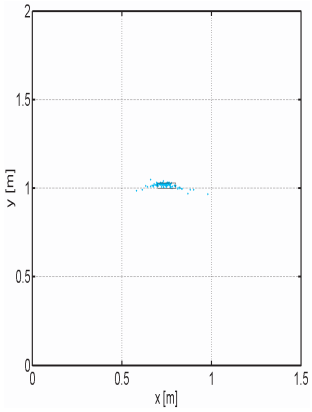

Figure 11: Defect as in Fig. 3.

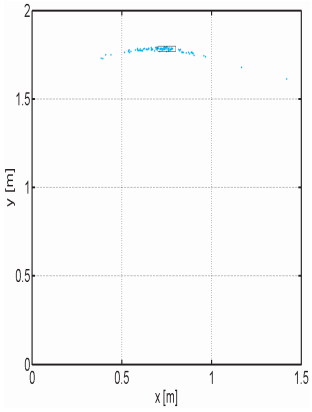

Figure 12: Defect as in Fig. 4.

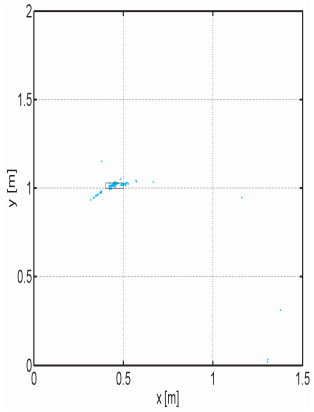

Figure 13: Defect as in Fig. 5.

For the kth sensors couple we write:

$$F_k(x_d,\, y_d) = \sqrt{(x_d - x_t)^2 + (y_d - y_t)^2} + \sqrt{(x_d - x_k)^2 + (y_d - y_k)^2} - D_k = 0, \quad k = 1,\, \ldots,\, N_S$$

Because of the errors in the estimate of the D_k's these equations cannot be simultaneously satisfied.

The least square solution is the classical approach. Here we propose a variation of this method. We firstly consider all the possible couples (21 when $N_S = 7$) of equations:

$$\begin{aligned} F_k(x_d,\, y_d) &= 0 \\ F_h(x_d,\, y_d) &= 0 \quad k = 1,\, \ldots,\, N_S;\ h = 1,\, \ldots,\, N_S;\ h \neq k \end{aligned}$$

and evaluate the corresponding solutions.

Subsequently we consider three equations at time (35 when $N_S = 7$):

$$\begin{aligned} F_k(x_d,\, y_d) &= 0 \\ F_h(x_d,\, y_d) &= 0 \\ F_j(x_d,\, y_d) &= 0 \quad k = 1,\, \ldots,\, N_S;\; h = 1,\, \ldots,\, N_S;\; j = 1,\, \ldots,\, N_S,\; j \neq h \neq k \end{aligned}$$

and perform a least square algorithm obtaining further solutions. We continue by considering four equations at time and so on. A total number of $2^{N_s} - N_S$ solutions have been finally obtained. Figs. 11–13 show the comparison between the effective position of the defects and the results of the described procedure in the three examples above described. The dispersion of the results in terms of x coordinate of the defect in the example ♯2 is caused by a relatively large sensitivity of the triangulation algorithm with respect to the measure errors when the angle taken on the defect that spans the region of the sensors is small.

4. CONCLUSIONS

In this paper we have investigated the feasibility of a diagnostic method for the Non Destructive Testing (NDT) for concrete structure based on the ultrasonic wave propagation. A simple but effective algorithm based on the multiple paths propagation has been used to detect the arrival instants of echoes from the defects on the sensors and a variation of the least square method has been used to estimate the positions of the defects.

ACKNOWLEDGMENT

This work was supported in part by the Italian Ministry of University (MIUR) under a program for the Development of Research of National Interest (PRIN GRANT 2005094532) and by the Fondazione Cassa di Risparmi di Livorno. The authors wish to thank Dr. Costantino Carbone for the valuable help in running the numerical simulations.

REFERENCES

1. Kumar, A., T. Jayakumar, C. V. Subramanian, and M. Thavasimuthu, "Testing of concrete structures for determination of strength and detection of flaws using low frequency ultrasonic and impact-echo techniques," *Journal of Non-dest Eval*, Vol. 19, No. 2, 43–46, 1999.
2. Kaltenbacher, M., *Numerical Simulation of Mechatronic Sensors and Actuators,* Spriger, Berlin, 2004.
3. Graff, K. F., *Wave Motion in Elastic Solids*, Oxford University Press, 1975.

Microwave Phase Interferometry for Nondestructive Testing in Industry

Ondrej Zak, **Jan Vrba**, **and Marika Pourova**
Department of Electromagnetic Field, FEE, CTU in Prague, Czech Republic

Abstract— In the paper contactless method for measurement of properties of constructional and machine material is dealt. It discuss phase microwave interferometry. We can determine e.g., moisture of material constructional and inner structure of material etc. via this method. Method is realized in a frequency range from 1 GHz to 8 GHz.

1. INTRODUCTION

At present monitoring is currently implemented by a variety of sensors, such as network of optical targets installed over the structure, strain gauges to measure deformations, collimation nets to measure displacements, inclinometers to measure rotations. Such sensors are accurate and reliable, but require contact with the structure to be surveyed, and information is local to the specific point of the sensor position. In a number of situations, moreover, placing of sensors on the structure is not possible or is too time consuming. Calibers are used in measurement of definite dimensions, which are very expensive.

Therefore the method of microwave phase interferometry is developed. This method is contactless method for measurement i.e., moisture masonry, warping object or finding inner inhomogeneous in various build of material. We can minimize the costs of place and time for compile of measured date.

This method is used for detecting defects of optic transparent materials. But wavelength of light is manifold smaller than wavelength in microwave spectrum that is why we can't inquired into material helped by optic, which they are not optic transparent.

Principle of method is to measure face of equiphase surface unknown microwave field, so that unknown field interfere with reference field and we carry out scalar measurement of electrical field strength in single points of interferential field. When we use for measurement matrix decoder, we can carry out measurement in short interval. We can determine phase inquiry field from measured values of electrical strength field in single points, so that we change phase of reference field known for style. Then we calculate phase from measured values helped by known algorithms. Algorithms used for evaluation are implied from optic spectrum.

2. MICROWAVE PHASE INTERFEROMETRY

Before we start measurement, we need to know strict definition of inquire material. Material must be perfect, otherwise we cannot determine whether material is defected. Therefore it would be preferable to create database of material, with which the measured values could be compared. Then it can be find by experimental measurement, how to show e.g., moisture of material, bubble of air in material or reduction and expansion dimension to distribution amplitude and phase, so that we can detect type of defect.

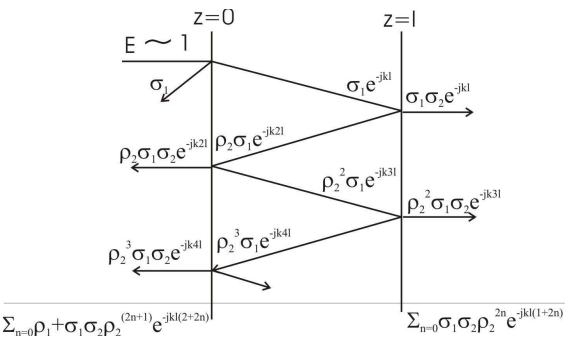

Figure 1: Vector diagram.

In the Figure 1 is described theoretic evaluation of incident plane wave to lossy material and passage through it. Plane wave on boundary line air and lossy material is partially reflected into air and it is partially transferred to the material, where it is absorbed. Inside material there are multiple reflections and partially transit of wave from the material back into air. At the end of figure are cited equations for calculation of wave on boundary line air-lossy material and lossy material-air.

In Figure 2 we compare a shift of phase and amplitude in the case of change of width of tested material about 2 mm.

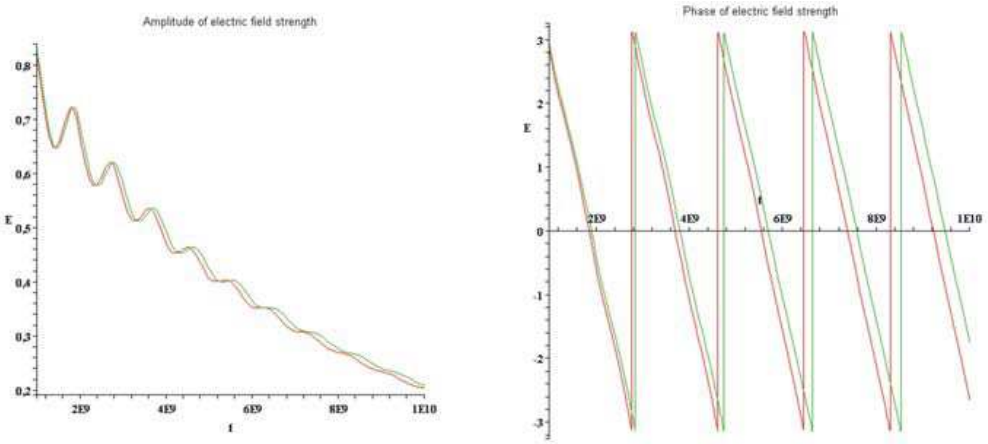

Figure 2: Phase and amplitude with respect to frequency.

We can see, that difference of phase and amplitude between good and bad material goes up with frequency. Red curve is for good material and green curve is for bad material.

It is evidential from simulation of electromagnetic field, that resolution of scanning phase and amplitude is increased with increase of measuring frequency. We cannot increase frequency ad infinitum. It is needed to define the highest frequency for every material by which part of energy goes through measured material. We calculate this frequency from dielectric properties of material

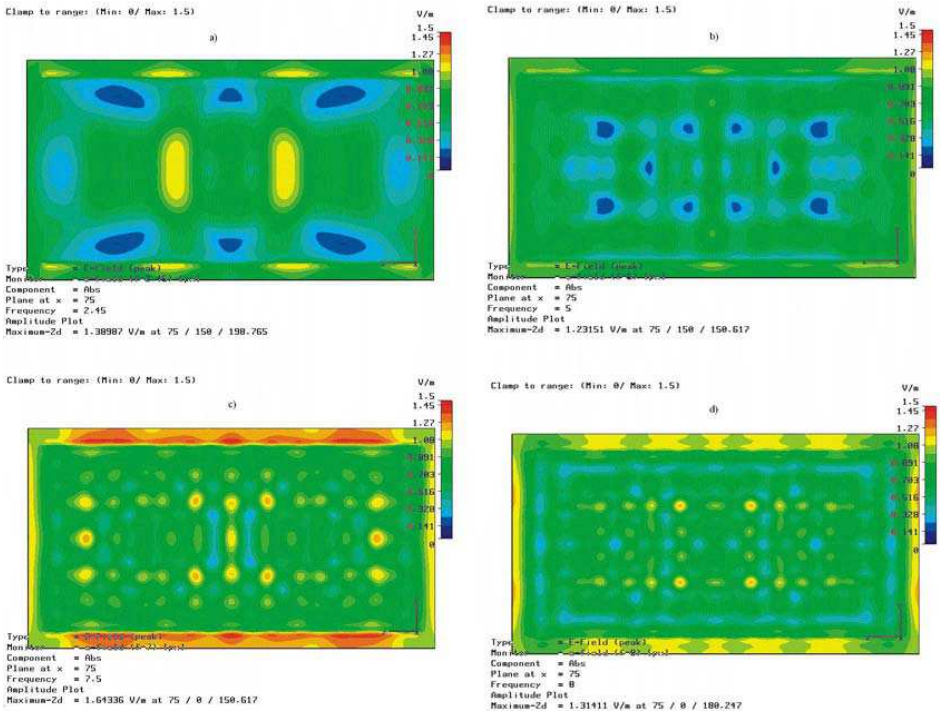

Figure 3: Resolution on the various frequency.

and thickness of studied material. Dielectric properties determine equivalent depth of penetration according to formula.

$$\delta = \frac{1}{\alpha} = \frac{1}{|\mathrm{Im}\{k\}|} \text{ [m]} \tag{1}$$

where α is constant of specific loss, which is imaginary part of constant of dispersion k

$$k = \sqrt{j\omega\mu(j\omega\varepsilon + \sigma)} \text{ [m}^{-1}\text{]} \tag{2}$$

7% energy goes through material in thickness of material 5δ, which should be sufficient for detection of signal.

Resolution on single frequency is shown in next graph 3. Graph describes resolution behind the brick on the frequency 2.45 GHz, 5 GHz, 7.5 GHz and 8 GHz. We can see, that distribution in brick is horizontally and vertically symmetric.

In next figure there is a description of distribution of amplitude of electrical field strength in front the brick and behind the brick. We can see failure of symmetry in these two cuts. In this case defect is in left top edge.

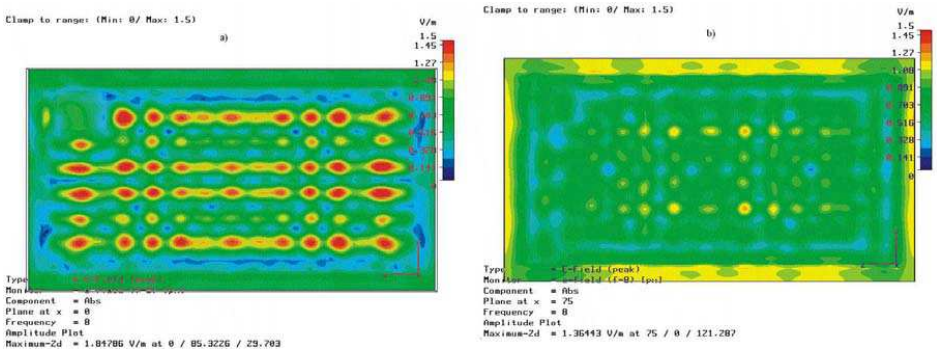

Figure 4: Distribution of electrical field strength in the bad brick.

3. CONCLUSION

We can inquire optic non-transparent of material by the studied method. It is evidential from simulation in simulator of electromagnetic field, that resolution of scanned phase and amplitude is increased with increase of measuring frequency.

ACKNOWLEDGMENT

This work was supported by the grant of the Czech grant agency "Microwave Phase Interferometry" (102/04/0898).

REFERENCES

1. Vrba, J., *Application of Microwave Technique (in czech)*, scriptum, CTU, Prague, 2001.
2. Mikš, A., J. Novák, K. Hoffmann, and J. Vrba, *Theoretic Analysis of Microwave Phase Interferometry (in czech)*, article, CTU, Prague, 2003.

A Signal Explanation for the Electromagnetic Induction Law

S. L. Vesely[1] **and A. A. Vesely**[2]

[1]I.T.B. - C.N.R., via Fratelli Cervi 93, Segrate (MI) I-20090, Italy
[2]via L. Anelli 13, Milano 20122, Italy

Abstract— We suggest to interpret the electromagnetic induction as a received electric signal, following a reasoning parallel to that of J. Clerk Maxwell that led to Faraday's law equation. Usually, the solutions of the entire set of equations for electromagnetism are interpreted energetically. The law of induction equation in particular, was interpreted in an energetic sense by Lenz. The interpretation we present is alternative to his one. The reason why we propose it is the conviction that telecommunications could take advantage of an interpretation of electromagnetism, updated for the technologies now in use.

1. INTRODUCTION

M. Faraday calls "magneto electric induction" the coupling between a magnet and a piece of metal wire through a vacuum, when detected as transient electric excitation at the terminals of the wire. Before him, among other people, B. Franklin, inventor of the lightning conductor, had anticipated a connection between electricity and magnetism. Already lightning itself can be considered an electric transient that magnetizes metallic objects: cutlery has been said to have been magnetized by lightning. With respect to this experience, the electric excitation observed in the laboratory as an effect of the movement of a magnet is just a small transient. For us however, Faraday's experiments are more fundamental, because Maxwell was able to connect them to the knowledge his contemporaries had. In the 19th century substantially two interpretations of the specific relation between electricity and magnetism gained ground.

The first, that we might call [A], is more traditional for those days. This describes the magnetic action at a distance in dynamical terms. To discuss action and reaction between magnet and circuit it establishes the equivalence of a magnetized body and a distribution of current by providing a magnetic representation of the electric current. According to Ampère, the magnetic dipole moment of a circuit with respect to the origin is given by $\mathbf{m}_{el} = \frac{1}{2} I \oint \mathbf{r} \times d\mathbf{l}$ where $\mathbf{r}$ is the radius vector from the origin to the point of observation and $d\mathbf{l}$ is an element of the electric circuit having an oriented loop. The mechanical action of $\mathbf{B}$ on $\mathbf{m}_{el}$ is evaluated as a torque $\mathbf{t} = \mathbf{m}_{el} \times \mathbf{B} = d\mathbf{D}/dt$, where $\mathbf{D} = m\mathbf{r} \times \mathbf{v}$ is the angular moment. This formally admits an electric equivalent thanks to the formula $\mathbf{m}_{el} \propto IA\mathbf{n}$, which originates from the representation of the circuits with magnetic shells, of use for calculation of the magnetic potential according to Poisson. Here $\mathbf{n}$ is a versor normal to the shell. Hence the magnetic expression for the torque becomes: $d\mathbf{m}_{el}/dt \propto \mathbf{m}_{el} \times \mathbf{B}$, or $d\mathbf{M}/dt \propto \mathbf{M} \times \mathbf{B}$, where the magnetization $\mathbf{M}$ is defined as a sum over the unit volume of molecular dipole moments $\mathbf{m}_{el}$. H. Lenz suggested that the force due to the magnet may induce within metals, besides the torque, also Faraday's non-mechanical transient flow of electricity.

According to the second interpretation of induced current, [B], the magnetic field is rather an emanation of the magnet. The electric transient at the terminals of a coil is generated in response to a change of the magnetic flux Φ linked with it, that is $d\Phi \approx d(A\mathbf{B})$, where A is the area enclosed by the coil, and $\mathbf{B}$ is the flowing magnetic quantity. Whether we conceive of $\mathbf{B}$ as a real entity or not, the displacement of the magnet induces in the circuit a current I exactly as would connecting a battery: $U_K = -LdI/dt$, with $\Phi = LI$ and L the inductance of the wire loop.

2. ON J. CLERK MAXWELL'S INTERPRETATION OF FARADAYS EXPERIMENTS

Before discussing Maxwell's interpretation of Faraday's experiments [1] in more detail, we must remark that interpretation [B] suggests that the field denoted by $\mathbf{B}$ is a quite stationary emanation, while the transient current measured by a ballistic galvanometer, and equated to $U = \oint \mathbf{E} d\mathbf{l}$, is a sudden change of its flux through the circuit according to: $U_K = -\partial(A\mathbf{B})/\partial t$ [1]. The interpretation we whish to highlight, [C], comes considering that U_K signalises a not better identified reactive status of the magnet, which is also responsible for attraction of iron. To better explain interpretation [C] we call the current transient a measure of the magnet-coil coupling. Under this meaning, the

[1]While watching mutual induction coupling, it is difficult to unravel which one of two bodies is the most reactive one.

electric coupling is picked up by the coil without involving a change in the reactive state of the magnet[2]. The difference between [B] and [C] is that under interpretation [B] we assume a flux of energy so as to compensate the effective variation of the reactive state of the wiring, while in [C] the measure affects the wire without necessarily affecting the magnet. Maxwell introduces the magnetic induction field **B** as a pure mathematical quantity identical, save for the sign, to the measured potential drop across the receiver coil. Today we would write: $\mathbf{B} = -(\int U_K\, dt)/(n_j A)$, where $n_j = 1$ is the number of windings per unit length. Then he presents the electrotonic or resonating state of the magnet as a trigger for the observed transient. To avoid referring the trigger to a potential function[3], he puts the current impulse U_K directly in relation with the magnet's state. This way **B** becomes electrically measurable by induction, which would not occur if by coupling with the winding the electrotonic state of the magnet changed. Hence, Maxwell's reasoning looks rather in accordance with [C].

Here we are not concerned with the performance of the measurement of magnetization by induction, but just with the conceptual approach. For more than a thousand years, before Ørsted, the quality of a loadstone was measured exclusively by the mechanical attraction of iron pieces, or by the change of direction with respect to magnetic North of a magnetized needle mounted for example on a floating cork or on a pin. Ørsted's discovery drew upon the fact, that an electric wire connected to a battery changes the direction of a magnetized needle that is free to rotate as if it were a magnet. Following this discovery, distinctions have been made between inductive current and other types of currents[4]. In connection with this research, between 1878 and 1889, H. Rowland using a vertical plate condenser, could detect a convection effect when rotating, outside the two plates of the condenser, two dielectric discs with gold plated rings on their edges towards the condenser, and fitted with guard-rings [2]. To detect the electric convection he used a small astatic needle system, hanging with the lower needle symmetric with respect to the condenser. He measured the swing obtained by switching the condenser polarity. Now, differing from Ørsted's method, it seems that if the needle is stably deflected under the electric action, an electric force must be in equilibrium with the torque in the suspending wire. So it seems that a detectable electric effect involves an energy balance with a mechanical moment. We think on the other hand that this balance could be put equal to zero for all practical purposes. If ϑ_ℓ is the torque produced by a wire of radius r and length ℓ, the torsion of the wire at length ℓ from the fixed point is: $\vartheta_\ell = \xi(\ell/r)$ and is proportional to the angle of rotation ξ. If this satisfies Hooke's law, the shear stress τ is expressed by: $\tau_r = G\xi = G\vartheta_\ell(r/\ell)$, where G is the stiffness modulus. The polar torsion moment M_ℓ relative to the centre of the wire at distance ℓ:

$$M_\ell = \oiint ds\, \tau_\rho \rho = \vartheta_\ell/\ell G \int d\phi \int d\rho\, \rho^2 \rho = \pi/2\vartheta_\ell G r^4/\ell = \vartheta_\ell C_4 \tag{1}$$

As can be seen, the torque $\vartheta_\ell = M_\ell/C_4$ is proportional to the fourth power of the radius r, with the torsion constant C_4. Thus we can balance mechanically even exceedingly small effects, by reducing the diameter of the suspending wire. In order to compare the strength of convected charge against that of induction current, we have to convert electrostatic into electrodynamic units of measure. Therefore it seems that convection current is much fainter than magnetoelectric induction proper. We must however take account that most electric measurements are very feeble, if they are performed "electrostatically". It is the iron core included in the experimental layout, which makes tiny induction responses easier to detect to such an extent.

In Maxwell's time there were various theories as to the action of a permanent magnet or of an iron core winding. According to some, the orientation of material elementary magnets already exhibiting those characteristics ensures that bulk matter takes on a characteristic that is specific to the element Iron. According to others iron pieces parametrically amplify the electric effect. In any case, if there were no radical differences between the effects produced by an electromagnet and by a coil on its own, we could write that a current I generates the magnetic field according to Ampère: $\oint \mathbf{H} d\mathbf{l} = n/\ell I$, where n and ℓ are the number of windings and the length of the generator coil. However, in permanent magnets the induced magnetization always shows non-linear performance. Hence neither the behaviour of permanent magnets nor that of electromagnets can be described by

[2]Under a classical logic, we do not expect that the mere information on the status of a loadstone modifies its properties.

[3]In Maxwell's time scalar potentials were introduced substantially in order to deal more easily with physical quantities.

[4]It is not easy to propose such distinctions. For example D. Arago had proposed a magnetic rotation, that is, a magnetic effect due to rotation of an electrostatically charged ring. Faraday could demonstrate however that the earth's magnetism can generate electromagnetic currents in a rotating conductor. Hence Rowland used cut conductor rings.

Ampère's linear law. To remove all so called hysteresis effects, Maxwell reduces to the mere theory of coils. So no magnetization effects enter his theory anymore. Only the received electric signal is taken into account.

3. INDUCTION AT HIGHER FREQUENCIES

We considered above the equation in which Maxwell summed up the electric effect determined by the movement of a magnet, that is, the expression for current induction in a conducting loop. To measure the value of the induction **B** a ballistic galvanometer is used, given that by definition integration is performed over the whole impulse $\int d\Phi = L \int dI$. On the other hand today the evolution of the voltage drop V induced in the loop due to movement of a magnet or, for that matter, under changing load conditions of the primary winding, can be monitored in time. From a certain time τ on, both typically decrease as to $V =\mid V_\tau \mid e^{-\alpha t}$, in agreement with the theory of linear circuits. To justify this behaviour of inductance in circuits people attribute to the conductor a small series resistance R, so that $\alpha = R/L$. If the coefficients R and L in the differential equation are assumed real, the linear response from $t = 0$ on,

$$V(t) = \int_0^t dt' U(t') X(t - t'), \tag{2}$$

does not oscillate. Nowadays, the technical problem of tracing in time damped signals $V =\mid V_\tau \mid \cos[(\omega - \omega_0)t + \varphi]e^{-\alpha t}$ oscillating at the pulsation ω_0 of a local oscillator has been solved with the heterodyne using phase-locking. Hence we can tackle the problem of interpreting the wavy or periodic facets of those traces.

We recall that, whatever the electric system, its stationary linear response may be calculated in the complex number field by using the Laplace transform method of solution. In the "frequency" domain we have:

$$L[V(t)] = \int_0^\infty dt V(t) e^{-st} = v(s) = \chi(s) u(s) = \int_0^\infty dt' U(t') X(t - t') e^{-st'} \tag{3}$$

where $u(s)$ is the transformed input function, and $s = (\alpha + j\omega) \in \mathbb{C}$. By comparing with (2), we see that we are supposing $X(t - t') > 0$. Again the lower integration bound can be extended to $-\infty$ simply by multiplying U with a step function. Insofar as the initial conditions are taken to be zero, the transfer function $\chi(s) = v(s)/u(s) = \chi_{dispersion} - j\chi_{absorption}$ does thus satisfy the Kramers-Kronig relationships [3]. They may be written for instance as contour integrals:

$$\chi_{disp}(s) - \chi_\infty = \pi^{-1} CH \int_{-\infty}^\infty ds' \chi_{abs}(s')/(s' - s) \tag{4}$$

and

$$\chi_{abs}(s) = -\pi^{-1} CH \int_{-\infty}^\infty ds' [\chi_{disp}(s') - \chi_\infty]/(s' - s). \tag{5}$$

Now, if the impedance is an analytic function, i.e., $X(t) = \Sigma c_n (t - \tau)^n$, then no problems arise in putting the Kramers-Kronig relations together once again, i.e., $\chi(s) = (j2\pi)^{-1} \oint ds' \chi(s')/(s' - s)$. This integral is associated with a response $\chi(s)$ in the s-domain having one pole in the complex plane, whether $\omega = 0$ or not. The Lorentz-shaped curve associated to a second order differential equation keeps in turn its familiar meaning as a system's gain.

Now, relying on a contribution by Felix Bloch, it should be possible to recover a periodic-transient function by resorting to first order equations. His equations concern the response of paramagnetic or dielectric substances filling the coil of an LC-circuit, and put in a quite homogeneous magnetic field under suitable conditions. They are called phenomenological, because he represents magnetization per unit volume, attributing a collective property to the system of spins, while in general it is thought that a microscopic explanation is essential to understand what happens. Bloch's starting point is the transposition to magnetism of the heavy rotor equation in

agreement with the ansatz of Ampère:

$$d\mathbf{M}/dt = \gamma\mathbf{M} \times \mathbf{B}, \tag{6}$$

where γ is a positive or negative coefficient. According to this vectorial equation which, as the corresponding mechanical one, can be geometrically visualised with Poinsot's cones, $\mathbf{M}$ precedes around the direction of $\mathbf{B}$ with an angular velocity $\boldsymbol{\omega}_B$. Using that representation it is possible to obtain a kinematical transformation for any rotating reference frame. The precession component can thus be separated from the total time derivative. Its differential operator symbol is: $d/dt - \boldsymbol{\omega}\times = \partial/\partial t$. When the selected rotating frame is stationary with respect to the direction of $\mathbf{M}$, so that $\partial\mathbf{M}/\partial t = 0$, the whole t-dependence is displayed by $\boldsymbol{\omega}$, the motion is periodic, and the vectorial relationship $\mathbf{B} = -\boldsymbol{\omega}_B/\gamma$ holds in particular. According to dynamics, in the non inertial $\mathbf{M}$-fixed frame a fictive force exactly balances the applied one. Hence a small force $\mathbf{B}_1 \equiv -\boldsymbol{\omega}_1/\gamma$[5] continuously applied to $\mathbf{M}$ in the frame attached to it, may be enough to produce any additional deflection from the direction of the effective $\mathbf{B}$. If $\boldsymbol{\omega}$ is the angular velocity of $\mathbf{B}_1$ around $\mathbf{B}$ in the laboratory frame, a condition $\mid \boldsymbol{\omega}_1 \mid = \mid \boldsymbol{\omega} - \boldsymbol{\omega}_B \mid$ can be stated. In the explanation of the electric phenomenon by analogy with the mechanical behaviour, this condition is the requisite of a periodic electromagnetic field to appreciably affect magnetization, as evaluated by the received electric signal. It can be seen that the modelling transposition of the rotator to electric circuits allows a discussion of periodic electrical behaviour using a geometrical picture, to introduce Bloch's constant angular velocity $\boldsymbol{\omega}_B$[6] When transposing the equation Bloch further hypothesises, as not done in mechanics when considering frames in relative motion, that the initial magnetization relaxes in time to a value $\mathbf{M}_0$ reaching thermal equilibrium with the lattice[7] [4]. Adding the magnetization decay to the geometric transformation, the vectorial first order Equation (6) becomes:

$$\partial\mathbf{M}/\partial t = \gamma\mathbf{M} \times (\mathbf{B} + \boldsymbol{\omega}/\gamma) + \alpha(\mathbf{M} - \mathbf{M}_0) = \mathbf{M} \times (\boldsymbol{\omega} - \boldsymbol{\omega}_B) + \alpha(\mathbf{M} - \mathbf{M}_0). \tag{7}$$

Lenz's statement about the non-mechanical actions of $\mathbf{B}$ was dismissed by arguing that at the microscopic level electricity carriers perform a mechanical motion. Thus, there would be no need to introduce a decaying term, and the Ampère's expression (6) could be already considered an exhaustive alternative to Faraday's induction law.

4. FREE INDUCTION AS A TRANSIENT RECORD OF RESONATING STATES IN BULK MATTER

By virtue of the undamped vibrating string equation an electric system with no externally applied stimuli is periodic at any frequency, because normal modes are determined only by further imposing boundary conditions on it. Actually all electrical experiments seem to agree on the need to connect a substance to a low-loss cavity to elicit stationary electric oscillation conditions, that is resonance. Furthermore, according to the literature, resonance is a forbidden gap for propagation of radiation. Nevertheless to obtain experimentally steady, nearly coherent irradiation an active means must be triggered, that can couple with its cavity once steadily excited. Again, many explanations have been given of the reasons for the decay of the periodical pattern under resonating conditions. In order to pick up many free echoing signals broadcast from an unfeeded system the receiver circuit must have a narrow band-pass filter tuned and matched at the expected resonance frequency of the cavity. We have tried to show that what is transient according to Maxwell's formulation, is not the state of the active means, but its coupling. Now, under resonance conditions the active material is coupled to its resonator, but this is not the directly measured coupling indeed; and it could be that while the activated means inside a high finesse resonator is left on its own, and until the entire system does not irradiate (or undergo other changes), there would be no appreciable decay of this coupling. In fact it is the transfer of power to the load — in our case the tuned receiver — that is maximised under matched reception conditions. This can spoil the resonating system, of course. But a receiver Q-factor much higher than is usual in mechanical and acoustic applications is compatible with power transfer effectively nil, which we call a signal. Finally, the resonating conditions exhibit neither linear nor periodic features. Therefore the angular frequency of rotation

[5] In this context this is a mere mathematical statement.

[6] The Larmor frequency $\boldsymbol{\omega}_L = -e/2mc\mathbf{B}$ (esu) may be obtained by assuming that an electron –e rotating around a nucleus in the reference system of the nucleus is subject to the Lorentz force $\mathbf{K} = -(e/c)\mathbf{v} \times \mathbf{B}$, and that this electrodynamic force is in equilibrium with that in the rotating system $\mathbf{K}_{\boldsymbol{\omega}} = m\{\boldsymbol{\omega} \times \boldsymbol{\omega} \times \mathbf{r} + \mathbf{2v}' \times \boldsymbol{\omega}\} \approx 2m\mathbf{v} \times \boldsymbol{\omega}$ (Coriolis force), where the precession velocity $\mathbf{v}'$ is approximately equal to $\mathbf{v}$.

[7] Bloch takes account of relaxation using two different time constants.

$(\omega - \omega_0)$ by which a damped oscillation differs from pure exponential decay in the induction equation at non-zero frequency as we have assumed, is determined by the nominal frequency of the local oscillator, as well as by the matching conditions to the probe of the tuned receiver. A perfectly stationary coupling condition to the receiver at ω_0 would be indistinguishable from a baseline. To us it seems, as we have tried to show, that Rowland was in a condition to detect a signal. So was Faraday.

5. CONCLUSION

The theory Maxwell gave of Faraday's magneto electric induction is as simple as the signal received from any complex phenomenon, like magnetism, can be. Using his electromagnetic representation of electrical phenomena it is assumed — we believe — that induction decay is not a jerky phenomenon such as lightning might be, but powerless.

The above interpretation [C] presents the induction law equation as an electric signal received by the wire. A rising coupling between the receiving circuit and the magnet is accountable for the effect that Faraday discovered. More generally, magnets can be replaced by whatever other object capable of coupling. It is the coupling, not the magnet, that is under investigation. Its measure is given by the transient excitation of the receiver.

Coupling, in the meaning used here, is a relatively new concept in science. It offers a way to understand phenomena that apparently defy explanations based on the cause and effect paradigm.

REFERENCES

1. Maxwell, J. C., *A Treatise on Electricity & Magnetism*, Vol. 2, Dover Publications Inc., New York, 1954.
2. Rowland, H. A. and C. T. Hutchinson, "On the electromagnetic effect of convection-currents," *Phil. Mag.*, Vol. 27, No. 5, 445–460, 1889.
3. O'Donnell, M., E. T. Jaynes, and J. G. Miller, "Kramers-Kronig relationship between ultrasonic attenuation and phase velocity," *J. Acoust. Soc. Am.*, Vol. 69, No. 3, 696–701, 1981.
4. Abragam, A., *The Principles of Nuclear Magnetism*, Oxford University Press, Oxford, 1961.

Analytical Solutions to the Applicators for Microwave Textile Drying by Means of Zigzag Method

M. Pourová and J. Vrba

Department of Electromagnetic Field, Faculty of Electrical Engineering, Czech Technical University
Technická 2, 166 27 Prague 6, Czech Republic

Abstract— This paper described the Zigzag method for solving microwave applicators for drying of textile materials, which is based on the solving transfer characteristics of waveguide with discontinuities. We can describe the wet textile as discontinuity by means of three quantities: the size of reflection coefficient $|\rho|$, its phase angle φ and phase angle ψ of transmission coefficient τ. The size of the transmission coefficient is defined by known relation $\tau\tau^* = 1 - |\rho|^2$ which results from the principle of conservation of energy. We created diagram of EM waves inside this structure and reached the resulting expression, which is used for calculation of electric field strength in the plane of drying textile. This quantity depends on electrical characteristics of wet textile such as permittivity and loss factor. Measurements of these dielectric properties for the coburg is complicated and this method makes it possible to solve our problem with dielectric parameters. We can also describe the absorbed power in the textile in dependence on the dielectric properties.

1. INTRODUCTION

In order to analyze microwave circuits we need to know mainly transmission capacity of microwave lines. In this paper we shall focus in particular on the problems of waveguides with discontinuities and applied for the evaluation of the effect of material which we want to dry by microwave energy in the waveguide transmission line.

If we create one or more discontinuities in the waveguide, we can induce the reflection of the desired size by them or contrary to compensate the reflection from another waveguide part. In both cases there originate standing waves in the waveguide section of the specific length. Suppose that only the dominant mode is propagating in the line. In addition to the deformation of the field the reflected wave will appear in the transmission line due to waveguide discontinuity. The field distortion can be explained by creating higher-order modes which are exponentially absorbed with increasing distance from the place of discontinuity.

The character of discontinuity can be described by means of three quantities: the size of reflection coefficient $|\rho|$, its phase angle φ and phase angle ψ of transmission coefficient τ. The size of transmission coefficient is defined by a known relation $\tau\tau^* = 1 - |\rho|^2$ which results from the principle of conservation of energy. The discontinuity can also be described by the equivalent circuit which produces reflected and transmission wave with the same values of ρ and τ. It is essential to know accurate distribution of fields at the point of discontinuity to determine the parameters of equivalent circuit elements of discontinuity. Deformed field in case of discontinuity can be analytically expressed by means of such suitable infinite series that satisfy Maxwell equations with appropriate boundary conditions. Every member of series can usually be interpreted as a "mode". The excited higher-order modes generate a perturbation which evokes the phase shifts differences in both reflected as well as transmission wave and the result is transformation of impedance at the point of discontinuity. From practical point of view the waveguide or line should transfer energy. At a greater distance from discontinuity this transfer is accomplished by propagating mode. Therefore, we can only consider the influence of discontinuity on this mode. It is important to know the distribution of the far electromagnetic field if we need to determine parameters of equivalent circuit elements [1, 2].

2. ANALYTICAL MODEL OF RESONANT APPLICATOR

We used the Zigzag method to calculate electric field intensity in a microwave drying applicator. The applicator (Fig. 1) consists of a waveguide segment which is ended by a funnel antenna. This part is used as a holder for magnetron which is regarded to be a source in first part of the analysis. Next part of the applicator is formed by two parallel metal conductive plates, between which there is moving textile right at the place with the maximum standing-wave which occurs between the plates. This part of a system has character of transmission line.

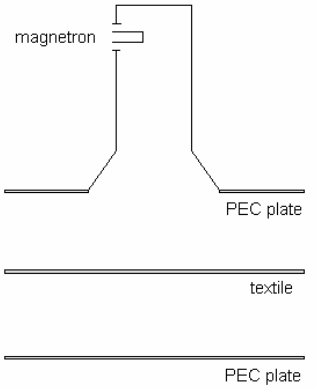

Figure 1: Basic scheme of the open-resonator type applicator.

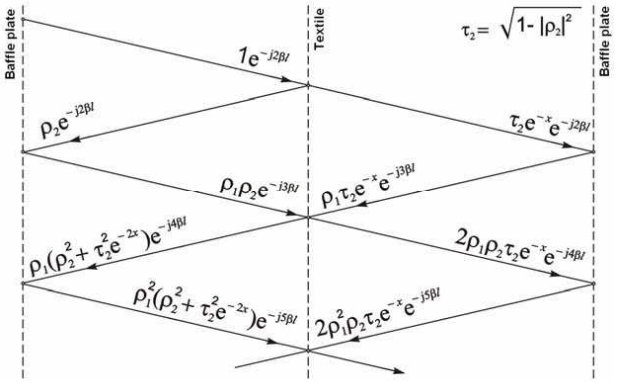

Figure 2: Chart of multiple reflection on the discontinuity of transmission line.

In this structure also occurs a multiple reflection and in this case the discontinuity is formed by the wet textile. Fig. 2 depicts how the individual parts of incoming wave are reflected [3].

To tune and optimize described applicator (Fig. 1) we have to reach the maximum electric filed strength in the plane of dried textile. Working with chart (Fig. 2) we will arrive to the resulting expression

$$E\left(l,\rho_2,\alpha_{tex}\right) = \sum_{n=0}^{\infty} \rho_1^n \left(\rho_2 + \tau_2 e^{-x}\right)^n \cdot e^{-j\beta l(l+2n)} \tag{1}$$

where is ρ_1 — reflection coefficient of metallic plate, ρ_2 — reflection coefficient of textile, $\tau_2 = \sqrt{1-\rho_2^2}$ — transmission factor, $e^{-x} = e^{-\alpha_{tex}\cdot t}$ — component which represent absorption in textile, α_{tex} — attenuation factor of textile, β — phase constant of free space, l — distance between reflective plate and textile.

Parameters ρ_2 and α_{tex} are given by dielectric properties of textile therefore we can write electric field strength dependent on relative permittivity ε_{tex} and loss factor $\tan\delta_{tex}$ as follows

$$E\left(l,\varepsilon_{tex},\tan\delta_{tex}\right) = \frac{e^{(j\beta l+\alpha_{tex}\cdot t)}}{e^{(\alpha_{tex}\cdot t+2j\beta l)} - \rho_1\rho_2\cdot e^{\alpha_{tex}\cdot t} - \rho_1\cdot\sqrt{1-\rho_2^2}}. \tag{2}$$

Some examples of application of this equation are given in Fig. 3. We can use the Equation (2) for schematic description of behaviour resonant applicator and effect of the textile on the applicator resonance. In Fig. 3(a) is a chart of dependence of electric field strength on distance l for the case

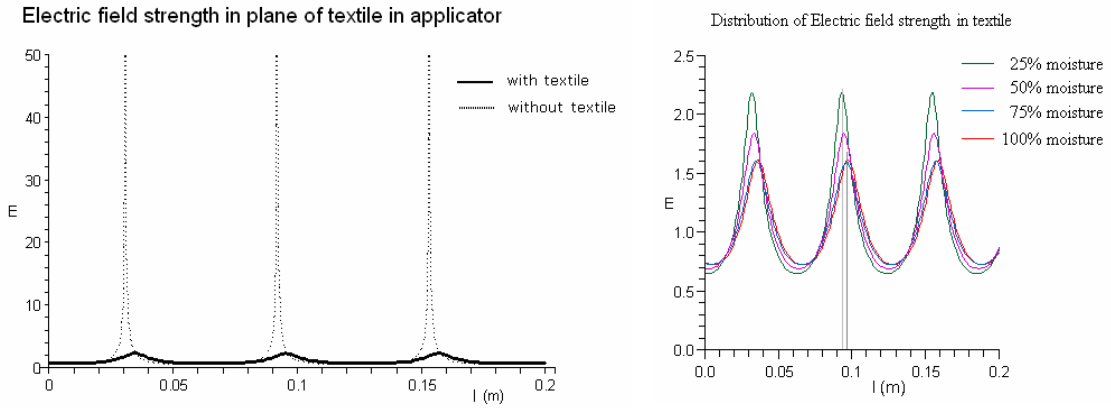

(a) (b)

Figure 3: Electric field strength in dependence on. distance l for case of resonator without textile (high peaks) and with a sample of wet textile (a) and electric field strength in dependence on distance l and content moisture (set of parametric curves) (b).

of resonator without a textile (high peaks) and with a sample of wet textile (attenuated peaks). Fig. 3(b) represents the chart of dependence of electric field strength on distance l for the case four different volumes of moisture. We can see that the distance of parallel plate and textile is changed in dependence on content of moisture.

During the drying process quantity of water in textile is changing. Relative permittivity and loss $\tan\delta_{tex}$ factor are decreasing with decreasing water content. As can be seen in Fig. 4(a), with decreasing permittivity electric field strength in the textile increases and position of its maximum does not change. This finding is very important. During drying process permittivity of textile decreases and thanks to increase of electric field strength and efficiency of drying does not decrease so quickly. In Fig. 4(b) we can observe dependence of electric field strength on distance l and loss factor (ε_{tex} is constant). We can see that due to $\tan\delta_{tex}$ electric field strength does not decrease significantly but changes position of its maximum value.

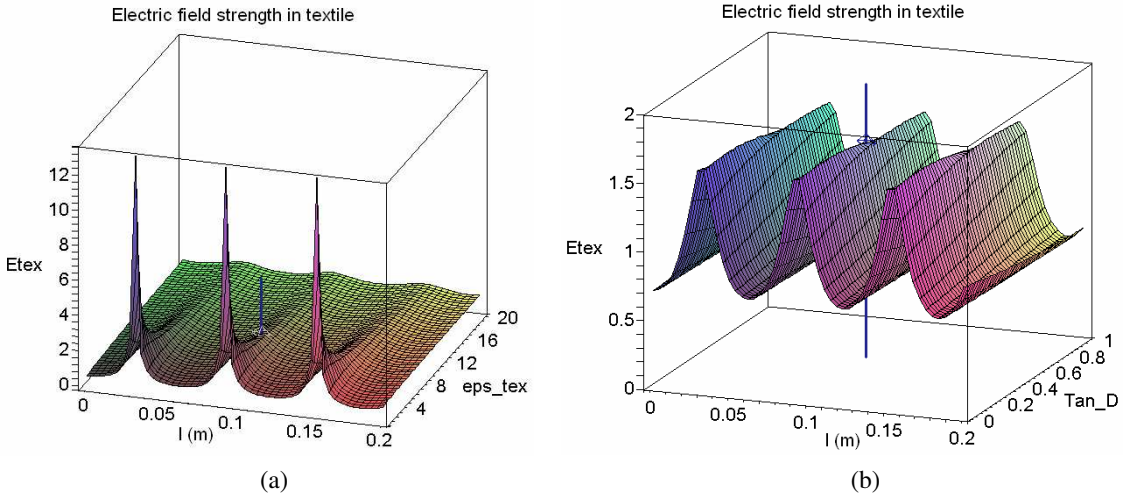

Figure 4: Dependence of electric field strength on distance l and relative permittivity $e_{tex}(\tan\delta = 0,566)$ (a), Dependence of electric field strength on distance l and loss factor $\tan\delta_{tex}(\varepsilon_{tex} = 8)$ (b).

3. ANALYTICAL SOLVING OF WAVEGUIDE APPLICATOR

Waveguide applicator is waveguide with a longitudinal slot in wider side of waveguide. This slot is situated in the middle of this side, because maximum of electric field strength is here. Waveguide proportions choose so as to dominant mode TE_{10} could spread only inside to waveguide on working frequency. Waveguide applicator is displayed on the Fig. 5. Working frequency of waveguide is 2.45 GHz.

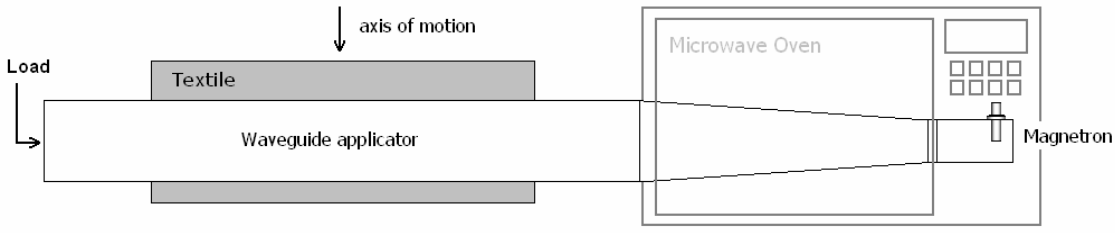

Figure 5: Waveguide-type applicator for drying of textile.

Very important property is ability of textile absorbed microwave energy. We can describe the wet textile like loss dielectric with dielectric properties. Then we can used the equation for absorbed power in dielectric materials

$$P_{ab}\left(\varepsilon_{tex}, \tan\delta_{tex}\right) = \frac{1}{2}\sigma \iiint\limits_{V} |E_y|^2 dV, \tag{3}$$

where is E_y electrical intensity of dominant mode TE_{10}.

Solving of the Equation (3) we can obtain dependence of absorbed power on the different parameters. In the Fig. 6(a) we can see dependence on the both dielectric parameters. Fig. 6(b) illustrates dependence on the thickness of the textile and its permittivity.

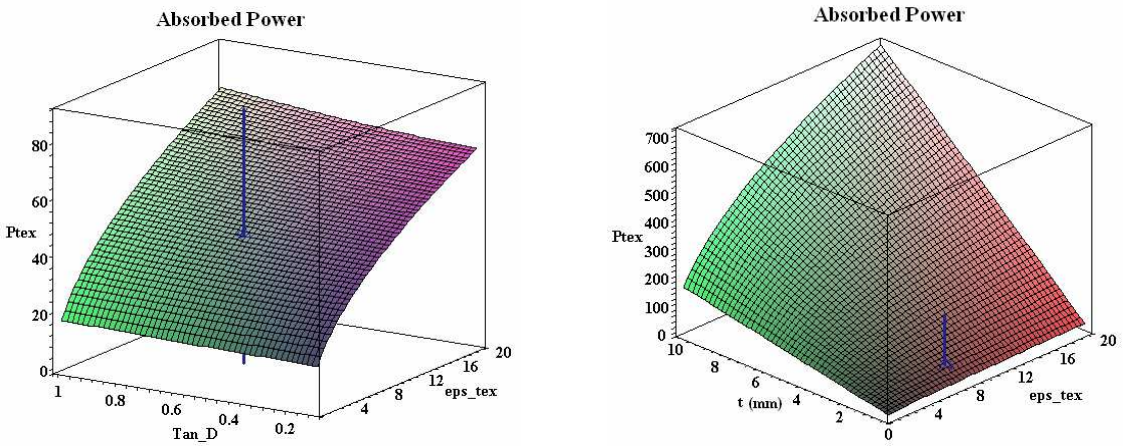

(a) (b)

Figure 6: Dependence of absorbed power on dielectric properties $\tan\delta_{tex}$, ε_{tex} (a), dependence of absorbed power on thickness t and relative permittivity $\varepsilon_{tex}(\tan\delta = 0,566)$ (b).

4. CONCLUSION

We used the Zigzag method for analysis microwave applicators for drying of textile materials, which is based on the solving transfer characteristics of waveguide with discontinuities. The results of the analysis show the dependence of electrical field strength on the several parameters. We described how to change the electrical field strength in dependence on the wet textile inside applicator. Measurements of the dielectric properties of the wet textile materials are complicated and this method makes it possible to solve our problem with dielectric parameters. We have shown the absorbed power in the textile in dependence on the dielectric properties and thickness of the drying materials.

ACKNOWLEDGMENT

This work has been supported by the Czech Grant Agency under grant 102/03/H086 Novel Approach and Coordination of Doctoral Education in Radioelectronics and Related Disciplines.

REFERENCES

1. Tysl, V. and V. Růžička, *Theoretical Principles of Microwave Technique* (in Czech), ISBN 80-03-00141-2, SNTL — Press of technical literature, Prague, 1989.
2. Vrba, J., *Measurement on the Centimetres Waves* (in Czech), NADAS, Prague, 1978.
3. Pourová, M., "Transmission characteristics of waveguide with discontinuities," *Modeling of Fields-Doctoral Grant of the Grant Agency of the Czech Repuclic 102/03/H086 "New Approach and Coordination of Doctoral Education in Radio-Electronics and Related Disciplines"*, 170–176, ISBN 80-86582-19-1, IEEE Czechoslovakia Section, Praha, 2006.

Modal Analysis of Miniature Microstrip Patch Antennas Based on Fractal Geometry

P. Hazdra and M. Mazanek
Department of Electromagnetic Field, FEE, Czech Technical University in Prague
Technicka 2, Prague 166 27, Czech Republic

Abstract— The paper deal with the fractal microstrip patch antennas with specific properties based on rearrangement of current densities on their surface by means of special fractal geometrical modifications. Description of physical behavior via surface current distribution and radiation properties is discussed. Different modal analysis approaches (cavity model and the Theory of characteristic modes) as well as full-wave simulations have been used for the simulations.

1. INTRODUCTION

Modal (eigen) solutions are being widely used in many physical areas (i.e., vibration of bridges, solving of acoustic resonators etc.). Cavity model for microstrip patch antennas introduces an antenna example [1]. Since the cavity model is very fast, some simplifications are introduced, i.e., no internal coupling is accounted in [2]. Very general approach is so-called Theory of Characteristic Modes (hereafter noted as TCM), invented in 70's by Harrington and Mautz [3]. Although the TCM can provide very usefull physical information about radiation of a given structure, it has been quite forgotten for years. In general, modal solution is obtained as set of eigen-currents (or more generally eigen-fields) which are independent of feeding together with corresponding eigen-numbers. Because of the Method of moments (MoM) framework, all the couplings through the radiation are taken into account, in contrary to the cavity model. Planar fractal structures are known to may have specific and interesting properties in terms of its modal fields. Plenty of such structures (especially those which involve slots) exhibit special surface current distribution leading to decreasing of its fundamental mode resonant frequency.

2. MODAL METHODS, CAVITY MODEL

The simplest approach to study microstrip patch antennas is to treat them as a 2D planar resonator lying say in the XY plane. We therefore assume that:

- height of the patch above the ground plane is small thus only one component of the electric field (E_z) is dominant, the others are omitted
- there is no fringing field at the boundary of the patch (i.e., the height of the patch above the ground is small). This condition results in Neumann boundary condition for electric field $\partial E_z/\partial n = 0$, where n is the outer normal to patch's boundary.
- there is no feeder connected to the antenna, we are interested only in the eigen-behaviour.
- no internal coupling is assumed

Under the assumptions above we are now able to write down the scalar Helmholtz wave equation with the Neumann boundary condition $\partial E_z/\partial n = 0$ (this represents the ideal PMC boundary), where n is the outer normal to patch's boundary:

$$\Delta_t E_z + k^2 E_z = 0 \tag{1}$$

and solve the PDE (usually employing FEM) for the set of eigenfields $E_{z,n}$ and eigenfrequencies

$$f_n = \frac{c_0 \cdot k_n}{2\pi\sqrt{\varepsilon_{reff}}}, \tag{2}$$

where $k_n^2 = \lambda_n$ are eigenvalues. Magnetic field (which is proportional to the surface current density $\boldsymbol{J}$ flowing on the patch) is then obtained as a gradient of the calculated electric field:

$$\vec{H} = \frac{1}{j\omega\mu_0}\vec{z}_0 \times \nabla E_z \tag{3}$$

3. MODAL METHODS, CHARACTERISTIC MODES

The main framework for the TCM is well-know Method of Moments (MoM) [4], EFIE (Electric Field Integral Equation) is usually considered:

$$\left[\mathbf{L}\left(\mathbf{J}\right) - \mathbf{E}^{i}\right]_{\tan} = 0, \tag{4}$$

where $\mathbf{E}^i$ is incident electric field intensity, $\mathbf{J}$ induced current density and operator $\mathbf{L}$ is defined as:

$$\mathbf{L}(\mathbf{J}) = j\omega\mathbf{A}(\mathbf{J}) + \nabla\phi(\mathbf{J}), \tag{5}$$

where $\boldsymbol{A}$ and Φ are magnetic vector and scalar potential respectively; operator $\boldsymbol{L}$ has the dimension of impedance

$$[\mathbf{L}(\mathbf{J})]_{\tan} = Z(\mathbf{J}). \tag{6}$$

So far, this is the standard EFIE integral equation which is then solved by the MoM method at given frequency, resulting in complex impedance matrix $[Z] = [R] + j[X]$.

The characteristic modes are afterwards calculated by modal decomposition of the $[Z]$ matrix, the operator matrix equation has the following form (weighted eigenvalue equation):

$$[X]\mathbf{J}_n = \lambda_n[R]\mathbf{J}_n. \tag{7}$$

The above mentioned equation could be solved i.e., by using standard methods in MATLAB (eig function).

Modal solution has the form of (theoretically) infinite number of real eigencurrents $\boldsymbol{J}_n$ and their associated eigenvalues λ_n.

Characteristic currents $\boldsymbol{J}_n = (J_{nx}, J_{ny}, J_{nz})$

- Are defined as the eigenfunctions of a weighted eigenvalue Equation (7)
- Are real or equiphasal over the surface on which they exist
- Form an orthogonal set over this surface
- Depend only on shape and size of the given structure and are independent of any specific source of excitation.

Characteristic numbers (eigenvalues) λ_n

- Are real eigenvalues associated to characteristic modes that determine the relative dominance of the mode
- These eigenvalues bring information about resonance, bandwith, radiation properties (radiation Q)
- $\lambda_n = 0 \ldots$ mode $\boldsymbol{J}_n$ is at resonance
- $\lambda_n < 0 \ldots$ mode $\boldsymbol{J}_n$ has a capacitive contribution
- $\lambda_n > 0 \ldots$ mode $\boldsymbol{J}_n$ has a inductive contribution
- The closer to zero an eigenvalue is, the more resonant the associated characteristic current is

Instead of λ_n, so-called characteristic angle α_n constitute an alternative to represent the variation of eigenvalues with frequency:

$$\alpha_n = 180^\circ - \tan^{-1}\left(\lambda_n\right) \tag{8}$$

For characteristic angle representation, the resonance occur when $\alpha_n = 180^\circ$. Furthermore, the slope of α_n at 180° determines the radiation Q of the mode.

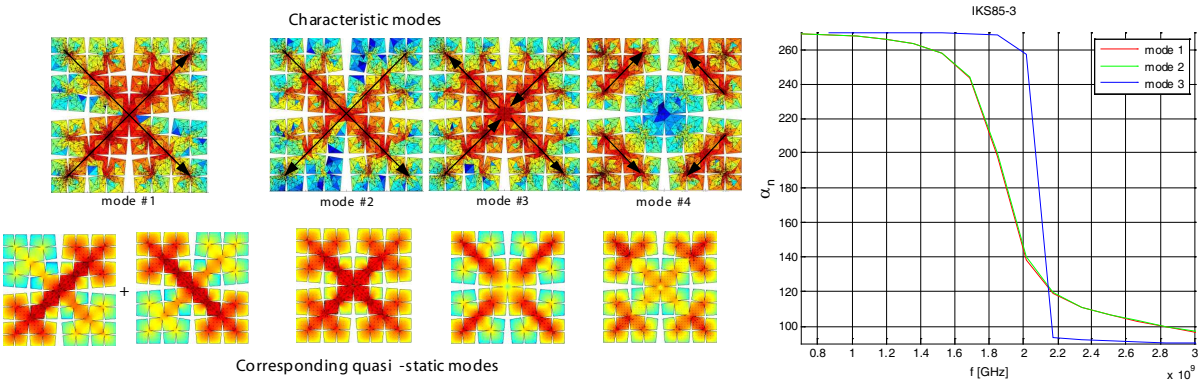

Figure 1: Surface currents obtained by the Cavity model and TCM (left), eigenangles behavior with frequency (right).

4. FRACTAL GENERATORS

So far, two different fractal generators were developed, using both L-System and IFS algorithms. They are connected with the cavity model and TCM analyzers, under the MATLAB framework. First example show modes of so-called IKS3-85 (Inverted Koch Square of iteration 3 and indentation angle 85°, [2]) fractal microstrip patch antenna (see Fig. 1) calculated by both methods. Patch dimensions are 37.5×37.5 mm. Arrows indicate main current paths, which are in quite good agreement with the solution obtained by quasi-static (cavity model) modal method.

From the characteristic angle behavior (Fig. 1.) it is observed that first mode resonates (α_1 passes 180°) at 1.9 GHz. Surprisingly, this mode has two in-phase current paths (in fact it could be understood as a superposition of two perpendicular modes), so one main-lobe broadside radiation pattern is expected. Moreover, electrical size of the patch at this fundamental mode is $0.225 \times 0.225\lambda$, that is quite good size reduction when compared to classical "$\lambda/2$" unperturbed patches. To proof that, full-wave simulation was performed, using CST-MWS. To excite the fundamental mode, proper feeding should be employed; in our case, an L-probe parralel to patch's edge was used (see Fig. 2). GIL-GML1000 ($\varepsilon_r = 3.05$) substrate $t = 1.55$ mm thick is placed under the metallic patch. Parameters L_h and L_v were determined by optimalization. Simulated directivity is 7.8 dBi, $f_0 = 1.8$ GHz, BW = 3.3% for VSWR = 2.

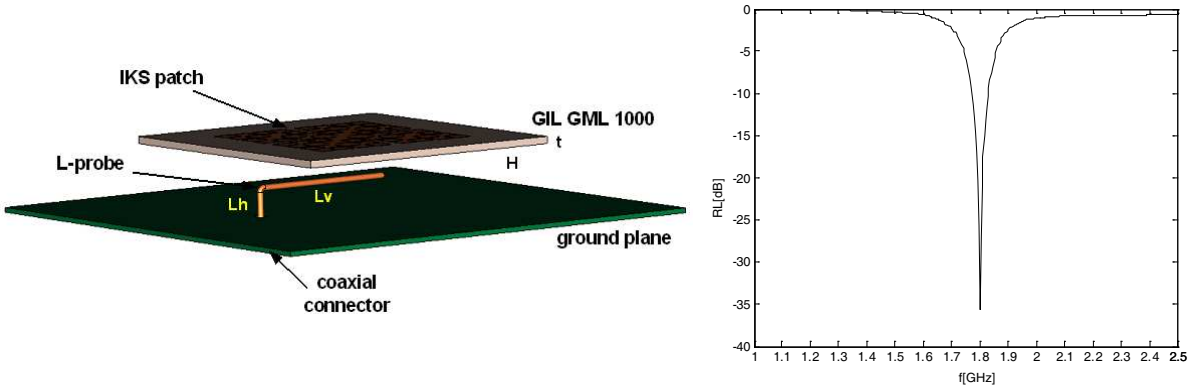

Figure 2: Layout of the IKS3-8 with finite ground plane and the L-probe feed and Return loss behavior.

Another study was aimed on resonant frequency of the fundamental mode variations with changing fractal iteration of the antenna but keeping occupied area constant. Characteristic mode analysis reflects that with increasing fractal iteration the fundamental mode frequency decrease dramaticcaly, see Fig. 3.

Second example is "Self-affine fractal antenna" (SAF) described in [5], see Fig. 4. Its structure was easily created with our IFS fractal generator, namely the SAF-3 (3th fractal iteration) sample was used for modal simulations. First few modes were analyzed both with the Cavity model and the TCM. Surface current densities for first two modes and both methods are shown at Fig. 4. Resonant

frequencies calculated with cavity model were $f_1 = 2.3\,\mathrm{GHz}$ and $f_2 = 4.0\,\mathrm{GHz}$. Compared with TCM, where $f_1 = 1.85\,\mathrm{GHz}$ and $f_2 = 4.4\,\mathrm{GHz}$ (red and green curves at Fig. 4 right), differences aren't crucial.

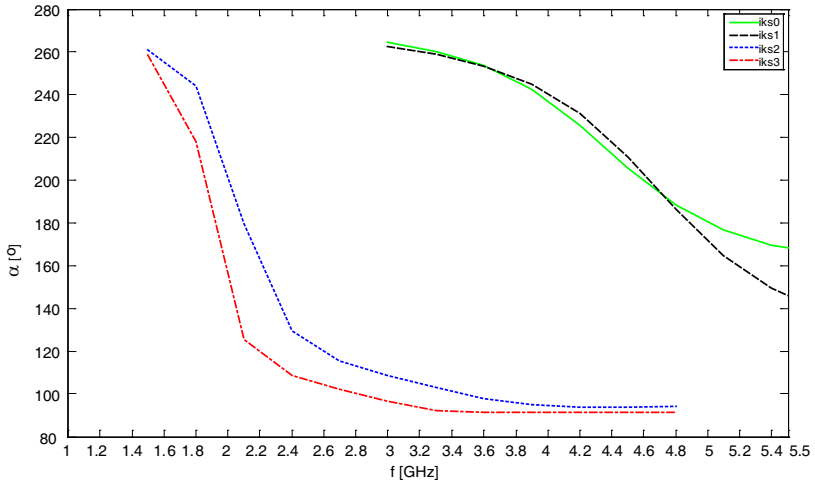

Figure 3: Characteristic angles of the fundamental modes vs. fractal iteration.

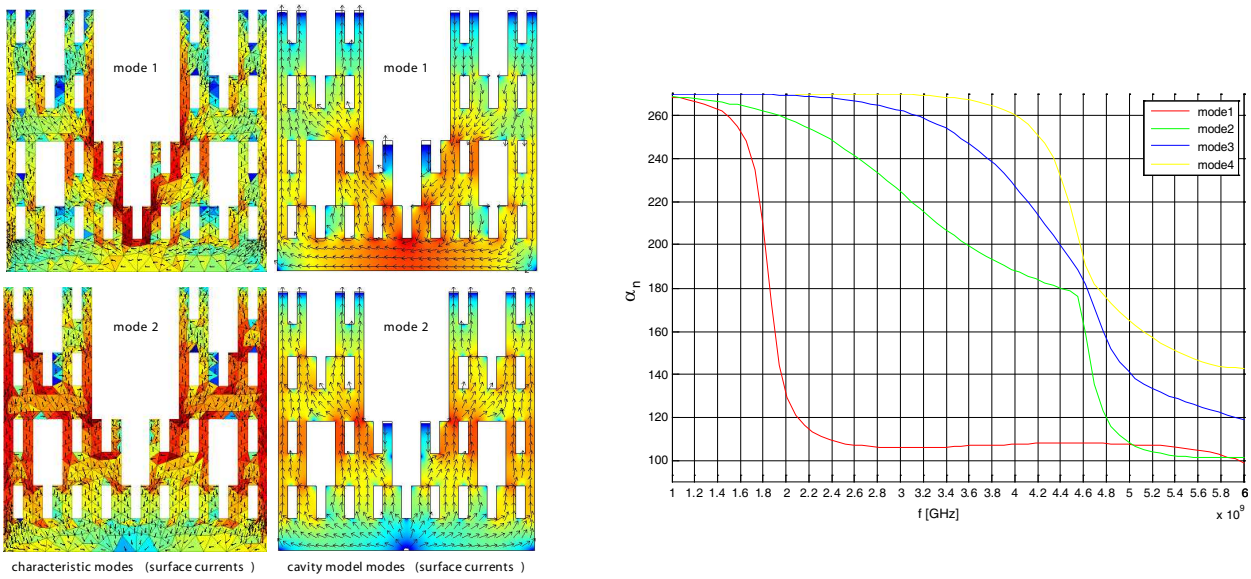

Figure 4: First two modal currents on SAF-3 calculated with both modal methods and characteristic angle behavior with frequency for SAF-4.

5. CONCLUSION

Paper discussed two modal methods utilizable for simulations of microstrip patches. Both approaches were implemented in MATLAB environment and connected to developed fractal generators. Modal analysis is very useful for getting deeper physical insight of fractal microstrip patch antennas behavior. Fast cavity model could be used for quick estimation of current shapes and resonant frequencies and then slower (but more accuracy and catching more informations) Theory of Characteristic Modes analysis follows.

ACKNOWLEDGMENT

This work has been supported by the Antenna Centre of Excellence (ACE-2) and by the Czech ministry of Education Youth and Sports in the framework of the project Research in the Area of Prospective Information and Navigation Technologies MSM 6840770014.

REFERENCES

1. Bahl, I., P. Bhartia, and R. Garg, *Microstrip Antenna Design Handbook*, Artech House, 2001.
2. Hazdra, P. and M. Mazanek, "The miniature fractal patch antenna," *Radioelektronika 2005 — Conference Proceedings*, 215–218, Brno, VUT FEI, Ústav radioelektroniky, 2005.
3. Harrington, R. F. and J. R. Mautz, "Theory of characteristic modes for conducting bodies," *IEEE Trans. AP.*, Vol. AP-19, No. 5, 622–628, Sept. 1971.
4. Makarov, S. N., *Antenna and EM Modeling with MATLAB*, Wiley, 2002.
5. Sinha, S. and M. Jain, "A self-affine fractal multi-band antenna," *AWPL, IEEE Xplore*.

Algorithm for Noise Reduction in Output Signal of Race-track Core Fluxgate

M. Butta[1], **P. Ripka**[1], **and J. Kubík**[1,2]

[1]Department of Measurement, Czech Technical University, Technická 2, Praha 166 27, Czech Republic
[2]Tyndall National Institute/MAI, Lee Maltings, Prospect Row, Cork, Ireland

Abstract— The investigation of new algorithm for noise reduction in fluxgate output signal is presented in this paper. Noise measurements have been performed on the output signal of the race-track core fluxgate. The measured noise was decomposed into the harmonic components of the excitation frequency, each having random amplitude and phase. A strong correlation between these harmonic components is clearly shown from their variation in time. The algorithm for noise reduction is proposed based on this key feature of the noise. The algorithm is based on the proper linear combination of even harmonics in order to obtain effective suppression of the noise. This is possible due to the fact that the signal-to-noise ratio is not the same at different harmonics.

1. INTRODUCTION

The algorithm presented in this paper has been developed for a race-track core fluxgate developed by Jan Kubík [2]. The core of the fluxgate is etched from 25 micrometers sheet of amorphous soft magnetic material VITROVAC 6025X kindly supplied by Vacuumschmelze Hanau. The core is contained in a four layer PCB; on the PCB are also printed the paths used as excitation and detection coil. The whole sensor is less than 1 mm thick. For this work both excitation and detection coil are connected in series, giving as a result a whole coil used to excite the core uniformly all over its length. An external detection coil is then wire wound around the PCB [Fig. 1].

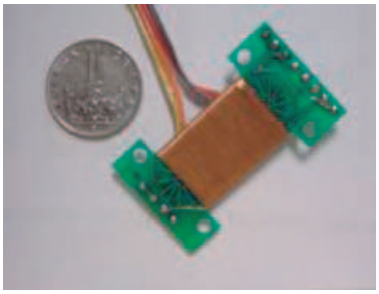

Figure 1: Race-track core fluxgate [2].

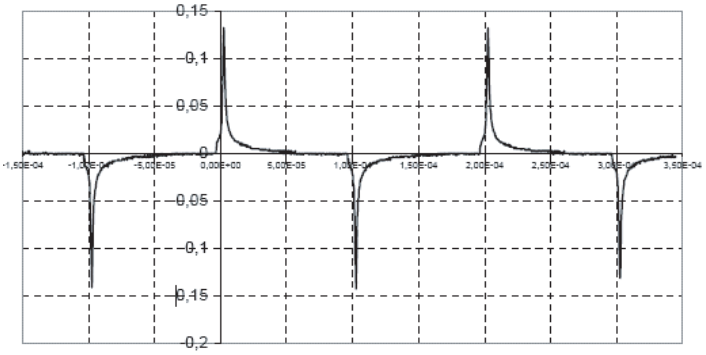

Figure 2: Excitation current, 250 mA pk-pk, 5 kHz.

We used narrow current pulses to saturate the core, in order to achieve low power consumption. Fig. 2 shows the excitation current measured with a current probe and an oscilloscope, when the amplitude of the current is 0.25 A peak-peak, and the frequency 5 kHz.

2. NOISE MEASUREMENT SET-UP

The first step of this work was an accurate measurement of the noise of the output voltage of the detection coil. The sensor was inserted into a six-layer magnetic shielding and the voltage induced in the detection coil was sampled with high resolution digitizer NI 5911. The digitizer and the board which provides the excitation current, were properly synchronized, in order to avoid asynchronous sampling. The anti-aliasing filter has been characterized, so that we could take into account only the frequencies of the noise measured in the flat range of its transfer function. The measured data were acquired by a PC and further numerically elaborated. Numerical computation was performed on the data sampled from the output voltage, and the even harmonics were obtained.

This method, based on digitizing of the signal, has a big advantage with respect to the classical extraction of the even harmonics performed with a lock-in amplifier. Indeed in this way we can

measure all the even harmonics (up to the limit imposed by the sampling frequency) at the same time. The same result would require excessive complex measurement set-up, when performed with lock-in amplifier.

Special care was taken about the reliability of the noise measurement. Comparison between the noise level measured during a day and during a night time has shown that there were no remarkable differences. Therefore we can rely on the shielding ability to remove the noise of the environment, which is well known to change during a day. Moreover, the noise of the other devices included in the measurement set-up was measured and proved to be negligible with respect to the noise of the sensor. Finally we compared the obtained amplitude of the noise of the second harmonic, with the same value measured with traditional lock-in amplifier. Both values proved to be similar. Therefore we can derive that this method provides reliable noise measurement of all of the even harmonics simultaneously.

3. NOISE FEATURE

Figure 3 shows the amplitude of the first 20 even harmonics, changing during the time. Basically, the output signal was numerically processed for several consecutive periods, and for each period the value of the even harmonics was computed. The series of these values gives as a result the evolution of the even harmonics in the time.

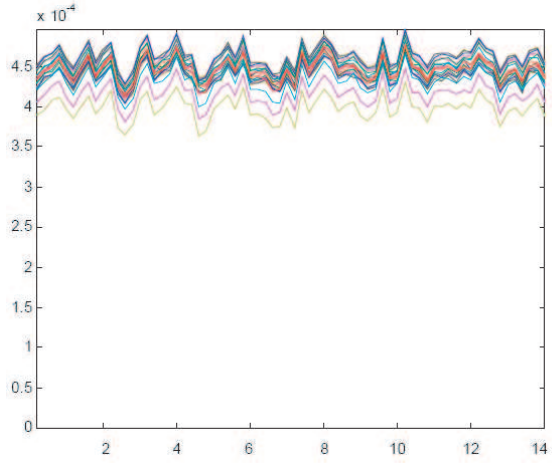

Figure 3: Amplitude of the first 20 even harmonics [V] vs. time [ms].

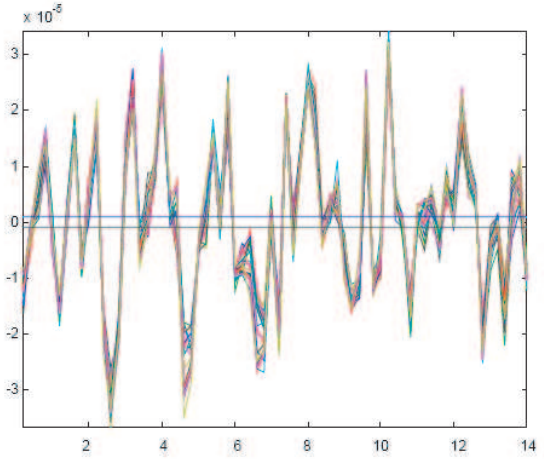

Figure 4: Amplitude of the first 20 even harmonics without average value [V] vs. time [ms].

The amplitude peak-peak of the current was 0.3 A, and its frequency 5 kHz. The sampling frequency of the digitizer was 500 kHz. The high resolution of the digitizer (18 bits) and proper amplification gain, made possible to achieve LBS = 1.9 μV, that is small enough to measure the noise.

We can see in Fig. 3 that all even harmonics of the output signal consist of offset component (average value) and noise component (random variations). The amplitude of the noise at the first 20 even harmonics, evolving in time, is shown in Fig. 4 after subtracting the constant level (i.e., offset).

We can see in Fig. 4 how the noise of the even harmonics is strictly correlated. As an example of the correlation between the even harmonics' noise in Fig. 5, the 4th harmonic is plotted vs. the 2nd harmonic.

The strict correlation of the noise is the key of the algorithm presented in the next section.

4. THE ALGORITHM

Let us consider the amplitude of the x-harmonic V_x as the sum of a component S_x, which is linearly dependent on the external measured DC field, and N_x, is the noise of that harmonic.

$$V_x(t) = S_x + N_x(t) \tag{1}$$

In Figs. 3–4 we can see that the noise of the even harmonics is not constant in time and that N_x is a function of time. Even if the DC external field is constant, which means constant S_x, the

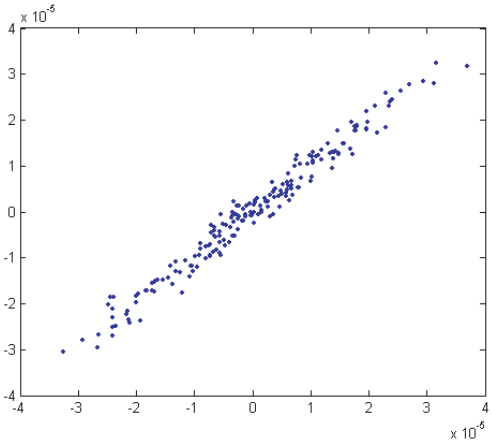

Figure 5: 2nd harmonic [V] vs 4th harmonic [V].

change of the noise in time made the measured amplitude of the xth even harmonic to be a function of time.

Let us consider now the 2nd and the 4th harmonic, for example. If we assume $N_1(t)$ to be equal to N_2(t) [Fig. 4], we can derive that subtracting the V_1 and V_2 we obtain self erasing of the noise:

$$V_{\mathrm{OUTPUT}}(t) = V_2(t) - V_4(t) = S_2 + N_2(t) - S_4 - N_4(t) = S_2 - S_4 \tag{2}$$

If we consider as an output signal the difference of two even harmonics we obtain noiseless signal. The drawback of this method is the reduction of the sensitivity. Indeed the sensitivity of the output signal calculated according to this algorithm, is equal to the difference between the sensitivities of the input harmonics.

Table 1

Excitation current [mA pk-pk]	Sensitivity of V_{output} [V/T]
1000	362
900	371
800	392
700	407
600	417
500	429
400	441
300	441
200	419
100	287

In order to minimize this disadvantage we chose as inputs for the algorithm, the harmonic which has the highest sensitivity and the second harmonic (which has usually much lower sensitivity).

The order of the harmonic whose sensitivity is the highest depends on the amplitude of the excitation current. In Table 1 we can see the sensitivity of the V_{output}, i.e., the output signal of the algorithm, which is quite satisfying. The best results are achieved when the excitation current is approximately 300 mA. Indeed, increasing the excitation current, the sensitivity at all the harmonics gets higher, but the difference among the harmonics' sensitivity decreases, and straightforward the remaining sensitivity of the output signal decreases as well.

A possible improvement of the algorithm could be achieved using four harmonics instead of two. For example we could calculate the output as follows:

$$V_{OUTPUT}(t) = V_2(t) - V_4(t) + V_6(t) - V_8(t) = (S_2 - S_4) + (S_6 - S_8) \tag{3}$$

The sensitivity of the resulting output is obviously higher than V_{output} computed only with two harmonics. However we should consider that the self-erasing effect of the algorithm does not cancel all the noise. Even if the noise is strictly correlated, it will not always be exactly the same for each harmonic. The output voltage of the algorithm V_{output} will have, in any case, noise equal to the difference between the noise of the harmonics used in the algorithm. For example Fig. 6 shows the noise of second harmonic, measured for 3000 subsequential periods, and the noise of the V_{output} computed from two harmonics.

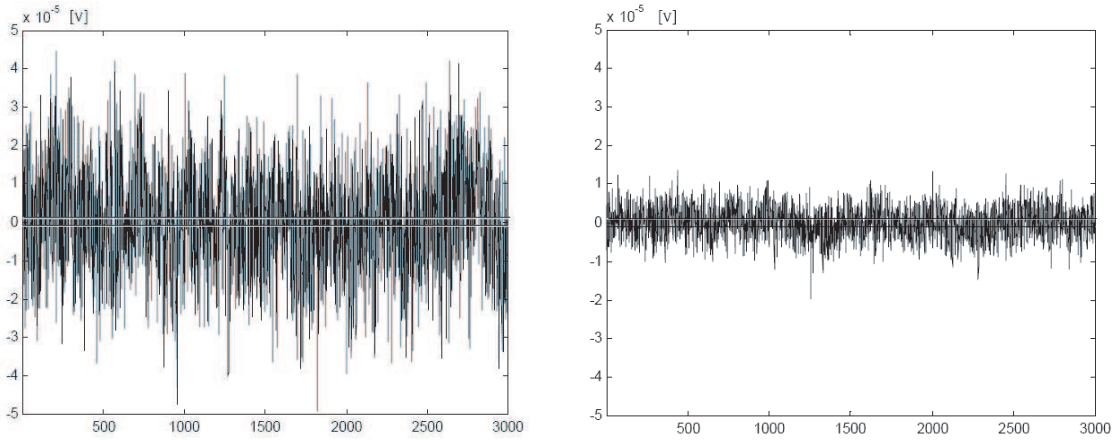

Figure 6: Noise of the Second harmonic [V] vs. time [ms] — left Noise of the Output voltage [V] vs. time [ms] — right.

We observed that if we use four harmonics instead of two, the noise of V_{output} is increased. If we consider the example of Eq. (3), we have to take into account the mismatch between the noise of the 2nd and 4th harmonic, and add the mismatch between the noise of 6th and 8th harmonic. Increasing the number of processed harmonics results in increased output noise. This shows that the "interharmonic" noise components are not correlated.

5. CONCLUSION

The algorithm presented in this paper has been proved to reduce the noise of the output signal of a race-track core fluxgate. The drawback is the reduction of sensitivity, which nevertheless can be compensated for by choosing proper excitation current and harmonics for the computation of the output. In any case, the sensitivity can be increased using more harmonics, even if the performance of the algorithm in reducing the noise gets worse. According to the main necessity the proper number of harmonics can be selected to be used in order to achieve better noise reduction or output sensitivity.

REFERENCES

1. *Magnetic Sensors and Magnetometers*, Pavel Ripka (ed.), Artech House, 78–79, 2001.
2. Kubík, J., L. Pavel, and P. Ripka, "PCB racetrack fluxgate sensor with improved temperature stability," *Sensors and Actuators A*, Vol. 130, 184–188, 2006.
3. Butta, M., "An innovative algorithm for noise reduction in a fluxgate output signal," *MSc Thesis work in Electrical Engineering*, Politecnico di Milano, 2005.

Microwave Applicator for Treatment of Atherosclerosis

Kateřina Novotná and Jan Vrba

Department of Electromagnetic Field, Czech Technical University in Prague
Technická 2, 166 27 Prague 6, Czech Republic

Abstract— Microwave angioplastic is one of the new domains of microwave thermotherapy, which is considered for treatment of atherosclerosis. Due to dysfunction of endothelium the sedimentation of cholesterol on a blood vessel wall can happen. This evokes its sequential closing. Basic principle of microwave angioplastic is, that heating gained by microwave energy irradiated into artery by microwave applicator, enables safe clear out of atherosclerotic plates in the wall of vessel.

1. INTRODUCTION

This paper describes the design of a special applicator for microwave angioplastic. As the most acceptable structure to create intracavitary applicator, coaxial quarter wave monopole, was chosen. Described applicator was designed for two frequencies (2.45 GHz, 5.6 GHz) and for numerical modeling electromagnetic field distribution the program CST Microwave Studio was used. The applicator in our model was inserted in to the vein with blood and surrounded by phantom of muscular tissue.

2. THEORY

The applicator is one of the basic elements of the thermo therapeutic microwave medical device. It decides about efficiency to transfer the high-frequency energy from microwave generator to human body. The applicator decides about the shape and about the size of heated region too. General microwave transmission line which consists two or more conductors can transfer electromagnetic TEM wave. Characteristics and way of propagation Electromagnetic wave depend on the parameters of dielectric space, i.e., ε and μ.

The main advantage of the intracavitary applicator like a coaxial line is especially their efficient geometric form, small size and relative cheep technological solution to production. Coaxial applicators are often realized like a half-wave or quarter-wave monopole. These applicators are useful for middle and higher frequencies.

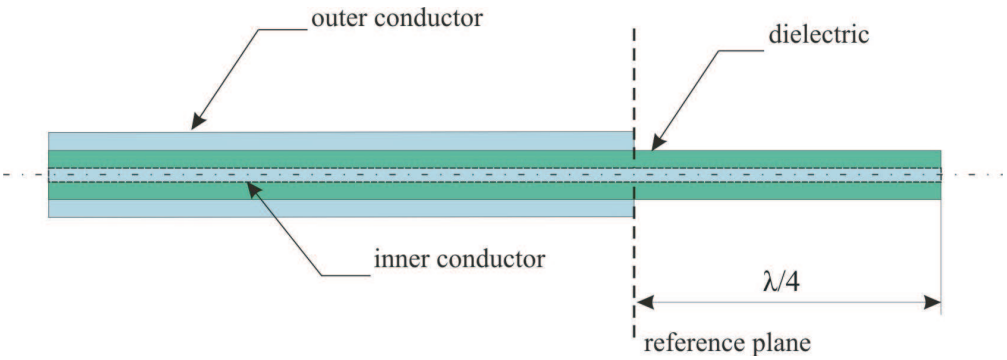

Figure 1: Coaxial quarter wave monopole.

On the Fig. 1 is demonstrated the basic structure of coaxial applicator like a quarter-wave monopole. At point of working plane is finished the outer conductor of the coaxial line and then there is only inner conductor. The length of this section corresponds approximately of quarter of the wave length λ on the conduction. The frequency in which will be radiated maximum power to the biological tissue, is given with this equation

$$f_r = \frac{c_0}{\lambda\sqrt{\varepsilon_r}}. \tag{1}$$

The fundamental conception about the distribution SAR around the coaxial applicator is that the maximum SAR is in the plane where finished outer conductor of coaxial line was. The value of SAR falls symmetrical along the inner conductor and along the outer conductor.

3. THE DESIGN OF APPLICATOR

Designing the intracavitary applicator for microwave angioplastic it is necessary to respect the dimension of the applicator, it has to be very thin. For the realization of the applicator we used the special coaxial cable, RG-174/U. The applicator was designed, evaluated and optimized in software CST Microwave Studio. It was necessary to put the applicator into the muscular tissue (Fig. 2).

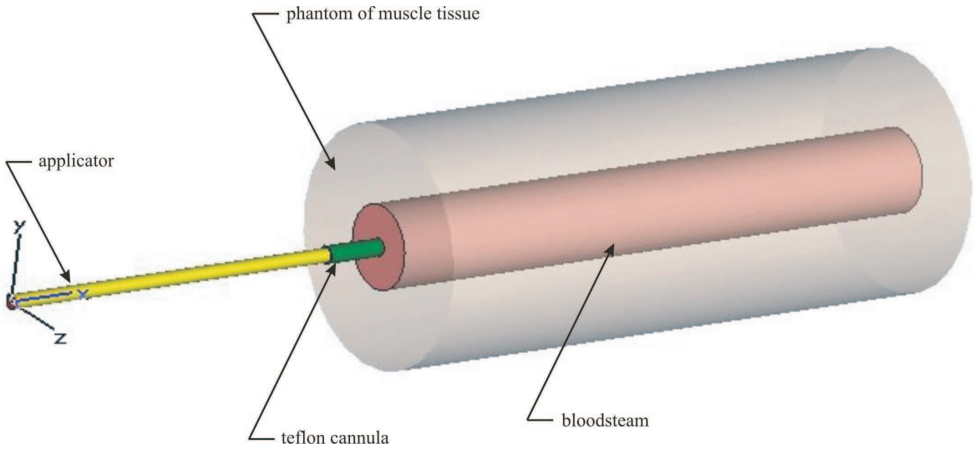

Figure 2: The applicator in the vein.

4. SOLUTIONS

First goal was to obtain good impedance matching between generator and microwave applicator. Then we studied the distribution of absorbed power (SAR) around the applicator. For the applicator working at 2.45 GHz was there maximum of SAR at the point of termination of outer conductor (Fig. 3). For applicator working at frequency 5.6 GHz two maxima were found (Fig. 4). This is not acceptable for clinical application.

It was a reason why only the applicator working at 2.45 GHz was constructed and tested.

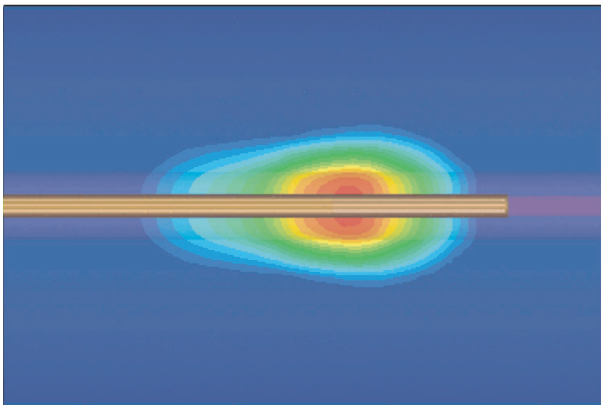

Figure 3: The distribution of SAR at 2.45 GHz.

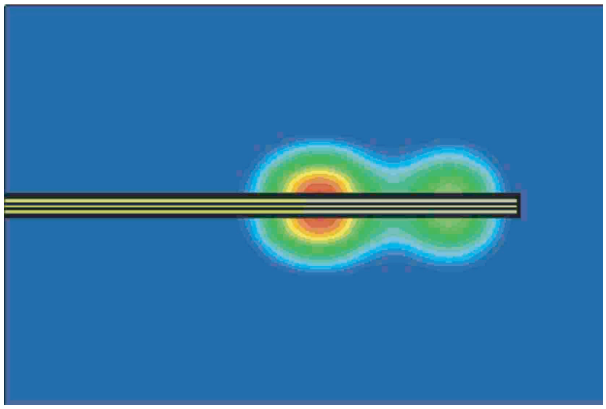

Figure 4: The distribution of SAR at 5.6 GHz.

The function of the microwave applicator was experimentally evaluated by measurement of reflection coefficient. This tested applicator had good impedance matching, −21.21 dB (Fig. 5).

Then the distribution of the temperature along the applicator was measured with IR camera. Described applicator was placed into the phantom of muscular tissue and exposed by 50 W during 1 minute. The temperature grew to 47°C (Fig. 6).

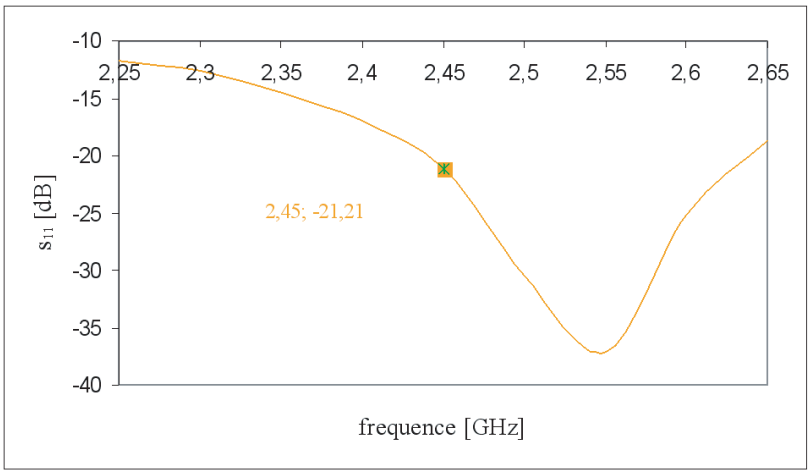

Figure 5: Impedance matching.

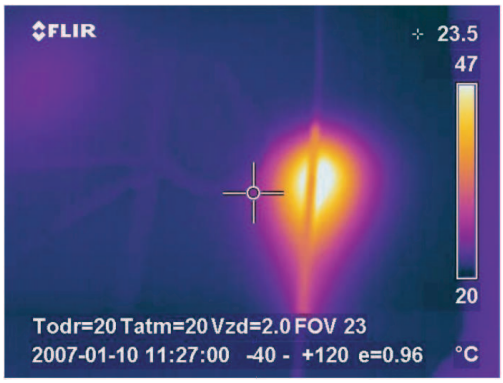

Figure 6: The distribution of the temperature around the applicator.

5. CONCLUSIONS

This paper describes only technical solution to design the intracavitary applicator for microwave angioplastic for treatment of atherosclerosis. In the future we plan the cooperation with doctors, who will provide us more medical information and help us with first experiments. Because the main goal of this project is to determine the optimal temperature for different stadium of this illness.

ACKNOWLEDGMENT

The described research has been financed by the Czech Grant Agency under the grant No. 102/05/0989, and by Czech Ministry of Education in the frame of the research plan No. MSM 6840770012.

REFERENCES

1. Novotná, K., "Intracavitary applicator for microwave angioplastic (in Czech)," Diploma thesis, Prague, 2007.
2. Vrba, J., "Medical applications of microwave thermotherapy (in Czech)," Publishing by CTU, Prague, 2003.

Antenna Rotation Aperture Synthesis for Short-range Personnel Scanning at mm-wavelengths

B. M. Lucotte and A. R. Harvey
Heriot-Watt University, UK

Abstract— Mm-wave interferometric synthetic aperture imagers are currently being developed for the detection of concealed weapons and usually operate in a snapshot. We investigate the potential of including a mechanical scanning between the scene and the array in order to reduce the number of antennas and to ease the calibration process. We show that rotational scanning achieves a more uniform coverage of the (u, v) plane than the linear scanning traditionally used in RADSAR systems. We optimize rotated evenly distributed Reuleux triangle arrays for maximum uniform (u, v) coverage with a genetic algorithm and present the improvements in the sidelobes of the Point Spread Function.

1. INTRODUCTION

Passive and semi-passive mm-wave imaging techniques are currently receiving considerable attention as personnel scanners due to their ability to detect concealed weapons through obscurants such as clothing [1, 2]. In comparison to conventional real-aperture imaging systems, synthetic aperture imaging enables images to be recorded with an infinite depth of field and using an essentially planar and sparse array. Interferometric synthetic aperture imagers have traditionally been considered for the recording of high spatial resolution images in a single snapshot. Snapshot operation necessarily requires a large number of antennas: this not only results in a high cost but also makes calibration highly problematic. It is highly desirable therefore to reduce the antenna count without adversely affecting the spatial resolution and radiometric sensitivity of the imager. We show that this can be achieved by introducing some degree of mechanical scanning between the source and the array in a similar *modus operandus* to the Earth Rotation Synthesis technique used in radio astronomy [3], but with the added complexity of near-field operation. Since the spatial frequencies are recorded in time-sequence the reduction in antenna count is achieved at the cost of a reduced imaging frame rate or a reduced radiometric sensitivity.

In the first section we adapt the fundamental imaging equations and image reconstruction algorithms for near-field synthetic aperture imaging [4], before considering the fundamental requirements of the array to adequately sample the image spatial frequencies. We then describe the necessary trade-off between the radiometric sensitivity, the imaging frame rate and the antenna count. In comparison to a snapshot aperture synthesis radiometer, the time-sequential recording of n_t individual images enables the number of antennas to be reduced by a factor of approximately $\sqrt{n_t}$ without reduction in spatial resolution. The second section presents the advantages of rotational scanning over linear scanning and describes the array optimization. The arrays are optimized with a Genetic Algorithm (GA) [5, 6] for maximum uniform (u, v) cover after rotational scanning. Antenna arrays that lay along Reuleux triangles achieve more uniform (u, v) coverage than other conventional arrays (T-shape, Y-shape and circular arrays) [7]. Small random perturbations were introduced in Reuleux triangle arrays in order to break the symmetry patterns of their spatial frequency coverage, and were optimized with a (GA).

2. IMAGING EQUATIONS

A set of N antennas positioned in a plane are recording radiations from a source in the near-field at a range R and with a brightness distribution $T_B(x, y)$. The correlation of the signals from antenna n and m is the visibility function and is given by:

$$V(x_n, x_m, y_n, y_m) = \frac{k_B \Delta v}{\sqrt{\Omega_1 \Omega_2}} \iint_S T_B(x', y') K_{nm}(x', y') F_{nm}(\Delta r_{(x',y')}, \Delta v)\, e^{-\frac{j2\pi}{\lambda_0}\Delta r(x',y')} dx' dy' \quad (1)$$

$$K_{nm}(x, y) = \frac{1}{r_n r_m} \left(P_n(x, y) P_m(x, y) \cos\theta_n \cos\theta_m\right)^{1/2} \quad (2)$$

$$r_n(x, y) = \sqrt{(x_n - x)^2 + (y_n - y)^2 + R^2} \quad (3)$$

$$\Delta r(x, y) = r_n(x, y) - r_m(x, y) \quad (4)$$

where $F_{nm}(\Delta r, \Delta v)$ is the fringe wash function and depends on the frequency response of the antenna channels, the bandwidth Δv of these channels and the path difference Δr. We now assume that artificial delay lines can be placed in any antenna channels in order to compensate for the path difference $\Delta r\left(\bar{x}_k, \bar{y}_k\right)$ between antennas n and m and a specific point source located at $(\bar{x}_k, \bar{y}_k)$. The visibility function $V_k\left(x_n, x_m, y_n, y_m\right)$ obtained by including the kth delay line to focus on the point source at $(\bar{x}_k, \bar{y}_k)$ is given by:

$$V_k\left(x_n, x_m, y_n, y_m\right) \propto \iint_S T_B\left(x', y'\right) K_{nm}\left(x', y'\right) \cdot F_{nm}\left(\Delta r_{(x',y')} - \Delta r_{(\bar{x}_k,\bar{y}_k)}, \Delta v\right) e^{-\frac{j2\pi}{\lambda_0}\left(\Delta r_{(x',y')} - \Delta r_{(\bar{x}_k,\bar{y}_k)}\right)} dx' dy' \quad (5)$$

The summation over the source S in Eq. (5) implies that the coherence length $c/\Delta v$ of the received signals is greater than $\Delta r\left(x, y\right) - \Delta r\left(\bar{x}_k, \bar{y}_k\right)$ for any (x, y) within the FoV. For a 15 GHz bandwidth imager, the coherence length is 20 mm and limits the extend of the integration in Eq. (5) to a small portion ΔS_k of the source S.

2.1. Image Reconstruction Algorithm

The image reconstruction is performed in two steps. First the image $T_{Bk}(x, y)$ of the source ΔS_k is estimated by performing the cross-correlation between the visibility function $V_k\left(x_n, x_m, y_n, y_m\right)$ and a function $\varphi_{(x,y)}\left(x_n, x_m, y_n, y_m\right)$ [4]:

$$T_{Bk}\left(x, y\right) = \frac{1}{N\left(N-1\right)} \sum_{\substack{n=1 \\ n\neq m}}^{N} \sum_{\substack{m=1 \\ m\neq n}}^{N} V_k\left(x_n, x_m, y_n, y_m\right) \varphi^*_{(x,y)}\left(x_n, x_m, y_n, y_m\right) \quad (6)$$

$$\varphi_{(x,y)}\left(x_n, x_m, y_n, y_m\right) = \frac{1}{K_{nm}\left(x, y\right) F_{nm}\left(\Delta r_{(x,y)} - \Delta r_{(\bar{x}_k,\bar{y}_k)}, \Delta v\right)} e^{-\frac{j2\pi}{\lambda_0}\left(\Delta r_{(x,y)} - \Delta r_{(\bar{x}_k,\bar{y}_k)}\right)} \quad (7)$$

Then, the final image $T_B\left(x, y\right)$ is reconstructed from the smaller images $T_{Bk}\left(x, y\right)$ as follow:

$$T_B(x, y) = \sum_k T_{Bk}(x, y) \quad (8)$$

The next section presents the Point Spread Function (PSF) of arrays of isotropic antennas and narrow band channels in order to characterize the antenna configuration only. The PSF at (x_0, y_0) is noted $PSF_{(x_0,y_0)}(x, y)$ and is given next:

$$\begin{aligned} PSF_{(x_0,y_0)}(x, y) &= \frac{1}{N(N-1)} \sum_{\substack{n=1 \\ n\neq m}}^{N} \sum_{\substack{m=1 \\ m\neq n}}^{N} e^{\frac{j2\pi}{\lambda_0}\left(\Delta r_{(x,y)} - \Delta r_{(x_0,y_0)}\right)} \\ &= \frac{2}{N(N-1)} \sum_{n=1}^{N} \sum_{m=n+1}^{N} \cos\left[\frac{2\pi}{\lambda_0}\left(\Delta r_{(x,y)} - \Delta r_{(x_0,y_0)}\right)\right] \end{aligned} \quad (9)$$

2.2. Spatial Resolution and Sampling Conditions

Let us denote by u and v the spatial frequencies recorded by the interferometer, D the longest baseline of the array, λ_0 the centre wavelength of the antenna channels and R the range of the source being recorded. When imaging in the near-field, i.e., when the condition $D^2/R << \lambda_0$ does not hold, u and v can be approximated as follow:

$$u(x, y) = \frac{\partial}{\partial x}\frac{\Delta r(x, y)}{\lambda_0} \qquad v(x, y) = \frac{\partial}{\partial y}\frac{\Delta r(x, y)}{\lambda_0} \quad (10)$$

We consider the spatial frequency $u_{\max}$ recorded at the centre of the source by the longest baseline D, formed of antennas with coordinates $\left(-\frac{D}{2}, 0, R\right)$ and $\left(\frac{D}{2}, 0, R\right)$. $u_{\max}$ is given by:

$$u_{\max} = \frac{1}{\sqrt{\frac{D^2}{4} + R^2}} \frac{D}{\lambda_0} \quad (11)$$

In the near-field of the antenna array, the visibility function expressed in Eq. (1) can be interpreted as the projection of the source distribution onto a set of weighted interference patterns, each of them having an orientation and a spatial frequency that varies over the source extend.

In synthetic aperture arrays, the (u, v) plane is generally not sampled on a regular grid and therefore the aliased responses in the image will not be periodic but will introduce noise like sidelobes with high levels. In order to maintain these sidelobes outside the synthesized map, the maximum spacing Δu and Δv between spatial frequency samples (u, v) recorded at the centre of the source must respect the Nyquist sampling requirements:

$$\Delta u \leq \frac{1}{2x_{\max}} \qquad \Delta v \leq \frac{1}{2y_{\max}} \tag{12}$$

where $x_{\max}$ and $y_{\max}$ are the maximum off-axis position within the FoV in each direction X and Y respectively.

In the case of a one-dimensional imager, the number of samples M required in the Fourier interval $[0, u_{\max}]$ is:

$$M = \frac{u_{\max}}{\Delta u} = 2x_{\max}\frac{1}{\sqrt{\frac{D^2}{4} + R^2}}\frac{D}{\lambda_0} \tag{13}$$

A diffraction limited system with an aperture diameter of 0.7 m is used a reference. For a source at a range of 2m and a centre frequency $v_0 = 94\,\text{GHz}$, the radius of the Airy disk is approximately 11.1 mm and should be small enough for threat detection applications. We consider a wide Field of View (FoV) configuration and a smaller FoV configuration. The wide and small FoV configurations have a FoV of 53^o and 30^o respectively in each direction. This corresponds to a maximum off-axis position of 1 m and 0.5 m for the wide and small FoV configurations. The number of measurements M required to Nyquist sample a circular region (with radius equals to $u_{\max}$) of the Fourier plane is approximately 146,500 and 36,500 for the wide FoV and small FoV configurations respectively.

2.3. Trade-off between Radiometric Sensitivity, Frame Rate and Antenna Count

The radiometric sensitivity achieved with a synthetic aperture imager depends on the source distribution and the redundancies in the spatial frequencies measured by the array. The radiometric sensitivity in the nadir-looking pixel of the image of a uniform source obtained with a synthetic aperture radiometer is given in [8]:

$$\Delta T = (T_B + T_R)\left(\frac{M}{2\Delta v \cdot \tau}\right)^{1/2} \tag{14}$$

where $M = N \cdot (N-1)$ with N the number of antennas. T_B and T_R are the total brightness temperature measured and the noise temperature of the receivers respectively. Δv is the bandwidth of the receivers and τ is the integration time. The number of antennas in the array can be reduced by introducing some degree of scanning between the array and the scene while maintaining the spatial resolution of the array. For an antenna array with N elements, an array scan including n_t different positions enables to record $N(N-1)n_t$ samples in a time sequence. Since one wishes to maintain constant the number of samples M in the Fourier domain, the antenna count can be reduced by a factor of approximately $\sqrt{n_t}$. The integration time τ can be expressed as follow:

$$\tau = \frac{1}{n_t \cdot F} = \frac{N(N-1)}{M \cdot F} \tag{15}$$

where F is the frame rate of the imager. Combining Eqs. (14) and (15) the radiometric sensitivity can be expressed as follow:

$$\Delta T = (T_B + T_R)\left(\frac{F}{2\Delta v}\frac{1}{N(N-1)}\right)^{1/2} M \tag{16}$$

Eq. (16) shows that reducing the number of antennas by a factor of $\sqrt{n_t}$ is made at the cost of a degradation in the radiometric sensitivity by a factor of $\sqrt{n_t}$ or a degradation in the imaging frame rate of the imager by a factor of n_t. Therefore there is a trade-off between the antenna count reduction, the radiometric sensitivity and the frame rate of the imager. Figure 1 shows the radiometric sensitivity achieved with various amount of scanning between the source and the radiometer. Table 1 and Table 2 summarize the number of antennas associated with various radiometric sensitivities and frame rates for the wide and small FoV configurations respectively.

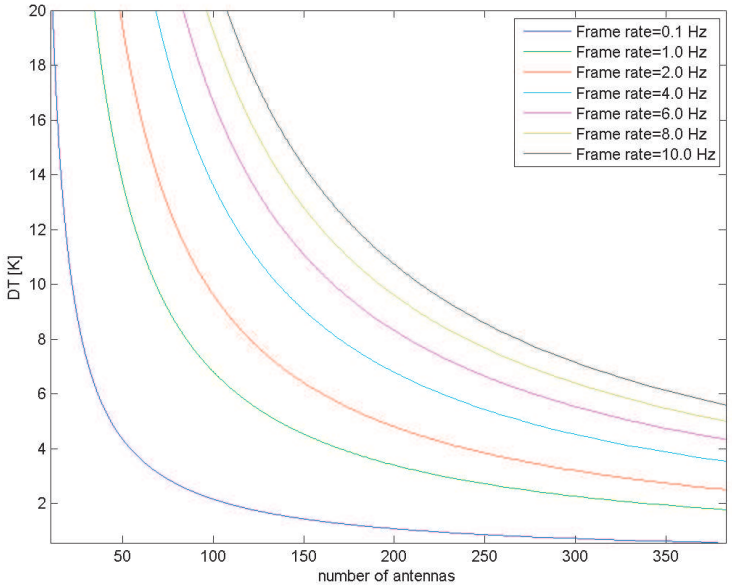

Figure 1: Radiometric sensitivity achieved by a synthetic aperture radiometer including various amounts of scanning. $T_B = 300\,\mathrm{K}$, $T_R = 500\,\mathrm{K}$, $\Delta v = 15\,\mathrm{GHz}$ and $M = N(N-1)n_t \approx 146,500$.

Table 1: Wide FoV configuration ($x_{\max} = y_{\max} = 1\,\mathrm{m}$): number of antennas N and number of scanning positions n_t required to achieve a radiometric sensitivity ΔT and a frame rate F. The total number of samples M is $146.5\,\mathrm{k} \pm 5\%$, the largest baseline considered is $D = 0.7\,\mathrm{m}$, $v_0 = 94\,\mathrm{GHz}$.

F [Hz]	0.1		1		2		4		8		10	
ΔT [K]	N	n_t	N	n_t	N	n_t	N	n_t	N	n_t	N	n_t
1	216	3										
2	108	13										
4	54	51	170	5								
6	36	116	113	12	160	6						
8	27	209	85	21	120	10	170	5				
10	22	317	68	32	96	16	136	8	193	4	216	3

Table 2: Small FoV configuration ($x_{\max} = y_{\max} = 0.5\,\mathrm{m}$): number of antennas N and number of scanning positions n_t required to achieve a radiometric sensitivity ΔT and a frame rate F. The total number of samples M is $36,500\,\mathrm{k} \pm 5\%$, the largest baseline considered is $D = 0.7\,\mathrm{m}$, $v_0 = 94\,\mathrm{GHz}$.

F [Hz]	0.1		1		2		4		6		8		10	
ΔT [K]	N	n_t	N			n_t	N	n_t	N	n_t	N	n_t	N	n_t
1	54	13												
2	27	52	85	5										
4	14	201	43	20	60	10	85	5	136	2				
6	9	509	29	45	40	23	57	11			80	6		
8	7	872	22	79	30	42	43	20	52	14	60	10	68	8
10	6	1221	17	135	24	66	34	33	42	21	48	16	54	13

2.4. System Design

In the previous section we have discussed the various trade-off between the radiometric sensitivity, the frame rate of the imager and the antenna count. Arrays of various complexities require to be optimized to minimize the sidelobes of their Point Spread Function (PSF) for a given width of the central peak. Optimizing antenna arrays with large antenna numbers N is a complex task because

the dimension of the search space is $2N$ for a snapshot array and $2Nn_t$ when a scan is included. Although the optimal system probably requires optimizing the array and its motion relative to the scene altogether, we have decided to reduce the search space by considering linear and rotational motions only.

2.5. Array Motion

Near field synthetic aperture techniques, like RADSAR and SAR, usually include a translation of the array relative to the source plane. When antenna signals are correlated by pair, as in RADSAR, the spatial frequency recorded by each baseline decreases as the array is translated away from the source. This means that the (u, v) coverage of the array at any position along the scan is simply a shrunk version, towards low frequencies, of the coverage achieved at nadir. In other words, translating the array does not improve the coverage of high spatial frequencies. Figure 2 illustrates this with a 30 antenna array evenly distributed along a Reuleux triangle. However, if we consider an array in rotation around the normal to the array plane, the spatial frequencies recorded will simply be rotated by the same angle. Figure 3 presents the same array as in Figure 2 with its (u, v) coverage after 10 rotations by 6°. Comparing the coverage achieved by translating and rotating the array shows that the density of measurements at high spatial frequencies is higher with a rotation than with a translation of the antennas. In addition, a rotational scanning may require simpler hardware and will enable higher frame rates to be achieved.

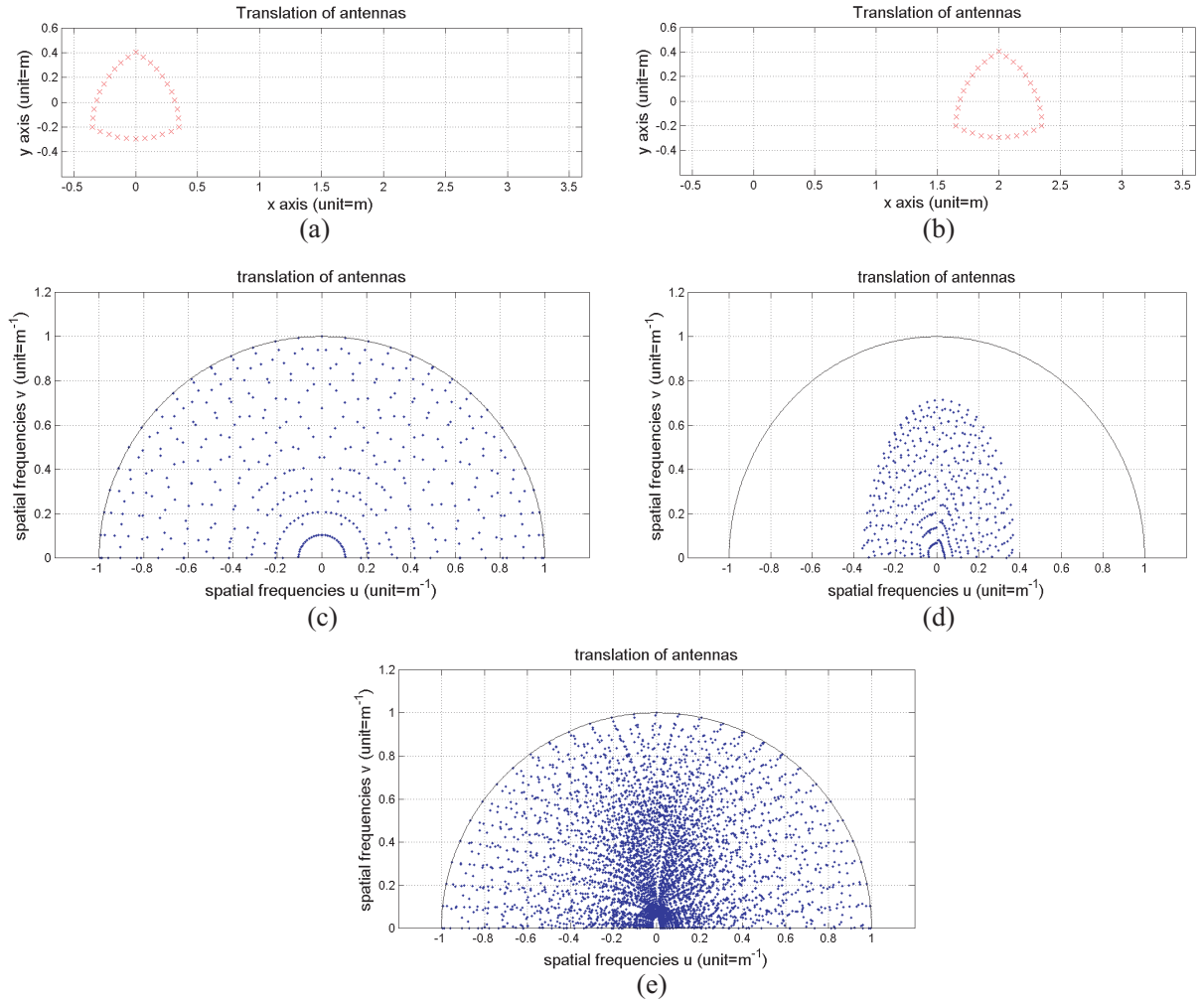

Figure 2: Evenly distributed Reuleux triangle array with 30 antennas centred (a) at the source origin $(x, y) = (0, 0)$, (b) at the point $(x, y) = (2, 0)$. (c) (d) Snapshot spatial frequency coverage of the array at positions shown in (a) and (b) respectively. (e) Spatial frequency coverage achieved when the array is translated by increments of 0.3 m up to 3 m.

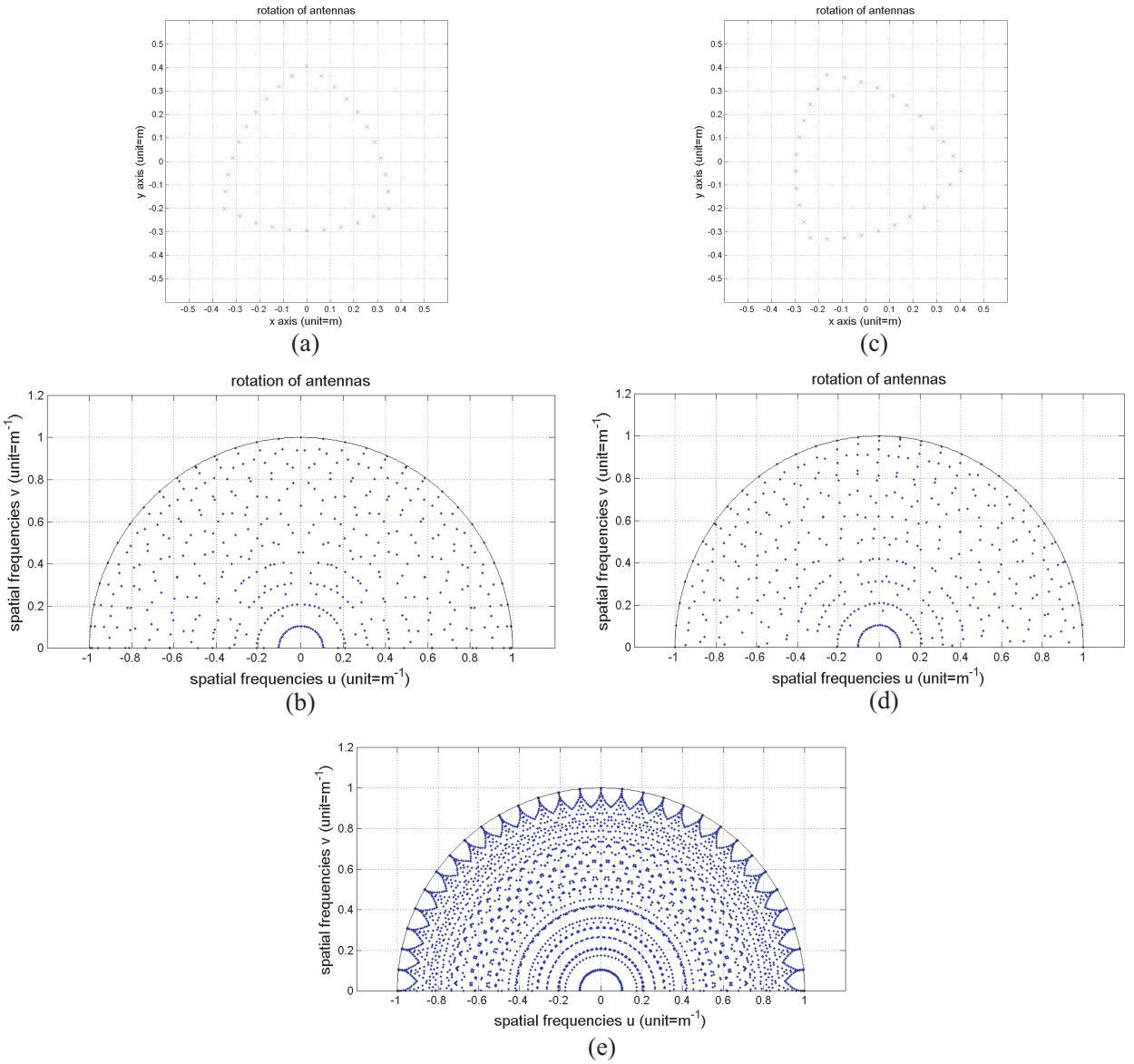

Figure 3: Evenly distributed Reuleux triangle array with 30 antennas (a) centred at the source origin $(x, y) = (0, 0)$, (b) rotated by 24°. (c) (d) Snapshot spatial frequency coverage of the array at positions shown in (a) and (b) respectively. (e) Spatial frequency coverage achieved when the array is rotated by increments of 6° up to 60°.

2.6. Array Design

Various approaches have been proposed to minimize the sidelobes of the PSF. One approach consists in sampling the (u, v) plane as uniformly as possible while avoiding redundant measurements. Uniform coverage has the advantage to minimize the width of the central peak for a given array size, and also reduces the sidelobes level away from the central peak since they are due to holes in the (u, v) cover. Uniform coverage of the (u, v) plane also requires an isotropic sampling, which can be achieved by arrays in the shape of curves of constant width [7]. When antennas are evenly distributed along curves of constant width with a rotational degree of symmetry n (invariance to a $2\pi/n$ rotation), the (u, v) cover suffers from a degree of rotational symmetry $2n$. Therefore antennas arrays distributed along Reuleux triangles ($n = 3$) provide the most uniform (u, v) cover among the shapes of constant width. This configuration can be used as the starting position of an optimization algorithm that will introduce small perturbations in order to break the symmetry patterns of the (u, v) cover and improve the sampling uniformity. Another approach consists in bringing the worst sidelobe of the PSF inside a given FoV below a specific threshold by using an analytical gradient descent [9]. Arrays have also been designed to achieve a tapered (u, v) coverage. Spiral arrays have

been shown to provide good uniformity of measurements with azimuth in the Fourier domain, and near-gaussian radial density of measurements. Concentric multi-ring arrays also provide tapered (u, v) cover. Such configurations have been optimized with Genetic Algorithms (GA) [10]. Given the dimensionality of the search space, finding a global optimal configuration that does not depend on the initial array does not seem to be tractable given the processing power currently available. The various approaches previously described have in common that they all require a "good" initial configuration according to a specific criteria (uniform or apodized coverage) prior to introduce small perturbations in the array with an optimization method in order to remove the symmetry patterns that degrade its (u, v) coverage.

Apodizing the Fourier samples degrades the Signal to Noise Ratio (SNR) in the image and

Table 3: Characteristics of the PSF of the non-optimized and optimized Reuleux triangle arrays. FWHM is the Full Width at Half Maximum, the 1st sidelobe is expressed in dB (dB = 10Log_{10}), and E_M/E_{SL} denotes the ratio of the Energy in the main beam E_M to the energy in the sidelobes E_{SL}.

N	n_t	Array type	$N.(N-1).n_t$	FWHM (mm)	1st sidelobe (dB)	E_M/E_{SL}
27	52	No optimization	36504	6.7	−9.4	0.18
		GA optimization	36504	6.7	−8.9	0.64
107	13	No optimization	147446	6.9	−8.5	0.28
		GA optimization	147446	7	−8.5	0.72

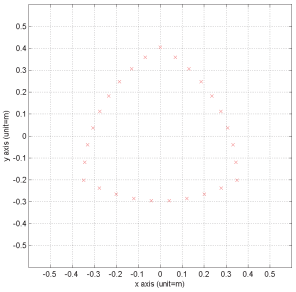

(a)

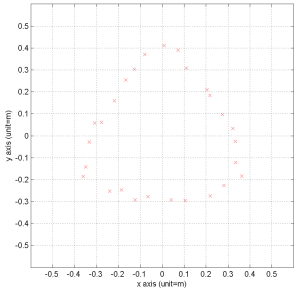

(f)

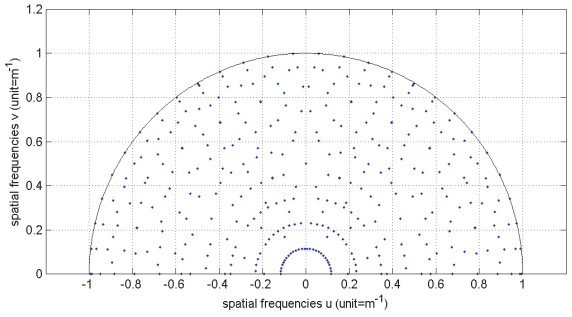

(b)

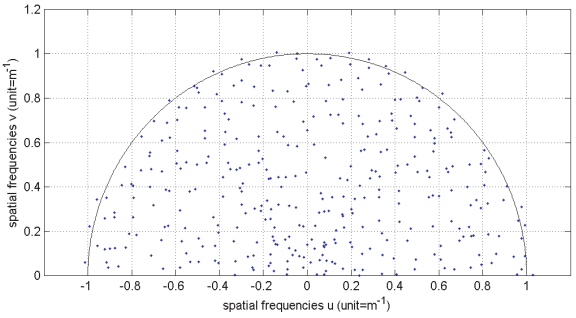

(g)

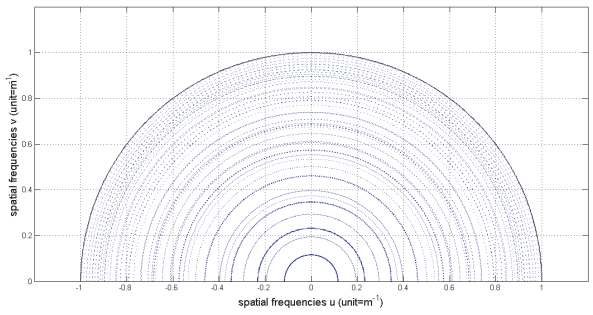

(c)

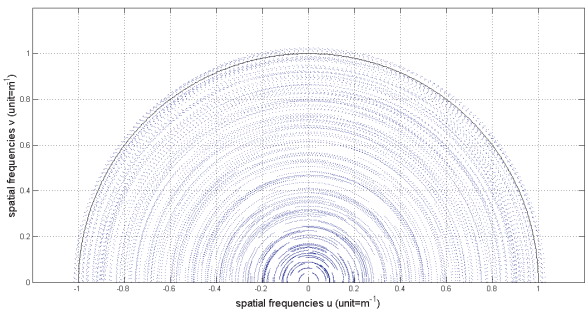

(h)

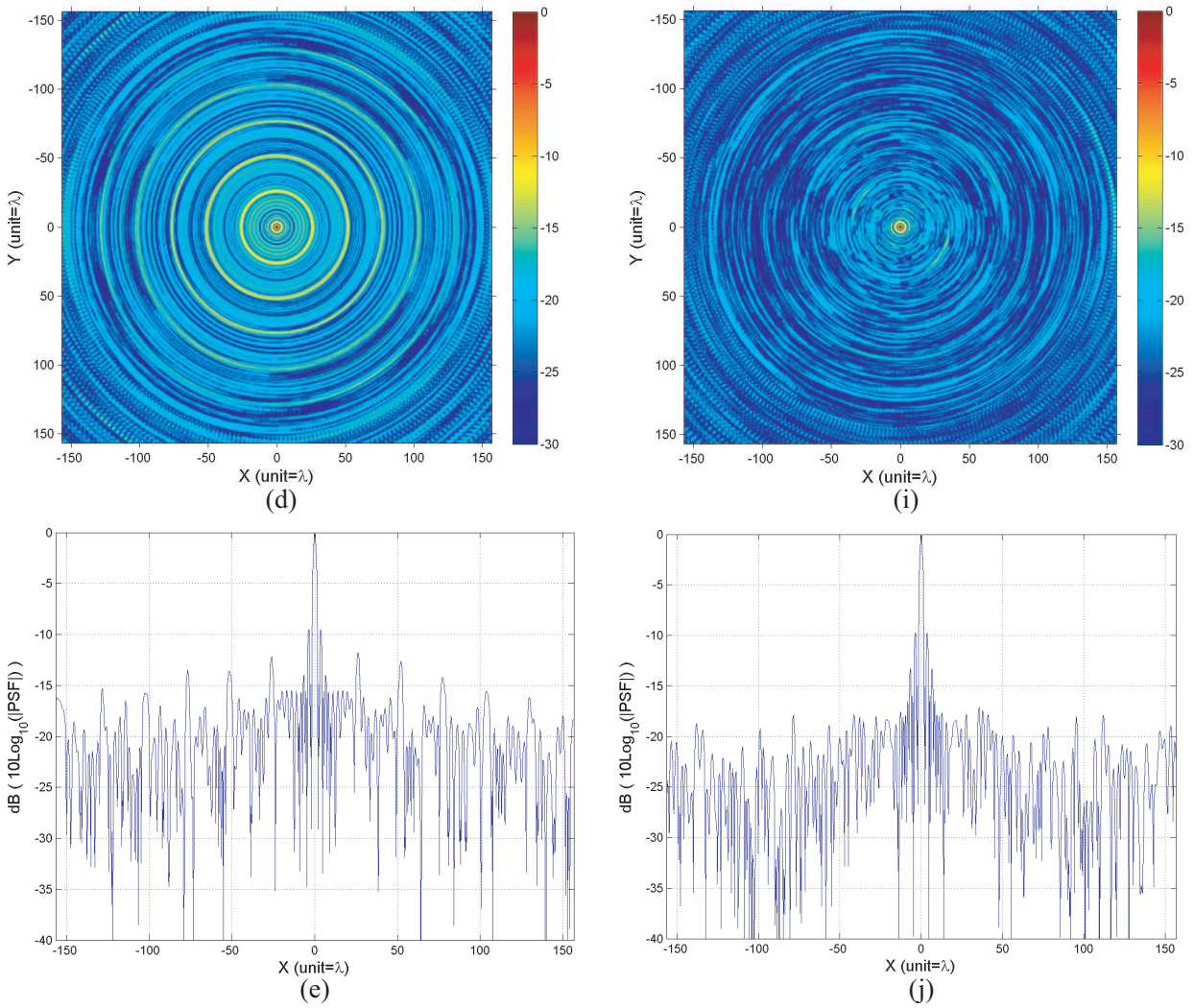

Figure 4: Small FoV configuration (FoV=28°) with 27 antennas and 52 array rotations up to an angle of 60°. $v_0 = 94\,\text{GHz}$, $D = 0.7\,\text{m}$, $R = 2\,\text{m}$. From (a) to (e) Characteristics of a non optimized Reuleux triangle array and from (f) to (g) characteristics of the Reuleux triangle array optimized for uniformity coverage of the (u, v) plane. (a) and (f): Antenna positions, (b) and (g) snapshot (u, v) coverage at nadir, (c) and (h) (u, v) coverage at nadir after rotational scanning, (d) and (i) density plot of the PSF in dB (10Log10(|PSF|)), (e) and (j) slice of the PSF along the x-axis at $y = 0\,\text{m}$.

therefore increases the radiometric sensitivity ΔT. Given an apodizing window, the worst case occurs when the imager is looking at a non resolved source, like in radio-astronomy, since all the spatial frequencies recorded contain signal information. In this case, a conventional tapering window like the Hanning function will degrade the SNR at the image centre by a factor of 0,63. However for typical mm-wave scenes, which contain less high spatial frequencies than radio astronomy sources, the SNR reduction will be less significant. As a consequence, we decided to design an array that is optimized for maximum uniform (u, v) cover, leaving the possibility of applying a taper function on the Fourier samples to reduce the sidelobes near the central peak. The initial array consists of a set of antennas evenly distributed along a Reuleux triangle and including a rotational scanning up to a maximum angle of $\pi/3\,\text{rad}$. Indeed, since Reuleux triangle arrays have an autocorrelation with a degree of rotational symmetry of 6 (invariance to a rotation by $2\pi/6$), rotating the array further than $\pi/3$ rad only adds redundant (u, v) samples. The symmetry pattern of the spatial frequency coverage of Reuleux triangle arrays is clearly shown on Figure 5 for a 107 antenna array. The cost function minimized is a metric of the uniformity of the samples distribution within the disk of radius $u_{\max}$. This metric is defined by considering the histogram of the nearest neighbour distances and taking the ratio of the mean over the standard deviation. Figure 4 and Figure 5 present the results of this optimization applied on Reuleux triangle arrays. The (u, v) cover and

PSF at the centre of scene are shown for optimized and non-optimized arrays. Two configurations with a different FoV are considered. The first configuration, shown on Figure 4, has a FoV of 28° whereas the second configuration has a wider FoV of 53° and is shown in Figure 5. The small and wide FoV configurations require 27 and 107 antennas respectively in order to image at a frame rate of 0.1 Hz with a radiometric sensitivity of 2 K. Note that the first sidelobe and Full Width at Half Maximum of the PSF of the non-optimized and optimized arrays are similar, as shown in Table 3.

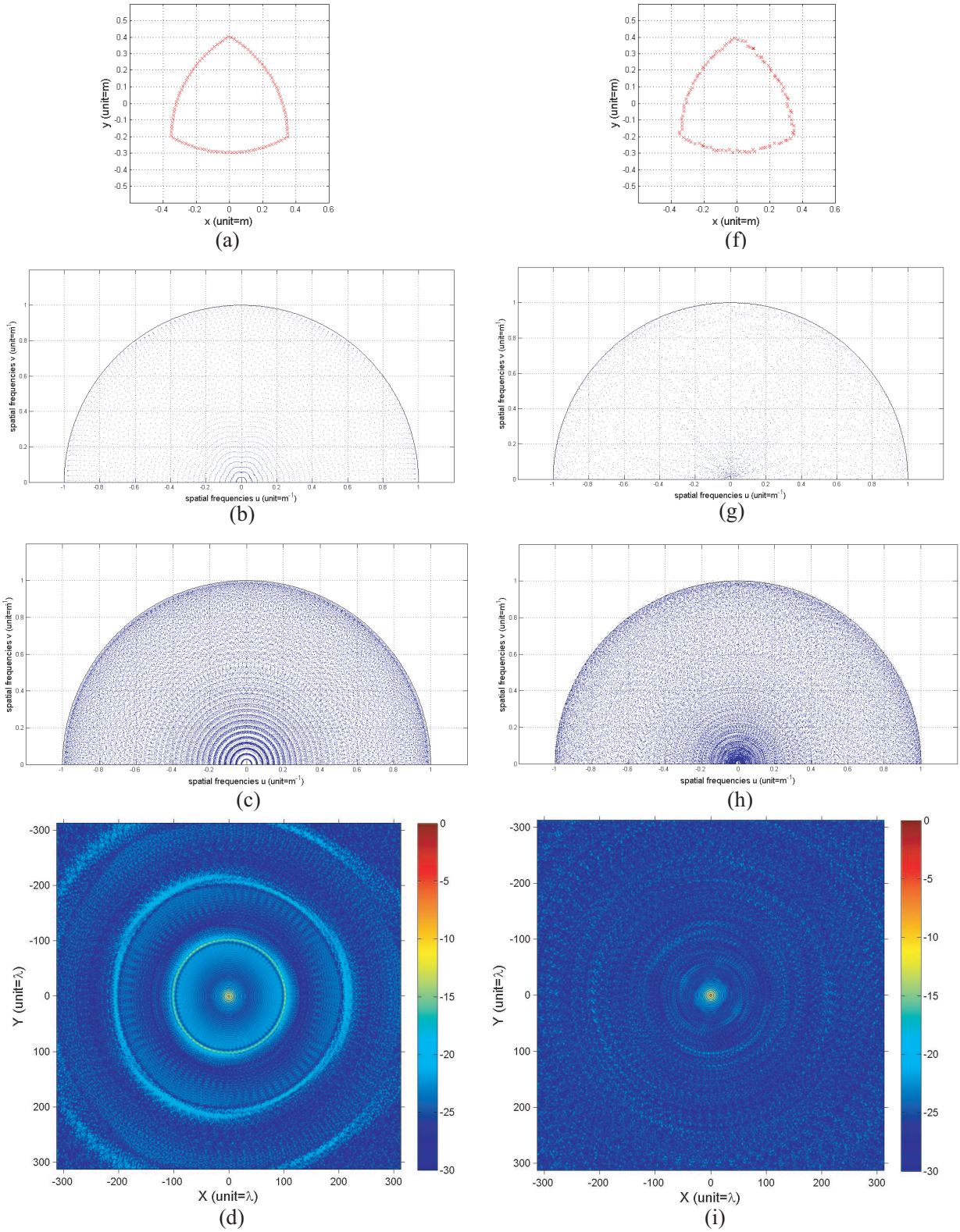

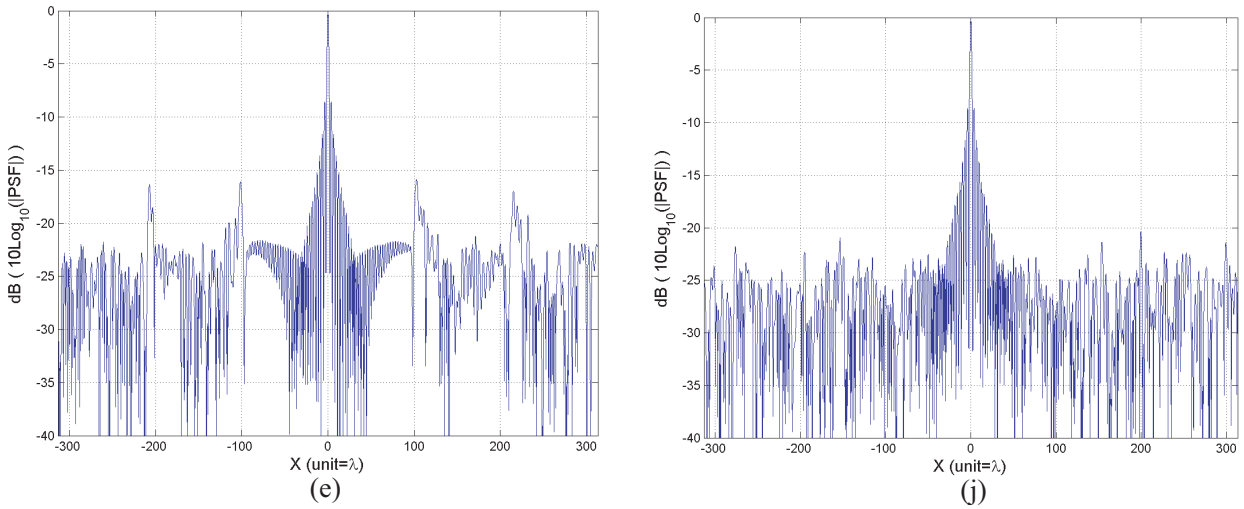

Figure 5: Wide FoV configuration (FoV=53°) with 107 antennas and 13 array rotations up to an angle of 60°. $v_0 = 94\,\text{GHz}$, $D = 0.7\,\text{m}$, $R = 2\,\text{m}$. From (a) to (e) Characteristics of a non optimized Reuleux triangle array and from (f) to (g) characteristics of the Reuleux triangle array optimized for uniformity coverage of the (u, v) plane. (a) and (f): Antenna positions, (b) and (g) snapshot (u, v) coverage at nadir, (c) and (h) (u, v) coverage at nadir after rotational scanning, (d) and (i) density plot of the PSF in dB (10Log10(|PSF|)), (e) and (j) slice of the PSF along the x-axis at $y = 0\,\text{m}$.

However the level of other sidelobes is greatly reduced with the optimized arrays. This is shown by the ratio of the energy in the main beam to the energy in the sidelobes, which is increased by a factor of 2.6 and 3.7 for the 27 and 107 antenna arrays respectively.

3. CONCLUSIONS

Recording n_t images in a time-sequence with an interferometric synthetic aperture array in motion relative to the scene enables to reduce the antenna count by a factor of $\sqrt{n_t}$ at the cost of a degradation in the radiometric sensitivity by a factor of $\sqrt{n_t}$ or a degradation in the imaging frame rate of the imager by a factor of n_t. We have presented the advantages of rotational scanning over linear scanning of the array in terms of spatial frequency coverage efficiency and imaging frame rates. We describe two arrays operating at 94 GHz with a bandwidth of 15 GHz and a largest baseline of 0.7 m, imaging a scene at a range distance of 2 m with a radiometric sensitivity of 2 K at a frame rate of 0.1 Hz. Rotating arrays of 27 and 107 antennas are designed to image a FoV of 28° and 53° respectively. This represents an antenna count reduction by a factor of 3.6 and 7.1 compared with a snapshot system. Arrays have been optimized with a genetic algorithm for maximum uniform (u, v) coverage at nadir, starting with evenly distributed Reuleux triangle arrays. Comparing the PSF of evenly distributed Reuleux triangle arrays with the PSF of the optimized arrays we conclude that the optimization maintain the first sidelobe to its initial level, $-9\,\text{dB}$ and $-8.5\,\text{dB}$ for the 27 and 107 antenna arrays respectively, but greatly reduces the level of other sidelobes. This improvement can be quantified by the ratio of the energy in the main beam to the energy in the sidelobes, which is increased by a factor of 2.6 and 3.7 for the 27 and 107 antenna arrays respectively. Finally we conclude that the concept of aperture rotation synthesis has the potential of reducing the number of elements by a factor of 10 for mm-wave imaging applications where low frame rates of the order of 0.1 Hz are acceptable.

REFERENCES

1. Sheen, D. M., D. L. McMakin, and T. E. Hall, "Three-dimensional millimeter-wave imaging for concealed weapon detection," *IEEE Transactions on Microwave Theory and Techniques*, Vol. 49, No. 9, September 2001.
2. Appleby, R., "Whole body 35 GHz security scanner," *Proceedings of SPIE*, 244–251, Bellingham, WA, August 2004.
3. Thompson, A. R., J. M. Moran, and G. W. Swensen Jr., *Interferometry and Synthesis in Radio Astronomy*, Wiley-Interscience, New York, 2001.

4. Peichl, M., H. Suess, M. Suess, and S. Kern, "Microwave imaging of the brightness temperature distribution of extended areas in the near and far field using two-dimensional aperture synthesis with high spatial resolution," *Radio Science*, Vol. 33, 781–801, May–June 1998.
5. Haupt, R. L., "An introduction to genetic algorithms for electromagnetics," *IEEE Antennas Propag. Mag.*, Vol. 37, No. 2, 7–15, Apr. 1995.
6. Marcano, D. and F. Duràn, "Synthesis of antenna arrays using genetic algorithms," *IEEE Antennas Propag. Mag.*, Vol. 42, No. 3, 12–20, Jun 2000.
7. Keto, E., "The shapes of cross-correlation interferometers," *Astrophys. J.*, Vol. 475, 843–852, 1997.
8. Ruf, C. S., "interferometric synthetic aperture microwave radiometry for the remote sensing of the earth," *IEEE Transactions on Geoscience and Remote Sensing*, Vol. 26, No. 5, September 1988.
9. Kogan, L., "Optimizing a large array configuration to minimize the sidelobes," *IEEE Transactions on Antenna and Propagation*, Vol. 48, No. 7, July 2000.
10. Hebib, S., N. Raveu, and H. Aubert, "Cantor spiral array for the design of thinned arrays," *IEEE Antennas and Wireless Propagation Letters*, Vol. 5, 2006.

Printed Antennas Tuned by Transversely Magnetized Ferrite Operating at a Novel Resonant Mode

A. A. Mavridis[1], **G. A. Kyriacou**[1], **and J. N. Sahalos**[2]

[1]Microwaves Lab., Department of Electrical and Computer Engineering
Democritus University of Thrace, Greece
[2]Radiocommunications Lab., Department of Physics, Aristotle University of Thessaloniki, Greece

Abstract— The excitation of a novel single mode in the negative μ_{eff} area is studied for rectangular patch antenna printed on magnetized ferrite substrates or tuned by a ferrite inclusion. In all cases the DC magnetic field is considered perpendicular to the substrate plane. The ferrite inclusion-post shape is considered either cylindrical or rectangular. Numerical simulation results reveal the existence of this novel resonating mode inside the negative μ_{eff} area for both the rectangular microstrip patch printed on ferrite substrate or tuned by a rectangular ferrite post. Also, the input impedance characteristics of these patch antennas are studied.

1. INTRODUCTION

A number of published works (e.g., Pozar [1]) show that in the case of patch antennas printed on transversely magnetized ferrite substrates, there is a cutoff frequency range where there is not any propagating mode in the substrate below the radiator. In this range the effective permeability μ_{eff} of the ferrite is negative, so the corresponding wavenumber becomes imaginary leading to an evanescent mode. The resonant frequency of circular and ring patch antennas printed on transversely magnetized ferrite substrate was analytically studied in our previous works [2, 3]. The analysis was performed using the perfect magnetic walls approximation and the ferrite losses were also taken into account. Closed form expressions were given for all the geometries studied. By including ferrite losses in our analysis and with the proper mathematical handling of the involved Bessel functions, the solution of the characteristic equation in the negative μ_{eff} area became possible revealing a novel single propagating mode. There is only one similar work published in the literature reporting on this mode as propagating in a grounded ferrite substrate [4]. Baccarelli et al. [4] have also considered a lossy ferrite substrate, but biased with an H_{DC} parallel to the ground plane. Assuming propagation along the substrate, but in a direction transverse to the H_{DC}, they indeed found a single mode denoted as TE_{1+} in the region of negative μ_{eff}.

Our previous studies on axially symmetric patches proved that the novel mode exists in the negative μ_{eff} range independent of the specific patch shape or the tuning ferrite inclusion. This observation motivated us to study the rectangular patch printed on transversely magnetized ferrite substrate and the same patch tuned by a circular or rectangular ferrite post. Thus, the aim of the present work is to identify the existence of any resonant mode in the negative μ_{eff} range, for rectangular patch radiators.

2. RECTANGULAR PATCH ANTENNA

The first geometry studied is the rectangular patch antenna printed on a ferrite substrate transversely magnetized at saturation, as shown in Fig. 1. The YIG Al doped type "GA-65" of Ferrite Domen is used for the ferrite substrate with $4\pi M_s = 650$ Gauss, $\epsilon_{rF} = 14.2$ and $\Delta H = 45$ Oersted. The whole geometry is inside a DC magnetic field perpendicular to the ferrite substrate plane. The existence of the resonant mode inside the negative μ_{eff} region is investigated using the Ansoft HFSS [5] software, which employs the finite element method to analyze random three dimensional geometries. The main reason for choosing this software is that ferrite losses can be taken into account.

The coaxial probe was preferred for the antenna feeding, because it has the least effect on the printed patch geometry. Moreover, the complex input impedance of the antenna can be easily matched by changing the feeding position. Fig. 1 also shows the position of the coaxial connector which feeds the microstrip patch.

The graph of Fig. 2 shows the resonant frequency of the rectangular patch antenna printed on a ferrite substrate versus the DC magnetic bias. Both sides of the microstrip patch are 10.6 mm and it was designed to cover the 800, 900 and 1800 MHz frequency bands. This can be achieved

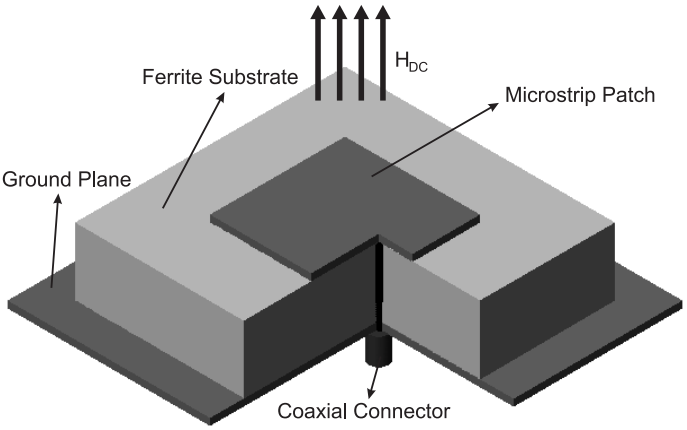

Figure 1: Geometry of rectangular patch antenna printed on transversely magnetized ferrite substrate.

by switching the antenna resonant frequency through the DC magnetic bias. The shaded area of Fig. 2 represents the negative effective permeability μ_{eff}. It is clear from the graph that the second resonating mode, does not vanish when it reaches the negative μ_{eff} boundary, but it continues to propagate inside the negative μ_{eff} region. This behaviour is exactly the same as for the case of the circular microstrip patch antenna printed on a transversely magnetized ferrite, which was studied in our previous work [2, 3]. Since ferrite losses are taken into account, revealing the existence of this novel mode is exactly what we expected. The justification of this mode based on the assumption of [2, 3] that the field below the radiator can be expressed as a superposition of right and left hand circularly polarized modes, falls outside the scope of the present work. However this can be an interesting subject for a future investigation.

The input impedance is a very important characteristic since it defines the antenna bandwidth. In order to further investigate the resonating mode inside the negative μ_{eff} range, the input impedance of the antenna at such a resonant frequency is studied. The graph of the rectangular microstrip patch antenna input impedance versus frequency is shown in Fig. 3. The geometry is the same as that of Fig. 1. The center of the coaxial feed inner conductor is placed 1.1 mm from the patch edge. This position of the coaxial connector yields a 50 Ohm maximum input resistance for the second resonating mode, inside the negative μ_{eff} area and for $H_0 = 800$ Oe. The resonant frequency of the antenna is 3.61 GHz, while the 3 dB bandwidth of the antenna is 1.52 percent. The input reactance at resonance is -12 Ohm. The above characteristics imply that the behaviour of the mode resonating inside the negative μ_{eff} area is similar to any other resonating mode of a rectangular microstrip patch printed on a transversely magnetized ferrite substrate.

3. RECTANGULAR MICROSTRIP PATCH ANTENNA TUNED BY A RECTANGULAR FERRITE POST

The main idea here is to design an antenna that retains the benefits from the use of ferrite substrate, like the control of the resonant frequency, offering at the same time less weight and losses. To accomplish this, the geometry of the rectangular patch printed on a dielectric substrate is used, only a part of the dielectric at the centre, underneath the patch, is substituted by a ferrite post. The shape of the ferrite post can be either rectangular, circular or ring shaped. In the design example presented here, the ferrite post is considered rectangular, similar to the shape of the patch. The antenna of Fig. 1 covering the 800, 900 and 1800 MHz frequency bands, is designed again using a 0.5 ratio of ferrite to patch dimensions. The ferrite post is embedded in a dielectric substrate, which for the studied patch antenna is the Rogers type TMM-10, with $\epsilon_r = 9.2$ and $\tan\delta = 0.0022$.

The resonant frequency of the rectangular ferrite post tuned antenna versus the DC magnetic bias is shown in Fig. 4. First, it is clear that the second resonating mode still enters the negative μ_{eff} area. Second, the control of the resonant frequency through the DC magnetic field is preserved, at least for the first resonating mode, even though the ferrite material volume is reduced to the 25 percent compared to the case of the antenna printed on a purely ferrite substrate. The curve of the second resonating mode shows that the resonant frequency is almost unchanged with the dc magnetic field. However, the same phenomenon was observed in the study of circular patches [2, 3]

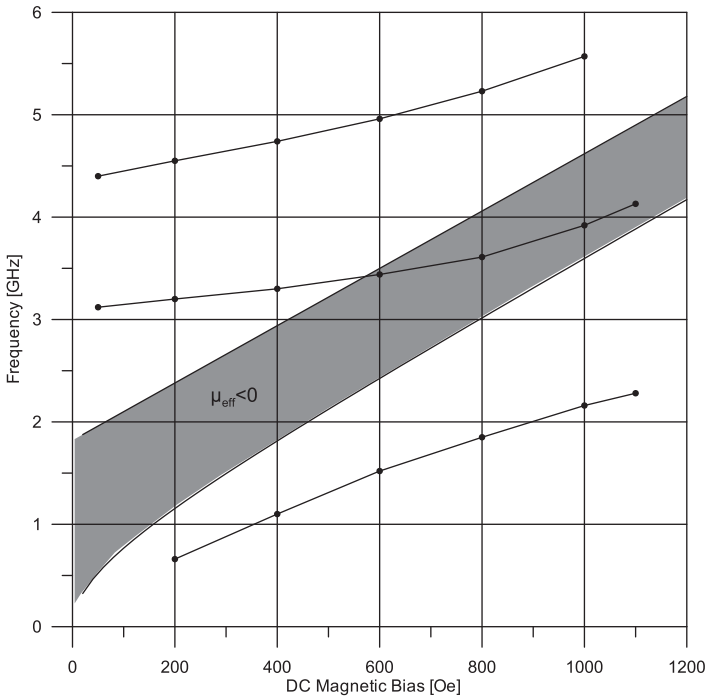

Figure 2: Resonant frequency versus DC magnetic bias of a rectangular patch antenna printed on transversely magnetized ferrite substrate.

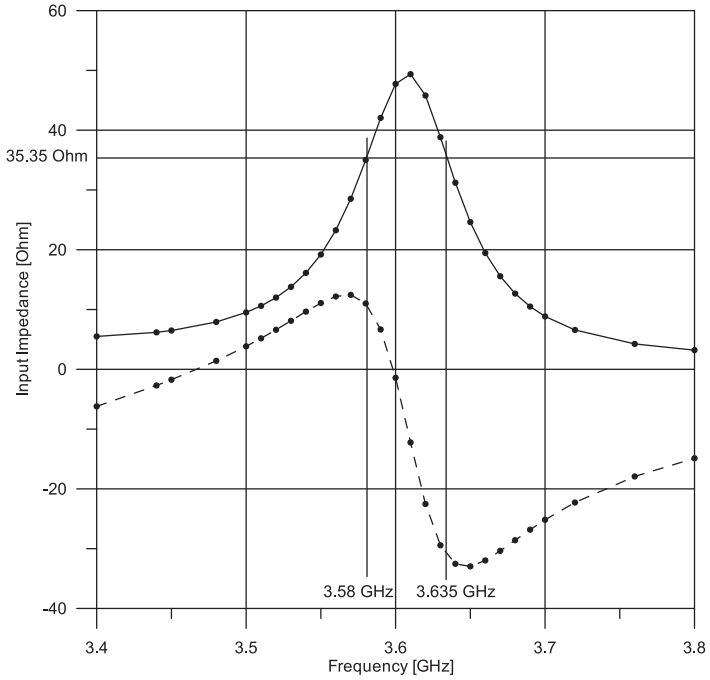

Figure 3: Input impedance of rectangular patch printed on transversely magnetized ferrite substrate.

and it was clearly proved that the resonance control-sensitivity can be greatly improved if a dielectric with lower dielectric constant is used. An identical behaviour is expected for the rectangular patch radiator.

Finally, another important advantage of the ferrite post tuned antennas is that the coaxial connector position can be shifted outside the ferrite. Since ferrites are hard to drill, it is very convenient if the feeding position is located in the dielectric part of the substrate.

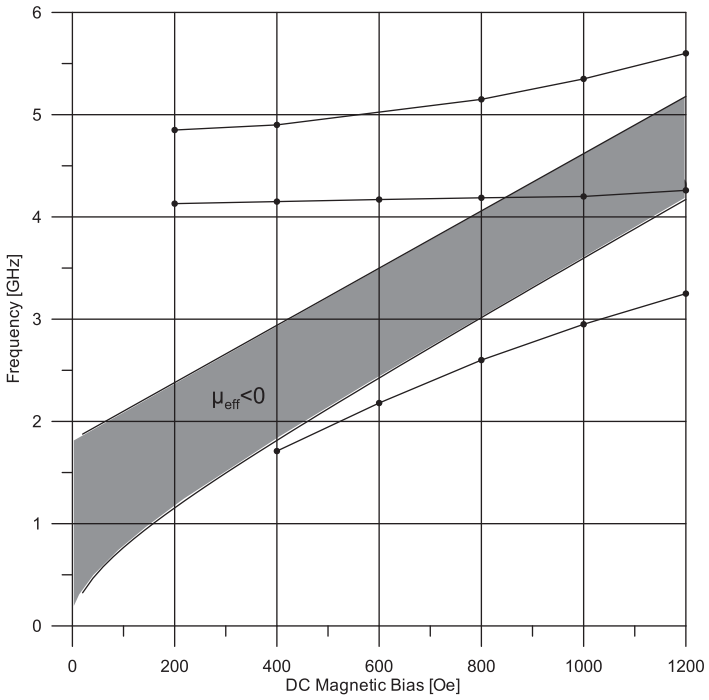

Figure 4: Resonant frequency of rectangular patch tuned by a transversely magnetized rectangular ferrite inclusion.

4. CONCLUSION

The resonating mode inside the negative μ_{eff} area was investigated for the rectangular microstrip patch antenna printed on a transversely magnetized ferrite substrate. Numerical simulations were performed using the Ansoft HFSS software, which provides the ability to include ferrite losses in the analysis. All the numerical results presented here were expected according to the analysis of the circular microstrip patch antenna printed on a transversely magnetized ferrite substrate which was thoroughly studied in our previous work [2, 3]. Results for all the cases studied, show that the investigated mode is excited even when small ferrite losses are considered. Besides the resonant frequency, a study of the input impedance versus feeding position is also presented. A theoretical explanation of the observed novel mode constitutes a challenging future research task.

REFERENCES

1. Pozar, D. M., "Radiation and scattering characteristics of microstrip antennas on normally biased ferrite substrates," *IEEE Trans. AP*, Vol. 40, No. 9, 1084–1092, 1992.
2. Mavridis, A. A., G. A. Kyriacou, and J. N. Sahalos, "Resonant frequencies of circular and ring patch antennas printed on partially magnetized ferrite substrates," *PIERS 2004*, Pisa, Italy, March 2004.
3. Mavridis, A. A., G. A. Kyriacou, and J. N. Sahalos, "On the design of patch antennas tuned by transversely magnetized lossy ferrite including a novel resonating mode," *Progress in Electromagnetics Research*, PIER 62, 165–192, 2006.
4. Baccarelli, P., C. Di' Nalo, F. Frezza, A. Galli, and P. Lampariello, "Anomalous propagation, loss and radiation effects in openwaveguides with gyrotropic media," *IEEE MTT-S Digest*, Vol. 1, 283–286, 1996.
5. Ansoft, HFSS version 8.0.21, Ansoft Corporation, copyright 1984–2001.

Neural Network — Based Design of EBG Surfaces for Effective Polarization Diversity of Wireless Communications Antenna Systems

T. Ganatsos, K. Siakavara, and J. N. Sahalos

The Radiocommunications Lab, Department of Physics, School of Sciences
Aristotle University of Thessaloniki, Thessaloniki 54124, Greece

Abstract— In the present work a Neural Network (NN) procedure for the design of Electromagnetic Band-Gap (EBG) structures with attributes useful to diversity antenna systems is proposed. EGB lattices which have the property to reflect, at the same frequency, x- and y-polarized waves via a 180 degrees phase difference are designed. The employment of EBG structures as reflection surfaces in dipole antenna systems yields results that prove the capability of the system to transmit or receive effectively, circularly polarized waves even if a single linear dipole is used.

1. INTRODUCTION

The signal fading in the mobile radio environment causes severe reception problems. Various techniques, such as, space, polarization, frequency or time and field component diversity are employed to reduce this effect. The most commonly used ones are the space and polarization diversity, due to their benefits. All the aforementioned techniques must not be applied at the cost of a complex or bulky radiating system. From this side of view the polarization diversity offers great advantages, especially to mobile stations' antennas. Low profile antennas using Electromagnetic Band Gap (EBG) printed structures have been proposed for polarization diversity antenna systems. The EBG lattices, unlike normal conductors, do not support propagating surface waves because the currents which flow in their textured metallic surface are very low and it means that the EBG performs as a perfect magnetic conductor (PMC). Therefore if an antenna is located in front of the EBG surface, its currents and their images are in phase and the theoretically expected phase inverse of the reflected field, as in the case of a perfectly conducting surface, does not occur. This property permits a source current to be positioned very close to the EBG surface, without the fields, produced by the source current and its image, to cancel each other. Thus the EBG can function as a unique new type of ground plane for low profile antennas [1–4].

The interesting property of an EBG surface is that the reflection phase varies continuously from 180° to -180°, versus frequency, instead of 180° for a perfect electric conductor (PEC) and 0° for a (PMC). This property should be useful in various applications e.g., a properly designed EBG surface could reflect a x-polarized wave with $+90^\circ$ phase shift, while a y-polarized one with a -90° phase shift. Due to this behaviour, even a single linear dipole antenna, positioned very close to this polarization dependent EBG (PDEBG) surface can effectively receive or transmit circularly polarized waves [5, 6].

The main problem of the entire mechanism is that the $\pm 90^\circ$ phase shifting does not generally occur at the same frequency. In the present work a Neural Network (NN) procedure for the design of EBG structures with pre-specified attributes is presented. The procedure focuses to the determination, via the NN-based algorithm, of the appropriate structural parameter values of the EBG lattice, in order to reduce the difference between the frequencies $f^x_{90^\circ}$ and $f^y_{-90^\circ}$ at which the $\pm 90^\circ$ reflection phase for x- and y-polarized waves is observed. The results extracted by this procedure are applied to a linear dipole antenna system. The antenna's operational characteristics, ascertained via simulation, prove the validity of the NN-based proposed procedure.

2. FORMULATION

The EBG structure under design is illustrated in Figure 1. The dielectric constant of the substrate and its height are $\varepsilon_r = 2.2$, $h = 3.175\,\text{mm}$ (Rogers RT/duroid 5880). The values of L, W, g_x, g_y are the unknown parameters of the problem and are the ones that the proposed NN-based methodology has to determine under the constrain, the frequencies $f^x_{90^\circ}$ and $f^y_{-90^\circ}$ to coincide. A Multiple Layer Perceptron NN [7, 8] was composed and was trained via the Back-Propagation algorithm. The NN's input layer accepts information of the EBG's geometry. It includes two nodes to which the values of the parameters L and g are presented (the initial consideration is that $L = W$ and $g_x = g_y = g$).

The output layer of 5 nodes, accepts the values of the frequencies f_{135°, f_{90°, f_{45°, f_{0°, f_{-45°, f_{-90°, coming from the respective EBG structure the geometry of which was presented to the input of the NN. In this way a mapping between the EGB geometry and its operational characteristics is established. Two hidden layers, each one including 100 nodes were used. These numbers were chosen under the criterion of the best convergence of the NN-algorithm.

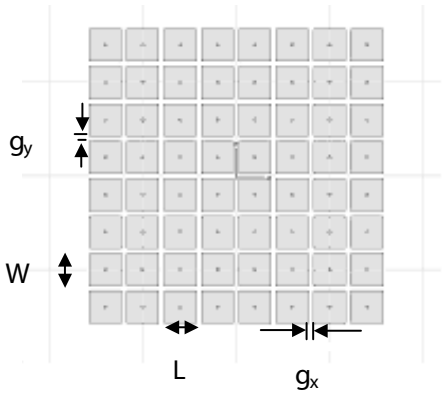

Figure 1: The geometry of the EBG structure.

A training set of 23 pairs of input-output set of values was created by simulation of the respective EBG lattices via the Optimetrics Tool of the HFSS software. By the same process a test collection of 22 input-output pairs of data was created for the valuation of the NN's performance. In the phase of the generalization, the best results, were obtained with an epoch size equal to 1500 and using as activation function the log sigmoid function, $\mathbf{logsig}(\mathbf{n}) = \mathbf{1}/(\mathbf{1} + \mathbf{exp}(-\mathbf{n}))$ and the linear function, $\mathbf{purelin}(\mathbf{n}) = \mathbf{n}$ for the hidden and the output layer, respectively. Two performance functions were used for the training of the NN a) the typical MSE (Eq. (1)) and b) the MSEREG (Eq. (2)) coming from the modification of the MSE by the addition of a new term that consists of the mean of the sum of squares of the network weights and the biases

$$MSE = \frac{1}{N}\sum_{i=1}^{N} e_i^2 = \frac{1}{N}\sum_{i=1}^{N} (t_i - a_i)^2 \tag{1}$$

where N is the number of the output layer nodes, t_i is the ith output node value and α_i is the respected value of the training set, which is presented to this node

$$MSEREG = \gamma MSE + (1-\gamma)\left(\frac{1}{n}\sum_{j=1}^{n} w_j^2\right) \tag{2}$$

where γ is the performance ratio.

The MSEREG function causes the NN to have smaller weights and this forces the network response to be smoother and less likely to overfit. The best generalization was achieved using $\gamma = 0.75$.

Four NN-configurations were used a) in the first one, named NN1, the MSE function was used and 10^3 iterations were made b) in the second one (NN2), the MSEREG with $\gamma = 0.75$ was used and 10^3 iterations were made c) the other two configurations (NN3 and NN4) were similar to the NN2 while in these two cases the number of iterations was dependent on a maximum threshold for the mean square error, defined equal to 0.1. The performance of all four NN procedures is analytically presented in Table 1.

The inverse problem, that is to synthesize the EBG surface with the appropriate geometry in order $f_{90^\circ}^x \simeq f_{-90^\circ}^y$, if the frequencies $f_{90^\circ}^x$ and $f_{-90^\circ}^y$ are pre-specified, is the requirement in the design of an antenna diversity system. Using the above mentioned NN- procedures a large number (10201) of pairs of sets (L, W, g_x, g_y) and the respective sets (f_{135°, f_{90°, f_{45°, f_{0°, f_{-45°, f_{-90°) were created. A computational algorithm based on the above results, was developed in the MATLAB software and yields a) the values of L, W, g_x, g_y and the ratio $\Delta f/f_o$ (where $\Delta f = f_{90^\circ}^x - f_{-90^\circ}^y$) if the frequency of operation f_o and the approximate values of g_x, g_y are given, b) the values L,

Table 1: Results of the NN-procedures' performance. The mean |error| is calculated by the difference between the results yielded by the NN and the respected desired ones.

Configuration	Performance Function	Iterations	Mean |error| Training set	Mean |error| Test set
NN1	MSE	10^3	$3.5\ 10^{-8}$	$4.86\ 10^{-2}$
NN2	MSEREG	10^3	$2.135\ 10^{-2}$	$3.248\ 10^{-2}$
NN3	MSEREG	118	$2.189\ 10^{-2}$	$3.642\ 10^{-2}$
NN4	MSEREG	4	$1.637\ 10^{-2}$	$3.656\ 10^{-2}$

W, g_x, g_y and the precise ratio $\Delta f/f_o$, if the frequency f_o and a maximum permissible value for $\Delta f/f_o$ are given and c) the values L, W, g_x, g_y if the frequency f_o, the ratios g_x/L and g_y/W and a maximum permissible value for $\Delta f/f_o$ are given. The above procedure is graphically presented in Section 3.

3. RESULTS

In this section results for EBG synthesis along with results for the performance of a linear dipole antenna in the vicinity of a designed EBG, are presented. In Figure 2 the ratio $\Delta f/f_o$ as a function of L/W for $g_x = g_y = 0.04\lambda_o$ are shown. For comparison reasons results for all four NN-configurations are presented. It is proved that the ratio $\Delta f/f_o$ tends to zero, that is $f^x_{90^\circ} \simeq f^y_{-90^\circ}$, for $0.8 < L/W < 0.9$. Inside this region, the results of all the NN procedures coincide and it was ascertained that the region is almost independent from the values of g. The results of Figure 3 illustrate the exact values of L and W, which the EBG must have in order to reflect the x- and y-polarized waves with $+90^\circ$ and -90° phase shift, for several values of $g_x = g_y = g$. By this graph the exact values of L and W for specified values of g and f_o can be found. If for example $f_o = 2\,\text{GHz}$ and the desired value of g is equal to $0.01\lambda_o$ then L must be equal to 0.031 m (point A) and $W = 0.036\,\text{m}$ (point B). If the desired value of g is equal to $0.005\lambda_o$ then $L = 0.415\,\text{m}$ (point C) and $W = 0.049$ (point D).

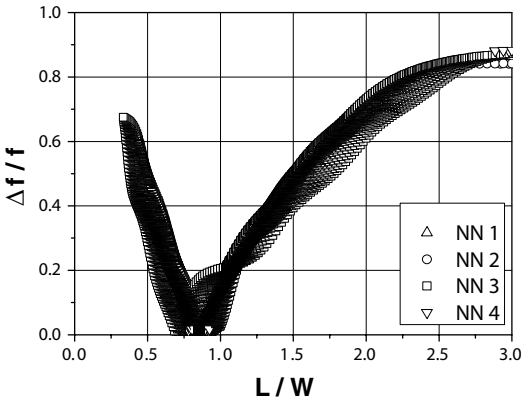

Figure 2: The ratio $\Delta f/f_o$ versus L/W for $g_x = g_y = 0.04\lambda_o$ at 2.1 GHz.

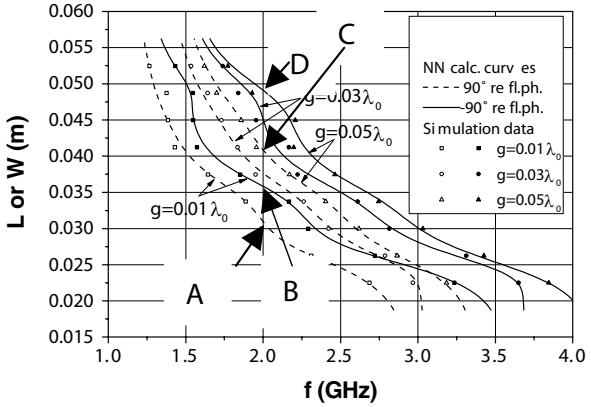

Figure 3: L and W values versus frequency for reflection of x-waves with a $+90^\circ$ phase shift and y-waves with -90°.

In Figures 4 to 7, results for the performance of a low profile linear dipole antenna in front of an EBG, are presented. The antenna system operates in the UMTS frequency band and was designed at $f_o = 2.1\,\text{GHz}$. The EBG reflection surface was synthesized via the NN2 procedure and is composed of a 8×6 planar patch array, positioned on the xz-plane. The size and the spacing of the printed elements are: $L = 44\,\text{mm} = 0.308\lambda_o$, $W = 38.5\,\text{mm} = 0.269\lambda_o$, $g_x = g_y = 4.5\,\text{mm} = 0.0315\lambda_o$ and they are textured on the dielectric substrate which is the Rogers RT/duroid 5880, with height $h = 3.175\,\text{mm} = 0.0222\lambda_o$. The dipole, of length $L_d = 58\,\text{mm} = 0.41\lambda_o$, is positioned in parallel to the EBG surface, at a distance $h_d = 4.42\,\text{mm} = 0.031\lambda_o$. The performance of the EBG was

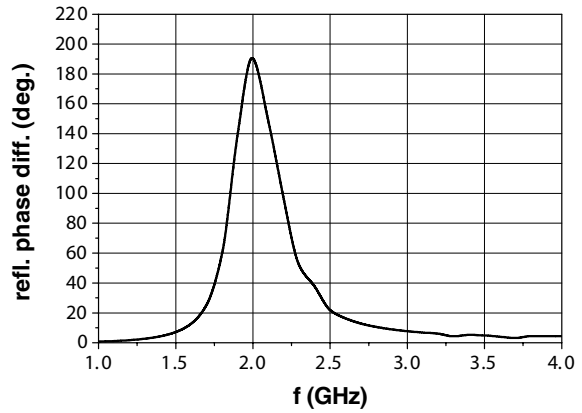

Figure 4: The difference between the reflection phases of the x- and y-waves.

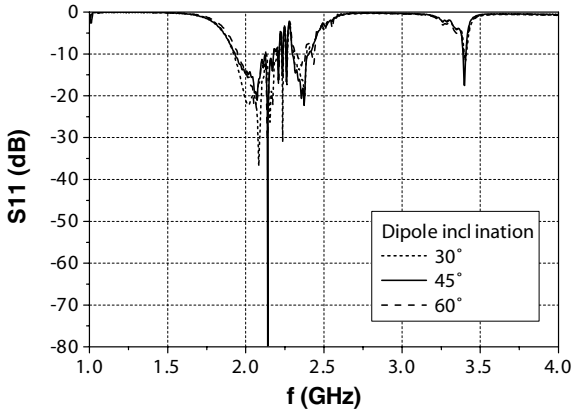

Figure 5: Reflection coefficient at the input of the dipole positioned in front of the EBG.

checked via simulation. In Figure 4 the difference between the reflection phases of x- and y-waves is presented. It is shown that this difference remains greater than 140° in the entire UMTS band. In Figure 5 the reflection coefficient at the feeding input of the dipole for different dipole's orientations with respect to x-axis, are illustrated. For all three orientations $|S11| < -10\,\text{dB}$ in the entire UMTS band and the frequency bandwidth is $\sim 13\%$. Moreover a number of frequency regions at which $|S11|$ is smaller than $-10\,\text{dB}$ appear, coming from the strong coupling between the dipole and the EBG due to their close proximity.

The radiation characteristics of the system are presented in Figures 6 and 7. The magnitude of the axial ratio of the radiated field on the main planes (Figure 6) is less than 3 dB in the UMTS

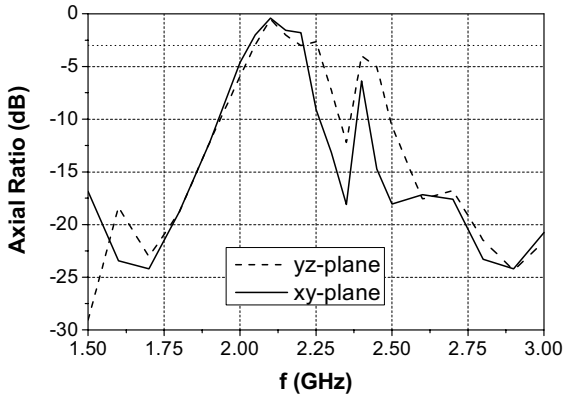

Figure 6: Magnitude of the axial ratio of the radiated field on the main planes. Dipole's inclination, 45°.

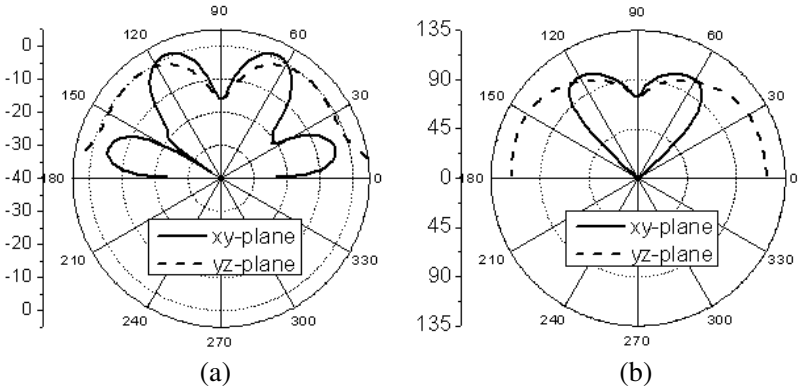

Figure 7: (a) Axial ratio, (b) phase difference between E_θ, E_φ versus θ and φ at 2.1 GHz. Dipole's inclination, 45°.

downlink band. The axial ratio variation, on the main planes, is depicted in Figure 7. Its magnitude is less than 5 dB in a range of $\pm 15^\circ$ around the $\varphi = 65^\circ$ and $\varphi = 115^\circ$ directions on the xy-plane while on the yz-plane it remains less than 5 dB in the range from $\theta = 15^\circ$ to $\theta = 75^\circ$ and from $\theta = 105^\circ$ to $\theta = 165^\circ$.

4. CONCLUSION

In the paper a NN-based methodology is introduced for the design of EBG conducting surfaces appropriate for low profile polarization diversity antenna systems. The target of the composed algorithm is to calculate the proper geometry of the EBG in order it, to reflect the x- and y-polarized waves with $+90^\circ$ and -90° phase shift at the same frequency. A low profile antenna, of a single linear dipole in close proximity to an EBG surface designed by the proposed procedure, was composed for the UMTS frequency band. The results show that the dipole can effectively receive or transmit circularly polarized waves.

REFERENCES

1. Sievenpiper, D., L. Zhang, R. F. J. Broas, N. G. Alexopoulos, and E. Yablonovitch, "High impedance electromagnetic surfaces with a forbidden frequency band," *IEEE Trans. Microwave Theory and Techniques*, Vol. 47, No. 11, 2059–2074, 1999.
2. Yang, F. and Y. Rahmat-Samii, "Reflection-phase characterization of the EBG ground plane for low profile wire antenna applications," *IEEE Trans. on Antennas and Propagation*, Vol. 51, No. 10, 2691–2703, 2003.
3. Siakavara, K., "Enhanced fractal microstrip antenna performance by using photonic bandgap fractal ground plane," *Microwave and Optical Technology Letters*, Vol. 42, No. 5, 397–402, 2004.
4. Ganatsos, T. and K. Siakavara, "Improved microstrip antenna polarization by using electromagnetic band-gap substrates," *Proceedings of International Conference on Antenna Technologies (ICAT 2005)*, 539–543, Ahmedabad, India, Feb. 2005.
5. Yang, F. and Y. Rahmat-Samii, "Polarization-dependent electromagnetic band-gap (PDEBG) structures: Designs and applications," *Microwave and Optical Technology Letters*, Vol. 41, No. 6, 439–444, 2004.
6. McKinzie, W. E. and R. R. Fahr, "A low profile polarization diversity antenna on an artificial magnetic conductor," *Proceedings of IEEE Antennas and Propagation Society International Symposium*, Vol. 1, 762–765, June 2002.
7. Mishra, R. K., "An overview of neural network methods in computational electromagnetics," *Int. J of RF and Microwave Comp. Aided Engineering*, Vol. 12, No. 1, 98–108, 2002.
8. Christodoulou, C. and M. Georgiopoulos, *Applications of Neural Networks in Electromgnetics*, Artech House, Boston, 2001.

Multiple Signal Direction of Arrival (DoA) Estimation for a Switched-Beam System Using Neural Networks

K. A. Gotsis, E. G. Vaitsopoulos, K. Siakavara, and J. N. Sahalos

Radiocommunications Lab, Department of Physics, School of Sciences
Aristotle University of Thessaloniki, Thessaloniki 54124, Greece

Abstract— A new Direction of Arrival (DoA) estimation method based on Neural Networks (NNs) is presented. The proposed NN-DoA procedure is especially designed for a Switched-Beam System (SBS), whose basic component is an 8×8 Butler Matrix (BM). The technique is simple and appropriate for real time applications. Simulations of DoA estimation tests show accurate results even for a big set of simultaneously incident signals.

1. INTRODUCTION

DoA estimation for signals impinging on an antenna array is a very important issue for wireless communications. Several methods have been proposed and developed concerning DoA finding in wireless systems [1–3]. The most widespread methods are the so-called subspace ones and the most popular algorithms amongst them are the *MUSIC* [4], the *ESPRIT* [5] and their variants. The implementation, [6], of the above super resolution algorithms is quite complicated and computationally intensive. Also, the signals have to be uncorrelated and there is a need for many signal snapshots. A faster DoA estimation algorithm is proposed in [7]. It is based on a pseudocovariance matrix and a small number of signal snapshots. In all the aforementioned techniques, for an N element array, the relation $M \leq N$ should be satisfied for the discrimination of M incident signals. Recently the *Matrix Pencil* (MP) method, [8, 9], has been introduced for DoA estimation purposes. Its main advantage is that it uses a single snapshot of the input signals, and therefore the computational time is reduced. However, accurate DoA finding can be made only for $M \leq (N+1)/2$ simultaneously incoming signals. Neural Network (NN) DoA estimation methods constitute a new sort of DoA finding procedure, [10–12]. The NN methodologies are based on the mapping between the signal autocorrelation matrix and the angles of arrival. Since they do not perform eigen-decomposition processes, they are found to be faster than the conventional super-resolution techniques. The majority of DoA estimation algorithms concern adaptive array systems, which perform either digital or analog beamforming. In most works digital beamforming is applied. However, in [13, 14] analogue beamforming architectures are presented proposing DoA finding for parasitic arrays. In this paper, a NN based DoA estimation method for a SBS system is presented, called the **NN-SBS** method.

2. BRIEF DESCRIPTION OF THE SWITCHED-BEAM SYSTEM

A smart antenna system that relies on a fixed Beam Forming Network (BFN), instead of a series of adaptive array processors, is called Switched-Beam System (SBS) [1]. In a SBS, a switch is used to select the best beam of receiving a particular signal, from a number of fixed beams. Such systems are quite popular, because they offer many of the advantages of the fully adaptive systems at less expense and complexity.

The radiating part of the SBS used in the present work is a linear array of eight, $\lambda/2$ spaced, microstrip patches structured on a single dielectric layer with substrate of $\varepsilon_r = 2.2$ (λ is the carrier wavelength).The array is fed by an 8×8 Butler Matrix, [15], and the entire system operates at 2.4 GHz. The input ports of the BM are connected to a switching network that performs beam switching using SPDT (Single Pole Double Throw) switches. The simulated radiation pattern of the described structure is shown in Figure 1.

3. DOA ESTIMATION METHOD AND NEURAL NETWORK TRAINING

The proposed DoA estimation method is based on the application of strict power control at the mobile stations and on the a priori knowledge of the number of simultaneously incoming signals. Due to power control, all signals are received at the base station with the same power level. Therefore, the contribution of each signal to the total measured power depends only on its angle of incidence.

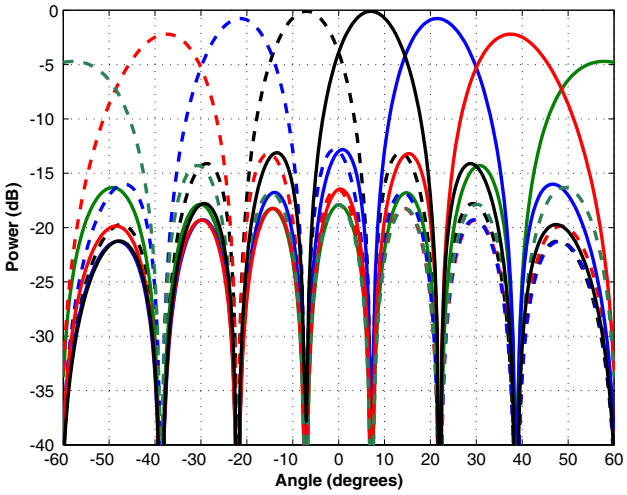

Figure 1: Radiation pattern of an eight patches SBS.

The input power coming from each beam is measured through an appropriate meter connected to the switching network.

Consider a random set of N signals arriving in a 120° sector from angles φ_i, $i = 1 \ldots N$, $-60° \leq \varphi_i \leq 60°$. The angles compose a vector $\boldsymbol{\varphi} = (\varphi_1, \varphi_2, \ldots, \varphi_N)$. If beam switching takes place, each one of the eight beams P_j gives a total power $P_{tj}, j = 1 \ldots 8$, where:

$$\begin{aligned} P_{t1} &= P_1(\phi_1) + P_1(\phi_2) + \ldots + P_1(\phi_N) \\ P_{t2} &= P_2(\phi_1) + P_2(\phi_2) + \ldots + P_2(\phi_N) \\ &\ldots\ldots\ldots\ldots \\ P_{t8} &= P_8(\phi_1) + P_8(\phi_2) + \ldots + P_8(\phi_N) \end{aligned} \quad (1)$$

Equation (1) gives a power vector $\mathbf{P} = (P_{t1}, P_{t2}, \ldots, P_{t8})$, thus a mapping between $\mathbf{P}$ and the corresponding vector $\boldsymbol{\varphi}$ is established. Our aim is to utilize this mapping to accomplish DoA estimation, based on neuro-computational techniques. A set of M angle vectors $\boldsymbol{\varphi}_\mathbf{m}$ is created, each one composed by randomly selected N angles of arrival. The index m denotes the mth angle vector. The random angle values are equal to integer multiples of $\Delta\varphi$, within the prespecified angular range. The value of the step angle $\Delta\varphi$ was defined equal to 0.5 degrees. A collection of randomly created pairs $(\boldsymbol{\varphi}_\mathbf{m}, \mathbf{P}_\mathbf{m})$ is generated that is used as training set for the NNs. The number of pairs is $M = 3000$ or $M = 4000$. Considering the entire set of different possible vectors $\boldsymbol{\varphi}_\mathbf{m}$, the training set volume is very small. This shows the effectiveness and the generalization capabilities of a properly trained NN.

Multilayer Perceptron (MLP) NNs are used, [16], composed by: 1) an input layer of eight nodes which is fed by the vectors $\mathbf{P}_\mathbf{m}$, 2) an output layer of N nodes that gives the corresponding vectors $\boldsymbol{\varphi}_\mathbf{m}$, and 3) one or two hidden layers. The number of hidden layers and the number of each layer's nodes depends on the value of N. The criterion of their choice is the better NN training convergence and the results' accuracy. The activation function of the hidden layers is the hyperbolic tangent function and the activation function of the output layer is linear. The NNs' training has been performed to MATLAB using the learning algorithm Levenberg-Marquardt (LM) [17]. The LM algorithm provides a relatively fast numerical solution to the minimization of the performance function, which is the Mean Square Error (MSE) (i.e., the averaged squared error between the network outputs and the target outputs during the training). The training stops when the MSE minimization reaches a plateau. Since the training of the NNs is over, the DoA estimation procedure is summed up to the following four steps: a) Simultaneous arrival of N signals. b) Beam switching and measurement of the total power for each beam. c) Feeding of the trained NN with the measured power vector. d) NN calculation of the DoA estimation vector.

4. DOA ESTIMATION SIMULATIONS

In this section the results of simulated DoA estimation tests using the proposed NN-SBS method are presented. The simulation procedure has been performed to MATLAB, following the steps

mentioned in the end of Section 3. Vectors $\boldsymbol{\varphi}_\mathbf{m}$ are randomly generated and from Equation (1) the vectors $\mathbf{P}_\mathbf{m}$ are calculated. These power vectors correspond to the power that would be measured in a real DoA estimation problem. The vectors $\mathbf{P}_\mathbf{m}$ are fed to the proper NN that instantly gives as output the DoA estimation vectors. The accuracy of the technique is tested by comparing the estimated DoA vector with the initial vector $\boldsymbol{\varphi}_\mathbf{m}$, which is considered as the real DoA. In Figure 2, DoA estimation simulation diagrams are shown, for 1, 4, 8, and 15 incoming signals. The number of random arrivals tested for each case is 12000, so as to obtain uniform angle of arrival distribution.

Table 1: DoA estimation simulations results.

Number of Signals	**Mean Value $\Delta\boldsymbol{\varphi}_\mathbf{DoA}$**	**Standard Deviation $\Delta\boldsymbol{\varphi}_\mathbf{DoA}$**	**$\Delta\boldsymbol{\varphi}_\mathbf{DoA} < 5°$ (%)**
1	0,13	0,07	100,00
4	1,77	1,46	96,42
8	2,34	1,87	90,68
15	2,41	1,98	89,84

The absolute difference between real and estimated DoA, $\Delta\varphi_{\mathrm{DoA}}$, is statistically processed over the sample of 12000 arrivals, and the results are shown in Table 1. The table gives the mean value and the standard deviation of $\Delta\varphi_{\mathrm{DoA}}$, and the percentage of $\Delta\varphi_{\mathrm{DoA}}$ that is less than 5 degrees. The simulations results and diagrams show a robust behavior of the NN and achievement of accurate DoA estimation, even if the number of incoming signals is greater than the number of the antenna elements.

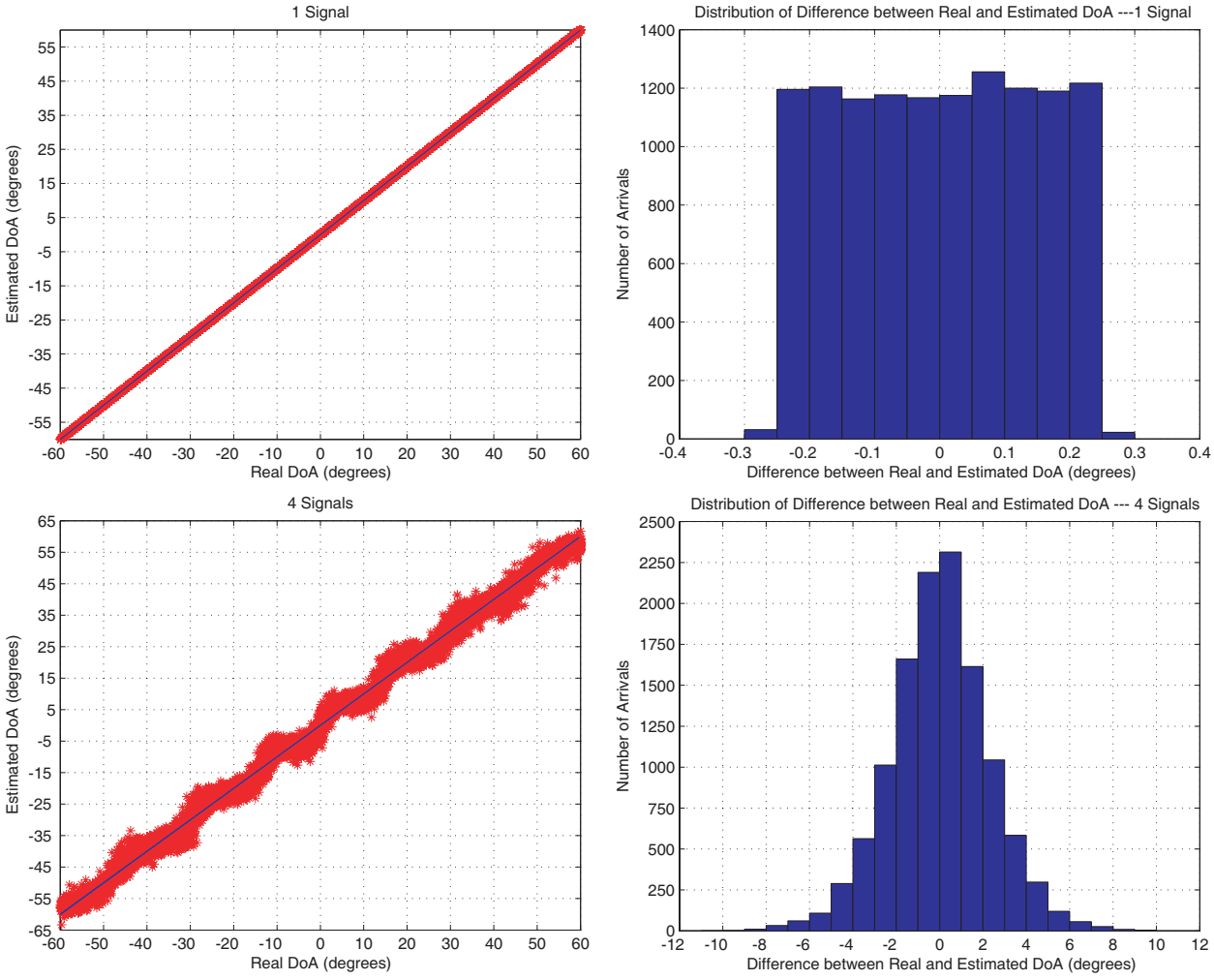

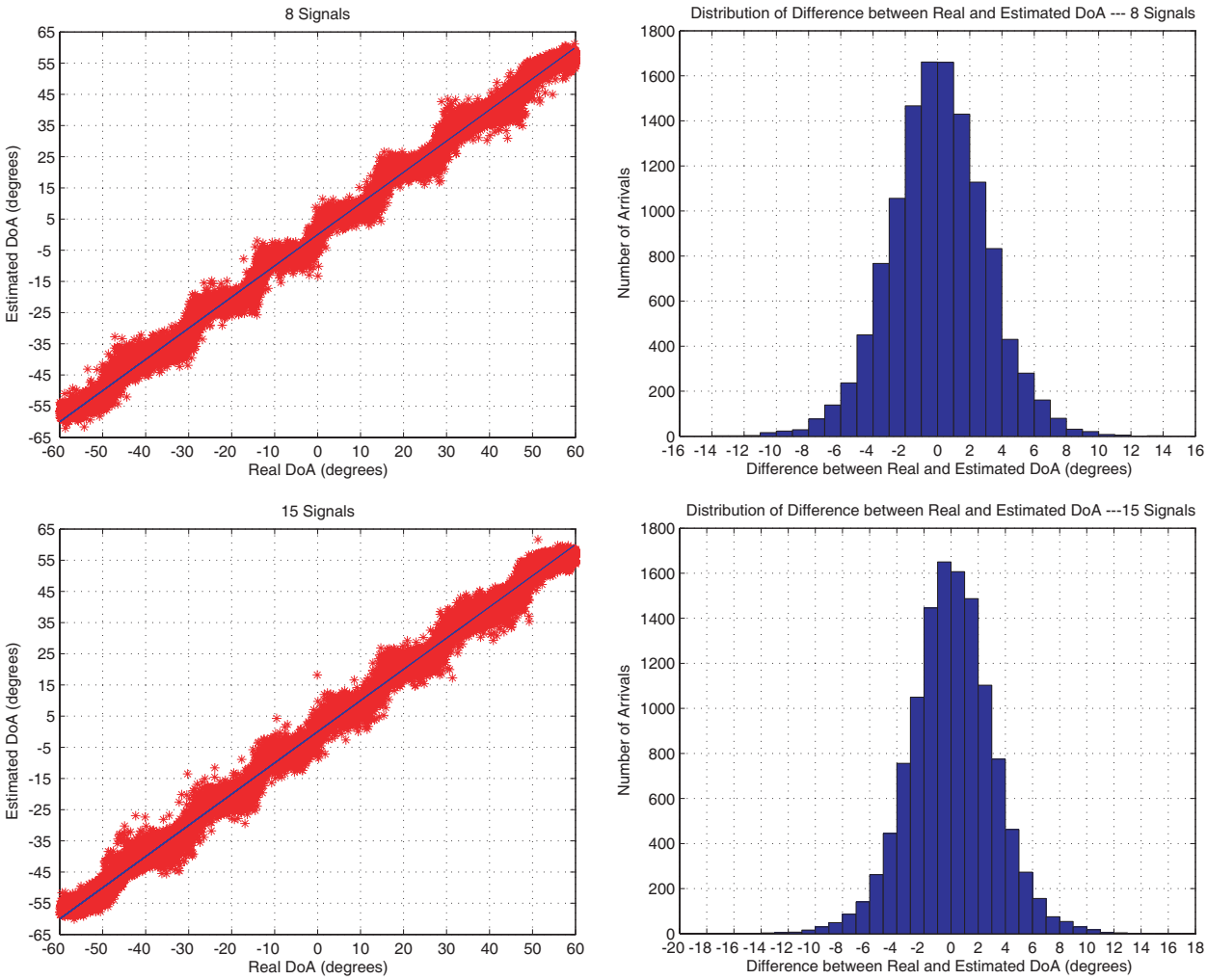

Figure 2: DoA estimation simulations diagrams.

5. CONCLUSION

A new DoA estimation method (NN-SBS) for a switched-beam system using neural networks was described. The synthesis, the requirements and the accuracy of the proposed method provide some interesting advantages. The most widespread super resolution algorithms (MUSIC, ESPRIT, Matrix Pencil etc.) need measurements at every antenna element and intensive signal processing in order to perform eigen-decomposition processes. Other NN based techniques require at least the calculation of the signal autocorrelation matrix. In the proposed method only power measurements at a single point of the system is needed, saving cost, complexity and time. Additionally, due to the simplicity of the technique and the speed of NNs, real time applications can be easily served into existing base stations. Finally, contrary to the majority of DoA estimation algorithms, accurate results are obtained even for a big set of incoming signals.

ACKNOWLEDGMENT

This work is implemented in the framework of Measure 8.3 through the O.P. Competitiveness 3rd Community Support Programme and is co-funded by: 75% of the Public Expenditure from the European Union — European Social Fund, 25% of the Public Expenditure from the Hellenic State — Ministry of Development — General Secretariat for Research and Technology, and Private Sector (INTRACOM S.A.).

REFERENCES

1. Liberti, J. C., Jr. and T. S. Rappaport, *Smart Antennas for Wireless Communications: IS-95 and Third Generation CDMA Application*, Prentice Hall PTR, New Jersey, 1999.

2. Godara, L. C., "Application of antenna arrays to mobile communications, part II: Beamforming and direction-of-arrival considerations," *Proc. IEEE*, Vol. 85, 1195–1245, August 1997.
3. Chandran, S., *Advances in Direction of Arrival Estimation*, Artech House, Boston, London, 2006.
4. Schmidt, R. O., "Multiple emitter location and signal parameter estimation," *IEEE Transactions on Antennas and Propagation*, Vol. 34, No. 3, 276–280, March 1986.
5. Ray, R. and T. Kailath, "ESPRIT-estimation of signal parameters via rotational invariance techniques," *IEEE Transactions on Acoustics, Speech, Signal Processing*, Vol. ASSP-37, 984–995, 1989.
6. Eric, M. and B. Igric, "Practical implementation and performance estimation of MUSIC method implemented on signal processor TMS 320c30," *Scientific-Technical Review*, Vol. LIV, No. 1, 2004.
7. Kim, J.-T., S.-H. Moon, D. S. Han, and M.-J. Cho, "Fast DOA estimation algorithm using pseudocovariance matrix," *IEEE Transactions on Antennas and Propagation*, Vol. 53, No. 4, 1346–1351, April 2005.
8. Koh, J. and T. K. Sarkar, "High resolution DOA estimation using matrix pencil," *Antennas and Propagation Society International Symposium, IEEE*, Vol. 1, 423–426, June 2004.
9. Yilmazer, N., J. Koh, and T. K. Sarkar, "Utilization of a unitary transform for efficient computation in the matrix pencil method to find the direction of arrival," *IEEE Transactions on Antennas and Propagation*, Vol. 54, No. 1, 175–181, January 2006.
10. Du, K.-L., A. K. Y. Lai, K. K. M. Cheng, and M. N. S. Swamy, "Neural methods for antenna array signal processing: A review," *Signal Processing*, Vol. 82, 547–561, 2002.
11. Zooghby, A. H., C. G. Christodoulou, and M. Georgiopoulos, "A neural network-based smart antenna for multiple source tracking," *IEEE Transactions on Antennas and Propagation*, Vol. 48, No. 5, 768–776, May 2000.
12. Mochida, E. and Y. Iiguni, "Adaptive DOA estimation using a radial basis function network," *Electronics and Communications in Japan*, Part 3, Vol. 88, No. 9, 11–20, 2005.
13. Taillefer, E., A. Hirata, and T. Ohira, "Direction-of-arrival estimation using radiation power pattern with an ESPAR antenna," *IEEE Transactions on Antennas and Propagation*, Vol. 53, No. 2, 678–684, February 2005.
14. Varlamos, P. K. and C. N. Capsalis, "Direction-of-arrival estimation (DoA) using switched parasitic planar arrays and the method of genetic algorithms," *Wireless Personal Communications*, Vol. 28, 59–75, 2004.
15. Butler, J. and R. Lowe, "Beam forming matrix simplifies design of electronically scanned antennas," *Electronic Design*, Apr. 1961.
16. Christodoulou, C. and M. Georgiopoulos, *Applications of Neural Networks in Electromagnetics*, Artech House, Boston, London, 2001.
17. Demuth, H. and M. Beale, *Neural Network Toolbox for Use With MATLAB, User's Guide (Fifth Edition)*, The Math Works, Inc., 1998.